PFC/RR-86-14 DOE/ET-51013-185

VUV Study of Impurity Generation during ICRF Heating Experiments on the Alcator C Tokamak

Manning, Herbert L.

June 1986

Plasma Fusion Center
Massachusetts Institute of Technology
Cambridge, MA 02139

VUV Study of Impurity Generation During ICRF Heating Experiments on the Alcator C Tokamak

A thesis presented

by

Herbert Leslie Manning, Jr.

to

The Department of Physics

in partial fulfillment of the requirements

for the degree of

Doctor of Philosophy

in the subject of

Physics

Harvard University

Cambridge, Massachusetts

May, 1986

Abstract:

A 2.2 meter grazing incidence VUV monochromator has been converted into a time-resolving spectrograph by the addition of a new detector system, based on a microchannel plate image intensifier linked to a 1024-element linear photodiode array. The system covers the wavelength range 15-1200 Å (typically 40 Å at a time) with resolution of up to .3 Å FWHM. Time resolution is selectable down to 0.5 msec. The system sensitivity was absolutely calibrated below 150 Å by a soft X-ray calibration facility. The spectrograph was installed on the Alcator C tokamak at MIT to monitor plasma impurity emission. There, cross-calibration with a calibrated EUV monochromator was performed above 400 Å. Calibration results, system performance characteristics, and data from Alcator C are presented.

Observations of impurity behavior are presented from a series of ICRF heating experiments (180 MHz, 50–400 kW) performed on the Alcator C tokamak, using graphite limiters and stainless steel antenna Faraday shields. Large increases in metal impurity levels were seen during the RF pulse, with iron increasing by a factor of 12 at the highest RF powers. Much smaller increases in carbon and oxygen were seen. Potential impurity sources and release mechanisms are discussed. Analysis of inferred iron source rates shows a linear dependence on RF power up to 400 kW, with no clear dependence on resonance conditions or bulk plasma parameters. However, a sharp increase in electron temperature, T_e, in the limiter shadow region, seen during the ICRF pulse, was well correlated with the iron influx rate. It is concluded from this and other evidence that enhanced sputtering of the Faraday shield due to an elevated sheath potential ($\phi_{sh} \sim 3T_e$) is the primary source of metal impurities during ICRF heating on Alcator C. This process, occurring at the limiter, is the dominant source of carbon and oxygen. These results are consistent with sputtering yields obtained from an edge erosion code, which utilized measured changes in edge T_e profiles.

Table of Contents

List of figures

List of Tables

Frequently Used Abbreviations and Symbols

CX	Charge eXchange	I_P	Plasma current
EUV	Extreme UltraViolet	n_e, n_i	Density of electrons, ions
HFS(A)	High Field Side (Antenna)	n_j	Impurity density, jth state
ICRF	Ion Cyclotron Range of Frequencies		
LFS(A)	Low Field Side (Antenna)	n_Z	Impurity density, all states
MCP	MicroChannel Plate	$P_{\rm RF}$	RF Power
MHD	MagnetoHydroDynamic	R	Major radius variable
NBI	Neutral Beam Injection	r	Minor radius variable
OH	Ohmic Heating	S_Z	Source rate of impurity Z
PDA	PhotoDiode Array	$S_{\rm Fe}$	Source rate of iron
PHA	Pulse Height Analyzer	T_e, T_i	Electron, ion temperature
PHD	Pulse Height Distribution	V	Convection velocity
PIXE	Proton Induced X-ray Emission		
RF	Radio Frequency	$Z_{\rm eff}$	Effective plasma ion charge
SOL	Scrape-Off Layer	β_T, β_P	Toroidal and poloidal beta
SXR	Soft X-Ray	$\Phi_{\rm sh}$	Sheath potential
VUV	Vacuum UltraViolet	λ	Wavelength
a, a_l	Limiter radius	λ_B	Blaze wavelength
B	Brightness	λ_n	Edge density decay length
B_T, B_ϕ	Toroidal magnetic field	λ_T	Edge temp. decay length
D	Diffusion coefficient		
n_{eb}, T_{eb}	Density, temperature of electrons in boundary layer (SOL)		

Acknowledgments

As one phase of my life comes to a close, and a new phase begins, I wish to thank some of the people who have helped me reach this point. Some are at Harvard, where I was enrolled, and some are at MIT's Plasma Fusion Center, where I did my thesis research.

At Harvard, I am grateful to Profs. Edward Purcell, Paul Horowitz, and especially Costas Papaliolios for serving as my academic advisors. I also thank the latter two and Prof. R.V. Pound for serving on my thesis committee. The friendship of several classmates helped make my coursework period much more enjoyable. They include Bill Danchi, Mike Aziz, Dean Bocobo, Bill Foster, Bruce Cortez, Kelby Chan, and Dave Abraham.

At MIT, Dr. James Terry has been much more than a research supervisor these past years. I value his friendship as highly as I value the vast amount of physics and research techniques he has taught me. He has given me encouragement, guidance, and advice when I needed them, and he has pushed me when I needed to be pushed. He has been directly involved in all of the work reported here, and he deserves much of the credit for the success of the VUV spectrograph. It has been a pleasure to work with "JT".

Dr. Earl Marmar, my group leader at Alcator, has offered many valuable insights and comments on my work, especially the analytical part. He too has been a source of guidance, encouragement, and friendship.

I also thank Prof. Ron Parker for letting an alien grad student from up Mass. Ave. join the Alcator group, and for his overall leadership of the Alcator project.

There are many other people in the Alcator group, both research staff and students (past or present), whom I thank for their friendship, and for technical contributions to this work (noted in parentheses). They include Mr. Russ Benjamin, Dr. Boyd Blackwell (ICRF heating experiments), Dr. Catherine Fiore (Charge exchange data), Mr. Steve Fairfax, Mr. Mark Foord ($Z_{\rm eff}$ data), Dr. Rex Gandy,

Dr. Bob Granetz, Dr. Martin Greenwald, Ms. Beth Koester, Dr. Brian LaBombard (Langmuir probe data), Dr. Bruce Lipschultz (erosion code and sputtering data), Dr. Steve (Graphics package) and Mrs. Eileen McCool, Mr. John Moody (ICRF data) Dr. Juan Moreno (EUV cross-calibration), Dr. John O'Rourke, Dr. Jeff Parker, Mr. Pat Pribyl (computer wizardry), Dr. John Rice (T_e data), Dr. Yuichi Takase, Mr. Alan Wan (edge analyzer), Dr. Reich Watterson, and Dr. Steve Wolfe (n_e data and shot logs). Brian, Mark, and Pat are especially thanked for their friendship over the years.

The rest of the Alcator C research and support staff are thanked for their help in operating the tokamak, fabricating equipment, taking data, etc. Special thanks go to Bob Childs, Bill Beck, John Heckman, Mark Iverson, Bruce Oliver, Charlie Park, Bill Parkin, Laurie Pfeifer, Harold Shriber, Frank Silva, Ed Thibeault, Eric Woodworth, and to Woody Woodworth and his crew.

I owe a word of appreciation to the various vendors with whom I worked during this project. They include Jim Manson (Soft X-ray calibration facility), Pete Besen and Don Schulsinger (Reticon electronics), John Gray (MCP image intensifier), and Bob Denault and Jack Parmley of McPherson Instruments. I thank Dr. Barney Doyle of Sandia Laboratory for the PIXE analysis of the graphite limiter block. This work was carried out under United States Department of Energy contract no. DE-AC02-78ET51013. I also acknowledge financial support from the National Science Foundation for a portion of my studies.

Finally, I thank those closest to me for their support and encouragement. I thank Paige Woltzen for bringing so much joy into my life in recent years. I also thank Molly, for always having faith that her big brother could do anything. And last, but far from least, I give much thanks to my parents for all their love and care through the years.

to my parents

Chapter 1

Introduction

1.1 Nuclear Fusion

Ever since prehistoric Man first discovered fire, the rise of civilization has involved a growth in energy consumption. Until relatively recent times, energy usage increased at a modest and unalarming rate. In the modern era, however, the combined effects of the Industrial Revolution and the world population explosion have propelled energy usage to such elevated levels that we are confronted with the limited supply of traditional fossil fuels contained in the earth. In the past two decades, futurists have warned of projections showing total depletion of the world's reserves of coal, oil, and gas, based on then current growth rates, within a few centuries or less. Conservation efforts, new explorations, and reduced growth rates have brightened the picture somewhat, but the spectre of fossil fuel exhaustion remains a very serious concern for the future. On a more local level, many industrial nations have become net importers of fossil fuel, raising fears of security impairment due to dependence on foreign sources of dubious stability. Alternative energy sources must be developed if these fears are to be allayed.

Renewable energy sources (solar, wind, biomass, hydro, etc.) show some promise, but at this time offer no clear remedies to the problem. Geothermal energy may also help, but seems unlikely to prove sufficient for significant power production. Nuclear fission has proven to be a viable power producing energy source, but non-breeding fission reactors also face the problem of limited uranium reserves. Breeder reactors can extend the lifetime of world uranium reserves many times.

However, they are relatively untested, and, like non-breeders, face considerable public opposition due to fears of safety, nuclear proliferation, and cost.

Nuclear fusion, the process which fuels the stars, holds considerable promise as an energy source [1-4]. The basic fuel for the simplest fusion reactor is deuterium, an isotope of hydrogen with a fractional abundance of approximately 1/7000. One cubic kilometer of water contains more potential fusion energy than there is chemical energy in all the world's known oil reserves. There is enough deuterium in the oceans to fuel civilization for billions of years, even at the highest energy usage rate possible without overheating the environment. Fusion reactors are inherently safer than fission reactors; they cannot melt down or run out of control, and the radioactive materials involved (tritium plus reactor component materials activated by neutron bombardmant) are much less toxic and easier to dispose of than are those from a fission reactor. The radioactive halflives are much shorter, and there is no concentrated fissile fuel to tempt terrorists or thieves. The realization of fusion's promise, however, is far from easy. Research which began in the 1950's has yet to reveal whether or not fusion can be utilized in a practical, economically feasible power plant. In fact, experiments have not even demonstrated net energy gain from a controlled fusion reaction, although current projects at several laboratories hope to do so within this decade.

The central problem is to efficiently heat the fusion fuel to the hundred million degree temperature regime necessary for a significant number of thermonuclear fusion reactions to occur, and to confine enough heated fuel for a long enough period of time to get substantially more energy out of the reactor than was required to reach these conditions. At these temperatures the hydrogen fuel is completely ionized, forming a plasma of free electrons and nuclei. The hot plasma must be isolated from the relatively cold material surrounding it, otherwise it loses its heat

too rapidly to the walls of the reactor chamber. A measure of the effectiveness of the insulation of the hot plasma is the energy confinement time, τ_E, which is roughly the energy content of the plasma divided by the rate of energy loss. A well-known criterion for net energy production, the Lawson criterion [5], states that

$$n\tau_E \geq 6 \times 10^{13} \text{ cm}^{-3}\text{sec}, \tag{1.1}$$

where n is the electron density of the plasma. For a realistic power reactor, with the plasma at or near self-sustaining ignition conditions, the criterion is stricter:

$$n\tau_E \geq 3 \times 10^{14} \text{ cm}^{-3}\text{sec} \tag{1.2}$$

How can one contain a hundred million degree plasma for any time at all, if it must be kept away from colder gases or material structures? One approach is inertial confinement fusion, which utilizes very high density and relatively short confinement times. This method, which is used in the successful but uncontrolled fusion Hydrogen bomb, heats the plasma so quickly that sufficient fusion reactions occur before the particles have time to escape the reacting volume. Attempts to reproduce this behavior in a controlled reactor setting are ongoing, using powerful lasers or particle beams to heat and compress the fusion fuel.

A second method for confining the plasma is through the use of strong magnetic fields. Since the electrically charged particles of the plasma tend to gyrate along the lines of a magnetic field, a suitably tailored magnetic field configuration can be used to keep the particles confined in a given region of space, where they may be heated to fusion temperatures and densities. This approach utilizes much lower plasma densities and much longer energy confinement times than does the inertial confinement scheme, and has so far met with more success in the laboratory. The current experiments which hope to achieve net energy gain use toroidal magnetic fields for confinement in a configuration known as a tokamak, which is a Russian

acronym for toroidal magnetic chamber. Basically, the magnetic field lines are bent into a circular doughnut-shaped volume, and the plasma particles follow these field lines, thus achieving isolation from the surrounding vacuum vessel and magnets. The tokamak has been the most successful plasma confinement configuration to date, although many other geometries have been tried and continue to be tested.

1.2 Thesis Structure

This thesis is concerned with a series of experiments conducted on an experimental tokamak at the Massachusetts Institute of Technology's Plasma Fusion Center, known as the Alcator C Tokamak. Alcator C is a basic physics research tokamak, never intended as an energy break-even device, with emphasis on issues related to particle and energy confinement and the use of radio frequency waves to heat the plasma and drive electric currents in the plasma. One of the problems facing fusion research is the presence of impurities (elements other than hydrogen) in the plasma, which can provide an important energy loss channel for the plasma and even lead to loss of plasma confinement, if the level of impurity contamination becomes too high. It is therefore important to monitor the levels of impurities in experimental plasmas, as well as to understand the sources and mechanisms for impurity generation and transport. Since each impurity ion species which still has at least one bound electron radiates light at well-known wavelengths, spectroscopic measurements of transition line radiation brightnesses yield information on impurity concentrations, impurity transport, etc.

The primary goal of this thesis is to gain a better understanding of a particular impurity problem that afflicts tokamaks utilizing ICRF (Ion Cyclotron Range of Frequencies) resonant heating. Although ICRF heating has been selected by several design studies as the method of choice for heating future tokamak reactor plasmas

[6-8] high powered ICRF experiments in many past and current tokamaks have been plagued with large influxes of impurities into the plasma. Understanding and overcoming this obstacle represents a key technological challenge for the tokamak fusion program. During a series of such ICRF heating experiments on Alcator C, large influxes of metal impurities were observed to accompany the pulsed application of ICRF power. The level of impurities in Alcator C was monitored via spectroscopic measurements in the vacuum ultraviolet (VUV) wavelength regime. A detailed analysis of the impurity influx during ICRF heating was undertaken to shed light on the source(s) of the additional impurities and the mechanism(s) responsible for their release.

The structure of this thesis is as follows: Chapter 1 provides background information on tokamak fusion research. The fundamental concepts of a tokamak device are reviewed, and specific parameters for Alcator C are given. The effects of impurities, both bad and good, are discussed. The use of plasma spectroscopy as a diagnostic of both impurities and overall plasma behavior is summarized. This chapter concludes with a statement of the thesis problem and motivation.

Chapter 2 describes the VUV time-resolving spectrograph used in these experiments to monitor the impurity concentrations. Attention is focused on the detector system, which was fabricated in the course of this work. Based upon a microchannel plate image intensifier coupled via a fiber optic imaging relay to a 1024-element self-scanned linear photodiode array, this system represents a major improvement over the previous single channel detector, which functioned as a monochromator. Design objectives, construction details, and alignment procedures are described, as is the installation on Alcator C.

Chapter 3 presents a summary of the measured system performance characteristics. The soft X-ray calibration facility used for absolute sensitivity measurements

and calibration is described, along with the procedures for the calibration. Measured performance characteristics are also presented, including gain curves, linearity, and temporal and spectral resolution. Several applications for analyzing tokamak data are presented, with examples and useful data reduction techniques.

Chapter 4 introduces the subject of impurities generated during ICRF experiments with a brief overview of ICRF heating. Impurity-related effects from previous and current ICRF experiments at other tokamaks are summarized. The Alcator C ICRF heating program is described, and it is shown that a large influx of metallic impurities accompanies the injection of RF power into the tokamak. The impurity concentrations are analyzed for a series of high power ICRF heating experiments, and it is shown that the impurity levels rise with the injected ICRF power.

Chapter 5 continues with a detailed analysis of the impurity generation process during ICRF heating on Alcator C. Possible impurity sources and liberation mechanisms are described. It is shown that the graphite limiter, the material structure closest to the plasma, is contaminated with surface deposits of metallic impurities, but that this is probably not the source of the enhanced metallic impurity influx. A systematic study of calculated edge source rates of iron impurity atoms is presented, and a conclusion is reached that thermal sputtering of the ICRF antenna's stainless steel Faraday shield is the dominant source of metallic impurities during ICRF heating. A numerical code which simulates edge erosion, and whose results qualitatively support the conclusion, is discussed. Comparisons to other tokamak results are presented, along with a discussion of uncertainties in the model and unanswered questions.

Chapter 6 closes with a summary of results and suggestions for future work. Both VUV spectroscopy in general and issues related to impurity generation and ICRF heating experiments in tokamaks are discussed.

1.3 Tokamaks and Alcator C

By far, the most successful plasma confinement scheme to date is the tokamak. Proposed independently by Igor Tamm and Andrei Sakharov in Moscow and by Lyman Spitzer at Princeton in the early 1950's, the tokamak was proven to be viable using a series of experimental devices built during the late 1960's at the Kurchatov Institute in Moscow. Following the impressive results of these early Soviet tokamaks, fusion research programs in the U.S. and elsewhere shifted their primary focus onto the tokamak, where it remains today. Other magnetic confinement schemes, especially a variety of linear mirror devices, continue to be tested and developed, as do inertial confinement experiments. However, it is likely that the first demonstration fusion reactor will closely resemble current designs based on the tokamak.

Excellent reviews of the tokamak concept may be found in the literature [1-4]; what follows is a brief summary. A tokamak consists of a toroidal vacuum chamber surrounded by several sets of magnetic coils, as shown in Figure 1.1, which is a schematic of the Alcator C tokamak. The largest component of the magnetic field used to confine the plasma is the toroidal field, B_ϕ (also denoted B_T). The toroidal coordinate system is illustrated in Figure 1.2. The terms toroidal, poloidal, and radial refer to the $\hat{\phi}$, $\hat{\theta}$, and $\hat{\mathbf{r}}$ directions, respectively. The large toroidal field also provides magnetohydrodynamic (MHD) stability to the plasma by suppressing the growth of several plasma instabilities, notably the kink modes [9,10].

The poloidal component of the field, B_θ, is generated mainly by a large toroidal current through the plasma itself. This plasma current, I_P, distinguishes tokamaks from other toroidal plasma devices such as stellarators. The electric field which drives the plasma current is generated by a changing magnetic flux through the core of the torus, creating a transformer circuit in which the highly conductive

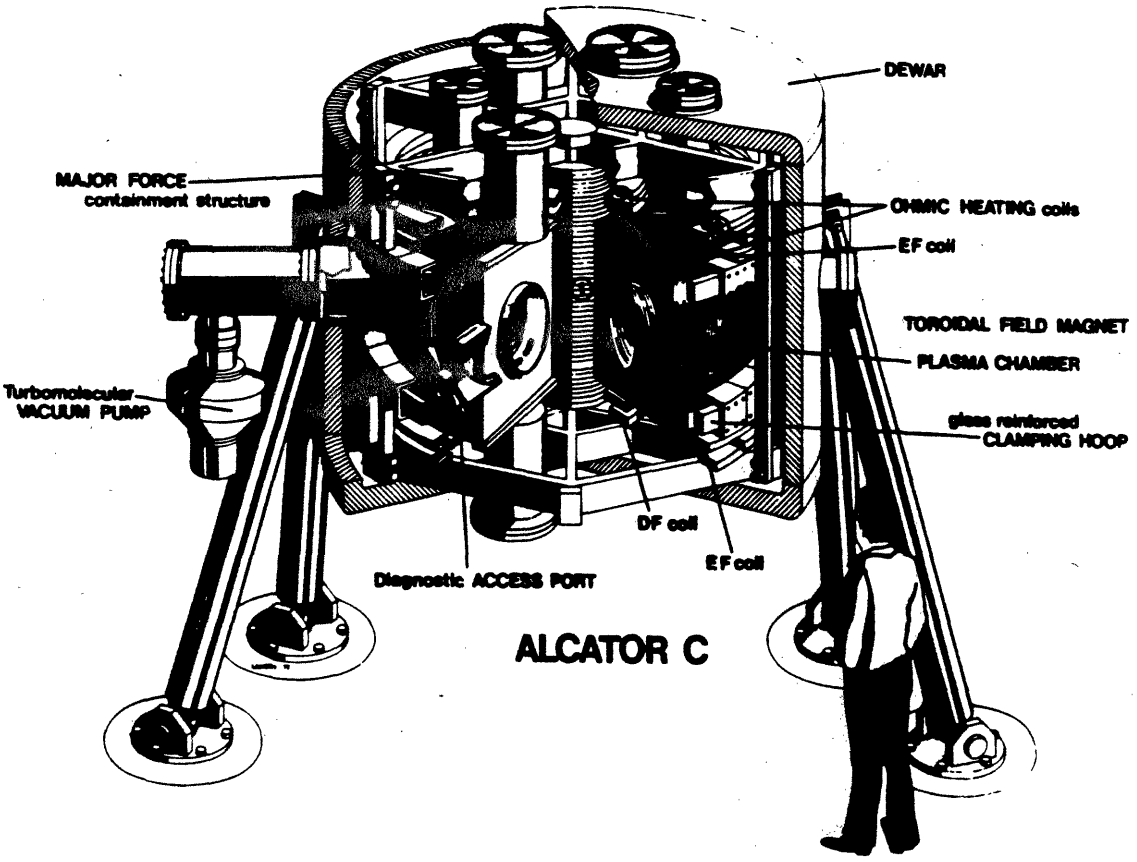

Figure 1.1 Alcator C schematic.

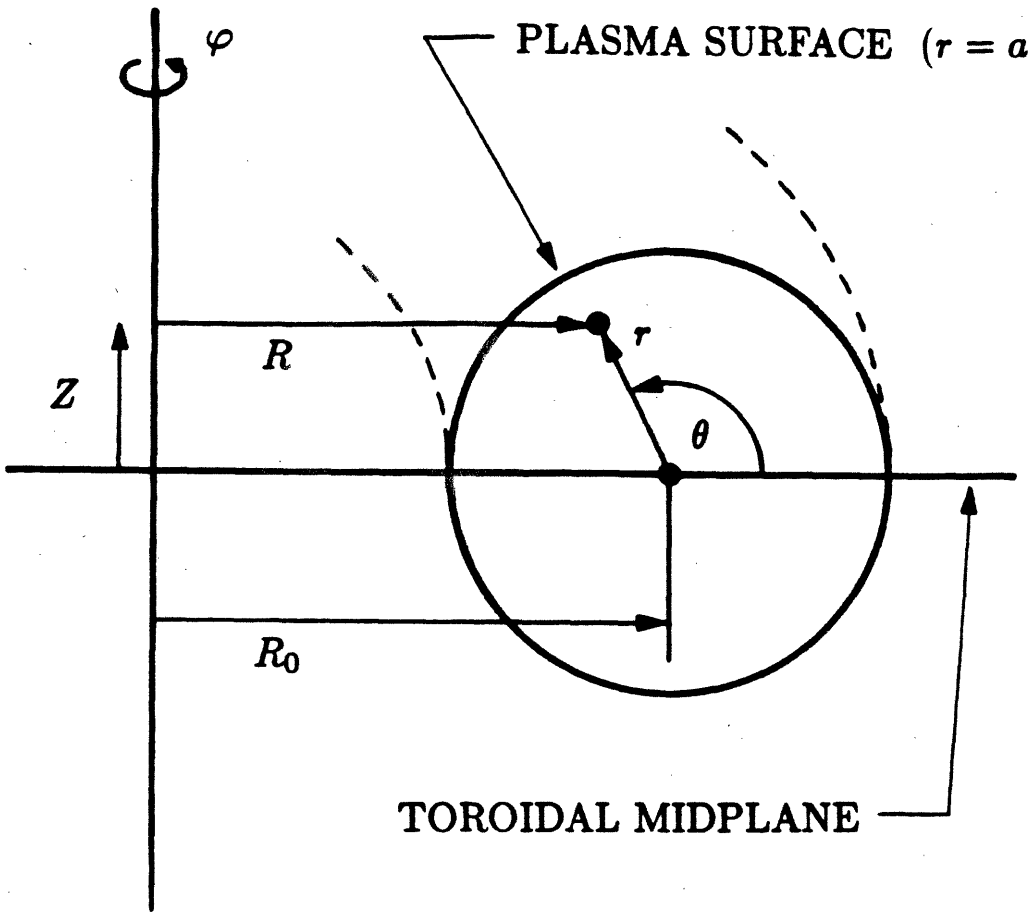

Figure 1.2 Toroidal coordinate system. The terms toroidal, poloidal, and radial refer to the $\hat{\phi}$, $\hat{\theta}$, and $\hat{\mathbf{r}}$ directions, respectively.

plasma acts as a secondary coil. On Alcator C a large air core coil in the center of the torus serves as the transformer primary; some tokamaks with smaller fields use iron cores to link the magnetic flux through the torus. The plasma current heats the plasma via I^2R Joule losses; it is therefore often referred to as the Ohmic Heating (OH) current.

The poloidal field, B_θ, plays the major role in confining the plasma radially (in the $\hat{\mathbf{r}}$ direction). As a current flows through a cylindrical plasma column, the plasma pinches in on itself, just as parallel wires carrying current in the same direction are mutually attracted. The phenomenon is also manifest when the plasma column is bent into a torus; hence the tokamak is an example of a toroidal diffuse pinch (diffuse because the current is distributed throughout the plasma column). In MHD theory, which treats the plasma as a highly conductive fluid, the pinching force is seen in the local force balance equation,

$$-\nabla p \approx -(\nabla p)_r = (\vec{J} \times \vec{B})_r = J_\phi B_\theta, \qquad 1.3$$

where $p = nkT$ is the plasma pressure, n is plasma density, T is plasma temperature, and $\vec{J}$ is the plasma current density.

The remaining contributors to the magnetic field are the vertical, horizontal, shaping, and divertor fields. The vertical field, B_z, is necessary to prevent the plasma from expanding outwards in the major radius direction ($\hat{\mathbf{R}}$). This is accomplished via an inward $\vec{I_p} \times \vec{B}_z$ force on the plasma column. By varying the vertical field about its equilibrium value, plasma in-out position can be controlled. Similarly, the horizontal field is a correcting field used to control the plasma up-down motion. On most large tokamaks, including Alcator C, plasma position sensing loops are utilized in an active feedback system with these positioning coils to keep the plasma centered in the chamber. Shaping coils carry current parallel or antiparallel to the plasma current, thus pulling or pushing the outer edges of the plasma column to

yield the desired plasma cross-sectional shape. Some tokamaks utilize non-circular plasma cross sections, which may have some advantages over circular cross section plasmas. Finally, in some tokamaks divertor coils bend some magnetic field lines at the edge of the plasma column away from the plasma, thereby diverting some of the edge plasma to a remote dumping area. Divertors show promise as a method of controlling particle and heat removal from the plasma. Alcator C, however, has neither non-circular shaping coils nor divertor coils.

Tokamaks suffer two fundamental limitations, each associated with the ohmic heating current. The first problem involves plasma heating. Although ohmic heating is very effective at raising the plasma temperature to the 2-3 keV range reached by Alcator C and similar devices, it is probably insufficient to heat plasmas to the 10-20 keV temperatures envisioned for fusion reactors (1 keV $= 11.6 \times 10^6$ °K). Due to the $(1/T_e)^{3/2}$ dependency of plasma resistivity, the efficacy of ohmic heating diminishes as the plasma temperature rises. (T_e is actually the electron temperature; the ion temperature T_i may be different.) Since the total plasma current I_p is constrained by MHD stability considerations to remain below a certain value, the ohmic input power I^2R drops as the plasma heats and T_e rises. While some experimental tokamaks have been proposed to attain ignited plasmas solely by using ohmic heating, it is generally believed that some form of auxiliary heating will be necessary to reach reactor temperatures economically.

One form of auxiliary heating is the injection of energetic neutral beams of hydrogen. The neutral atoms penetrate the magnetic field and are ionized in the plasma, where they give up their kinetic energy via Coulomb collisions. Another auxiliary heating technique is adiabatic compression of the plasma, in which magnetic field energy is transferred to particle thermal energy. A further method of heating involves the launching of electromagnetic plasma waves which give up their

wave energy by plasma damping and absorption processes. Such radio frequency (RF) heating experiments have centered primarily on four plasma resonances: the ion cyclotron range of frequencies (ICRF, $\omega \approx n\Omega_i$, where $\Omega_i = qB/m_ic$ is the ion cyclotron frequency and n is usually 1 or 2), electron cyclotron resonance heating (ECRH, $\omega \approx \Omega_e = eB/m_ec$), lower hybrid heating (LHH, $\omega = \omega_{LH}$, where

$$\omega_{LH}^2 = \frac{\omega_{pi}^2}{(1+\omega_{pe}^2/\Omega_e^2)} \qquad 1.4$$

and ω_{pe} is the electron plasma frequency and ω_{pi} is the ion plasma frequency,

$$\omega_{pe}^2 = \frac{4\pi n_e^2}{m_e} \qquad 1.5$$

$$\omega_{pi}^2 = \frac{4\pi n_e^2}{m_i} \qquad 1.6$$

and Alfvén wave heating, $\omega/k_{||} \approx v_A = B/\sqrt{4\pi\rho}$, where ρ is the plasma mass density. Development and use of both ICRF and LHH systems has been a key research area of the Alcator C program in recent years.

The second drawback of the ohmic heating transformer circuit is its inherently pulsed nature. A toroidal plasma current is required in a tokamak to generate the necessary poloidal field, as described above. Because plasma current can only be driven while the flux through the torus core is changing, the maximum flux capability of the OH coil limits the duration of the plasma discharge. A typical plasma shot, or discharge, on Alcator C might last for 500 msec. Although ohmic current could be transformer-driven for minutes by using OH coils with higher current capacities and larger power supplies, there will always be an upper limit for any given system. Since pulsed reactors would have to contend with increased structural fatigue due to thermal cycling and relatively low duty cycles, a steady state device would be preferable.

One approach to such a system incorporates external magnetic coils to generate all or part of the poloidal field, rather than the plasma current used in a tokamak.

Such devices (stellarators, torsatrons, etc.) have much more complicated geometries than do tokamaks, generally utilizing helical magnet coils. Early experiments with stellarators met with little success, perhaps due to errors in the complex magnetic geometry. Experiments in recent years, however, have shown considerable promise [11,12].

A second approach, which retains the basic features of the tokamak, is to couple resonant electromagnetic waves into the plasma so as to impart some toroidal momentum to the plasma electrons, thus driving electric current. The same lower hybrid resonance used for plasma heating has proven effective for this purpose [13]. By adjusting the relative phases of multiple waveguide LH antenna arrays, waves can be launched into the plasma with some toroidal directionality. Such lower hybrid current drive (LHCD) experiments have successfully driven hundreds of kiloamperes for sustained periods in both Alcator C [14] and the Princeton Large Torus (PLT) device [15]. Ultimately, a tokamak reactor utilizing LHCD, either alone or in combination with transformer-driven ohmic current, might operate in a steady state or quasi-steady state mode. Experiments aimed at understanding LHCD and increasing the wave-plasma coupling efficiency form a large part of the current Alcator C program.

An impuritiy is any element found in the plasma other than the working gas (usually hydrogen, deuterium, or helium). In order to minimize the amount of impurity ions in the plasma, strict standards of ultra-high vacuum cleanliness must be applied to the material tokamak components which surround the plasma. The vacuum chamber in Alcator C consists of a toroidal stainless steel bellows, interrupted by six port flanges which provide small apertures to the plasma volume for fueling, pumping, and diagnostic access. The bellows is protected from the energetic particles of the main plasma by one or more "limiters", protruding poloidal rings or bars

made either from a metal with a high melting point, such as molybdenum, or from a low-Z refractory material such as graphite. By intercepting the magnetic flux surfaces at the edge of the plasma, the limiter absorbs most of the bombardment due to outward radial heat flux from the bulk plasma. However, due to plasma flows perpendicular to the magnetic field, a much colder plasma can exist in the "shadow" region outside the limiter radius. Due to this edge plasma, the bellows walls and other structures in the edge region (RF antennae, diagnostic probes, etc.) do interact with the plasma and must be kept extremely clean. In addition, the walls are bombarded by energetic neutral atoms which have undergone charge exchange or radiative recombination in the bulk plasma and escape with an energy corresponding to the local ion temperature at the recombination site, as well as a class of energetic particles which are poorly confined due to magnetic trapping effects. The plasma therefore inevitably contains some concentration of intrinsic impurities such as molybdenum or carbon from the limiter, iron and chromium from the walls, carbon and oxygen from methane, carbon monoxide, carbon dioxide, water vapor, and atmospheric oxygen adsorbed on the walls, and oxygen from metal oxides formed on the exposed surfaces during vacuum breaks. One key to good plasma discharges is to minimize the level of these contaminants in the plasma, for reasons elucidated in the following section.

To that effect, the vacuum vessel is baked to remove loosely bound contaminants. Poorly confined low energy plasma discharge pulses help remove more tightly bound molecules prior to experimental runs in a process called "discharge cleaning" [16]. A base pressure of less than 1.0×10^{-7} Torr is maintained in the chamber. During tokamak discharges, the vessel is filled with typically $2 \cdot 10^{-5}$ Torr of the working gas, usually either hydrogen of deuterium.

Upon the initial ionization of the working gas, a low density plasma is rapidly

formed whose density is gradually increased and maintained in a controlled fashion by puffing in more working gas at the plasma edge. Although gas puffing succeeds in establishing stable plasma density profiles, it suffers from relying on plasma transport mechanisms to bring the fuel from the plasma edge, where it is quickly ionized, to the plasma center.

Pellet fueling, in which small frozen pellets of hydrogen or deuterium are injected directly into the plasma interior, avoids this difficulty. The pellet ablates as it travels through the plasma, increasing plasma density and reducing plasma temperature along the way. The temperature recovers fairly quickly after successful pellet injections, yielding hot, higher density plasmas. The size of the pellet and the plasma parameters determine the ablation rate and thus the post-pellet density profile. Pellet fueling allows the attainment of higher densities and more centrally peaked profiles than possible with gas puffing. By utilizing these features of pellet fueling, researchers at Alcator C recently surpassed the Lawson criterion for fusion energy break-even, achieving an $n\tau_E$ value of $8 \cdot 10^{13}$ cm^{-3}–sec [17]. Experiments designed to elucidate the dynamics of pellet fueling, particle confinement time τ_p, and energy confinement time τ_E continue to play a large role in the Alcator C research program.

Because material sensors are incompatible with the hot plasma interior, it is necessary to employ a variety of non-intrusive plasma diagnostics to probe tokamak experiments. Inductive pickup loops measure macroscopic parameters such as the plasma current and various moments of its internal distribution, plasma position, and the toroidal loop voltage which drives the ohmic current. Electromagnetic radiation from the plasma is monitored from radio waves to X-rays, yielding information about plasma temperature, density, and impurity content. Particle flux from the plasma is measured by neutron detectors, charge exchange (CX) neutral analyz-

ers, edge probes, and bolometers which integrate total energy flux (particles and radiation). Non-perturbing beams of light or neutral particles are also used. For example, phase shift interferometers reveal chord-integrated plasma density. The intensity and Doppler broadening of Thomson scattered visible laser light provides local measurements of electron density, n_e, and electron temperature, T_e.

The time evolution of key plasma parameters for a typical Alcator C pellet-fueled plasma shot are shown in Figure 1.3. The range of plasma parameters achieved in Alcator C is given in Table 1.1.

1.4 Detrimental Effects of Impurities

Ideally, an experimental fusion plasma would consist only of electrons and hydrogen ions. However, "impurity" ions of other elements are invariably present as well, as mentioned in the previous section. The presence of even small concentrations of plasma impurities can have large consequences, through a variety of interactions. Most of the impurity effects, unfortunately, are detrimental to the goals of economical fusion energy production. A detailed understanding of impurity generation, behavior, and effects on plasma performance is therefore vital to achieving these goals. Much attention has been focused on the problem of plasma impurities, especially in the past decade after the problems of gross plasma confinement and stability became better understood [18-21].

Why are impurities bad for a fusion plasma? To begin with, impurities lead to enhanced radiative power losses. Partially ionized impurities absorb electron energy via collisional excitation and then promptly radiate the energy away through transition line emission, chiefly in the soft X-ray range ($1 - 10$ Å) and the vacuum ultraviolet (VUV) range ($10 - 2000$ Å) for current tokamaks with central electron temperature $T_{eo} \approx 1-4$ keV. Visible and ultraviolet radiation (2000−7000 Å) is also

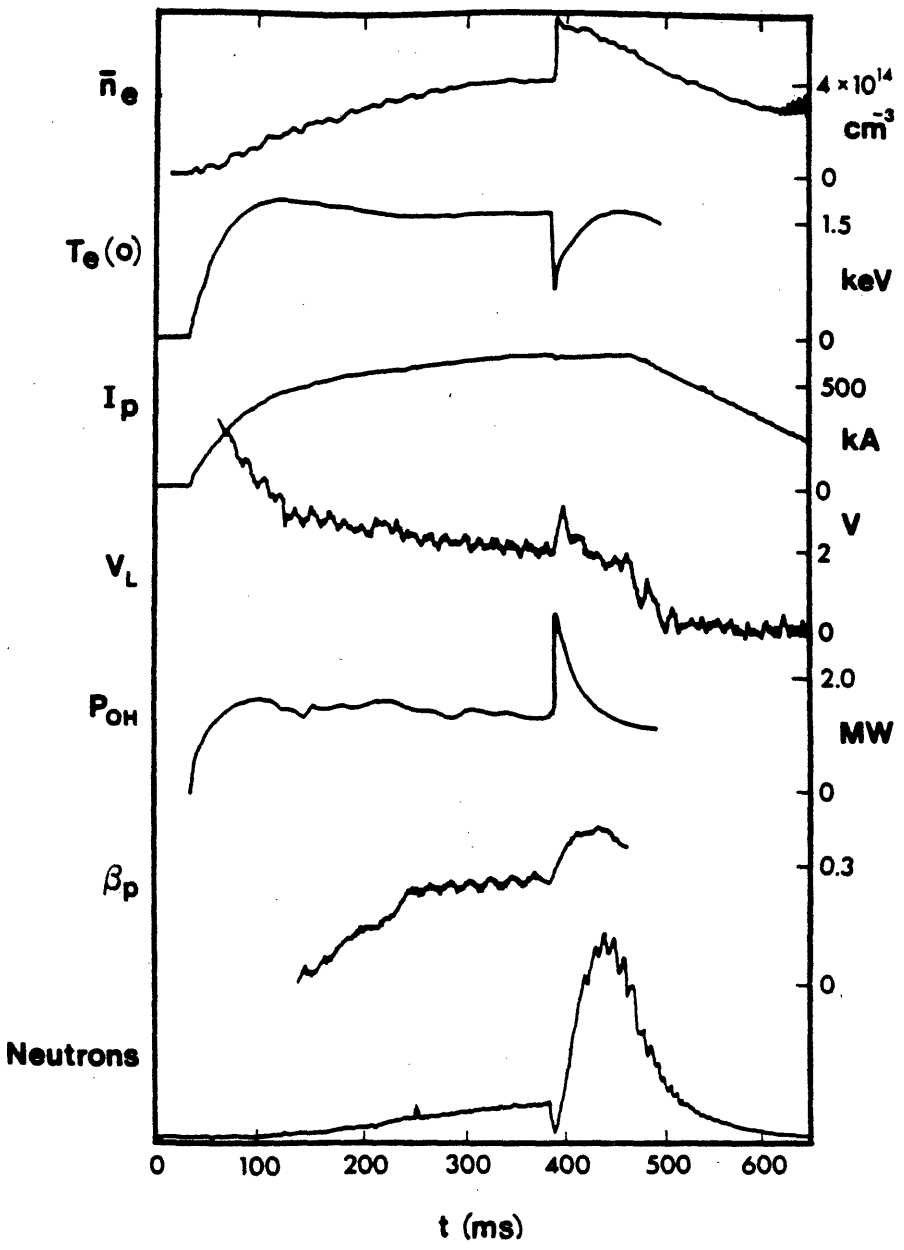

Figure 1.3 Evolution of key plasma parameters for a typical Alcator C pellet-fueled plasma discharge. A single deuterium pellet is injected into a deuterium discharge at 390 msec (from [17]). Traces are: Line averaged electron density, central electron temperature, plasma current, loop voltage, ohmic input power, poloidal beta (ratio of plasma pressure to pol. magnetic pressure), and neutron flux.

Alcator C Parameters

Parameter	Typical Value	Range of Values
Major Radius R_o	64 cm	57 - 71 cm
Minor Radius a	16.5 cm	10 - 17 cm
Toroidal Field B_T	80 kG	40 - 130 kG
Plasma Current I_P	450 kA	100 - 800 kA
Plasma Density n_e	2×10^{14} cm^{-3}	0.1 - 20 $\times 10^{14}$ cm^{-3}
Electron Temperature T_e	1500 eV	800 - 3000 eV
Ion Temperature T_i	1100 eV	500 - 2000 eV
Energy Confinement Time τ_E	20 msec	10 - 50 msec
Z_{eff}	1.25	1.1 - 1.6 (but up to 15)
Pulse Length	500 msec	300 - 600 msec
Auxiliary Heating	Ion Cyclotron, Lower Hybrid	
Limiter Materials	Mo, C, SiC	

Table 1.1 Alcator C range of plasma parameters.

emitted from impurity ions, primarily from the cooler edge regions of the plasma. Since tokamak plasmas are optically thin to all of the above, the radiated energy escapes directly to the wall of the tokamak. Impurity line radiation comprised the dominant energy loss channel in many early tokamak devices which lacked current standards of plasma purity [22,23].

Line radiation is especially problematical for high-Z impurites such as tungsten, molybdenum, and iron. Low-Z impurities such as carbon and oxygen are fully stripped of their electrons over most of the hot central plasma volume, and thus cannot radiate via transition lines except in the cooler outer edges of the plasma. Heavy impurities can cause severe cooling of the plasma core, however, leading to hollow temperature profiles and even disruptions [24]. Small admixtures of heavy impurities greatly increase the difficulty of achieving $n\tau_E$ values sufficient for fusion break-even or ignition. In fact, as little as 0.1% concentration of tungsten will prevent ignition at any temperature [25,26]. Hollow profiles are an extreme case of a very important impurity effect: non-uniform radiative cooling rates due to impurities can have a large impact on the electron temperature profile, $T_e(r)$, which in turn affects the current density profile, $j(r)$. Large irregularities in either profile generally lead to the growth of various MHD instabilities, which may or may not end in termination of the plasma discharge.

Impurities also emit recombination radiation and enhance the level of electron bremsstrahlung radiation. When the impurity ion has one or more bound electrons, di-electronic recombination generally predominates over simple radiative recombination in the temperature range of interest. In this process, a free electron is captured into an excited level while exciting a bound electron. The system can stabilize by subsequent radiative decay (di-electronic recombination) or by losing one of the excited electrons (auto-ionization). Radiation losses due to recombination

are especially large when the plasma temperature falls rapidly due to a disruption, pellet, or controlled shot termination.

Bremsstrahlung radiation due to free electron scattering off of ions scales as $n_e n_i Z_i^2$, where Z_i is the charge of the ion. The total power lost through bremsstrahlung is conveniently expressed as $P_B = P_B^H \times Z_{\text{eff}}$, where P_B^H is the bremsstrahlung power in a pure hydrogen plasma with the same electron density n_e, and the effective ion charge Z_{eff} is given by [27,28]

$$Z_{\text{eff}} = \frac{\Sigma n_i Z_i^2}{\Sigma n_i Z_i} = \frac{\Sigma n_i Z_i^2}{n_e} \qquad 1.7$$

The impurity content of a plasma is frequently referred to in terms of Z_{eff} , which typically was in the range $3 \leq Z_{\text{eff}} \leq 10$ on early tokamaks. With careful conditioning of the vacuum vessels, clean plasmas with $Z_{\text{eff}} \approx 1.0$ have been obtained in Alcator C and several other current tokamaks. Visible bremsstrahlung measurements on Alcator C are in fact used to infer the value of Z_{eff} (r) [29].

In addition to radiation processes, the presence of impurities influences the plasma in more subtle ways. In particular, the electrical resistivity increases linearly with Z_{eff} . Impurity concentrations thus influence the ohmic power deposition and current density profiles $j(r)$, which in turn determine MHD stability and electron temperature profiles, $T_e(r)$. Impurities have been theoretically linked to several microinstabilities [30]. which can enhance energy and particle transport rates. A non-fatal edge instability observed in Alcator C and dubbed "marfe" [31] has been tentatively explained as due to a thermal instability in edge impurity cooling rates: the colder the edge plasma, the more power radiated away by certain low-Z impurity ions.

Impurities also affect the plasma power balance by soaking up electron thermal energy as they diffuse into the plasma, become totally or partially ionized, and are heated (along with their lost electrons) to the local plasma temperature. These ions

and electrons, which are useless for fusion reactions, thus consume some fraction of the input heating power which might otherwise go to the fusion fuel. Since, for a given tokamak system, total electron and plasma energy density are constrained by stability and power balance considerations, this dilution of fusion fuel could have serious consequences for a reactor. This will impose particular restrictions on low-Z impurities, which are relatively benign in current tokamak experiments owing to the low radiation losses from fully stripped low-Z ions in the central regions of the plasma.

Finally, large impurity concentrations can impair the effectiveness of auxiliary heating or current drive. Neutral beams penetrate less deeply into a dirty plasma due to charge exchange ionization with edge impurity ions. Ion cyclotron waves may be resonantly damped by impurity ions, rather than fuel ions as desired. A plasma whose edge is cooled by excessive impurity radiation attenuates lower hybrid waves more severely than does a clean plasma. Furthermore, the enhanced resistivity of a dirty plasma reduces the efficiency of LHCD (measured in kiloamps per kilowatt injected) [32].

1.5 Beneficial Effects of Impurities

Impurities are not entirely unwelcome in experimental fusion plasmas. In low or moderate concentrations, they may play several beneficial roles. First, ohmic input power can be higher in an impure plasma. Since I_P is limited by MHD stability criteria for a given tokamak, $I_P^2 R$ heating can only be increased by raising R, which scales as Z_{eff} . As long as impurity radiation losses aren't too great, this can lead to higher temperatures in the plasma, enabling researchers to more closely approach reactor temperature regimes without auxiliary heating.

A second benefit involves radiative cooling of the edge plasma by impurities. By thus uniformly removing energy from the plasma periphery, the localized heat load to the limiter is reduced, as is particle bombardment of the wall and other edge structures. A mantle of cool plasma can form and protect the limiter, etc., from erosion or melting. In particular, a sufficient admixture of low-Z impurities can reduce the influx of the more detrimental high-Z materials from the limiter or walls, thereby yielding hotter central plasmas than those with a similar $Z_{\rm eff}$ due to heavy metals, which are not fully stripped at the center. For a similar reason, low-Z impurities are much preferable for increasing the plasma resistivity. Too much edge cooling, however, can cause the plasma current channel to shrink away from the edge, leading to MHD instabilities.

Finally, spectroscopic measurements of impurity radiation can provide much diagnostic information about impurity behavior and the plasma itself, as summarized in the next section. The study of impurity behavior in reactor-like plasmas is particularly relevant to predicting the effects of large concentrations of alpha particles, which are formed by D-T fusion events. Once the energetic fusion alphas have slowed down in the bulk plasma, they can be considered as another ultra-low-Z impurity.

1.6 Plasma Spectroscopy

The passive, non-intrusive measurement and analysis of radiation emitted from high temperature plasmas can yield much information about conditions in the plasma [33,34]. Because tokamak plasmas are optically thin to wavelengths below the far infrared, visible through X-ray spectroscopy can probe the entire plasma interior. Obviously, the absolute brightnesses of impurity ion transition lines can be used to infer impurity concentrations in the plasma. Also, the presence of radiation

from relatively highly ionized ions indicates a relatively hot plasma. Perhaps less obvious is the use of line intensity ratios to infer electron density [35,36] and electron temperature [37]. This is due to the rate dependence of the atomic processes involved (ionization, recombination, excitation) on T_e and n_e . Ion temperature and plasma rotation velocity can be determined from the Doppler broadening and shift [37,38] of selected impurity lines. Stark broadening becomes important in the higher density plasmas characteristic of inertial confinement fusion experiments.

Impurities have proven to be very useful in studying plasma transport processes. By injecting trace amounts of various non-intrinsic, non-recycling impurities into the plasma and then spectroscopically monitoring the subsequent spatial and temporal evolution of the impurity ions' concentrations, much information may be gleaned regarding ion diffusion coefficients, particle confinement times, and particle convection velocities [39]. Such studies of gas-fueled Alcator C discharges indicate a large, anomalous impurity diffusion coefficient, leading to shorter particle confinement times than theoretically predicted. Understanding the mechanisms responsible for this poor confinement might help explain the electron or ion thermal conductivity, for example, which are also anomalously high, causing shorter energy confinement times. Small amplitude electrostatic fluctuations or magnetic turbulence have been suggested [40] as possible causes for this enhanced transport.

Although tokamak plasma spectroscopy usually uses existing atomic data to infer plasma conditions or impurity concentrations, experiments sometimes reverse the process. Under sufficiently controlled conditions, atomic data such as energy levels and absorption oscillator strengths can be measured or inferred. This is especially useful for highly ionized heavy impurities, for which existing atomic data are often scarce. Many transition wavelengths are still unmeasured, only predicted, especially for electric dipole forbidden lines. Such atomic data are vital for atomic

theory, fusion research, and the analysis of astrophysical spectra.

1.7 Statement of Problem and Motivation

The attainment of high quality tokamak plasmas has always been contingent upon successful control of impurity concentrations, even in the most straightforward ohmically heated devices. The additional demands of auxiliary heating and non-inductive current drive, processes with high promise of pushing plasma parameters towards reactor grade conditions, have raised new issues involving impurity behavior. Not only can impurities limit the effectiveness of these techniques, as mentioned earlier, but the use of neutral beams and radio frequency waves can under certain conditions lead to large impurity influxes, thus compounding the problem. This thesis will only deal with ICRF heating effects. Impurity generation during recent Lower Hybrid Heating experiments on Alcator C has been presented elsewhere [41], and will not be dealt with in this thesis. Neutral beams are not available on Alcator C.

Large impurity influxes during ICRF experiments, especially metallic elements, have been reported by numerous tokamak groups, including the Princeton Large Torus (PLT), Tokamak Fontenay-aux-Rose (TFR) in France, tokamak T-10 in Moscow, and the tokamaks JIPP-TII, JIPP-TIIU, JFT-2, and and JFT-2M in Japan. However, no general consensus yet exists as to the principal source and physical mechanism for this impurity release. This will be discussed in detail in Chapter 4.

Alcator C is by no means immune to these impurity problems arising from the use of RF power, and that is a major thrust of this thesis. Significant influxes of iron, chromium, and nickel were observed during ICRF heating experiments via VUV spectroscopy, with lesser increases in molybdenum, carbon, and oxygen. Large

influxes of the limiter material (silicon carbide or molybdenum) were seen during many LHCD discharges, and to a lesser extent in LHH experiments. Only the ICRF results are presented here.

The time-resolving VUV spectrograph used for these measurements was designed to serve as a general plasma impurity diagnostic for Alcator C, with considerably more power and flexibility than the VUV monochromator which it replaced. In addition to serving as a routine monitor of intrinsic impurity concentration levels, its ability to simultaneously monitor a range of wavelengths makes it ideally suited to qualitatively and quantitatively observe any dynamic changes in impurity levels and behavior associated with RF heating, RF current drive, pellet fueling, impurity injections, and other experiments conducted on Alcator C. The major motivation for, and emphasis in, this thesis consists of observations of the impurity influx during the ICRF series of experiments. Absolute brightness measurements combined with a numerical code, simulating impurity transport, are employed to yield impurity source rates at the plasma edge and inferred radial distributions within the plasma as a function of time relative to the ICRF pulse. The scaling of the impurity influx with various plasma and RF parameters is analyzed in order to understand the probable impurity source and release mechanism. It is imperative that researchers obtain a clearer understanding of these issues, so that future ICRF experiments, and ultimately fusion reactors, may be designed so as to alleviate any harmful effects of RF-induced impurities.

Chapter 2

The VUV Time Resolving Spectrograph

2.1 Design Considerations

The impurity behavior on Alcator C, such as that reported in the following chapters, was chiefly monitored by a time-resolving grazing incidence spectrograph, the detailed description of which is related in this chapter. This instrument was originally a standard vacuum ultraviolet (VUV) grazing incidence monochromator, McPherson model 247, utilizing a 2.2 meter diameter Rowland circle configuration in which the entrance slit, concave diffraction grating, and exit slit all lie on the Rowland circle [42,43]. A single detector (usually a photomultiplier or channeltron) sits behind the exit slit, where it detects photons whose wavelength λ fulfills the diffraction equation,

$$n\lambda = d(\sin\alpha - \sin\beta), \tag{2.1}$$

where n is the order of the image, d is the spacing of the grooves on the diffraction grating, and α and β are the angles of incidence and diffraction, respectively, relative to the grating normal (Figure 2.1) With the entrance slit fixed ($82° \leq \alpha \leq 88°$), wavelengths may be scanned by moving the exit slit assembly. This is accomplished by means of a stepping motor and gear assembly which moves the exit slit carriage along a curved track, keeping the exit slit centered on the Rowland circle. A pivot assembly keeps the exit slit facing normal to the incident photons. Because VUV photons are quickly absorbed by the atmosphere, the entire system is maintained in a high vacuum environment, with flexible metal bellows allowing the motion of the entrance and exit slits. An oil-free vacuum is also necessary to prevent surface

contamination of both the grating and the detector, which could severely impair their efficiencies. The wavelengths of interest, typically 15 Å $\leq \lambda \leq$1200 Å, cannot pass through glass, quartz, or MgF_2 windows, thereby necessitating a clear optical line of sight from the detector to the grating and thence to the plasma or other light source.

When used during brief, dynamic tokamak plasma discharges, the chief drawback of a such a standard VUV monochromator is the single wavelength capability. For a single tokamak discharge, lasting a second or less, a monochromator can give excellent temporal measurements of the brightness at whatever wavelength it is set to monitor. However, it cannot give the background brightness or the brightnesses of nearby spectral lines. This limitation may require several plasma shots just to find the peak brightness location for a given impurity line, given the normal uncertainties in detector location, and several more shots to monitor the background brightness to either side of the line of interest. To survey the entire VUV emission spectrum from $15 - 1200$ Å with a resolution of 0.5 Å could require ~2400 reproducible discharges, or over two full months of normal Alcator C operations.

This restriction is lifted if the single exit slit and detector are replaced with a film holder, such that a large region of the VUV spectrum is focused onto the film, which lies on the Rowland circle. This approach sacrifices time response, yielding one spectrum per plasma shot. The time between data taking and data analysis is naturally long, depending on removing and developing the film.

An electronic imaging system combines the best features of monochromator operation and film operation, providing both temporal and spectral resolution. By imaging a portion of the VUV spectrum onto a linear photodiode array with rapid readout and digitization, a monochromator is transformed into a time-resolving spectrograph. The goal of the design work was to effect such a transformation while

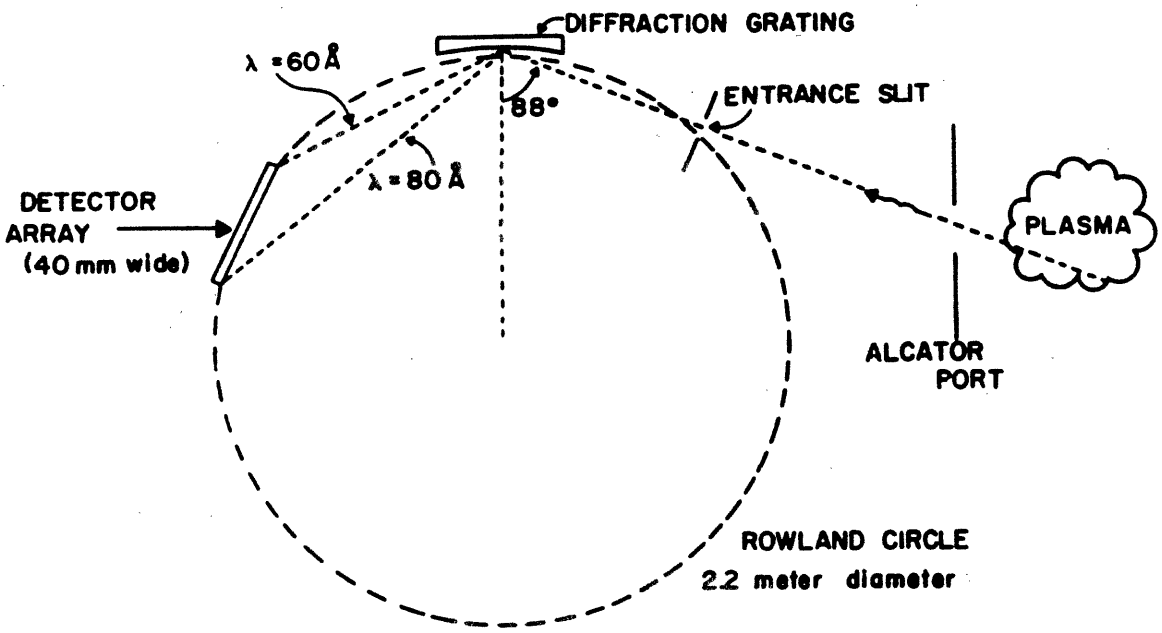

Figure 2.1 Geometry of grazing incidence spectrograph with scannable detector array (not to scale). Dispersion is appropriate for 1200 line/mm grating.

preserving the spectral resolution, temporal resolution, sensitivity, dynamic range, and spectral coverage provided by the original instrument, as much as possible.

To that effect, the monochromator was converted to a time resolving spectrograph by the installation of a detector similar to that described by Bell *et al* [44] and others [45-47], consisting of a microchannel plate (MCP) image intensifier which is coupled fiber-optically to a Reticon 1024-element self-scanned linear photodiode array (PDA). A schematic diagram of the modified instrument is shown in Figure 2.2. The MCP image intensifier, positioned with the center tangent to the Rowland circle, serves as the front end of the detector system. The visible (green) spectral image thus produced is relayed through a fiber optic image conduit onto the input faceplate of a Reticon 1024-element linear photodiode array (Figure 2.3). Readout rates as fast as possible, with 10 to 14 bit digitization, were desired, with real-time memory storage. This system totally replaces the exit slit assembly, but still utilizes the moving carriage to maintain position on the Rowland circle. A detector chamber was designed to house the detector, incorporating the following features: high voltage feedthroughs, a vacuum seal between the MCP and the Reticon, and provisions for fine focusing adjustments performed while under vacuum.

2.2 Detector System

2.2.1 Microchannel Plate Image Intensifier

The detector assembly described below was supplied by Galileo Electro-Optics Corporation of Sturbridge, Massachusetts, in accordance with detailed specifications provided by the author and J.L. Terry. It consists of a windowless microchannel plate image intensifier, mounted in a vacuum re-entrant tube assembly on a 6″ Conflat-style vacuum flange, and attached via fiber optics to a Reticon self-scanned linear photodiode array (supplied separately by EG&G-Reticon Corporation).

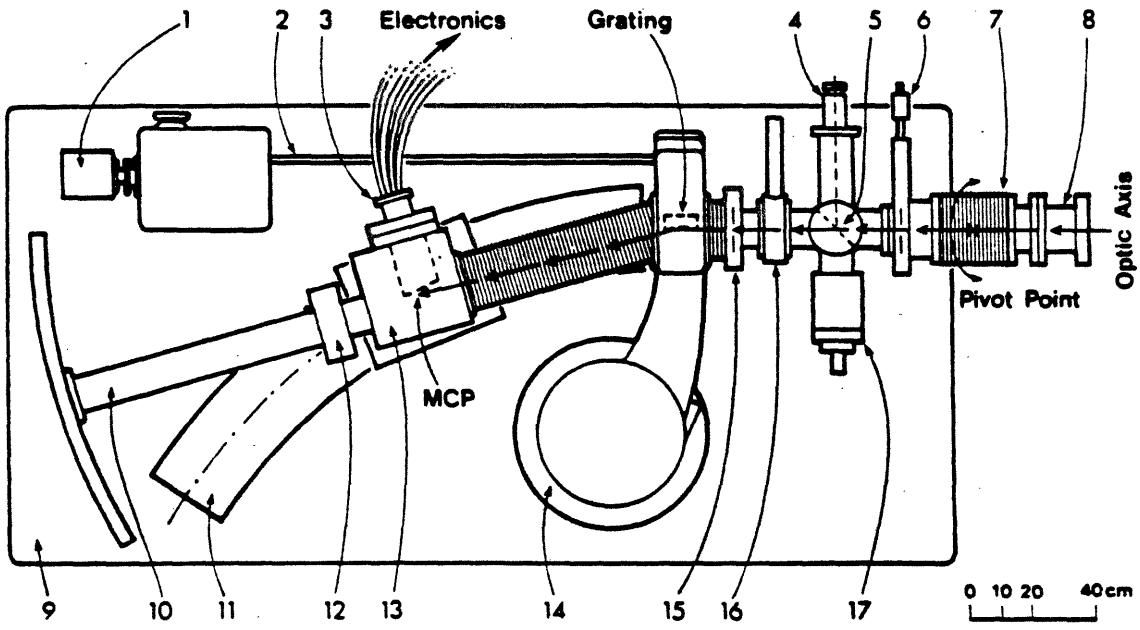

1. STEPPING MOTOR
2. DRIVE SHAFT
3. PHOTODIODE ARRAY & PREAMP
4. ALIGNMENT TELESCOPE
5. INSERTABLE MIRROR
6. PRESLIT
7. BELLOWS
8. CERAMIC BREAK
9. GRANITE BASE
10. DRIVE SCREW
11. ROWLAND CIRCLE TRACK
12. 8 L/SEC ION PUMP
13. DETECTOR CHAMBER
14. TMP PUMPING STACK
15. ENTRANCE SLIT
16. GATE VALVE
17. FILTER HOLDER

Figure 2.2 Schematic diagram (to scale) of the Time Resolving VUV Spectrograph. The viewpoint is from above in the normal orientation. For use on Alcator C, the instrument was turned up on its side (90° rotation). In that orientation, viewpoint is from in front of the instrument, with the tokamak to the right.

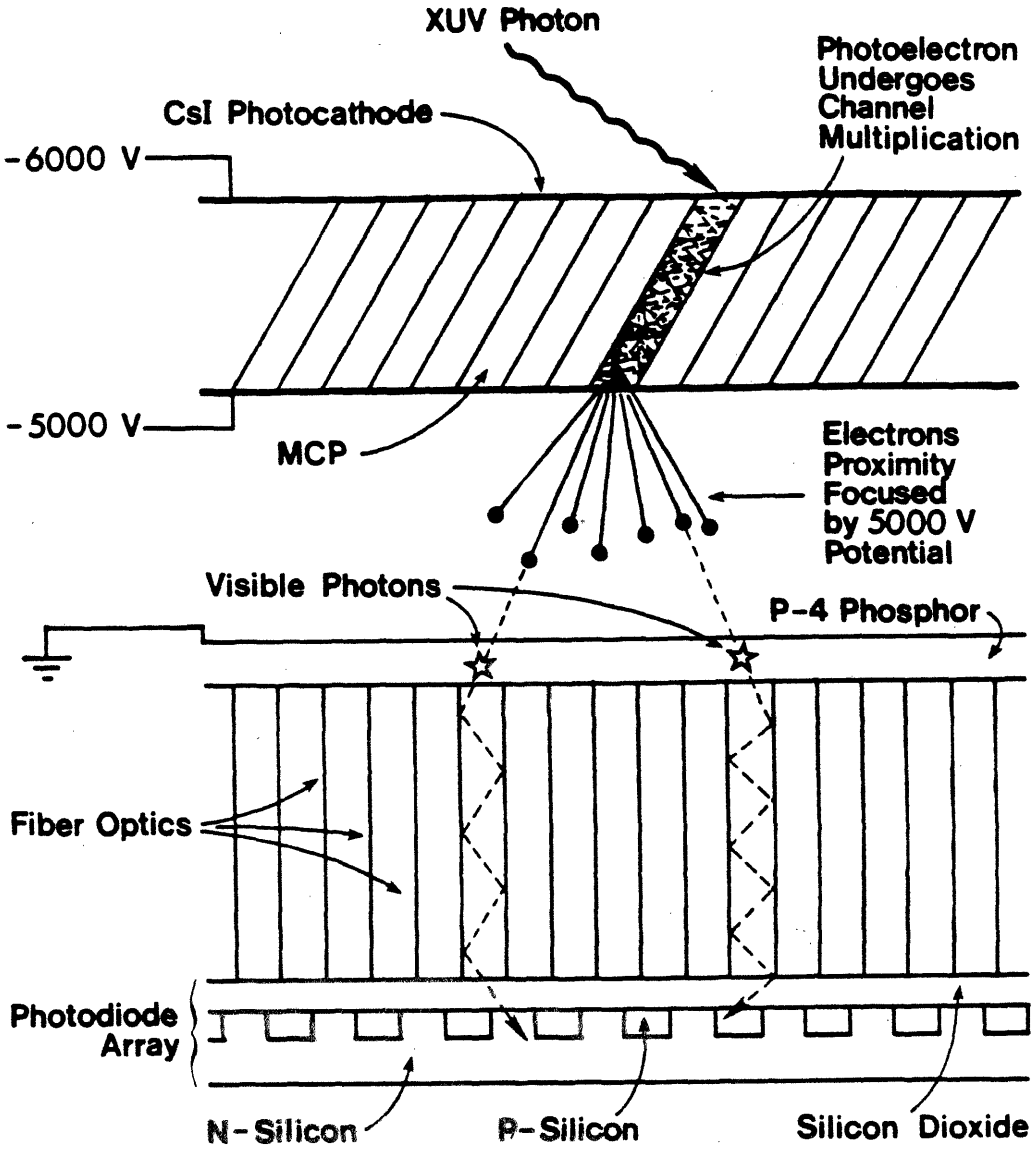

Figure 2.3 Detector schematic (conceptual, not to scale).

A microchannel plate, or MCP [48], is a thin leaded glass wafer, perforated by an array of tiny, parallel holes (the microchannels) with a length to diameter ratio of between 40 and 100. Each channel, with a diameter of 10–100 μm, acts as a continuous dynode electron multiplier (channeltron), due to the secondary emission properties of the leaded glass. Parallel electrical biasing of typically 1 kV is applied to the channels via conductive coatings applied to the front and rear faces of the plate, providing a bias, or strip, current of typically 1–100 μA. Electrons generated at the front of the MCP are accelerated down the channel until they strike the wall, liberating more electrons in a cascade effect. Single MCP's yield an electron gain of typically 10^4 with a time resolution as fast as 100 ps; higher gain may be obtained by stacking MCP's in a cascade arrangement. Spatial resolution is determined by the channel spacing; the MCP used in this work is a single plate with 12 μm diameter straight channels and 15 μm center-to-center spacing. The channels are slanted at an 8° bias angle relative to the normal axis of the plate (a standard MCP feature).

Electrons exiting the rear side of the MCP are accelerated by a 5 kv potential difference across a 1 mm gap onto the phosphor-coated front surface of the fiber optic image conduit. This strong electric field and small separation combine to minimize transverse spreading of the electrons, preserving the spatial integrity of the image. This MCP-phosphor combination forms a "proximity-focus image intensifier". The front end of the fiber optic conduit is a nominal 40 $\rightarrow$ 25 mm image reducing taper, with 10 μm optical fibers drawn down to 6 μm, thus the 40 mm diameter image of the MCP is reduced to a 25 mm diameter. A straight fiber optic image conduit with 6 μm fibers connects the reduced end of the taper to the Reticon photodiode array. With an area of 25.6 mm by 2.5 mm, the photodiode array thus views an "active region" of the MCP measuring nominally 40 mm in the wavelength dispersion direction by 4.0 mm in the transverse direction (parallel to the grooves

on the diffraction grating). Each pixel (photodiode element) of the Reticon is 25 μm wide by 2.5 mm high, and therefore views a nominal 40 μm by 4 mm slice of the spectral image at the MCP. This 100:1 aspect ratio is especially designed to match the image formed by typical spectroscopic entrance slits (e.g., 5 mm by 50 μm).

In order to enhance the quantum efficiency of the MCP for VUV photons, a 3000 Å thick layer of CsI was deposited on the front side of the MCP to serve as a photocathode. Cesium iodide was selected due to its favorable efficiency in the 100 Å region [49]; the deposition was conducted according to the method outlined by Saloman [50]. Special precautions were employed to minimize the exposure of the CsI layer to the atmosphere, due to its somewhat hygroscopic nature. The MCP was kept either in a dry nitrogen environment or under vacuum whenever possible. Unavoidable atmospheric exposure during installation or vacuum breaks did not noticeably degrade the MCP performance during the first 30 months following installation. Of course, it is impossible to say whether the detector stabilized in a partially degraded condition before it was ever turned on. Some apparent degradation was noticed about three years after first installing the detector, however. This was manifested by a non-uniform loss of sensitivity, with the most severe change (factor of two or so) occurring at the edge nearest the grating. This deterioration was not wavelength dependent and was therefore not necessarily due to a change in the CsI photocathode layer; the MCP itself or phosphor layer may have undergone some change. No significant change was seen in the bias current to the MCP, which tends to eliminate any considerations of non-uniform biasing voltage. MCP gain is known to degrade as a function of total accumulated output charge per unit area [48,51,52]. This could explain the apparent degradation, but not the spatial dependence.

The MCP was "funneled" on the input side to further increase its quantum ef-

ficiency by enlarging the front end of the channels. The matrix between the channel openings is etched slightly so that the openings of adjacent channels touch, increasing the open area from 55% to about 75%. A "P-4" phosphor was chosen as having the best combination of quantum efficiency, coupling to the Reticon photodiodes, and short persistence time.

A repelling plate was positioned parallel to the MCP front surface and 18 mm away. The separation was determined from optical considerations, leaving enough space so that the long wavelength end of the MCP (the side most distant from the grating) would have a clear line of sight to the grating under all conditions. The purpose of the repeller is to increase the capture fraction of photoelectrons generated at the photocathode surface of the MCP. Due to design spatial constraints, the phosphor layer is kept at ground potential. This necessitates a biasing of typically -5.0 kV on the output side of the MCP and -6.0 kV on the input side. The repeller is run at -6.0 kV for no electric field in front of the MCP, or at ~ -8.7 kV to produce a field of ~ 150 V/mm in order to turn outward bound photoelectrons back onto the MCP front surface near their point of origin [53]. The actual detector configuration is shown in Figure 2.4.

When a photo-electron is multiplied in one of the MCP microchannels, the electrons depleted from the side of the channel are replenished by the bias voltage with a time response depending on the conductivity of the leaded glass, typically a few milliseconds. Nonlinear effects due to this deadtime are noticeable if the electron current leaving a local region of the MCP exceed $\sim$10% of the strip (bias) current density. For a bright source such as a tokamak plasma, a high density of microchannels and a high strip current are therefore desirable to minimize saturation effects. The MCP utilized here has 12 μm channels and a relatively high strip current of $\sim 94 - 100$ μA at a bias voltage of 1 kV. This strip current generally

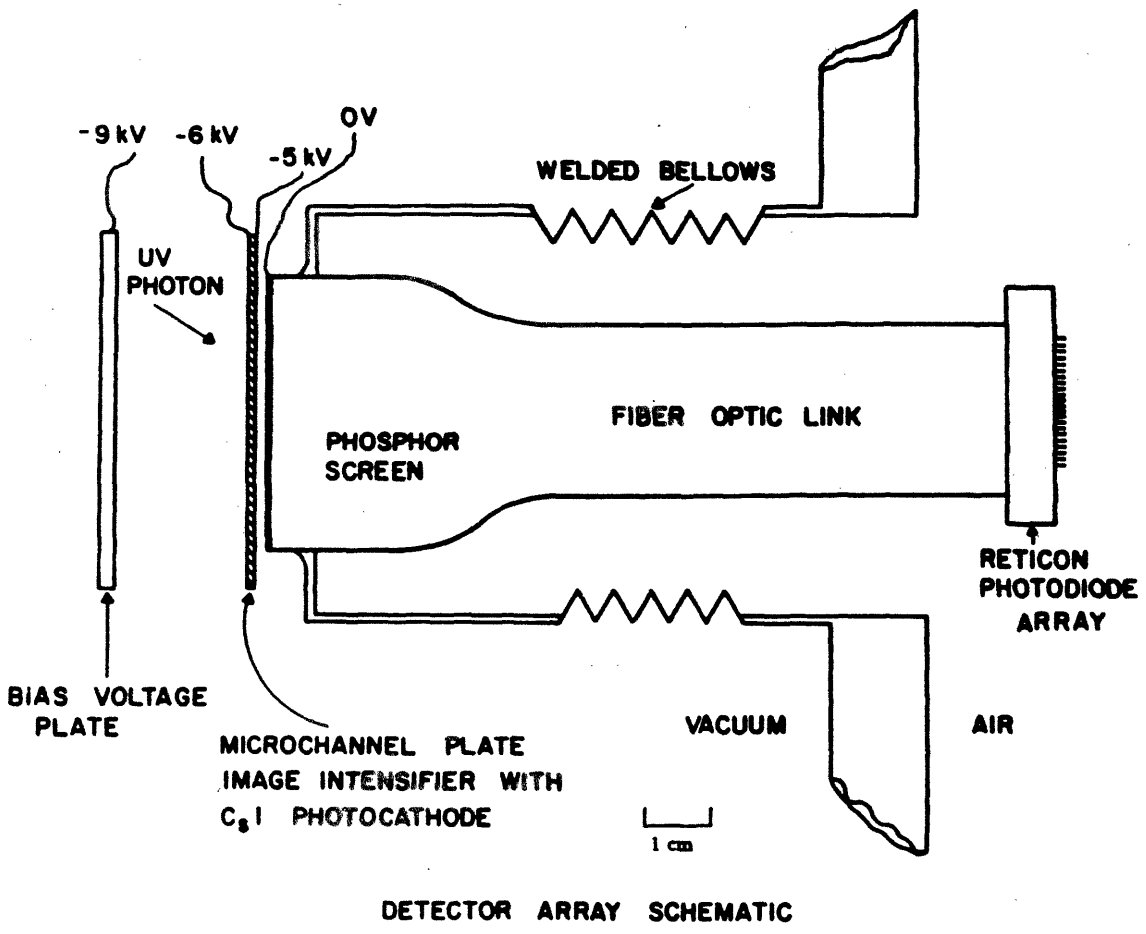

Figure 2.4 Scale drawing of MCP detector system, including repeller ("bias voltage") plate. The grating (not shown) would be in direction of the top of the page.

increases a few μA after initial turn-on, probably due to an increase in conductivity as the semiconductor MCP glass warms up. The strip current is usually highest when the laboratory environment is hottest. The MCP gain is not dependent on the strip current (up to the saturation point), but only depends on the bias voltage.

The biasing voltage was provided to the MCP by a Bertan model 1739N dual high voltage power supply, with one module connected at -6 kV to the MCP input side, and the other module connected at -5.0 kV to the output side. A 33 MΩ resistor to ground, connected in parallel to the MCP output side, allows both modules to sink net current (as they are designed to do) despite the $\sim$ 100 μA MCP strip current flowing between them. Each module is equipped with a fast overcurrent protection which trips the current and shuts down the high voltage for a current exceeding $\sim$ 800 μA. A Bertan model NIM 310N high voltage power supply, including arc protection, is used to bias the repeller plate at -6.0 to -9.0 kV. This biasing circuit is shown in Figure 2.5. All three power supplies are remotely programmed by a single control circuit, which allows each voltage to be adjusted separately, or in unison. Typically, the detector voltages are slowly increased together from zero, so as to prevent more than $\sim$ 700 Volts from ever appearing across the MCP. After the MCP output side reaches -5.0 kV, the final adjustment slowly raises the MCP input side to -6.0 kV. The two trip monitors on the 1739N are tied into the control circuit so as to shut down all three supplies in the event of any arcs. The success of these protective measures is indicated by the longevity of the MCP, which is still functioning after over 40 months of use, despite numerous trippings of the power supplies and one vacuum failure during operation.

A cylindrical shield covers the entire image intensifier, serving primarily as a barrier to stray, reflected light (visible or UV). The shield itself is made of stainless steel and is electrically grounded through the attachment screws to the mounting

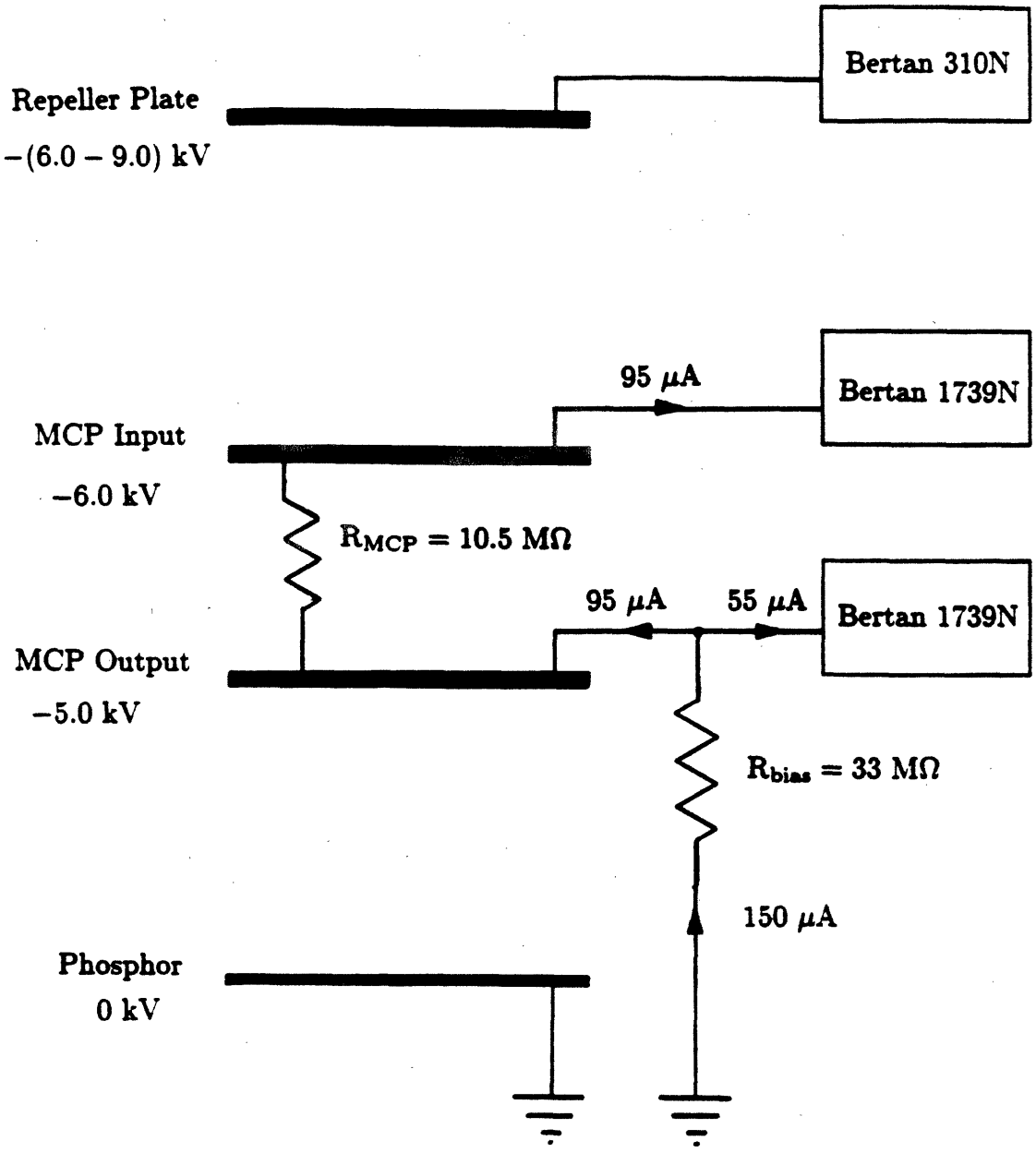

Figure 2.5 Biasing circuit for the MCP detector system.

structure. In retrospect, a non-conducting shield would have been preferable due to the fringing fields between the detector surface, repeller plate, and the cylindrical shield. The interior and exterior are both black anodized to minimize reflections. A window slot is provided on the grating side to allow the desired photons to illuminate the active region of the MCP. Several additional holes were added to the side of this cover away from the grating to allow better pumpout of the MCP, as a high vacuum (less than 10^{-6} Torr) is vital for reliable MCP performance. Higher pressures can induce ion feedback in the microchannels, in which residual gas molecules inside the channels are ionized and drift back to the input side [48,51]. Worse yet, arcing is more likely at higher pressures, potentially leading to MCP damage if the high voltage power supplies are not protected against overcurrents. In order to minimize pressure stresses on the fragile MCP during pumpdown or vacuum breaks, particular care was taken to vent the region between the MCP and the phosphor.

A flat MCP cannot conform perfectly to the Rowland circle; therefore not every pixel of the system can simultaneously be in perfect focus. However, the 40 mm active region of the MCP can be positioned on the 2.2 meter diameter Rowland circle so that the center of the MCP is 90 μm inside the circle, with the edges of the active region 90 μm outside the circle. Two locations along the detector would cut the Rowland circle and be in perfect focus. In this optimum configuration, simple calculations show that the image of an infinitely narrow entrance slit is almost always sharper at any location on the detector than a perfectly focused image of a practical 50 μm entrance slit, and comparable to a perfectly focused image of a 25 μm slit. Since little resolution would therefore be sacrificed, a flat MCP was chosen rather than a more costly and specialized cylindrical MCP (which would also require a cylindrical phosphor faceplate to avoid distortion).

The fiber optic coupling from the phosphor screen to the photodiodes consists

of three stages, all bonded and optically coupled: the reducing taper, a straight extension, and the fiber optic faceplate supplied on the Reticon chip, covering the semiconductor photodiode array. The phosphor P-4 was deposited by the vendor on the front side of the 40 → 25 mm reducing taper by a settling technique. This taper, produced in large quantities for military applications, originally had a reduction factor closer to 53 → 26 mm. The reduced side was polished back to create the 40 → 25 mm reduction necessary to couple the 40 mm active region of the MCP to the 25.6 mm Reticon array. (This was actually done incorrectly, as described below). The large side of the taper was machined to accept a fritted glass-to-metal seal with a metal ring, which in turn was welded to a vacuum re-entrant tube, thereby forming the vacuum barrier between the MCP image intensifier and the Reticon.

The straight extension allowed the Reticon (a monolithic 22-pin integrated circuit chip) to be positioned outside the detector mounting chamber, so that the pre-amplifier board could be attached directly to it. In the noisy electrical environment of a tokamak, this yields better signal-to-noise characteristics than connecting the chip (inside the chamber) to the circuit board (outside the chamber) with a shielded cable. The total separation between the MCP and the Reticon is $\sim$ 13 cm. To minimize distortion of the spectrum, a maximum shear distortion of 100 μm was specified for the total fiber optic connection.

Opaque inter-fiber cladding would have been preferred to prevent cross-talk between adjacent fibers, but this feature is not available in the standard taper components. The presence of scattered light in the fiber optic image conduit was verified by the application of non-conductive black paint to the exposed glass surfaces of the fiber optic extension rod and Reticon fiber optic face plate. This yielded a large reduction in background signal levels caused by ambient light reaching the Reticon.

2.2.2 Linear Photodiode Array and Electronics

The Reticon RL1024SF self-scanned linear photodiode array is one of a series of commercial solid state devices designed specifically for use in spectroscopic applications, featuring a length-to-width aspect ratio of 100:1 for each sensor element, or pixel. Each pixel has an associated storage capacitor which integrates photocurrent between scans. An internal shift register scanning circuit multiplexes the charge pulse from each pixel sequentially into the electronic readout circuit. Each pixel begins integrating signal immediately after being scanned, even as its neighboring pixel is being processed. As there are actually two readout lines on the Reticon chip, one for even pixels and one for odd, the readout circuit contains two identical, parallel circuits which clock out one even and one odd pixel simultaneously. The control and readout circuit consists of four modules, shown schematically in Figure 2.6. The first circuit board, attached directly to the Reticon, contains pre-amplifiers which convert the charge pulses (0–14 pcoul) to voltage pulses (0–5 V). The second board contains Sample and Hold circuits and 12-bit Analog to Digital converters. A video output connection is also provided for each readout line, enabling the user to monitor the output spectra in real time. The digitized even and odd data words are multiplexed together and passed to the third board, a programmable CAMAC controller module. The 12-bit data words are joined with 4 status bits, and the final 16-bit data words are clocked into the final module, an Interface Standards DM series dual port CAMAC memory module with 132K 16-bit word capacity. The 4 status bits are used for several bookkeeping purposes, including frame number and elapsed time. The first three boards were designed and supplied by Terrapin Consulting, in accordance with specifications provided by the author and J.L. Terry of MIT.

The controller board contains all the logic and interface circuits needed to

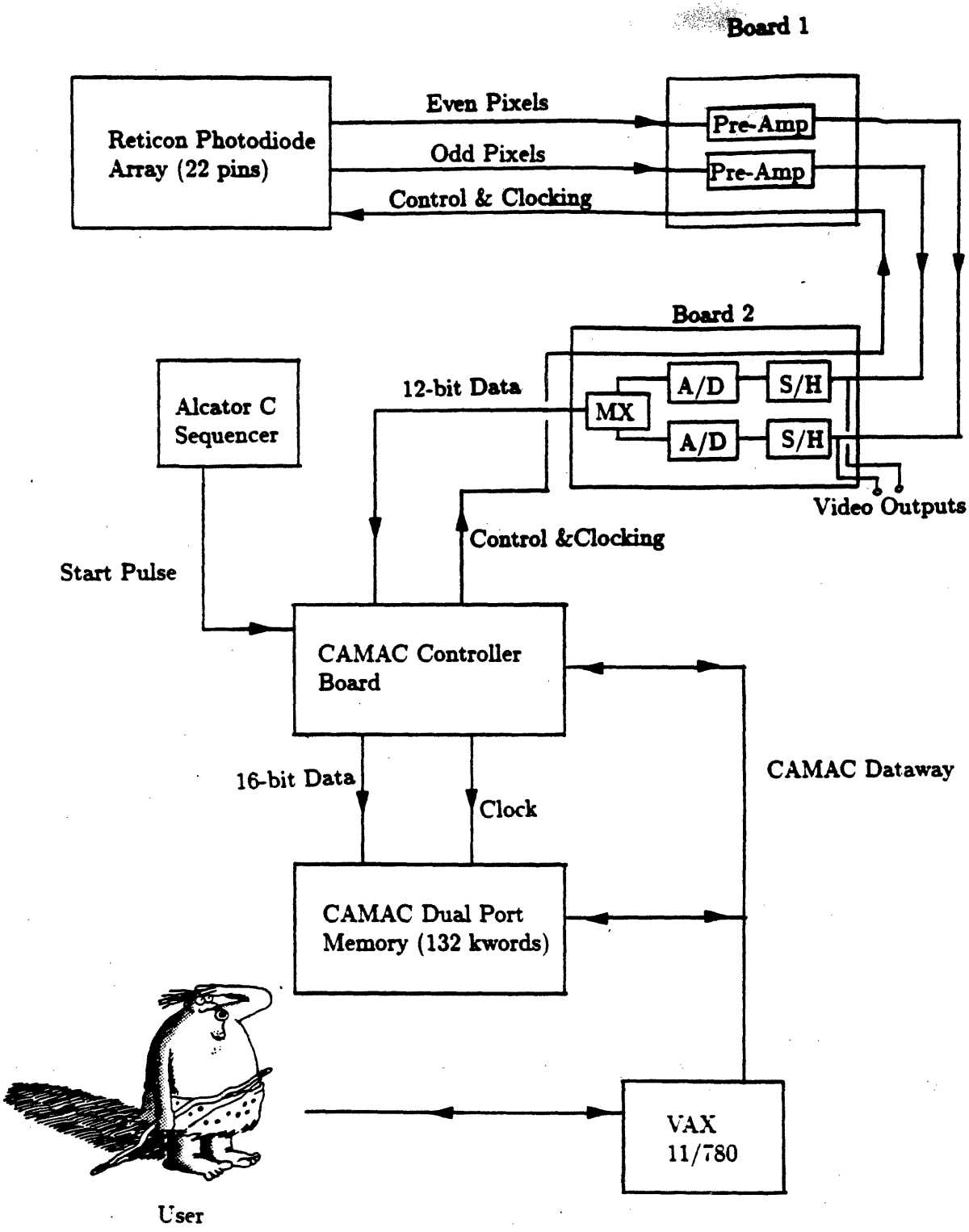

Figure 2.6 Schematic diagram of Reticon control and digital readout circuit.

communicate with both the Reticon and the CAMAC dataway, which in turn communicates with the Alcator computer system (a VAX 11/780) and hence the user. This board generates clocking pulses according to pre-programmed control sequence instructions; incorporating a number of features not found in the video readout circuit available from Reticon. The fastest components available, compatible with 12-bit resolution, were employed in the two parallel analog readout circuits. Digitization occurs at 250 kHz in each channel, yielding a net rate of 500 kHz. Thus, an entire 1024-pixel scan, or "frame," can be completed in just over 2 ms. However, if the user is not interested in the entire spectrum, the controller allows for "pixel select" mode, in which only specified pixels are digitized and stored in memory. Since the unselected pixels are not used, it is possible to process them without regard for resolution at the faster net rate of 5 MHz, so that partial frames can be scanned in 0.5 ms or less. Pixel select has the added virtue of saving memory requirements, as the unselected pixels are not stored. This pixel select feature divides the 1024 pixels into 256 independently selectable groups of 4 each.

The controller can be programmed for signal integration periods ranging from 0.5 milliseconds to 8 seconds, in discrete steps of factors of 2. The user also chooses the fraction of frames to be stored in the memory: every frame, every other frame, every fourth frame, etc., up to 1 in 64. This allows for economy of memory while preserving flexibility of integration times, particularly useful when monitoring a bright spectrum (necessitating brief integration times to avoid saturation of the Reticon) during a steady or slowly changing portion of the plasma discharge (allowing long intervals between data sampling). Up to four such "states" (combinations of integration time and storage fraction) are programmed into the controller prior to data acquisition, along with the number of frames to be stored in each state before changing to the next state.

An example may help to illustrate this system: Suppose a plasma shot is set up to have a sudden injection of a non-intrinsic impurity (e.g., silicon) 250 msec after initiation of the discharge. The VUV spectrograph is monitoring the spectrum near the bright 500 Å Si-XII resonance line ($2p - 2s$). The plasma discharge can be treated as consisting of four phases: (1)— plasma breakdown and current ramp-up, when the spectrograph monitors a rapidly changing spectrum of relatively low brightness, (2)— discharge "flat-top," when the quasi-steady state plasma radiates a slowly changing spectrum of low or moderate brightness, (3)— the Si injection, which produces a very bright, rapidly changing spectrum, and (4)— more flat-top followed by current ramp-down, with a spectrum similar to phase 2. The programmable controller allows the user to optimize the integration period and data sampling fraction for each phase of the discharge.

The data from the Reticon contain both noise and a fixed dark pattern [54,55]. The dark pattern is due to dark photocurrents, non-zero offsets in the ADC's, and slight differences in the even and odd pixel analog circuits. Noise consists of random fluctuations in these quantities, plus any pickup of local electrical noise. Both the dark current and the noise associated with it can be dramatically reduced by actively cooling the Reticon. However, the 12-bit resolution incorporated in this system does not clearly warrant the added expense and design constraints required by active cooling, and therefore no cooling was used. Cooling would be needed if higher sensitivity and dynamic range were required. To compensate for the fixed dark pattern, a background data acquisition cycle is completed after each plasma discharge (or other data cycle), using the identical controller sequence. Averaged dark background frames for each state are then subtracted from the data frames, leaving the true spectrum plus a small random noise component.

While taking plasma data, the sequence of events proceeds as follows: The user

has previously selected the data acquisition options as outlined above (integration periods, etc.). These coded instructions are transferred into the CAMAC controller board, initializing both it and the CAMAC memory module. Upon receipt of a pulse from the Alcator C sequencer circuit, the data acquisition cycle begins, and the data are stored at real-time rates in the memory module. After the tokamak shot, these data are retrieved and stored, along with the coded setup file. A background data cycle is then completed and stored, and the modules are re-initialized for the next tokamak shot.

2.2.3 Mounting Chamber

A new detector chamber, replacing the old exit slit assembly, was designed and constructed at MIT in order to house the MCP detector system and position it properly on the Rowland circle of the spectrograph. In order to utilize the existing drive assembly on the McPherson, the mounting chamber was designed to attach directly to the old moving carriage, leaving room between the two for the drive screw assembly which pulls the carriage along the fixed track. A special pivoting adapter plate was constructed to connect the carriage to the drive screw assembly, a function which had been performed within the old pivoting exit slit assembly. Note that while the old exit slit had to pivot to face the grating as the carriage moved, the new chamber is instead fixed with respect to the carriage in order to keep the front of the MCP tangent to the Rowland circle.

The chamber is essentially a box with several openings and a removable lid, all machined from 304 Stainless Steel to strict tolerances and joined with interior welds to minimize virtual leaks. All parts were electropolished prior to welding. Copper gasket seals are utilized in Conflat-style flanges at all openings except the lid and the grating side port, which are sealed with Viton synthetic O-rings. An O-ring is

used at the grating side port to match the flange of the flexible vacuum bellows, which connects the movable detector chamber to the fixed grating chamber. The irregular shape of the lid prevented the use of standard copper gaskets there. A 6″ flange is provided for mounting the detector; internal supports described below are also provided. The detector flange resides on the side of the chamber outside and roughly tangent to the Rowland circle. Opposite the detector flange there are two "mini-Conflat" style 1.75″ flanges for attachment of two rotary motion vacuum feedthroughs, used to position the detector while under vacuum. Finally, opposite the grating side port there is a 4.75″ flange, normally used for attachment of an auxiliary 8 liter/sec ion pump. All copper-seal flanges were welded into the chamber, while the O-ring groove on the grating side was machined into the side of the chamber wall. The other O-ring groove was machined into the lid, where it seals against a flat, polished collar welded around the top sides of the chamber.

The chamber was designed with several objectives: to allow the closest possible approach of the detector to the grating chamber (in order to view the shortest wavelengths), to minimize the off-axis bending of the bellows as the chamber moved and turned, to avoid fixed obstacles as the chamber moved along the track (e.g., drive screw gear box and connection rod, and extended grating chamber), to minimize the vertical extent from the base to the lid, and to allow sufficient extra space for alignment movements. The actual chamber has a 77° interior angle at the corner between the grating side and the detector side, so that the flexible bellows is straight when the detector chamber is in the middle of its scanning range. The lid (which overlaps the sides of the box) is further cut away on the side nearest the grating to allow the closest approach to the grating chamber.

Inside the chamber, the detector is held in a mount with two degrees of freedom: a linear motion in the plane of and normal to the Rowland circle (to position

the front of the MCP on the Rowland circle), and a rotary motion whose axis is parallel to the grating grooves and passes through the center of the MCP (to position the MCP tangent to the Rowland circle. These two motions were judged to represent the most critical alignments, given the expected precision of the machining along other axes. To effect these movements, a linear translator stage coupled to a rotation stage are built into the mount, as follows: the linear translation stage is attached directly to the base of the chamber via precisely located blind-tapped screw holes. Above it is attached an adapter plate containing mounting holes for the rotation stage, with an offset in the direction of the linear motion due to space constraints. The rotation stage supports a right angle bracket, whose "vertical" side supports the detector via a mounting ring. A flexible metal bellows between the detector head and the chamber which houses it allows the detector enough mobility for these focusing adjustments. Figure 2.7 shows a layout schematic of the detector mounted inside the chamber, as viewed from the grating.

As the mount is too large to fit through the hole in the detector's 6″ flange, it is attached to the chamber prior to the installation of the detector. The connections between the detector and the support ring are made after the detector re-entrant tube is inserted through the side of the chamber. Both the translation and rotation stages are micrometer driven; external positioning is accomplished via the vacuum rotary motion feedthroughs. Special couplers were made to connect the rotary feedthrough shafts to the drive screws of the motion stages; provisions for slight mis-alignments were incorporated in the design. Both stages were prepared for ultra-high vacuum by the manufacturer (Klinger Corp.), including venting of all screws and air pockets, thorough cleaning and degreasing, and re-lubrication with molybdenum disulfide.

In order to reduce vacuum forces on the mount, the re-entrant vacuum bellows

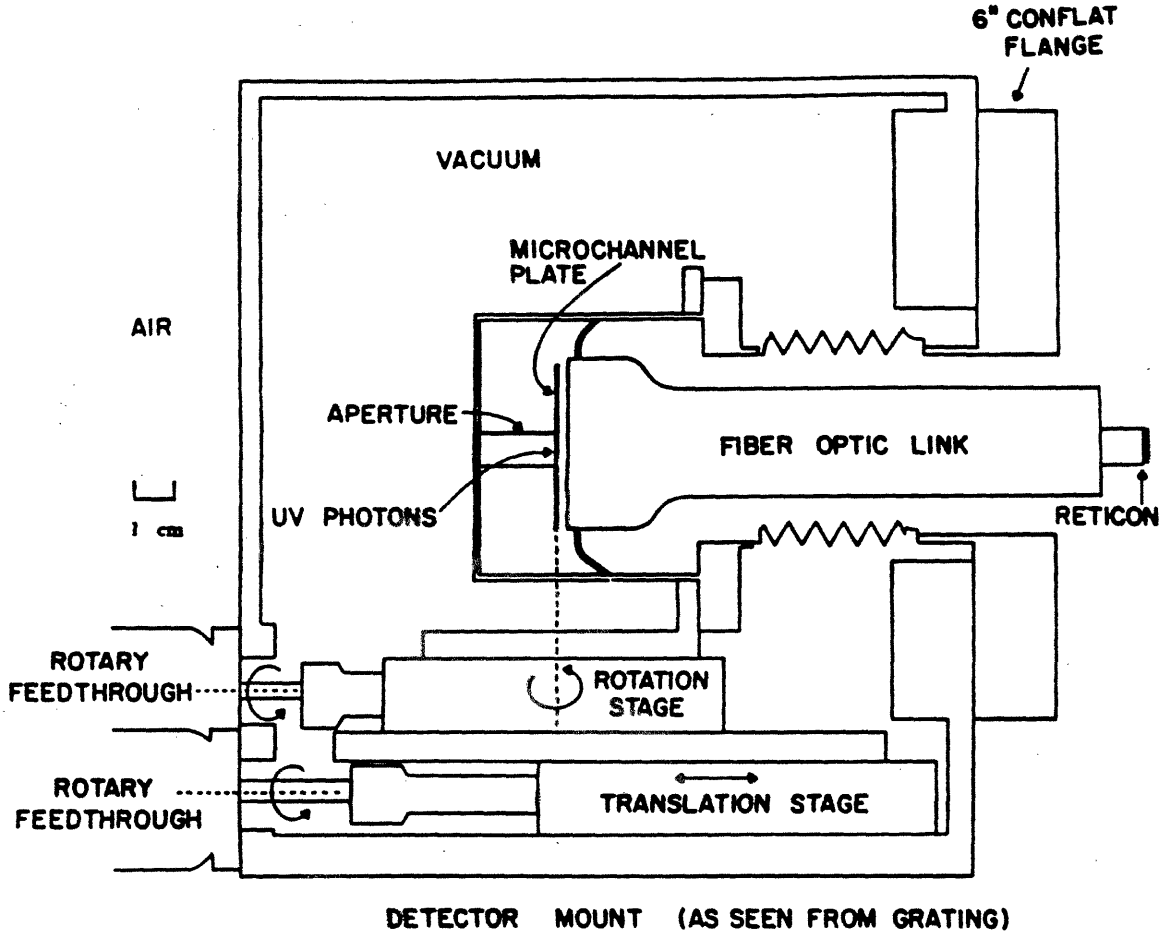

Figure 2.7 Schematic of detector assembly inside mounting chamber (drawn to scale).

between the phosphor screen and the detector flange were chosen to have the smallest diameter possible, since the force pulling the detector into the chamber equals the cross sectional area of the bellows times atmospheric pressure. The bellows diameter is in fact smaller than that of the detector can structure which attaches to the mounting ring. The force is opposed by the linear translation stage, yielding a stiff response on that rotary motion feedthrough. Clean graphite powder was added to the moving parts of this assembly to minimize binding.

2.3 Alignment and Installation

Proper alignment of all the optical components is crucial for high resolution spectroscopy. Alignment of the VUV spectrograph is divided into two distinct operations: grating alignment and detector alignment. These operations are described in this section, along with the installation of the instrument on the Alcator C tokamak.

2.3.1 Grating Alignment

The optical elements of the McPherson Model 247 are anchored to a large granite slab. The granite slab provides good optical stability and has good mechanical damping properties to alleviate the effects of pump vibrations, etc. Gratings are held in individual, removable holder assemblies which are reproducibly positioned in the grating chamber via a precision three-point mounting system. The Rowland circle is defined by the motion of the entrance slit and exit slit assemblies, which are constrained to move along a precision machined stainless steel track, or curved way. When properly adjusted by the factory, this motion keeps the centers of the entrance and exit slits positioned on this 2.2 meter diameter circle. Four adjustment

micrometers built into the grating holders provide the necessary degrees of freedom to position a grating correctly.

The first two adjustments align the spherical concave grating's normal axis so as to point towards the center of the Rowland circle. This is accomplished by positioning a small HeNe laser beam along the correct line, defined by the following two points: 1) a cross-hair formed by stretching two fine threads across fiducial marks provided at an alignment port on the instrumental vacuum chamber, and 2) the center of the grating, as determined by a grating alignment mask with a tiny hole bored at the center. Once the laser beam is aligned on this nominally horizontal line of sight, the grating is pivoted up/down and right/left about its center so as to bring the reflected laser beam back onto itself. The HeNe laser was positioned on a tripod roughly 8 meters distant from the grating.

The third alignment motion ensures that the grooves of the grating are perpendicular to the Rowland circle. This is accomplished with the same HeNe laser, positioned as before. The beam is not only reflected by the zeroth order reflection (mirroring) of the grating, but is also diffracted by the grating into several angles satisfying the grating equation (Eqn. 2.1) with $\alpha = 0$. Each of these diffracted rays lies in the plane normal to the grooves. With the granite slab and Rowland circle in the normal, nominally horizontal position, correct groove alignment is indicated when the height of the diffracted rays, measured from the table-top surface of the granite slab, is the same as the height of the incoming laser beam and grating center. This is achieved by rotating the grating about its normal axis.

The final alignment is the focusing adjustment, which translationally moves the grating along its normal axis until the grating center is tangent to the Rowland circle defined by the granite slab. This was accomplished by examining the zeroth order image (ordinary focused reflection) of the entrance slit with a photodiode

detector located just behind the exit slit. The entrance slit was illuminated from behind with a high intensity lamp, yielding a bright source of visible light. The image was measured by scanning the original exit slit assembly through the bright central (zeroth order) image and recording the photodiode response with a strip recorder. By moving the grating in and out along its normal axis, the image could be optimized to a sharp, narrow peak. This indicated that the entrance slit, grating center, and exit slit assembly were all positioned on the Rowland circle.

The slits are rotatable by a few degrees in their flange assemblies, and it was found that careful re-alignment of the slit vertical orientation was necessary to achieve the narrowest images. It was also found experimentally that the peak signal varied linearly with the nominal slit widths, but with a finite offset with regard to the nominal readings on the controlling micrometers. This offset was duly noted and accounted for in subsequent work. Finally, it was noted that the peak position of the central order image was a more sensitive and reproducible monitor of the grating rotation about its nominal vertical axis than was the reflected laser-crosshair method. When correctly aligned, the entrance slit and its zeroth order image should be symmetric about the center of the grating.

This alignment procedure was conducted in air, using visible light and the original exit slit assembly (not the new MCP detector system). Steps 1–3 were checked and adjusted, if necessary, after each movement of the focusing micrometer. The focusing was adjusted coarsely with both the entrance and exit slits open to 100 μm or more; progressively narrower slits were used to fine tune the focus. The two slits were usually set to the same width initially. As the entrance slit width was decreased below approximately 20 μm, however, diffraction due to the finite projected width of the diffraction grating itself limited the image sharpness. The ruled area of the grating is 5 cm wide; viewed from the 87.5° grazing incidence

angle used at the time it only presented an effective aperture of 2.2 mm to the admitted beam of light ($\lambda \approx 5000$ Å). The image, some 10 cm from the grating center, has minima at angles $\theta = \lambda/a$ from the central peak, yielding a calculated FWHM limit of ~ 20 μm. Entrance slit widths below 20 μm were therefore not very practical for the focusing procedure, yielding progressively less signal without much improvement in image sharpness.

As the image came into focus, it went from a broad, flat profile to a two-peaked profile. The two peaks then merged into a single peak, whose profile became narrower with continued focusing. Beyond a certain point, the full width at half maximum (FWHM) changed very slowly with continued adjustment. For final tuning, the full width at quarter maximum (FWQM) was found to be a more sensitive indicator and was therefore used to determine the optimum focus. The image formed by a 20 μm entrance slit was scanned with a 15 μm exit slit for the final adjustment. The best focus achieved with a 20 μm entrance slit corresponded to a projected image width (perpendicular to the direction of propagation) with FWHM of ~ 34 μm and FWQM of ~ 50 μm. With 2 μm entrance and exit slits, the corresponding numbers were 28 and 42 μm.

Two gratings were aligned, each seated in its own holder assembly. The first grating was a 600 line/mm replica of a ruled grating, with a blaze angle of 2°4′. For an angle of incidence set at 88°, used during calibration and on the tokamak, the MCP detector has a range of $\sim 30 - 1165$ Å. In this configuration, the grating yields an especially bright image (blazes) due to planar reflection off the individual groove facets for $\lambda \approx 83.2$ Å in first order, 41.6 Å in second order, and so forth. The second grating was a 1200 line/mm holographic grating, whose sinusoidal grooves have no particular blaze angle. This grating allows higher resolution coverage of the region $15 - 560$ Å. Both gratings had gold overcoatings to enhance reflectivity

at VUV wavelengths.

After final grating alignment, all positioning micrometers were locked, and a grating mask was attached to the side of the grating holder facing the entrance slit. This mask restricts the area of the concave grating visible from the entrance slit, thereby improving the theoretical resolution of the instrument [42]. A second function is to restrict the amount of stray light that gets through the system, especially when there is a direct line of sight from the entrance slit to the detector. The vertical extent of the illuminated area of the grating is also defined by the mask. The masks were aligned so as to keep the illumination from the high intensity lamp centered at the grating center, Tic marks along the mask assembly then allowed one to accurately adjust for different angles of incidence, if necessary.

2.3.2 Detector Installation and Alignment

After the gratings were aligned, the original exit slit assembly was replaced with the new detector chamber. The new MCP detector system was installed in the chamber, and the entire system was pumped out with the 600 line/mm grating in place. A hollow cathode platinum lamp, filled with neon and with a MgF_2 window, was attached to the entrance slit assembly with an O-ring vacuum seal. The entrance slit was moved to $\alpha = 85°$ in order to allow the central order image to be scanned across the entire MCP input side for alignment and gain studies. These initial studies were conducted with a different electronic readout system than that described earlier. Rather than the fast, digital CAMAC system used for the calibration studies and tokamak work, a simpler video readout circuit supplied by EG&G Reticon was used in conjunction with an oscilloscope for most of the studies described in this section. The platinum hollow cathode lamp was typically operated with a bias voltage of 50 V and discharge current of $10 - 20$ mA.

Three problems were rapidly found with the detector system. First, the sensitivity to ambient light was corrected by the application of black paint to the portion of the fiber optics extending outside the vacuum chamber, as described earlier. Second, the high voltage overcurrent trip monitors shut down the MCP biasing with alarming regularity during the first few months of operation, usually accompanied by a sudden rise in the pressure in the detector chamber. Finally, a spontaneous emission process was noticed, manifested by a rapidly changing output "spectrum" in the absence of any light input at the entrance slit. This emission only occurred when the repeller plate was biased more negatively than the input side of the MCP by $\sim$ 500 V or more, and could be visibly seen on the uncovered end of the protruding fiber optic bundle as a flickering green glow (due to the phosphor) before the black paint was applied. The power supplies would generally trip if the amplitude of this emission became large enough.

The power supply tripping was attributed to arcing somewhere in the detector assembly. The absolute voltages seemed to make more difference with regard to arcing than did the voltage across the MCP, which probably indicates arcing between the MCP or biasing rings and the shield or mounting structure, rather than internal arcing inside the MCP. The video output level was sometimes seen to undergo a sudden, marked increase across the frame, coincident with the tripping of the power supply. The arcing was apparently small enough, brief enough, and/or far enough removed from the MCP so as not to damage the MCP image intensifier. There was a clear connection between relatively high pressures and the frequency of the tripping. It is suspected that the physical condition of the MCP (amount of residual gases adsorbed on microchannel walls, sharpness of various edges, etc.) is also related to the arcing. By adding an ion pump to the detector chamber and cutting additional pumpout holes in the detector shield, the pressure at the detec-

tor was lowered. The detector was operated for several days, at reduced voltages with no input light, to "scrub" the microchannels; the gain was gradually raised to normal levels during this process. In addition, the detector was usually turned on very slowly, being allowed to settle for a few minutes at each increment of 50–100 V across the MCP. Scrubbing was later conducted with the platinum light source on. By such measures, the arcing situation gradually improved to the point that the detector could be turned on all day, at full voltage (1000 V) across the MCP, with no tripping. This stable operating regime was achieved prior to installation on the tokamak.

The flickering spontaneous emission is believed to arise from ion feedback processes. It was found to occur more readily when the ion pump was on, even though there was no line of sight from the detector to the pump. The pattern seen on the protruding fiber optic extension was dynamic, moving about without sharp boundaries. For unknown reasons, it generally was brightest along a diameter of the MCP angled at about 20° with respect to the horizontal Reticon. The biasing which pulls electrons towards and through the MCP causes ionized residual gas molecules to accelerate in the opposite direction. These ions can collide with the sides of the microchannels and cause additional electrons to be released. Ion feedback is a recognized problem inside MCP's if the pressure is too high [51,48]. In the case of the detector described here, however, there is an additional electric field in front of the MCP which can accelerate ions into the repeller plate. If the impact energy is sufficient to liberate electrons from the surface of the repeller, which in turn can ionize more residual gas, a self-sustaining plasma discharge can be formed in the region between the MCP and the repeller plate. Because this phenomenon only appeared when the repeller plate was biased more negatively than the MCP, and because the gain across the MCP was non-uniform when the repeller was so biased

(see Chapter 3), the repeller plate was almost always kept at the same voltage as the input side of the MCP while taking data.

Two other undesirable features were noted, both related to the fiber optic relay which transferred, or mapped, the image formed on the phosphor screen onto the Reticon PDA. First, the Reticon has 1024 pixel elements, but only ~ 930 pixels are actually mapped back onto the active region of the image intensifier. Roughly 60 pixels on the long wavelength side and 35 pixels on the short wavelength side of the Reticon are optically connected not to the phosphor, but rather to the stainless mounting rings or some other structural component. These pixels were therefore rendered useless. This problem was not deemed serious enough to warrant the delay involved in obtaining a corrected assembly.

The second problem with the image mapping was more subtle. It was found that the central order image of the platinum lamp was consistently more sharply peaked at the short wavelength side of the detector than at the other side. Furthermore, for the same discrete displacement of the detector assembly along the Rowland circle, the image center moved by more pixels on the high wavelength side than on the low wavelength side. The differences were significantly larger than the slight effect due to the turning of the detector as the carriage moved along the Rowland circle. This was initially assumed to be due to poor detector alignment, but no amount of aligning seemed to remedy this discrepancy. The mapping transformation was measured by scanning the image across the MCP, moving the detector carriage along the Rowland circle and noting the carriage position and the corresponding position (pixel number) of the image peak. A numerical code was written to model the effects of various possible errors in the assumed position and alignment of the detector, but no combination of parameters could be found to explain the results. It was finally deduced that the fiber optic taper had a significant amount

of non-uniformity, with an image reduction factor that varied across the face of the taper. This is unfortunately impossible to measure directly without complete disassembly of the detector.

The alignment of the detector was therefore accomplished by first moving the detector in and out along the radius from the center of the Rowland circle. Keeping the carriage position adjusted so as to maintain the location of the image peak at the center of the detector ($\sim$ pixel 512), the optimum focus position was found. At this point it was assumed that the center of the MCP input face was on the Rowland circle.

The next step involved rotating the detector around the vertical axis perpendicular to the Rowland circle at the MCP center so that the plane of the MCP would be tangent to the Rowland circle. It was verified that the rotation axis of the detector passed through or near the MCP site corresponding to pixel 512 by noting the displacement of the image center as the detector was rotated slightly. This displacement was zero when the image started near pixel 512; the displacement increased markedly if the image started to either side of this "center pixel." Now the detector was moved in towards the center of the Rowland circle by an amount calculated to position simultaneously pixels 100 and 900 on the Rowland circle when the angle of rotation was correctly set. As this angle was changed by discrete steps, the quality of focus was noted when the image was positioned at these two locations. It was expected that the best focus would occur at the same angle of rotation for the two sites. However, the two pixel locations came into best focus at slightly different angles, indicating that these two corresponding sites on the MCP were not simultaneously positioned on the Rowland circle. The results indicated that when the detector rotation was set at the average of the two angles, these two points were outside the Rowland circle by about the same distance that the center pixel

was inside the circle. This could occur if the MCP was slightly bowed by mounting stresses, with a radius of curvature in the dispersion plane which unfortunately pointed in the opposite direction to that of the Rowland circle itself. The detector was therefore left in this position, with all three focusing points estimated to be 135 ± 10 μm off of the Rowland circle. Had the MCP been perfectly flat, it could have been positioned with pixels 1, 512, and 1024 all mapped to locations within 90 μm of the focal circle.

With the detector aligned, the actual transfer function that mapped the image from the MCP onto the Reticon was measured. To do this, the image was scanned across the detector by moving the detector carriage. The carriage position was moved in discrete steps so as to move the center of the image by 10 pixels. The pixel number and carriage position were noted for each location. Then, assuming that both the light path and the position of the MCP site which mapped onto the center pixel were known, and treating the MCP as flat and correctly oriented, the effective distance from center along the MCP was calculated for each pixel recorded (1 out of every 10). This process is possible because the focused ray of light is fixed in space as the detector moves by, while the relative motion of the detector is calculable from the precisely indicated position of the carriage. The effective position of the remaining pixels was calculated by interpolation. The net result is a list of pixel number vs. effective position in the wavelength dispersion direction, relative to the center pixel. As expected, the inter-pixel spacing is largest where apparent resolution is the best, i.e. at the short wavelength end. Obviously, this mapping function is crucial in order to convert pixel number to wavelength.

2.3.3 Installation on Alcator C

Due to space and access constraints, it was necessary to rotate the spectrograph by 90° for installation on Alcator C. This orientation had the additional advantage of aligning the long axis of the entrance slit and pre-slit along the horizontal toroidal direction of the tokamak plasma (nominal symmetry direction), allowing better spatial resolution in the vertical radial direction. The granite slab which normally served as a flat table-top base was turned with the long side down, as indicated in Figure 2.2. A two-tiered mounting frame was used to hold the instrument in position. The first held the instrument in a pivoting arrangement, such that the entire instrument could be pivoted about a horizontal axis which intercepts and is normal to the incoming optical line of sight. This was accomplished by raising and lowering the end away from the tokamak via an electric jack. Scans across the minor radius of the tokamak plasma were thus made possible. The second frame served to support the first so that the optical line of sight from the grating to the plasma would be level with the center plane of the tokamak, some 3 meters off the floor. The first frame was rolled onto the second and secured by bolts.

Special precautions were taken to support the detector chamber in this new position. A trolley system was devised, with a movable cart positioned on a horizontal track above the detector chamber. Constant tension roller springs were attached from the cart to the detector chamber, supporting its weight in order to relieve the torque on the precision curved track and screw assembly. As the chamber moved along the Rowland circle, the cart moved freely with it, remaining above the chamber. The springs played out as the vertical separation between the chamber and the cart changed. A rigid brace was also provided to support the turbomolecular pump, which was reconnected to the instrument with a right angle bend so as to maintain its required vertical spin axis.

To align the spectrograph with the tokamak, an alignment telescope could be sighted along the entrance beamline through the use of an insertable mirror. The plasma is visible through a "keyhole" in the port, measuring approximately 8 cm high by 2.0 cm wide. The distance from the plasma center to the grating is approximately 270 cm. Some motion in the horizontal direction could be achieved by adjusting the bolts between the top and bottom frames. Vertical alignment was adjusted via threaded leveling screws on the bottom frame, as well as with the jack already mentioned. A bubble level positioned across the top side of the granite provided a simple check of the levelness, as the incident light is parallel to this side when $\alpha = 88°$, as was the case for all tokamak spectra.

Chapter 3

Spectrograph Performance

3.1 Sensitivity

In order to measure the absolute brightness of a source, such as a tokamak plasma, the system sensitivity must be established as a function of wavelength. This sensitivity, coupled with a knowledge of the viewing geometry (solid angle, etc.) is necessary to convert the output signals from the Reticon into units of brightness (photons/Å−sec−ster−cm^2). The spectrograph sensitivity was therefore absolutely calibrated [56] in the region 20–150 Å with a mini-focus e-beam soft X-ray source referenced to a proportional counter. Cross calibration at longer wavelengths was obtained through simultaneous comparisons of several impurity resonance lines with an absolutely calibrated 0.2 meter EUV monochromator. Details of each procedure are presented below.

3.1.1 Soft X-ray Calibration System

The soft X-ray calibration system used for the region 20–150 Å was supplied by J.E. Manson Co. [57] to MIT specifications, and is shown schematically in Figure 3.1. The system consists of a mini-focus X-ray source, a reference proportional counter with gas flow system, biasing electronics for the source, readout electronics for the proportional counter, and a vacuum chamber to house the source, proportional counter, movable filters and apertures, etc. The X-ray source is a vacuum

diode, utilizing an ohmically heated tungsten hairpin filament as a thermionic cathode. The anode is kept at positive high voltage; characteristic K_α X-rays are emitted from the anode material upon impact excitation by the electron beam. Emission of electrons from the tip of the filament is regulated by a self-biasing passive feedback circuit which keeps the filament at about 100 V positive. The filament is kept hot enough to remove temperature effects on the beam current (saturation regime). Similar systems are used in scanning electron microscopes. This circuit yields a stable beam current, constant to within about 2% after the filament has reached an equilibrium operating temperature. The source typically operates at 1.3–5.0 kV and 60–400 μA.

The electron beam is focused by an electrostatic field onto a spot of $\lesssim 750$ μm diameter on the anode, 11 mm away. The anode is actually a small, screw-on cylindrical cap made of either graphite, aluminum, or magnesium. By interchanging anodes, the emission spectra of various elements are obtained. The metal anodes can be coated with a surface layer of various solutions or powders to provide different elements for calibration. When operated with a graphite anode at 5 kV and 100 μA, the source spot yields a typical output of $\sim 1.2 \times 10^{11}$ phot/sec-ster in the carbon K_α band (44.7 Å). The anode surface is angled at 45° to the direction of the X-ray beamline, which points toward the instrument to be calibrated.

To measure the absolute brightness of the X-ray source, a gas flow proportional counter can be inserted in the beamline. This proportional counter is mounted on a linear motion vacuum feedthrough and can be inserted into the beamline while the source is operating. The counter is flushed with a 50-50 mixture of argon and methane, maintained at a pressure of 200 Torr. Photons enter the counter chamber through a window made of 25 μg/cm^2 VYNS plastic supported on a fine 60% transparent 400 lines per inch nickel mesh. VYNS is a copolymer of 90% vinyl

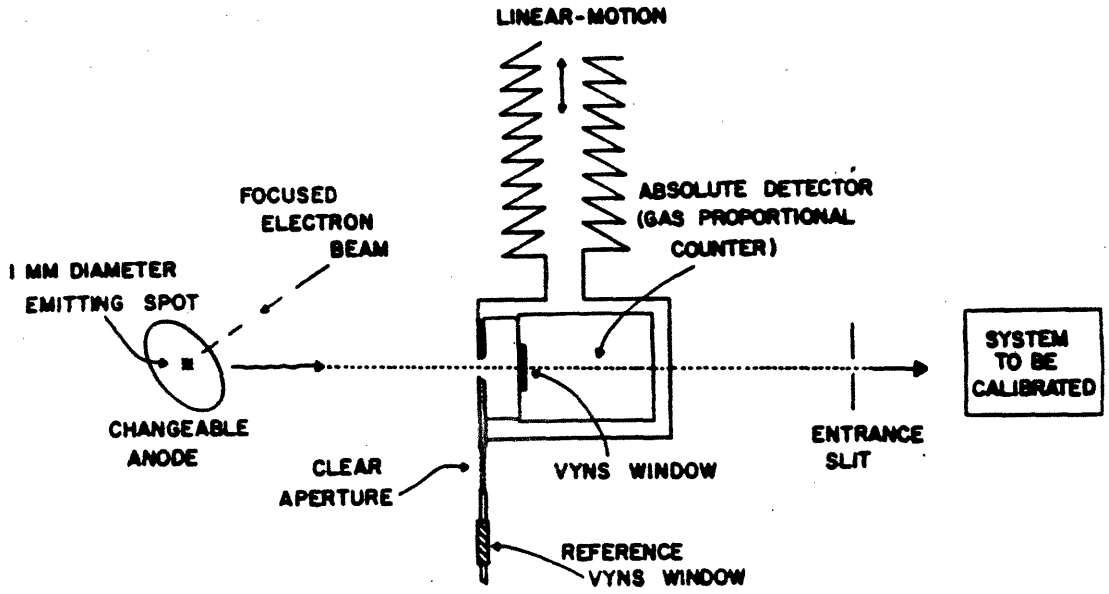

Figure 3.1 Soft X-ray calibration facility schematic.

chloride and 10% vinyl acetate, resembling common household plastic wrap. The central anode wire was typically biased at 1350 V. Under these conditions, the gas is over 99% efficient for photoionization at the wavelengths of interest, and the overall quantum efficiency of the proportional counter depends mainly on the measured transmission characteristics of the VYNS window, supplied by the vendor. Two crossed slits, each .005″ wide, are positioned in front of the window in order to limit the flux of X-ray photons, so that the electronics can operate in a photon counting mode. This yields an acceptance solid angle of 9.1×10^{-7} sterradians.

The electronics for the proportional counter were mostly standard nuclear instrumentation components. A Manson model PAL-01 preamp, mounted close to the anode feedthrough to minimize capacitive pickup, was the only custom made component. It converts the charge pulse on the high voltage anode into a pulse accepted by a main shaping amplifier (Tennelec TC 202 BLR), which is connected to a single channel analyzer (Tennelec TC 440) and counter. A multichannel analyzer (MCA) was used to monitor the pulse height distribution (PHD) of the proportional counter, which had a typical form shown in Figure 3.2. The gas pressure in the proportional counter was allowed to stabilize prior to the calibration measurements, as this variable affects the PHD. By using a variable amplitude pulser in conjunction with the MCA, the upper and lower discriminators on the SCA were set to levels corresponding to the desired band in the pulse height distribution, as indicated in the figure. The low energy peak in the PHD is primarily due to noise attributed to capacitive pickup of vibrational motions in the anode cable. This cable has some slack inside the vacuum chamber to accommodate the movement of the proportional counter. It was found necessary to isolate the source chamber from its turbopump by a flexible coupling in order to minimize this microphonic noise, which had a large component at 660 Hz (the frequency of the pump motor). The upper level

discriminator was generally set at a level for which the signal was 5–10% of the peak amplitude, in order to cut off the background bremsstrahlung radiation.

To make a calibration measurement, the source was first turned on and used to illuminate the entrance slit of the spectrograph. Source alignment was checked as needed by shifting the source position and watching the video output signals from the detector. The spectrum was scanned with the MCP detector, and the positions of the source lines to be calibrated were noted. Some anodes had more than one element present, and even single element anodes produced observable signals in several diffraction orders. After the initial determination of the anode spectral output, the proportional counter was inserted in the beam line. The PHD was analyzed, and discriminator levels were chosen for the line(s) present. The X-ray flux was optimized to yield about 15000 total counts per second, roughly the upper limit of the proportional counter before saturation effects become of concern. With the source turned off, a background count rate was established in the proportional counter. The source was turned back on, and count rates were then recorded for the line(s) to be calibrated, with approximately 10 readings taken for statistics. Variations were normally less than 1%. Then, without changing the source controls, the proportional counter was quickly removed from the beamline, allowing the X-ray flux to pass through to the spectrograph. Spectra were recorded at each line of interest, typically with 512 ms integration periods for 100 frames. Finally, a gate valve was closed between the X-ray source and the spectrograph, and background detector scans were recorded.

Calibration was measured in units of "raw counts" per accepted photon. An accepted photon is defined as one whose optical path passes through the entrance slit and grating mask, strikes the grating, and would reach the active area of the MCP if the grating were 100% efficient and focusing all photons at the wavelength

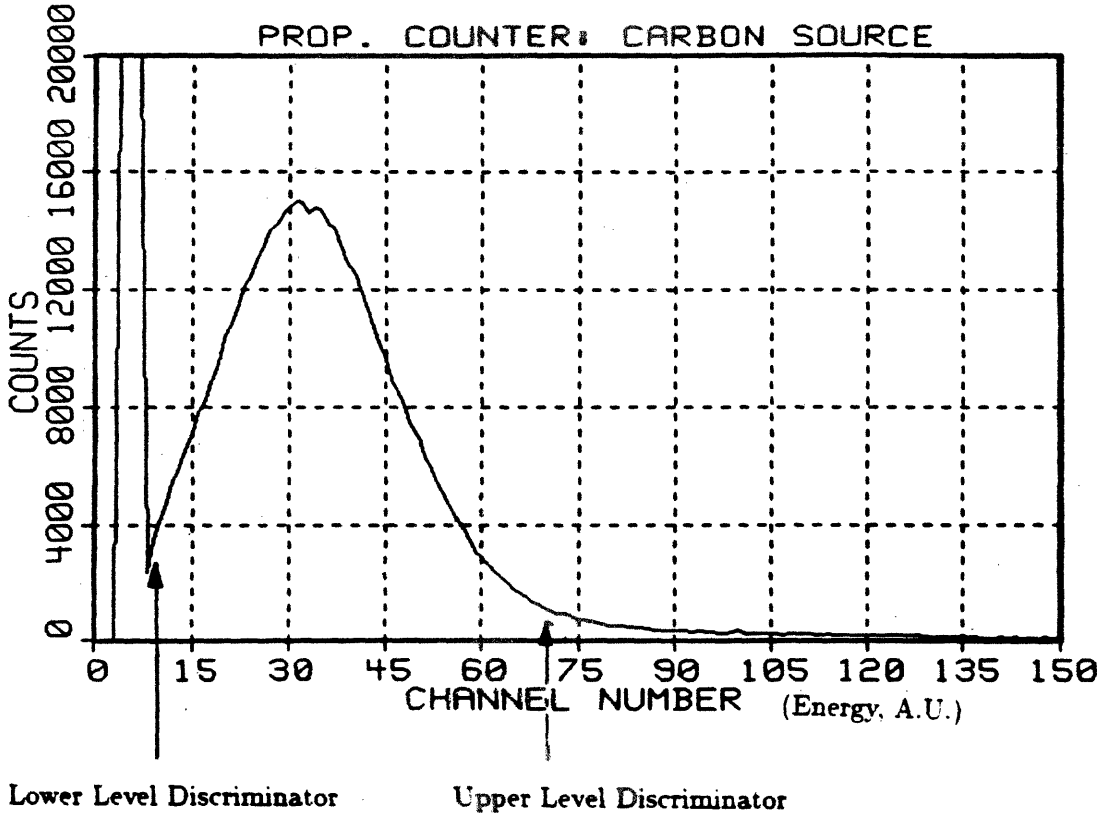

Figure 3.2 Pulse height distribution from proportional counter for graphite anode, showing typical levels for upper and lower discrimination.

of interest into the measured diffraction order. Given the measured proportional counter results, plus a knowledge of the geometry of the slit sizes, separation distances, and window transmission characteristics, the number of accepted photons is then calculable. Consideration is given to the fact that the concave grating does not focus in the nominally vertical dimension perpendicular to the dispersion direction, and that the effective height of the detector (4 mm) is less than that of the projected height of the entrance slit. The X-ray source is treated as a perfectly aligned point source in this calculation. This is justified because the area viewed by a point on the grating, looking through a typical 300 μm by 8 mm entrance slit, is much larger at the plane of the source than is the emitting spot ($\sim$ 750 μm diameter). The grating is roughly five times closer to the entrance slit than is the source. A "raw count" is defined as one digitized bit (out of the 12-bit ADC's) on a single pixel, after subtraction of the background dark scan. The total number of raw counts in a given line is obtained by summing over the pixels illuminated by that line, and subtracting any background level that is seen to the sides of the line. This is equivalent to integrating the area under the curve of counts vs. pixel number, with a background baseline. The lines are fairly wide due to the broadness of the K_α emission band from a solid matrix, but individual lines were well-separated. A typical calibration spectrum is shown in Figure 3.3, showing the first order peak of the carbon K_α line at 44.7 Å. The baseline, centroid, and FWHM are also indicated.

The spectrograph sensitivity was measured in the above fashion at six wavelengths, for both the 600 line/mm grating and the 1200 line/mm grating. All available orders up to the fourth were measured if possible. The wavelengths, elements, and anode material used were: 9.89 Å (Mg K_α, from solid Mg or $Mg(OH)_2$ solution), 23.6 Å (O K_α, from $Mg(OH)_2$ solution), 31.6 Å (N K_α, from AlN powder), 44.7 Å (C K_α, from graphite), 67 Å (B K_α, from boron powder), and 114 Å(Be K_α,

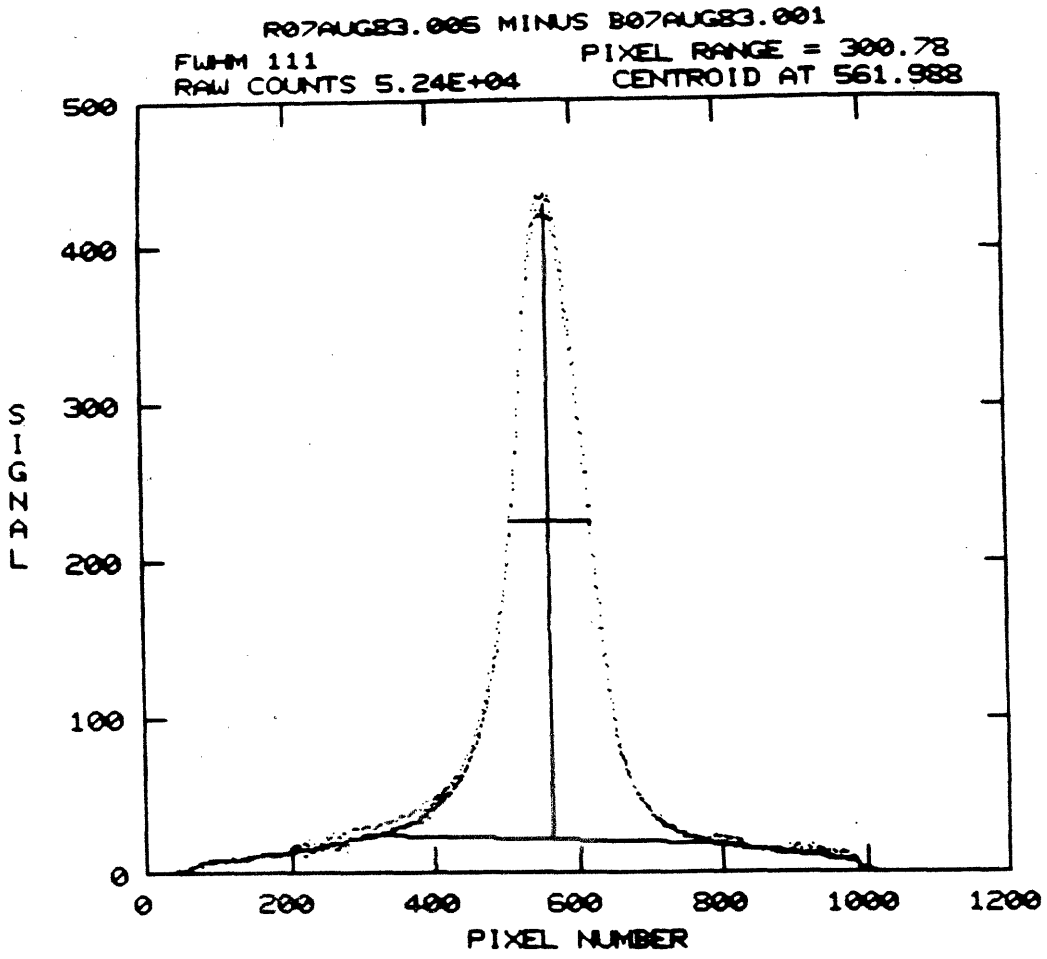

Figure 3.3 Calibration spectrum of carbon K_α radiation (44.7 Å). The total number of "raw counts" is the area between the carbon line and the baseline. Entrance and exit slits were 500 μm. Spectrum is from 600 line/mm grating, in first order.

from BeO powder in $Mg(OH)_2$ solution). Some anodes were prepared by J. Manson, others at MIT by the author. The preparation of anodes was often no more complicated that the application of household variety $Mg(OH)_2$ solution (Phillip's Milk of Magnesia) to a clean, polished aluminum anode cap.

The measured sensitivity is a system measurement, with no attempt to measure the quantum efficiency of the individual components (grating, CsI photocathode, MCP, phosphor, fiber optic link, and Reticon). This sensitivity can be expressed as

$$S(\lambda, V_i) = T(\lambda)Q(\lambda)R(V_i) \qquad 3.1$$

where $T(\lambda)$ is the efficiency of the grating, $Q(\lambda)$ is the quantum efficiency of the CsI photocathode, and $R(V_i)$ is the voltage-dependent detector system conversion factor for raw counts per photoelectron created at the MCP input surface. All sensitivity measurements were made under "standard" detector voltage conditions of -5.00 kV on the MCP output side, -6.00 kV on the MCP input side, and -6.00 kV on the repeller plate (the phosphor screen is always at ground). The functional dependence of $R(V_i)$ on the three voltages involved is independent of wavelength, and is discussed below.

The discrete sensitivity data points were joined not by the simplest possible curve, but rather one which preserved the characteristics of the published CsI sensitivity as a function of wavelength in this region [50,58]. In particular, CsI is known to have a strong sensitivity peak at $\lambda \approx 115$ Å. The effect of the grating blaze angle was also considered in constructing the calibration curves for the ruled (600 line/mm) grating. The resulting system sensitivity curves with the 600 line/mm grating are shown in Figure 3.4(a–d), for the first through fourth diffraction orders. The system sensitivity data with the 1200 line/mm grating are shown for the first order only in Figure 3.5. These sensitivity curves are estimated to be accurate to

$\pm 40\%$, given the uncertainties related to the proportional counter (chiefly window transmission, solid angle subtended, and upper and lower discriminator settings) and the spectrograph (chiefly alignment, solid angle subtended, and measurement reproducibility).

3.1.2 Cross-calibration with 0.2 Meter EUV Monochromator

The system sensitivity for $\lambda \gtrsim 140$ Å was initially taken to follow the form of the CsI quantum efficiency curve [50,58]. After installation on Alcator C, this sensitivity could be directly measured by cross-calibration with another, absolutely calibrated extreme ultraviolet monochromator.

This instrument was a 0.2 meter normal incidence vacuum monochromator, covering the spectral range 350 Å $< \lambda <$ 1200 Å. It had been absolutely calibrated at the Johns Hopkins University EUV (extreme ultraviolet) calibration facility, which utilizes emission lines from various gases in a hollow cathode source and relies upon an absolutely calibrated photodiode from the National Bureau of Standards for reference. The calibration of this monochromator was estimated to be accurate to within $\sim \pm 15\%$ for $\lambda \gtrsim 450$ Å, and $\sim \pm 40\%$ for shorter wavelengths. By monitoring the same impurity emission line during tokamak discharges, the sensitivity of the 2.2 meter VUV instrument could be calibrated by using the monochromator as a reference detector. This was done for several bright impurity emission lines in the region 420 – 1035 Å. The results indicated that the extrapolated sensitivity curve was somewhat low, requiring a correction factor ranging from 1.3 to 2.5 in this region.

The overall uncertainty in the corrected sensitivity curve is estimated to be a factor of 1.5 in the region $\lambda \gtrsim 450$ Å, and roughly a factor of 2.5 for the extrapolated

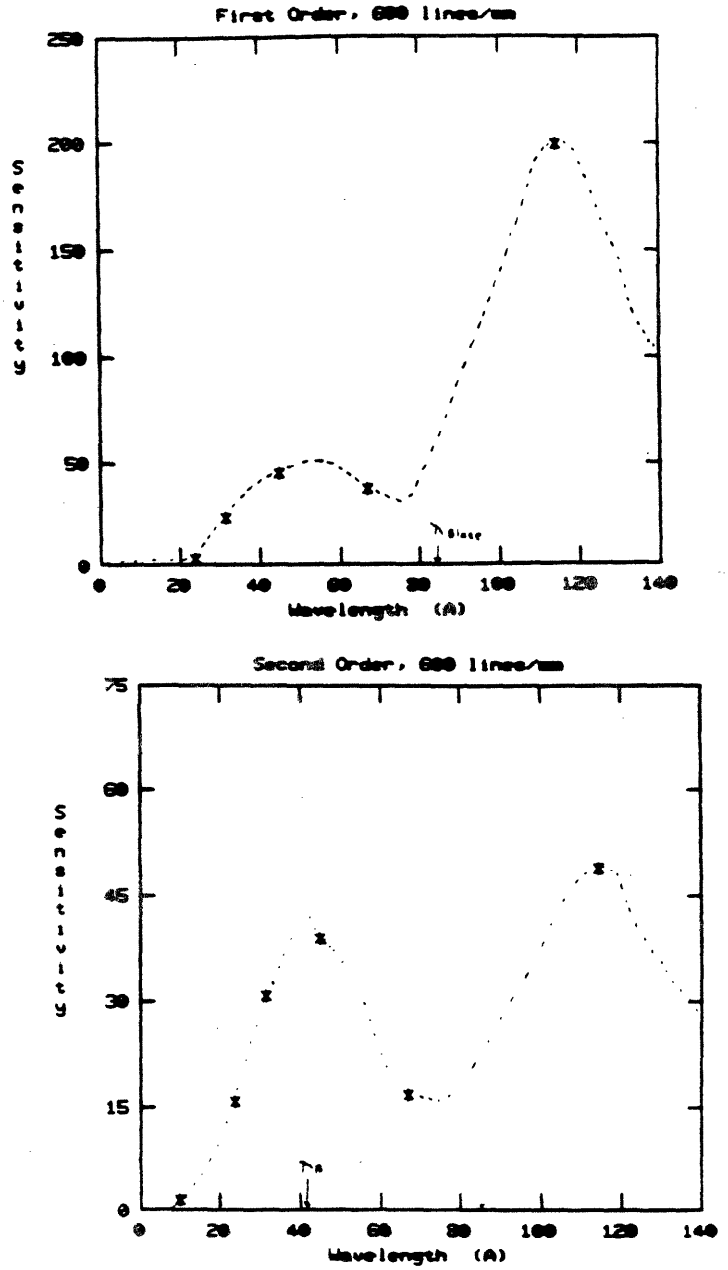

Figure 3.4(a,b) System sensitivity with the 600 line/mm grating, first and second orders. Calibration points (*) are connected with a curve retaining the features of the CsI photocathode, as well as the effects of the grating blaze ($\lambda_B = 83.2°$ in first order). Units are "raw counts" per 1000 accepted photons (see text).

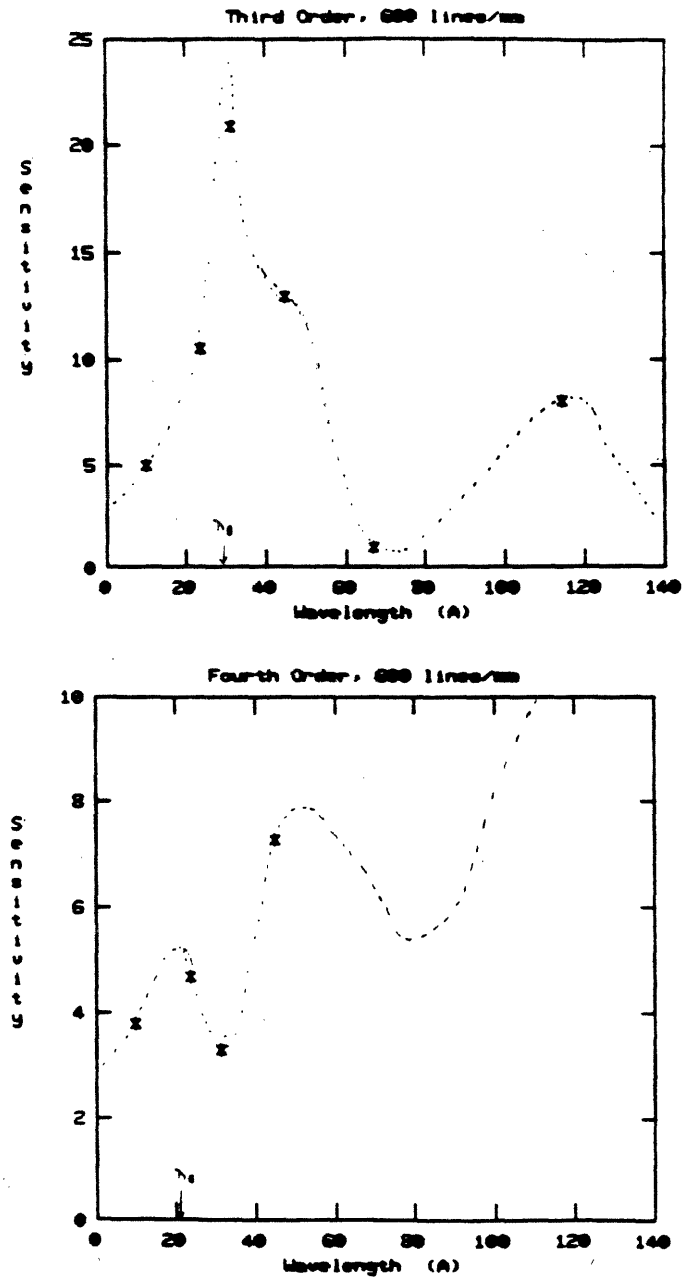

Figure 3.4(c,d) System sensitivity with the 600 line/mm grating, third and fourth orders. Calibration points (*) are connected with a curve retaining the features of the CsI photocathode, as well as the effects of the grating blaze ($\lambda_B = 83.2°$ in first order). Units are "raw counts" per 1000 accepted photons (see text).

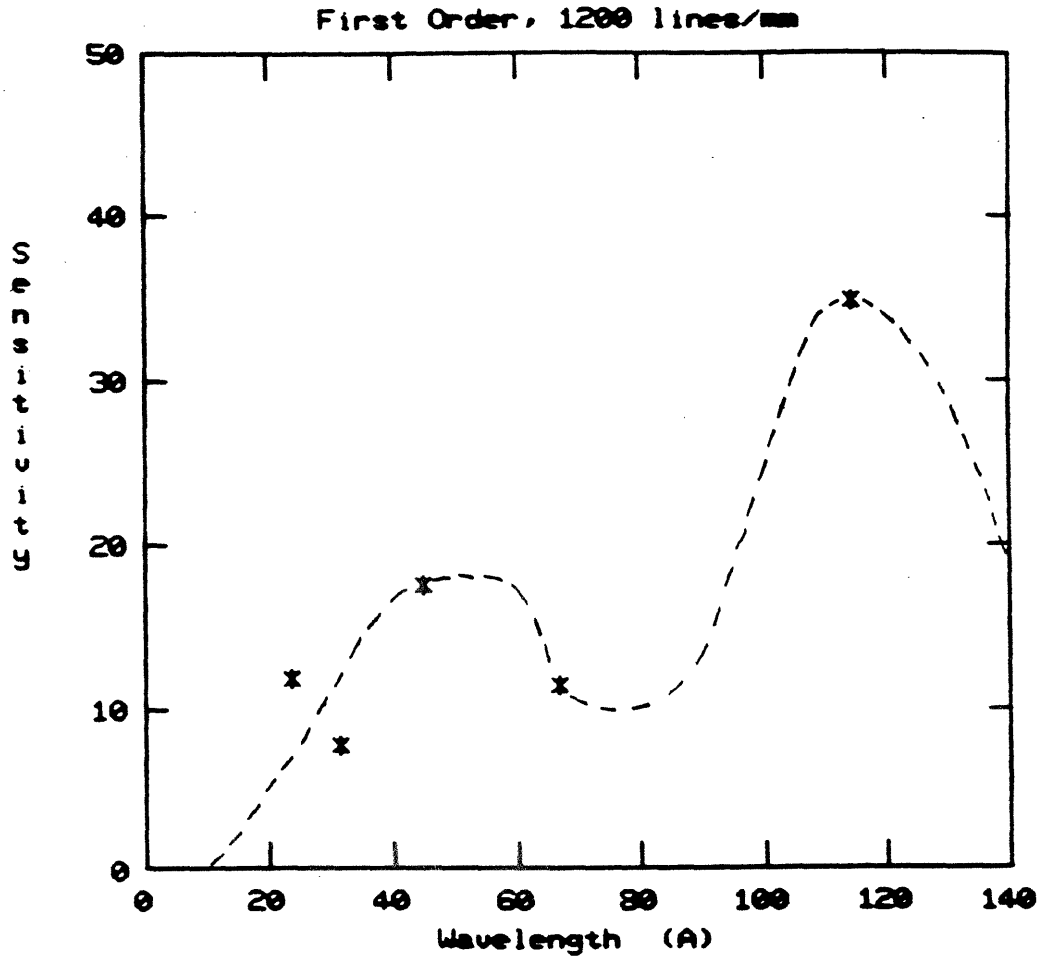

Figure 3.5 System sensitivity with the 1200 line/mm grating, first order. Calibration points (*) are connected with a curve retaining the features of the CsI photocathode. This grating is holographic and has no blaze angle. Units are "raw counts" per 1000 accepted photons (see text).

region $150 \lesssim \lambda \lesssim 450$ Å. This reflects the estimated error due to alignment, shot-to-shot variations, and toroidal effects, as well as the uncertainty in the calibration of the 0.2 meter instrument and extrapolation between measured points. As already stated, the values below 150 Å are estimated to be correct to within 40%. These estimates of uncertainty are probably a bit conservative, as comparisons of the relative brightnesses of different impurity emission lines from the same element generally agree with predicted ratios to within a factor of 1.5, and deduced absolute impurity concentrations yield values of $Z_{\rm eff}$ which agree with the independently obtained visible bremsstrahlung value to within 25%.

The original sensitivity curve was corrected to reflect the measured points from the cross-calibration. To date, only the 600 line/mm grating has been cross-calibrated in this manner. The resulting full system sensitivity curve is shown in Figure 3.6. All of the calibrated brightness measurements presented in this thesis were taken with this grating. The 1200 line/mm grating and the 0.2 meter monochromator have never been simultaneously installed on the tokamak.

3.2 Detector Gain Characteristics

Several tests were conducted in order to study the variation of $R(V_i)$, the gain of the detector system, with detector voltages, signal intensity, and signal position on the MCP. These variations should be independent of wavelength, since they only represent the processes occurring subsequent to the creation of a photoelectron at the MCP surface.

MCP Bias Voltage: The bias voltage across the MCP was varied from 700 to 1000 V, keeping a constant 5 kV potential between the MCP output side and the phosphor screen. With the platinum lamp illuminating the entrance slit, the amplitude of the central order image was recorded. The detector sensitivity to this

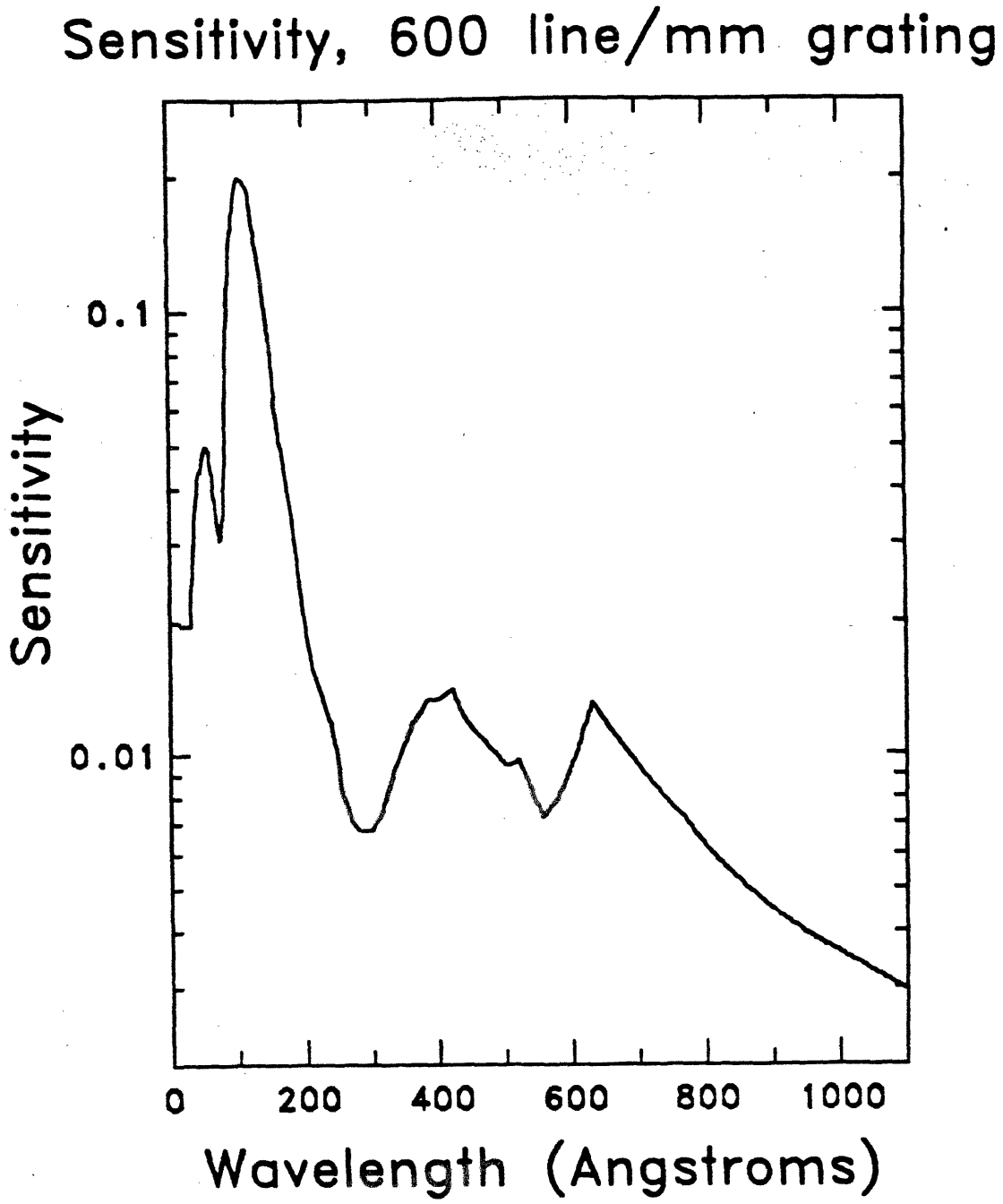

Figure 3.6 Full system sensitivity curve with 600 line/mm grating in place. Units are "raw counts" per accepted photon (see text). Uncertainties are discussed in the text.

light was quite adequate for these studies, even though the minimum wavelength passed by the lamp's MgF_2 window is about 1200 Å. The video output of the Reticon readout circuit was used for this study. At the time of this test, the repeller plate was not physically present on the detector system. The results of this test are shown in Figure 3.7. The point at 900 V is normalized to test data supplied by the detector vendor, indicating an electron gain of 10^4 for the MCP alone at this bias voltage. The exponential increase in gain with respect to bias voltage is characteristic of non-saturated MCP's, and the form of the curve presented agrees very well with test data provided by the vendor for the particular MCP supplied.

MCP-Phosphor Voltage Under the same conditions, the response of the detector system to variations in the accelerating voltage between the output side of the MCP and the phosphor screen was examined. In this test, the MCP bias voltage was kept at a constant 900 V. The results are shown in Figure 3.8, indicating a fairly linear dependence above a turn-on threshold of $\sim$ 1650 V. This threshold was unexpected. Such effects are expected if the phosphor screen has a thin aluminum reflective coating on the surface, as they often do. The detector system specifications did not call for such a coating, however, and the vendor stated that none was applied. In any case, the threshold posed no problems in actual use. For virtually all calibration and tokamak data taken to date, the detector has been run with 1000 V MCP bias voltage and 5000 V between the MCP and phosphor screen. Had it been necessary to lower the gain to avoid saturation, these curves would have been used to calculate the reduced sensitivity. In practice, however, adjustment of integration periods or pre-slit widths was normally used to avoid saturation.

Repeller Plate Using the same set-up as before, but with the repeller plate and cylindrical shield back in place, the effect of the voltage between the input side of the MCP and the repeller plate (18 mm away) was studied. Three

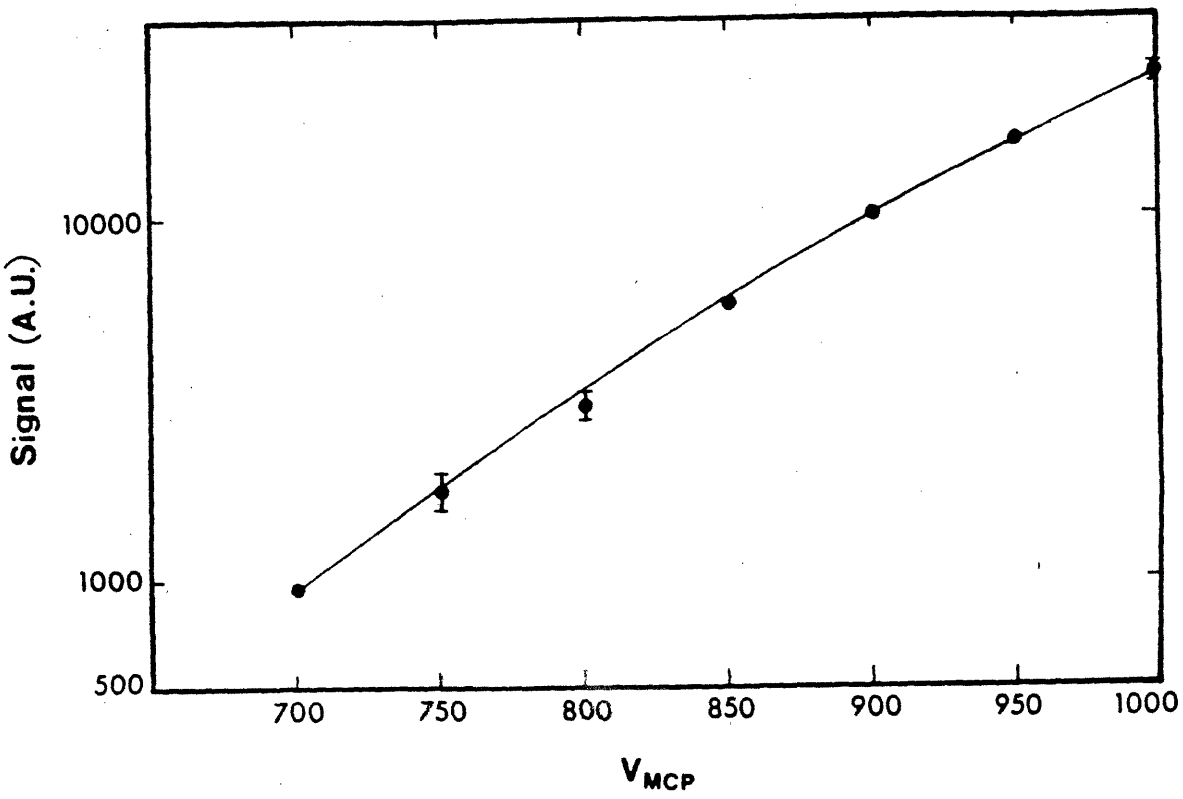

Figure 3.7 Variation of detector gain with bias voltage applied across the MCP. The point at 900 V is normalized to test data supplied by the detector vendor, indicating an electron gain of 10^4 for the MCP alone at this bias voltage.

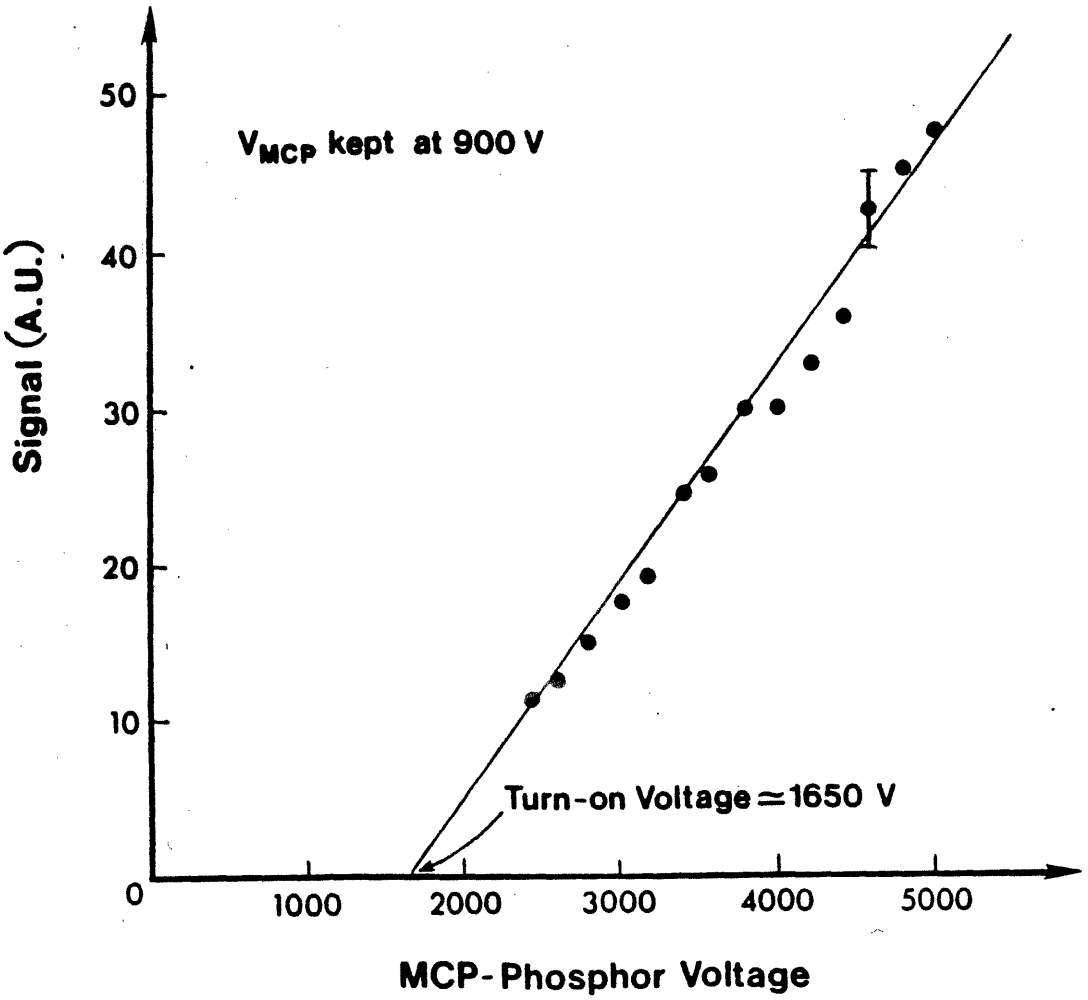

Figure 3.8 Variation of detector gain (arbitrary units) with accelerating potential between the MCP output side and the phosphor screen. MCP bias voltage was kept constant at 900 V.

main observations resulted. First, the repelling voltage worked in that the gain of the detector rapidly increased by a factor of $3-5$ as the repelling voltage was increased above some threshold. For a fixed voltage on the MCP input side, the gain was fairly flat as the threshold voltage was approached. The gain increased quickly as the repelling voltage was increased by about 250 V beyond the threshold, then leveled off again as the repelling field was further increased. The second feature noted was that the threshold voltage was not constant across the detector. The enhanced gain appears first at the center of the detector, and it spreads to the edges as the voltage is further increased. Approximately $650-1200$ V is required to see the effect at the center of the detector, depending somewhat on the absolute voltage on the MCP input side. To enhance the gain at the edges of the detector, roughly 3000 V is required between the two surfaces. When the spectral image falls partly in an enhanced region, and partly outside, image distortion obviously occurs. The third observation was that the "glow instability" described in Chapter 2 generally became problematical only when the repelling voltage was applied, becoming worse as the voltage was increased. With 3 kV between the two surfaces, the presence of this phenomenon was almost certain to appear within a matter of minutes.

A later test, with the new digital readout system and 44.7 Å light from the graphite anode, clearly shows the spreading of the enhancement as the magnitude of the repeller voltage is increased. In Figure 3.9, the total number of raw counts in the carbon signal is plotted vs. the position of the image center for four different settings of this reflection voltage. For the standard conditions ($V_R = 0$, where V_R is the voltage between the repeller and the MCP input side), the response is fairly flat across the detector face. The falloff at the ends of the detector is partially because a broad image ($\sim$ 100 pixels FWHM) was used, and some of the image is lost as the centroid nears the edge of the useful pixel range. Other than that,

the sensitivity is uniform to within 5% across the MCP. This was also verified at the other wavelengths used from the soft X-ray source. Although the image grew broader with lower amplitude as the image approached the long wavelength end of the MCP, the total counts under the curve remained fairly constant. As the reflection voltage was increased, however, the enhancement factor came into play with its spatially non-uniform gain. At 1 kV, only the center of the MCP is affected. At 3 kV, the effect has spread to most of the detector. It was also noted that the use of the repelling voltage generally degraded the resolution of the image. This is not surprising, as electrons whose trajectories away from the MCP have been turned around will generally fall some small distance from the site of origin.

In hindsight, it is easy to see why the repelling voltage has a spatially dependent threshold. The presence of a grounded metal surface (the cylindrical shield) surrounding the area between the flat disk-like electrodes (repeller plate and MCP input side) leads to strong fringing effects in the electrostatic field between the electrodes. The axial electric field above the MCP input side is spatially dependent, being strongest at the center of the detector. The threshold voltage corresponds to the local electric field above the MCP surface being strong enough to reverse the motion of photoelectrons emitted away from the plate, returning them to the plate near the spot where they were emitted. With the input MCP side at -6 kV, a bias of -9 kV on the repeller is sufficient to yield this condition across the detector. With -6 kV on the repeller, the field lines at the MCP surface actually go the wrong way, pulling stray electrons toward the grounded shield. This field is zero by symmetry at the detector center and increases toward the edges. However, this situation yielded the most stable, glow-free, uniform sensitivity across the detector. For that reason, it was chosen as the standard operating condition. Had there been no problems with the instability, a non-conducting shield could have been tried.

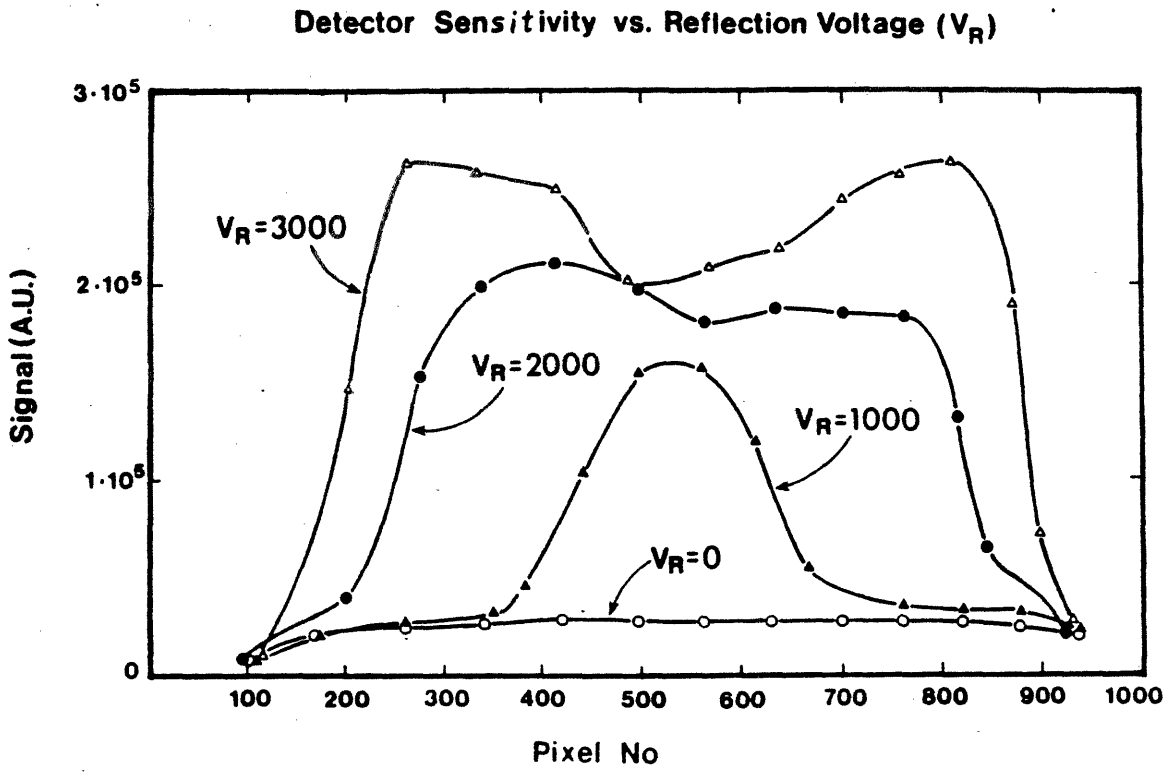

Figure 3.9 Detector gain as a function of repelling potential between the MCP input side and the repeller plate (called Reflection Voltage V_R in the figure). Spatial variations across the MCP are clearly dependent on repelling voltage.

With the instability, however, it was decided that such a change was not worth the added delays and risks.

The linearity of the detector with respect to image brightness was examined by comparing the line shapes obtained with a low brightness platinum lamp setting and 80 ms integration time to those resulting from a bright lamp setting and 5 ms integration time. The latter set-up was close to saturating the Reticon signal, and corresponded to a signal brightness roughly 60 times brighter than the former set-up. No obvious saturation effects were seen on the detector response, and an upper level of approximately 10% was established as the maximum deviation from linearity under these conditions.

A similar check was performed subsequent to the installation of the new digital readout system. While no substantial saturation effects were seen with respect to source intensity, a small effect was seen based on the integration period of the Reticon. By comparing the signal ratio of a spectrum taken with 4 ms integration time on the photodiode array to a spectrum taken with 2 ms integration time, one would expect a flat ratio of 2.0. In fact, this value was seen over most of the spectrum, but decreased to approximately 1.85 where the signal was brightest. This non-linearity could only occur in either the Reticon or the readout electronics, as the source and MCP conditions were kept constant. Charge leakage in the internal capacitors of the Reticon could explain this effect. However, the effect was small enough to be of limited concern, given the rather large uncertainties present in the sensitivity calibration already discussed.

3.3 Spectral Resolution

The question of spectral resolution may be divided into two related issues: the ability to resolve two closely spaced lines, and the accuracy with which the absolute wavelength of a given line can be specified. The former is addressed first.

3.3.1 Instrumental Response Function

For pure Gaussian line shapes, the instrumental response to a single line (monochromatic source) and the ability to resolve adjacent lines can both be simply expressed in terms of the FWHM of the Gaussian. The response of the detector system used here does exhibit a sharp central peak with a FWHM as small as 6 pixels, but there is also a broad shoulder, or wing, decaying exponentially away from the peak with a typical decay length of 35 pixels. This instrumental response is shown in Figure 3.10, which is actually a bright argon resonance line from a tokamak discharge. The FWHM of 6 pixels represents approximately the best resolution obtained with this detector system, although it must be noted that this line was recorded at the short wavelength end of the detector where the dispersion (Å/pixel) is largest. After a little trial and error, it was found that the line shape could be reasonably well modeled by the function

$$f(x) = A\left[\frac{6}{7}f_L(x) + \frac{1}{7}f_e(|x|)\right] \qquad 3.2$$

where A is the peak of the line shape, $x = N - N_o$ is the distance in pixels from the line center, and f_L and f_e represent, respectively, a narrow Lorentzian peak and a broad, exponentially decaying wing:

$$f_L(x) = \frac{\Gamma_L^2}{\Gamma_L^2 + x^2} \qquad 3.3$$

$$f_e(|x|) = e^{-\alpha|x|}, \qquad \alpha = 0.693/\Gamma_e \qquad 3.4$$

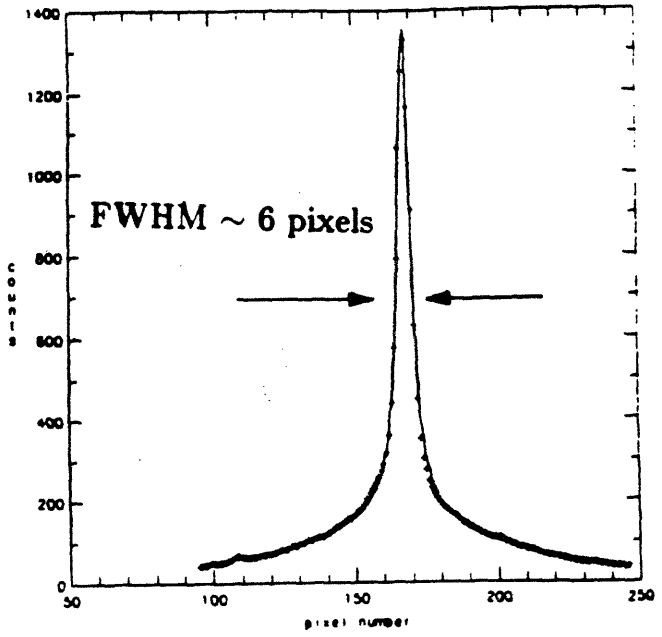

Linear Scale

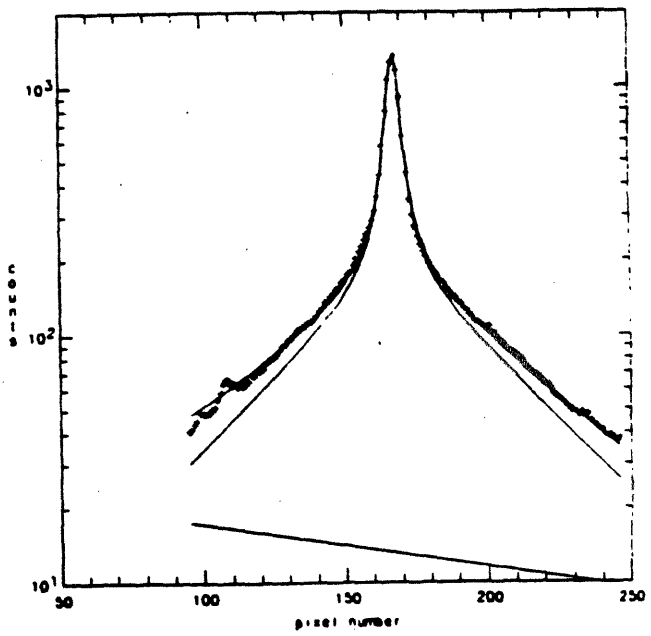

Log Scale

Figure 3.10 Instrumental response function, characterized by a peaked Lorentzian plus a broad, exponentially decaying side wing. A bright argon resonance line is shown, along with the numerically calculated fit based on this function. Linear and semi-log plots are shown. Evident in the lower plot are three solid curves: total fitted curve, fit to the single line, and fit to the background.

The exponential term generally contains about 67% of the total counts in a given line, although the Lorentzian term represents the more prominent peak. It is felt that the Lorentzian term is representative of the normal spectroscopic instrumental response function, while the exponential wings are due to some defocusing effects internal to the detector. Scattering of photons within the fiber optic components is one likely source of this degradation of focus, since there is no opaque cladding between individual fibers and ambient light is known to leak through. Photons may also be scattered in the phosphor screen before entering the fibers. Another possible mechanism is the spreading of the electron charge packet in the 1.0 mm region between the output side of the MCP and the phosphor screen. Simple estimates based on typical MCP parameters indicate that this effect is probably not due to charge repulsion, but could be caused by the initial distribution of transverse momentum as the electrons exit the MCP. A smaller gap could be expected to improve resolution if this were in fact the case.

The Lorentzian FWHM ($2\Gamma_L$) is typically $8-12$ pixels, while the exponential FWHM ($2\Gamma_e$) is typically $50-80$ pixels. Both values vary across the detector face due to the non-constant reduction factor of the fiber optic taper, and there is also some dependence of Γ_L only on detector position (i.e., wavelength). A numerical line fitting code varies the amplitude (A), center position (N_o), and two characteristic widths (Γ_L and Γ_e) for one line or many adjacent lines to fit this formula to the actual spectrum. The line shown in Figure 3.10 includes the fitted line shape as well as the actual data points. A linear background is also included in the fit. The exponential nature of the broad wings is evident from the semi-log version of the figure.

In a crowded tokamak plasma spectrum, this fitting procedure is very useful for estimating the total number of raw counts in a given line, especially when the

wings of crowded lines are indistinguishable from the continuum background. This continuum is believed to be chiefly composed of low-intensity, unresolved spectral lines and stray or scattered light. By knowing the instrumental response function and the linear characteristics of the detector system, a good estimate of the counts in a line can be obtained even if only the tip of the line is visible. An example is shown in Figure 3.11. Here, a tokamak spectrum is fitted to a sum of a background level plus several individual lines, which are shown beneath the fitted curve. This spectrum, obtained with the 1200 line/mm high resolution grating, also illustrates a Rayleigh criterion measure of the instrumental resolution: the two lines which are nominally resolved at 218.415 Å and 218.649 Å are separated by .234 Å, yielding a resolving power $\lambda/\Delta\lambda$ of roughly 1000.

The dispersion, given in Å per pixel, is a function of grating and position on the Rowland circle, being smallest at the shortest wavelengths. Therefore the absolute resolution (in Å FWHM) is also dependent on the same parameters. The best resolution seen is obtained with the smallest pre-slit and entrance slit practical. Using the 600 line/mm grating and an entrance slit width of about 30 μm, a typical resolution of $\sim$ 0.3 Å FWHM was seen for $\lambda \lesssim 150$ Å. With the 1200 line/mm grating, a resolution of 0.2 Å is achievable.

3.3.2 Absolute Wavelength Accuracy

Due to uncertainties in the absolute position of the detector on the Rowland circle, the alignment of the detector and gratings, and the distortion effects in the fiber optic reducing taper, it is very difficult to assign an absolute wavelength to a given pixel with an accuracy of more that about 0.2%. Even with the measured mapping function of the taper, it is difficult to adjust the assumed offsets in the detector carriage position, etc., in a way that simultaneously yields the correct

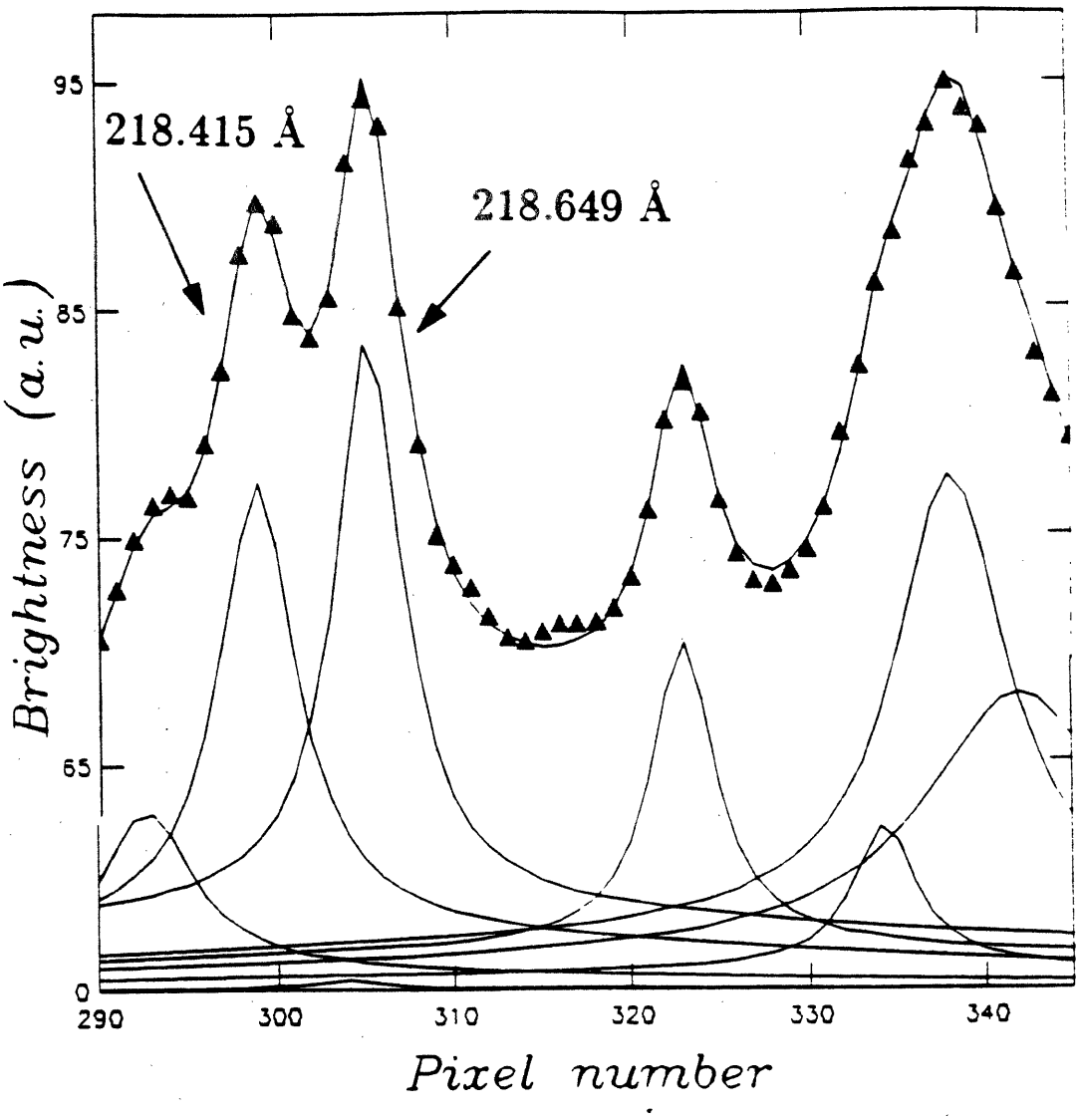

Figure 3.11 Crowded tokamak spectrum (triangles) taken with 1200 line/mm grating, and the curve fitted to it (solid line) by modeling the individual lines contained plus a background. The individual lines are shown below. Separation of the two lines near 218 Å yields a resolving power of roughly 1000.

calculated wavelengths for all identified lines across a single viewed spectrum with an accuracy better 0.1%. Practically speaking, for the purpose of obtaining the absolute wavelength of a unknown line, the experimental uncertainty in the assigned wavelength is directly related to the proximity of the unknown line to a known line whose wavelength is well established. This is simply because the relative spectral separation can be measured much more accurately than the absolute wavelength. Ideally, the accuracy is limited only by the dispersion and the pixel width, which would give an accuracy of order 0.03%. Note that the accuracy with which the centroid of a given line can be located is roughly 0.3 pixels, even though the line may have a FWHM of $6 - 10$ pixels.

3.4 Temporal Resolution

The temporal resolution of the detector system is governed by two characteristic times: the shortest integration time allowed by the Reticon and the readout electronics, and the persistence time of the phosphor screen. The electronics can read out all the usable pixels every 2 ms. By digitizing and storing only the signals from a fraction of the pixels (156 or less), scans can be obtained every 0.5 ms. Although the P-4 phosphor used in the image intensifier was characterized by the vendor as having a sub-millisecond persistence time, tests indicated an afterglow at the few percent level for $\sim 20 - 40$ ms.

Two tests were performed, using the 0.5 ms integration period of the electronics. First, with the detector on and the platinum lamp illuminating the entrance slit, a pneumatic gate valve between the lamp and the spectrograph was shut. Second, under the same initial conditions, the DC power to the hollow cathode discharge lamp was interrupted. In each case, a rapid loss of signal was followed by a gradually decaying signal which did not subside to the noise level for several tens of

milliseconds. The data from the unplugging test, which had the faster initial decay, are shown in Figure 3.12. The initial fast falloff is attributed to the extinguishing time of the discharge. The longer afterglow, however, is believed to be due to the phosphor. Although undesirable, this slight persistence level was judged insufficient to warrant special software measures to deconvolve the tokamak data, which generally varied on a time scale of tens of milliseconds anyway.

As example of the instrumental response to a rapidly changing plasma impurity emission line is shown in Figure 3.13. In this plasma discharge, a trace amount of molybdenum was injected by a method known as the laser blow-off technique [59,60], in which a ruby laser is focused onto a glass slide coated on the opposite side with a $\sim$ 1 μm film of the material to be injected. The coated side faces the plasma, and the laser pulse causes a small cloud of neutral ablated material to propagate towards the plasma edge. In the example shown, the resonance line of Mo-XXXII at 127.81 Å is followed with 0.5 ms integration times during and just after the injection at $\sim$ 293 ms. The large amplitude oscillations following the initial rise in brightness are due to a plasma instability known as the sawtooth mode, which results in large swings in the electron temperature. Both the soft X-ray emission and the brightness of the Mo-XXXII line are very dependent on T_e in this regime. The point of the figure is that the oscillations shown agree quite well, in both phase and relative amplitude, with soft X-ray photodiode measurements which have a much faster temporal response, demonstrating the 0.5 ms capability of the spectrograph.

3.5 Utility as a Tokamak Diagnostic

Since its installation on Alcator C, the VUV time-resolving spectrograph has served reliably as one of the principal impurity diagnostics on the tokamak. It has

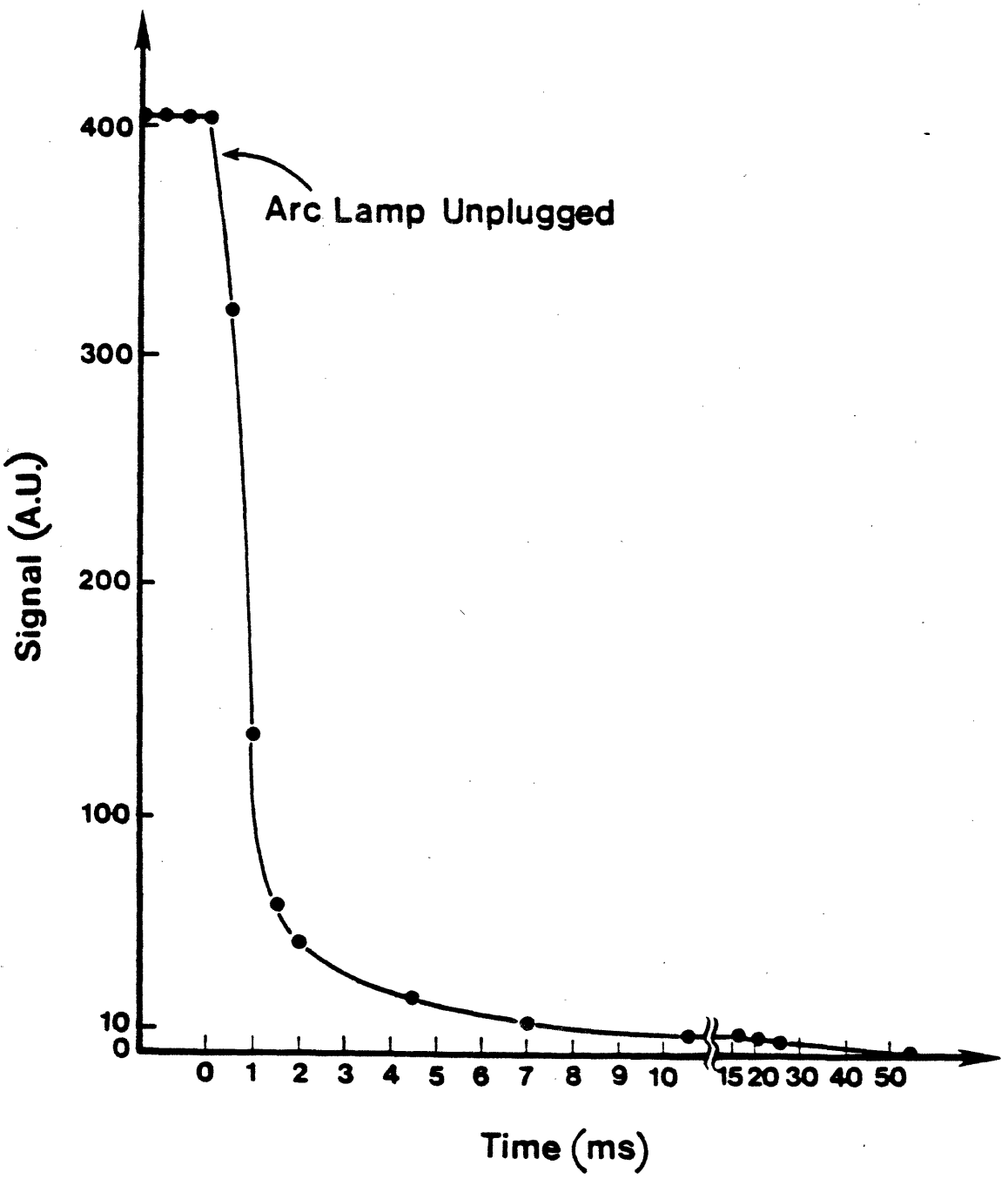

Figure 3.12 Temporal response of the MCP detector system to a rapidly extinguished light source (unplugged platinum hollow cathode discharge). Signal is the total raw counts in the central order image. The initial fast falloff is attributed to the extinguishing time of the discharge. The longer afterglow, however, is believed to be due to the P-4 phosphor.

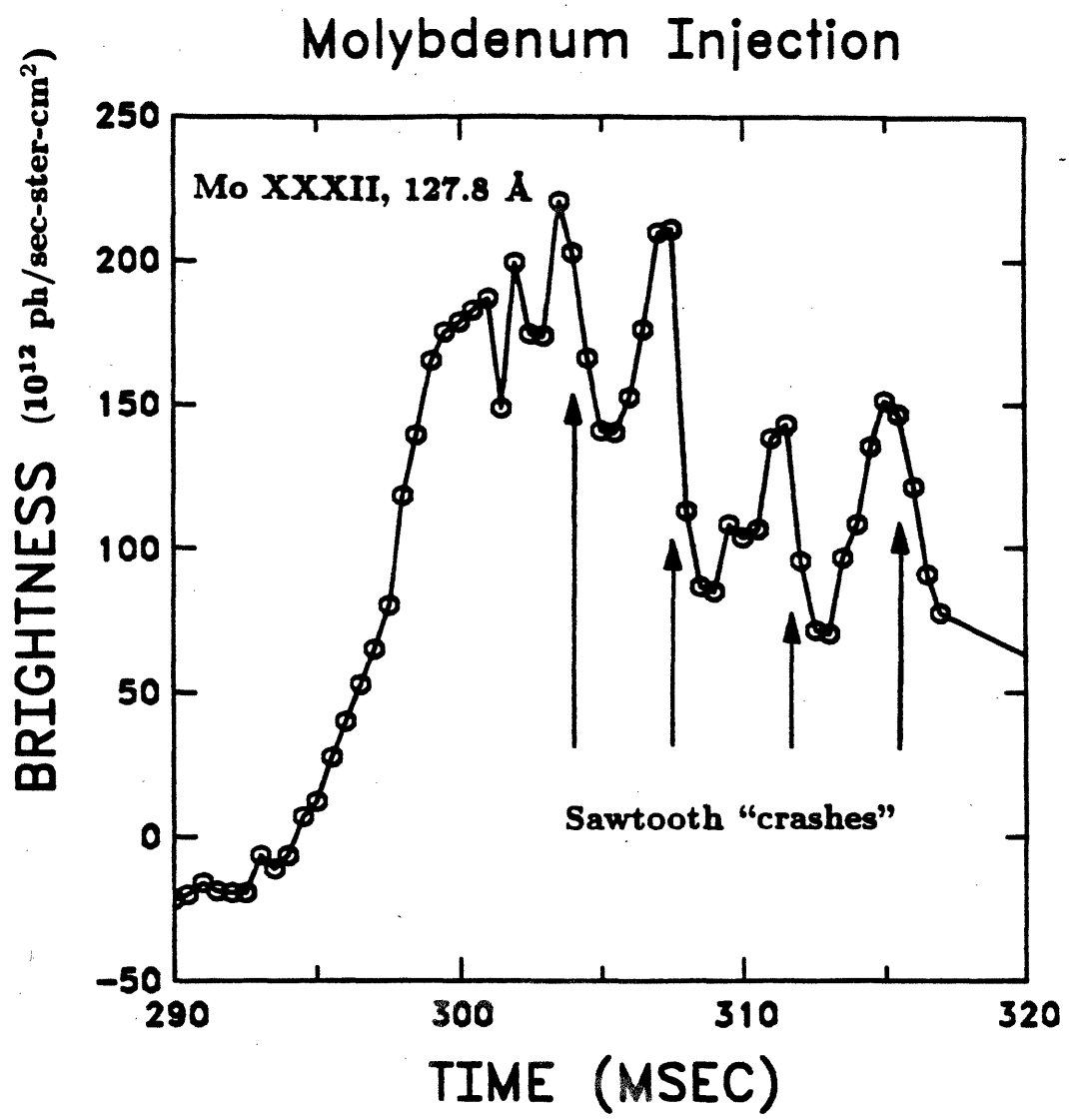

Figure 3.13 Brightness of Mo-XXXII resonance line at 127.81 Å following artificial injection of molybdenum into plasma discharge. The sawtooth oscillations following the initial rise agree well with separate soft X-ray photodiode measurements which have a much faster temporal response, demonstrating the 0.5 ms capability of the spectrograph.

been used for a variety of purposes in addition to its primary mission of monitoring the intrinsic impurity levels in the plasma. Several such applications are briefly discussed in this section, with some illustrative examples.

3.5.1 Impurity VUV Survey Spectrograph

The basic purpose of the instrument for routine tokamak discharges is to measure the brightness of various emission lines from the different impurity species present in the plasma. As already discussed, the detector system is designed to allow the simultaneous monitoring of line radiation from numerous impurity species. When used with the 600 line/mm grating, the spectrograph has a spectral range of 20–1160 Å, with simultaneous coverage of 20 Å when centered at 30 Å and 100 Å when centered at 1110 Å. Spectral resolution is typically 0.3 Å FWHM at the lower wavelengths. With the 1200 line/mm grating in place, the useful range is 15–565 Å, with correspondingly smaller windows of simultaneous coverage and resolution. In either configuration, the entire available spectrum can be surveyed in only 15 or so plasma shots.

Hydrogen or deuterium is the usual working gas in Alcator plasmas, although helium is used on occasion. The major intrinsic impurities present in the Alcator C plasmas are carbon, oxygen, molybdenum, iron, chromium, nickel, and silicon. Except for oxygen, all these elements were at some time initial constituents of the structural elements (stainless steel wall, various limiters) exposed to the plasma. Chlorine (from cleaning solvents) and nitrogen are often evident for several days following a vacuum break, and argon is often puffed in for diagnostic reasons. Krypton, neon, and sulfur hexaflouride have also been deliberately added to the plasma at times. Various additional elements have been injected by the laser ablation method, including aluminum, titanium, vanadium, and tungsten, plus several

elements already mentioned. Transition line radiation from each of the above elements has been identified in spectra taken with the VUV spectrograph. A typical plasma spectrum is shown for the region near 120 Å in figure 3.14, with several prominent impurity lines identified.

Because the instrument sensitivity is absolutely calibrated, the measured line brightnesses can be used to deduce impurity concentration levels, if desired. Such knowledge is important for calculating several plasma parameters, such as $Z_{\rm eff}$ and the radiated power due to impurities. Through modeling of impurity transport, the source rate for impurity ions at the plasma edge can also be deduced. This type of analysis forms the basis for much of the work in Chapter 5.

The ability to monitor many impurities at once is very useful for troubleshooting unruly plasma discharges, which often result from an unusually high concentration of one or more impurity species. In particular, natural brief injections of wall or limiter materials occur without warning in some plasma shots, often leading to disruption and loss of plasma confinement. By recording the behavior of a whole region of the VUV spectrum, rather than a single wavelength, it is usually possible to figure out which element(s) were involved in the injection. This in turn gives the tokamak operator an idea of what corrective measures, if any, are called for on the next discharge.

3.5.2 Transport Studies

Impurity transport may be studied by using the laser blow-off technique to examine the time dependent brightnesses of lines from various ionization stages of the injected element. Generally, a trace amount of a non-intrinsic, non-recycling element is injected. The amount injected is kept sufficiently small so as not to perturb the plasma discharge. The amount of time required for the injected ions

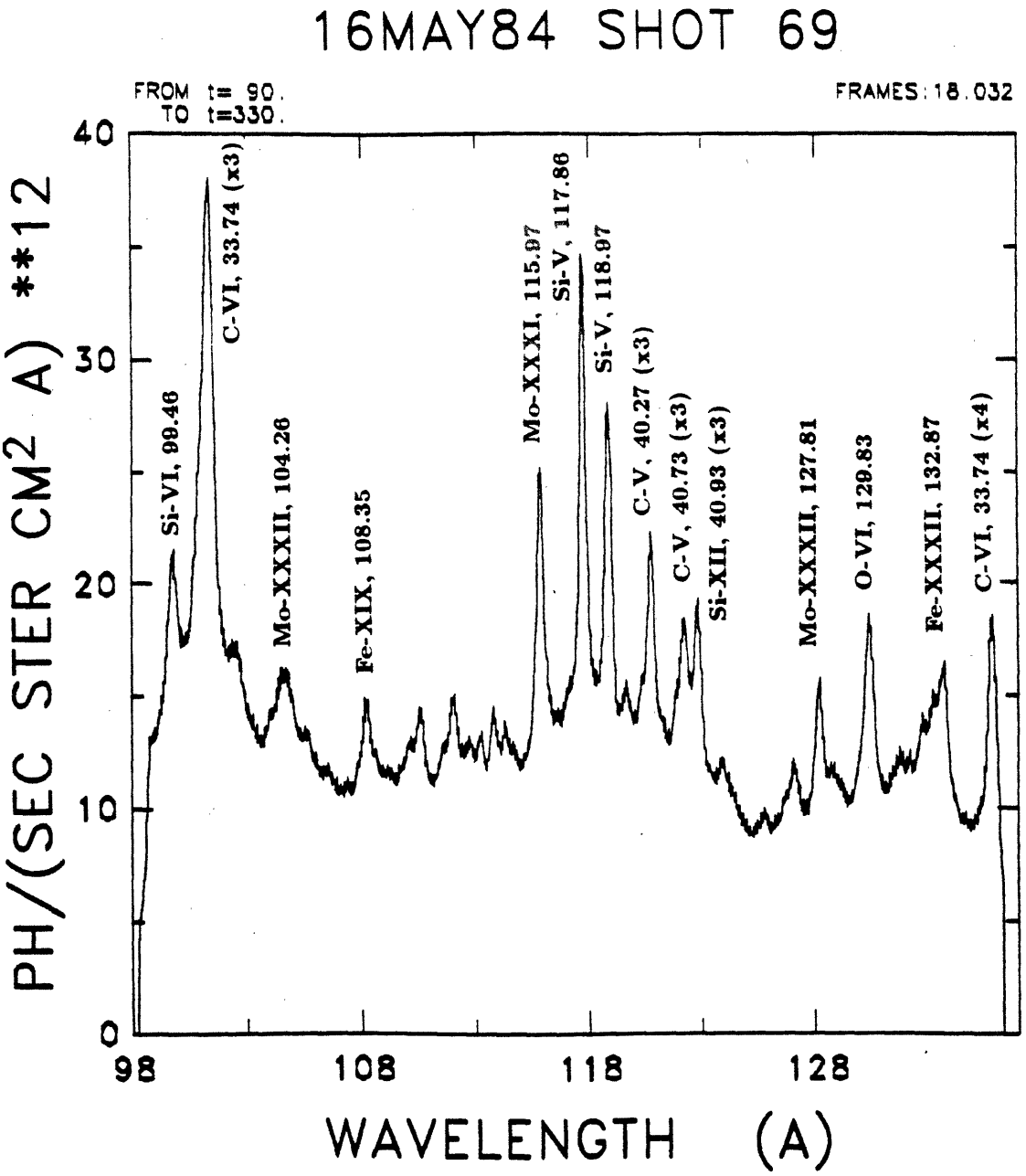

Figure 3.14 Typical Alcator C VUV spectrum of intrinsic impurity emission lines in the region near 120 Å.

to diffuse into the central plasma and back out again is dependent on the impurity diffusion coefficient and the impurity convection velocity, both of which may vary spatially in the plasma. Impurity transport studies conducted on Alcator C prior to the installation of this spectrograph [60] have been continued, especially with regard to the effects of pellet fueling of the plasma [61]. In simplest form, the brightness of a centrally located ionization state of the injected element is monitored, and an exponential decay time is observed in the brightness sometime after the line has peaked. This decay time is essentially an impurity particle confinement time, which is a function of the transport parameters. An example is shown in Figure 3.15, in which vanadium was injected and an exponentially decaying curve has been fitted to the brightness vs. time graph for V-XXI ($2s - 2p$, 239 Å).

3.5.3 Transient Phenomena

On a typical tokamak shot, the VUV spectrograph may record well over 50,000 words of 12-bit data. In order to provide a rapid overview of how the observed region of the spectrum behaved, a three-dimensional surface plotting routine was used. In this graphic scheme, the individual spectra (signal vs. wavelength) are slightly smoothed and plotted against a third axis representing time. The result is a surface plot in which height represents signal, and the two horizontal axes are wavelength and time.

A good example is shown in Figure 3.16, which shows data from a shot in which tiny pellets of frozen hydrogen were injected into the plasma for fueling. On this shot, three separate pellets were injected. The first two were absorbed by the plasma, leading to a general increase in impurity emission due to the elevated electron density. The third pellet, however, was not successfully absorbed. Rather, it caused the plasma to disrupt, as manifested by the sudden jump in light across

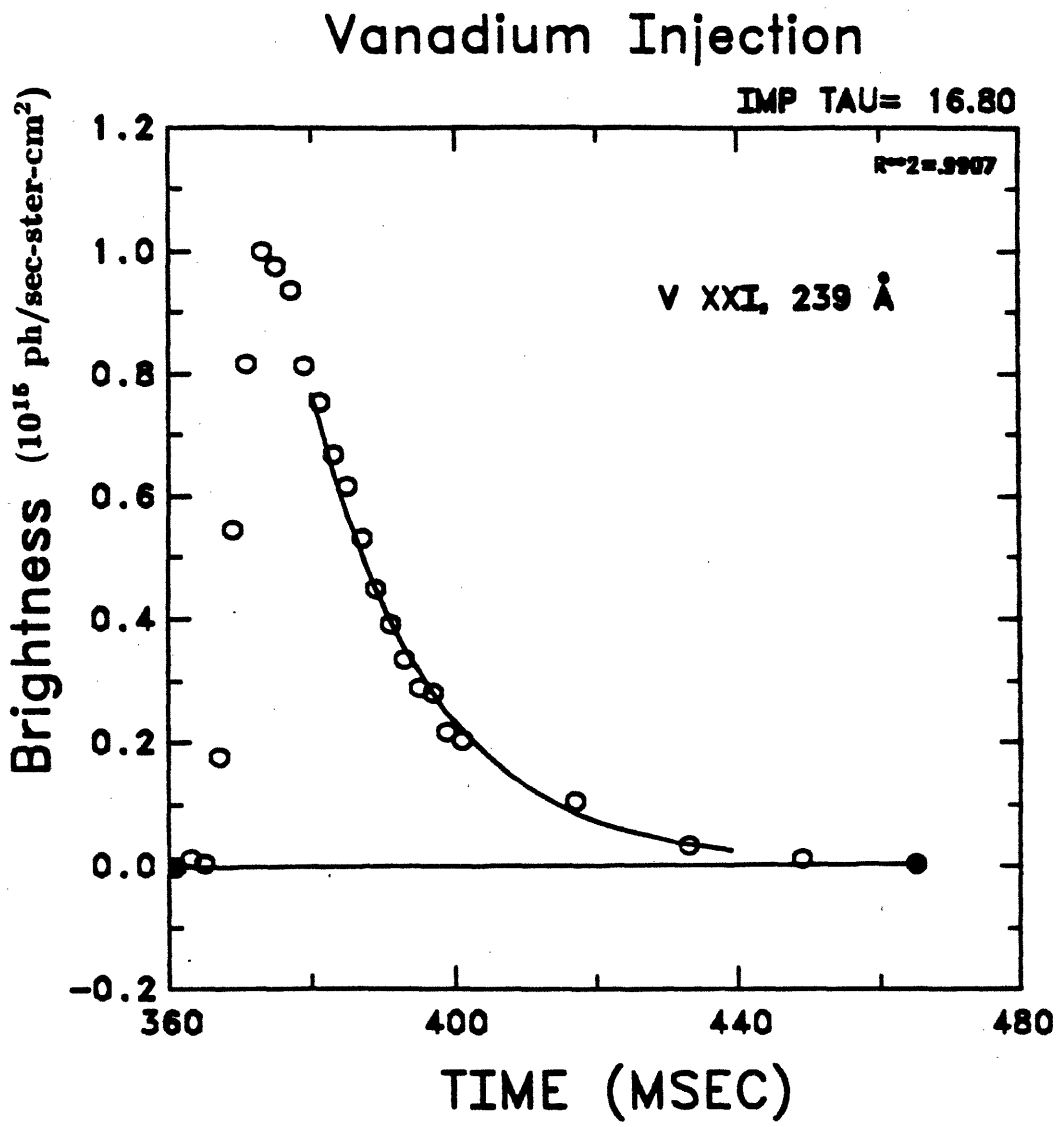

Figure 3.15 Brightness of V-XXI line ($2s-2p$, 239 Å) following artificial injection of vanadium by the laser ablation method. By fitting an exponentially decaying curve to the falling brightness after the line has peaked, an impurity particle confinement time is deduced, useful for impurity transport studies.

the detector. In fact, the detector is saturated at the disruption, yielding the high, flat spectrum which resembles a wall in the surface plot.

Short of disruptions, the most striking changes in the VUV spectrum occurred during the artificial injection of non-intrinsic impurities. Shown in Figure 3.17 is the surface plot representation of an injection of silicon for transport studies. At the time, there was very little background intrinsic silicon in the tokamak. The two resonance lines of the Si-XII doublet ($2s - 2p$, 499.40 and 520.67 Å) are clearly visible at the injection.

Almost as dramatic was the increase in impurity emission during a series of ICRF heating experiments, typified by Figure 3.18. Inspection revealed that the large rise in the VUV emission was chiefly due to an increased influx of metal impurities. This phenomenon and an attempt to understand its origins form the basis for the remaining chapters of this thesis.

3.5.4 Differential Spectra

The instrument is very efficient for assembling composite spectra from a given artificially injected impurity. Following such an injection, the viewed spectrum contains both lines from the injected impurity and lines from the intrinsic impurities already present in the plasma. Assuming the injection does not significantly perturb the plasma, the intrinsic spectrum is fairly constant on the time scale of the injection ($10-20$ ms). Therefore, by subtracting the spectrum recorded prior to the injection from the spectrum recorded after the injected impurity has penetrated the plasma interior, a differential spectrum is obtained which can be attributed solely to emission from the injected element. By repeating the process as the detector is scanned along the Rowland circle (on a shot-to-shot basis), a complete spectrum

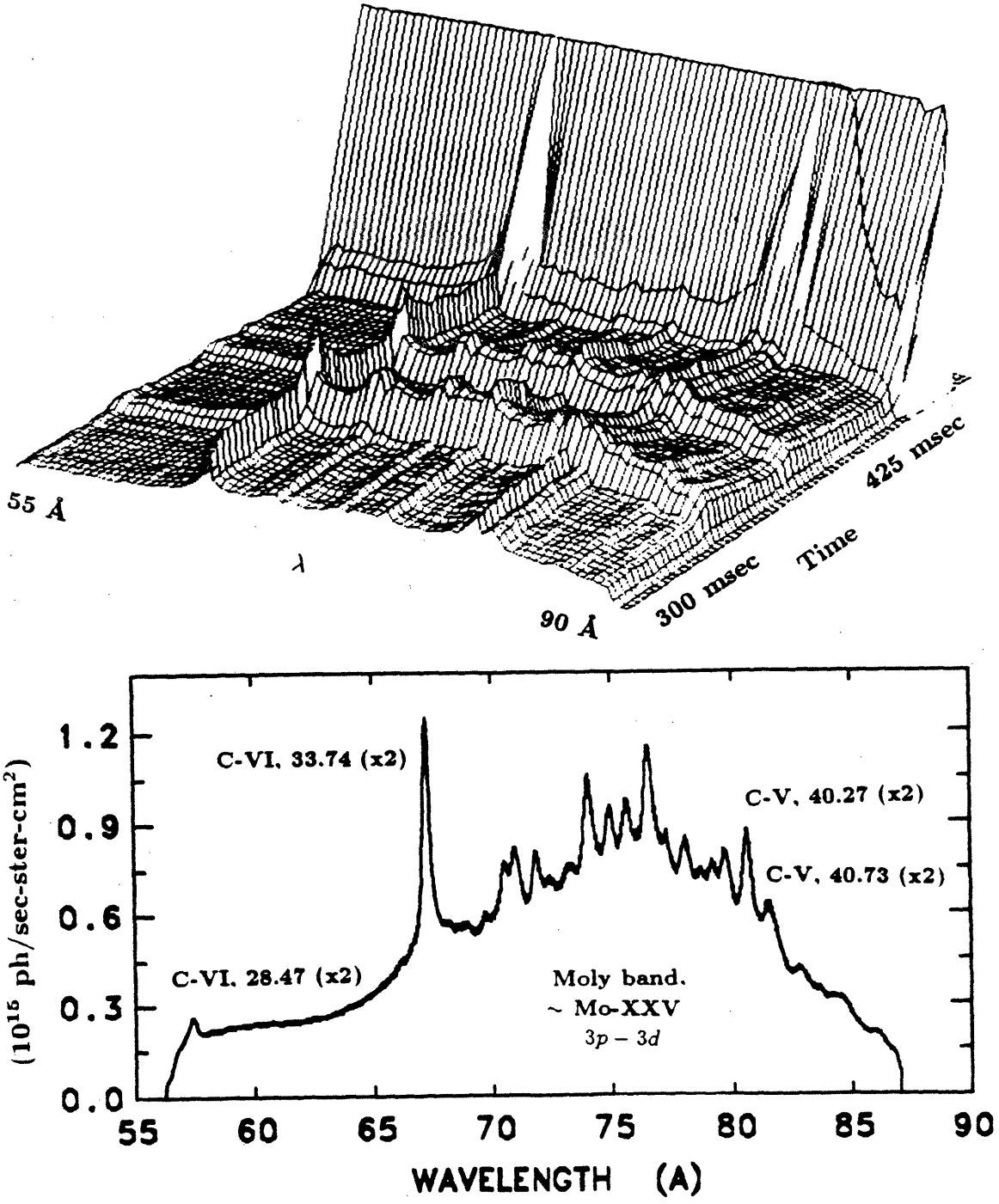

Figure 3.16 Surface plot representation of spectra taken during injection of three pellets of frozen hydrogen into the plasma. The first two were absorbed by the plasma, while the third caused the plasma to disrupt. A typical spectrum is shown beneath the surface plot.

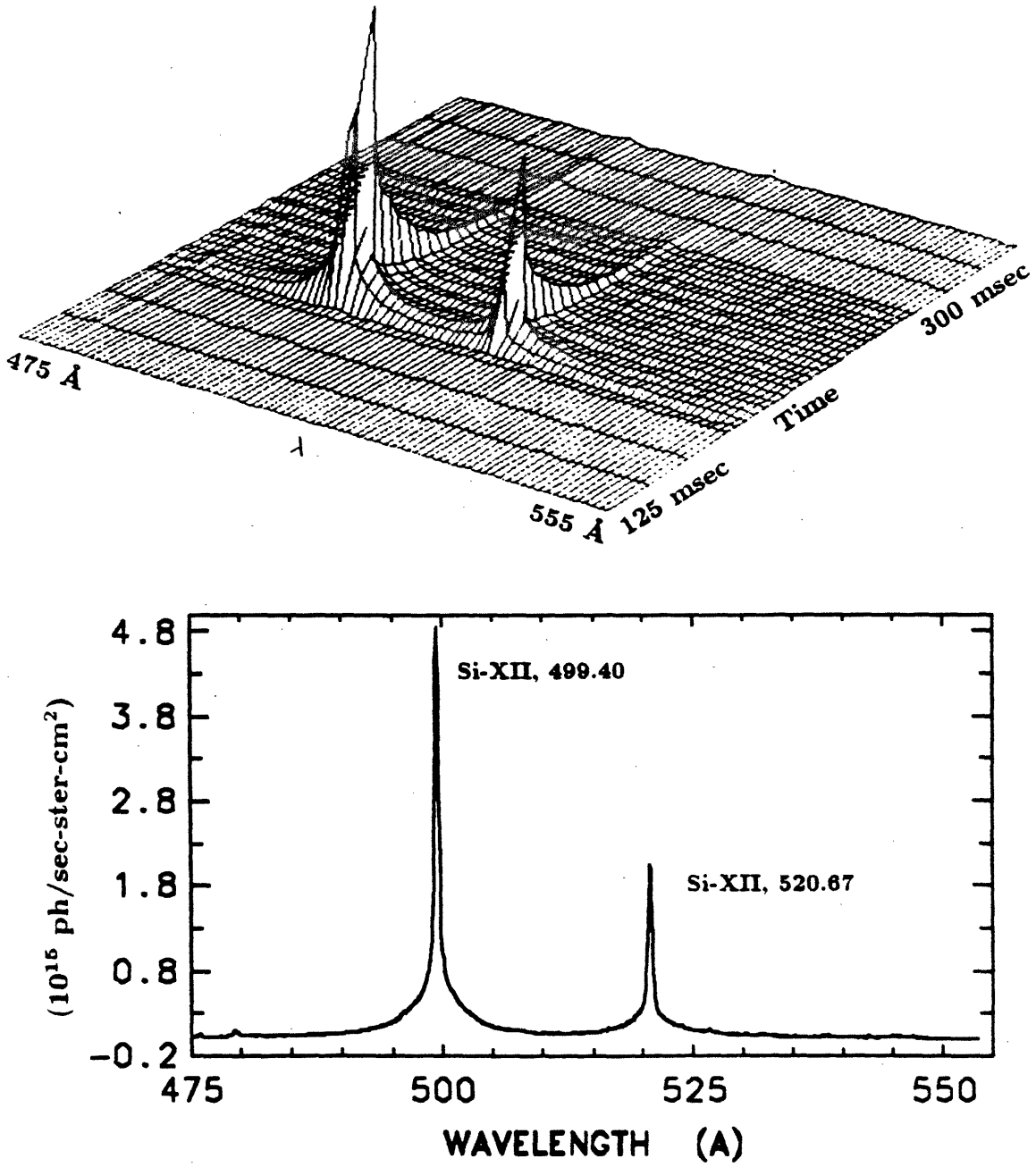

Figure 3.17 Surface representation of VUV spectra during artificial injection of silicon for transport studies. Shown below is a typical spectrum during the injection, with the Si-XII doublet ($2s - 2p$, 499.40 and 520.67 Å).

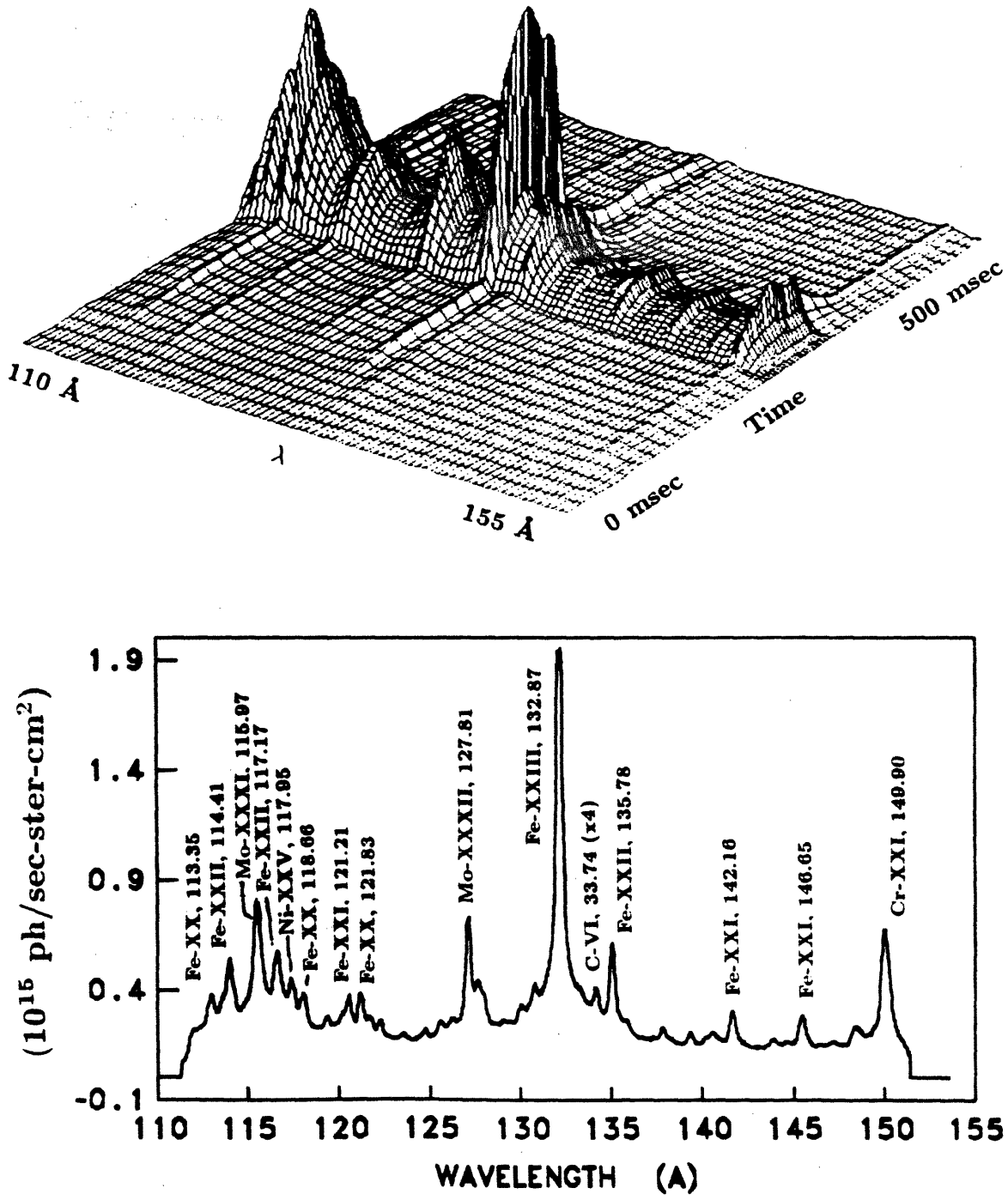

Figure 3.18 Surface representation of VUV spectra during high power ICRF heating experiments on Alcator C. Shown below is a typical spectrum during the RF pulse.

can be assembled for the element of interest. For convenience, such composite spectra were constructed for molybdenum and argon, two impurities with rich emission spectra in the wavelength region monitored. Prominent lines were identified by use of wavelength tables such as that by Kelly [62].

The same technique was used to construct an emission spectrum for tungsten, a heavy element injected chiefly for transport studies. For the plasma temperatures found in Alcator C, the tungsten spectrum was virtually flat but for an emission band identified as an unresolved transition array [63,64]. This feature contains a few thousand individual transition lines involving electron transitions from the $4f$ to the $4d$ subshell; ionization states from W-XX to W-XXXV are involved. The feature is centered about 51 Å and was observed in both second order (Figure 3.19) and third order with the 600 line/mm grating. Aside from this emission band, the only other features tentatively identified as being due to tungsten were several weak lines at roughly the following wavelengths: 162 Å, 173.5 Å, 176.1 Å, 177.5 Å, 284.5 Å, 292 Å, and 296.3 Å.

The same spectral subtraction technique was used to study the change in the VUV emission spectrum during the ICRF heating experiments mentioned above. Spectra recorded prior to the RF pulse were subtracted from those obtained during or just after the RF pulse (with the accompanying impurity rise). The resulting differential spectra represented emission due to additional impurities present due to the ICRF pulse. A composite spectrum was formed for a series of high powered ICRF pulses ($350-400$ kW of RF power injected into the plasma, minority hydrogen heating regime). Details of the ICRF experiments and ensuing impurity rise are presented in the following chapters. The composite spectrum is presented in Appendix 1, entitled "Stainless Steel Spectrum" since iron, chromium, and nickel are dominant and the source is believed to be a stainless steel component of the

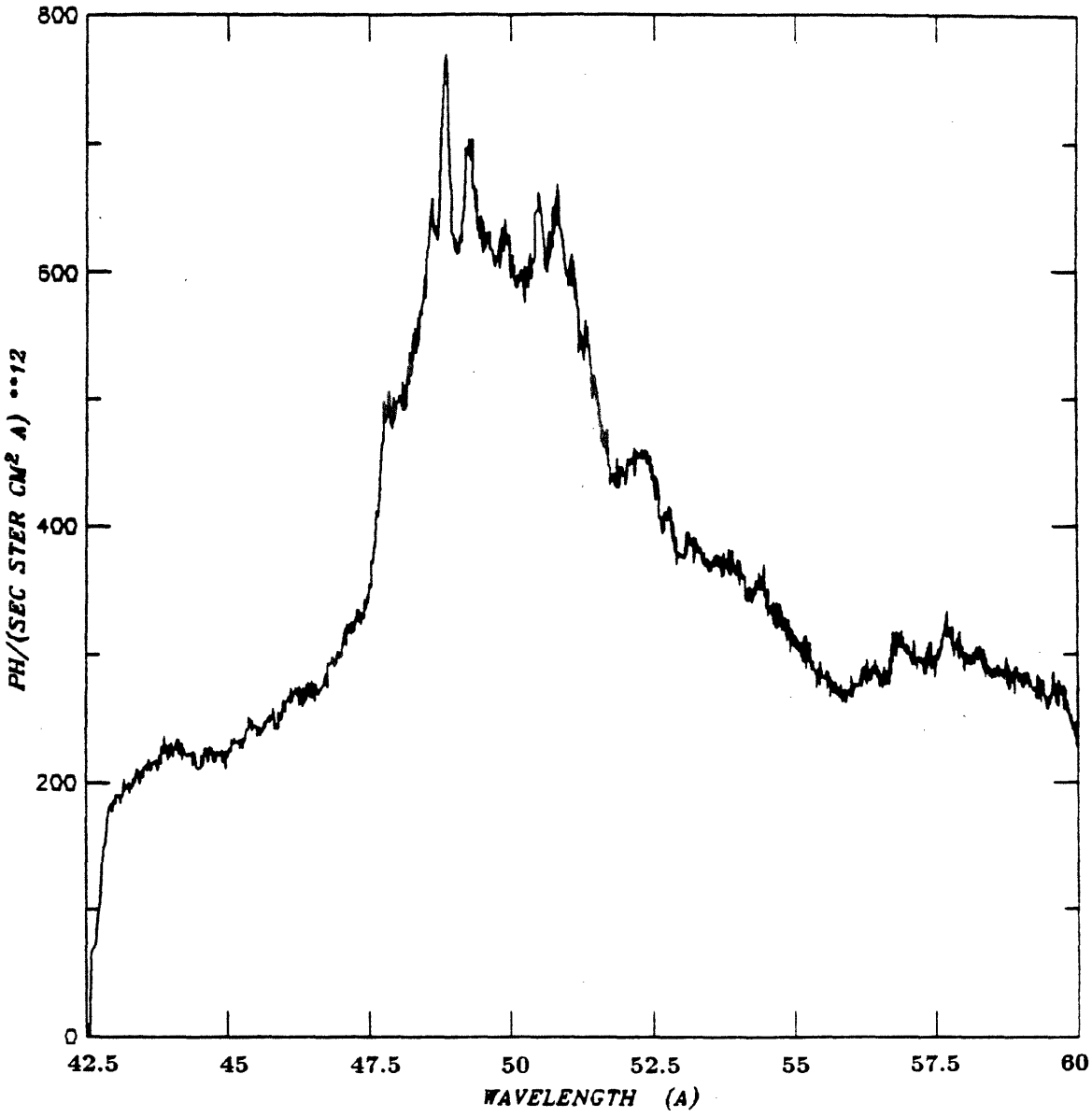

Figure 3.19 Tungsten emission band attribute to unresolved transition array involving $4f$ to $4d$ transitions in ionization states from W-XX to W-XXXV. Differential spectra technique was used to remove the intrinsic impurity radiation lines.

ICRF antenna. Identification of the prominent lines is also given in the appendix.

Chapter 4

Impurity Generation During ICRF Heating Experiments

4.1 Overview

ICRF heating of tokamak plasmas, as described below, shows considerable promise as a means of economically achieving reactor level ion temperatures. However, a key experimental difficulty is the problem of enhanced impurity influx during ICRF heating, particularly metal impurities. To overcome this problem, it is important to understand the source of these metal impurities and the dominant mechnanism responsible for their release. This chapter and the next address these issues on Alcator C, arriving at the conclusion that, for the experiments described, the large increase in metal impurities is due to an elevated rate of thermal sputtering of the stainless steel Faraday shield which covers the ICRF antenna structure. This is a direct consequence of a prompt increase in the electron temperature in the edge region of the plasma, where the antenna is located.

On a high field, high density tokamak such as Alcator C, the high density plasma and limited port access render auxiliary heating via neutral beam injection (NBI) difficult. It is therefore especially important to understand the physics of RF heating on such devices. Impurity control is also vital, since the high electron densities involved (compared to most tokamaks) lead to relatively high radiated power losses per impurity ion. This section of the thesis presents the first impurity measurements during ICRF heating experiments on the Alcator C Tokamak.

These RF experiments were conducted at a frequency of 180 MHz over a wide variety of plasma conditions and heating regimes. Graphite limiters and stainless

steel Faraday shields were employed during these experiments. Spectroscopic observations of impurity line radiation revealed dramatic increases in metal impurity concentrations (Fe, Cr, Ni, Mo) during the RF pulse. Much smaller increases in carbon and oxygen were seen. Analysis of the inferred iron source rates shows an approximately linear dependence on RF power, with no clear dependence on working gas (H or D), number of antennas used, or on resonance conditions (H 2nd harmonic, H minority in D, or off resonance). No correlation is observed with the presence of an ion tail or bulk ion heating. However, Langmuir probe data indicated a sharp increase in the temperature in the limiter shadow region during the ICRF pulse, well correlated with the iron influx rate. The behavior of carbon and iron during high power ICRF shots is in reasonable agreement with calculated sputtering yields by thermal ions (both hydrogen and impurity) striking, respectively, the graphite limiter at r =12.5 cm and the Faraday shield at 13.2 cm. (The stainless steel wall is located at r = 19.2 cm.) This calculation uses the measured changes in the plasma edge temperature and density profiles.

Section 4.2 presents a brief review of ICRF heating in tokamaks, introducing several relevant topics (including impurity generation). Section 4.3 contains a review of impurity effects observed during ICRF heating experiments at other tokamaks. The variety of results and conclusions serves to point out the lack of consensus regarding the optimum procedure for minimizing detrimental impurity effects. Experimental details from Alcator C are presented in Section 4.4, with descriptions of the ICRF heating program and diagnostics used. Representative VUV data, taken with the instrument described in chapter 2, are presented. Typical VUV spectra from before and during ICRF heating are shown. Section 4.5 gives detailed information on the impurity influx. Impurity concentrations, $Z_{\rm eff}$ contributions, radiated power, and temporal behavior are presented. A one dimensional impu-

rity transport code used to relate measured line brightnesses to derived quantities (concentrations, source rates, etc.) is described. The change in $Z_{\rm eff}$ during the RF pulse is shown to increase with increasing $P_{\rm RF}$. A detailed analysis of the possible sources and mechanisms responsible for this impurity influx is given in Chapter 5.

4.2 Introduction to ICRF heating

Resonant heating of fusion plasmas via absorption of plasma waves launched in the Ion Cyclotron Range of Frequencies (ICRF) has long been considered an attractive method of efficiently raising plasma temperatures to reactor levels [65]. Experiments involving radio-frequency (RF) heating have been a part of fusion energy research almost from the beginning, going back to work in the mid-1950's on the model B-65 Stellarator at Princeton [66]. There exists an extensive literature of both theoretical and experimental ICRF results, including several review papers [6-8,65,67,68]. Only a brief discussion of relevant topics is presented here.

It is generally accepted that Ohmic heating (OH) of tokamak plasmas will be insufficient to push the plasma temperature of a practical reactor into the necessary regimes for economical power generation. Some form of auxiliary heating will be required for tokamak reactors. Reactor designs based on alternative geometries without Ohmic heating (e.g. mirrors, stellarators) depend entirely on other heating methods, chiefly neutral beam injection (NBI) and various RF heating schemes. ICRF heating has several advantages over other methods. The technology of efficiently generating and transmitting megawatt levels of RF power in the ICRF range of 4–200 MHz is fairly mature; equipment developed for radio, television, and radar is readily adaptable to fusion applications. Standard coaxial transmission lines can deliver power over long distances, allowing the RF generators to be located in a non-radioactive area well away from the reactor. This frees up valuable space around

the tokamak, and it removes the problems of irradiation and remote handling for the RF generators.

Recent experiments utilizing the fast magnetosonic wave (one of several ICRF plasma waves possible in a plasma) have demonstrated that efficient ICRF heating of both ions and electrons is possible [6]. Among the various RF heating schemes, ICRF heating has delivered the most power and achieved the highest efficiencies. Up to 4.3 MW of ICRF power has been delivered in tokamaks, with a five-fold increase in the stored energy of the plasma [8]. No saturation of heating efficiency has been observed, even at these power levels. Although NBI has yielded the most successful auxiliary heating results so far, several recent reactor studies have selected ICRF heating as the primary heating approach [6-8]. This choice was partially due to considerations of overall cost and efficiency. Also, ICRF heating is not limited by high plasma densities, which can prevent NBI from effectively penetrating and heating the central plasma.

ICRF heating has the further advantage of depositing power chiefly in a narrow resonance layer, in principle allowing some control over the heating profile. The position of this layer is determined by the condition that $\omega_{\mathrm{RF}} \approx n\Omega_i$, where ω_{RF} is the frequency of the launched waves, $\Omega_i = q_i B/m_i c$ is the ion cyclotron frequency for the particular ion species involved, and n is an integer (usually 1 or 2). Since the main (toroidal) component of the magnetic field has a $1/R$ dependence on major radius, this effectively defines a cylindrical resonance layer which cuts almost vertically through the plasma torus at the radius for which $\Omega_i(R) = \omega_{\mathrm{RF}}/n$. This resonance layer is normally centered at $R \approx R_o$, the major radius of the plasma, for optimum heating. In this situation the RF power may be converted to plasma thermal energy primarily at the plasma center, where high plasma density and temperature can lead to efficient wave damping and energy absorption.

The possibility of enhanced fusion reaction rates is another reason that ICRF heating is regarded favorably [65,69]. The idea involves the fusion reaction cross section, σ_F, which depends strongly on collision energy. The total fusion reaction rate, of course, goes as the average value of $(\sigma_F v)$, where v is the velocity variable in the particle distribution function $f(v)$. For a deuterium-tritium plasma, the peak value of σ_F occurs at a collision energy of 110 keV; the cross section at 10 keV is smaller by a factor of $\sim$ 2500. Thus, in a Maxwellian D-T reactor plasma with $T_i \approx$ 10–20 keV, the bulk of the fusion events are due to ions far out in the tail of the energy distribution function. Because some ICRF heating schemes create non-Maxwellian fast ion "tails" in the distribution, the fusion reaction rate can in principle be much higher than for a Maxwellian plasma with similar energy content. This could lead to savings in the peak power requirements for a reactor.

Finally, some experimental evidence suggests that ICRF heating of selected impurity ions can lead to significant reduction of that impurity in the plasma. ICRF is therefore a possible method of impurity control [65].

A key ICRF engineering issue is the design of antennas to effectively couple the RF power into the desired plasma waves [7]. The large vacuum wavelengths involved (5 m for 60 MHz) often preclude the use of standard half-wavelength cavities; most current experiments use induction coils located inside the vacuum vessel but outside the hot plasma core. The RF current in the coil runs in the poloidal (θ) direction in order to provide a strong RF magnetic field component in the toroidal (ϕ) direction, parallel to the main DC magnetic field (B_ϕ). This field then excites fast magnetosonic waves (also called compressional Alfvén waves) in the plasma edge. In the ideal case, the fast wave propagates radially inward and is fully absorbed in the plasma center.

In order to avoid exciting other, undesirable waves in the plasma edge, a

Faraday shield is required to short out the toroidal component of the antenna RF electric field. Important for proper antenna operation, the Faraday shield consists of a conducting cover over the antenna loop with slots or gaps cut in the toroidal direction to allow the RF magnetic flux to penetrate, thus acting as an electrostatic screen. The absence of a Faraday shield can lead to electron heating in the edge plasma and enhanced production of impurities [65]. Faraday shields also serve to protect the antenna loop from bombardment by the particles in the plasma edge [8]. In addition, they can minimize the effects of plasma rectification at the antenna, which could otherwise lead to sheath potentials at the antenna comparable to the peak antenna voltage (up to 1 kV on Alcator C). Such potentials could lead to large sputtering of the antenna [70]. An ICRF antenna system used on Alcator C is shown in Figure 4.1.

There are several important questions regarding the interaction of ICRF waves with the edge plasma, through which the waves must propagate in order to heat the central plasma. In particular, it is not clear what experimental arrangements will minimize wave absorption in this region. Waves absorbed in the plasma edge are undesirable for two reasons. Such waves include slow magnetosonic waves propagating along the poloidal field, surface modes in the steep edge density gradients, and coaxial modes propagating in the quasi-vacuum layer between the wall and the main plasma [71]. First, they are parasitic in that they decrease the amount of energy deposited in the central plasma. Second, any heating of the plasma in the region between the limiter radius and the wall will lead to an increase in impurity production. This region is called the boundary layer or scrape-off layer (SOL); it includes that volume outside the outermost plasma flux surface which "scrapes" against the limiter. It is typically characterized by electron density and temperature profiles which decay exponentially with radial distance outside the limiter radius,

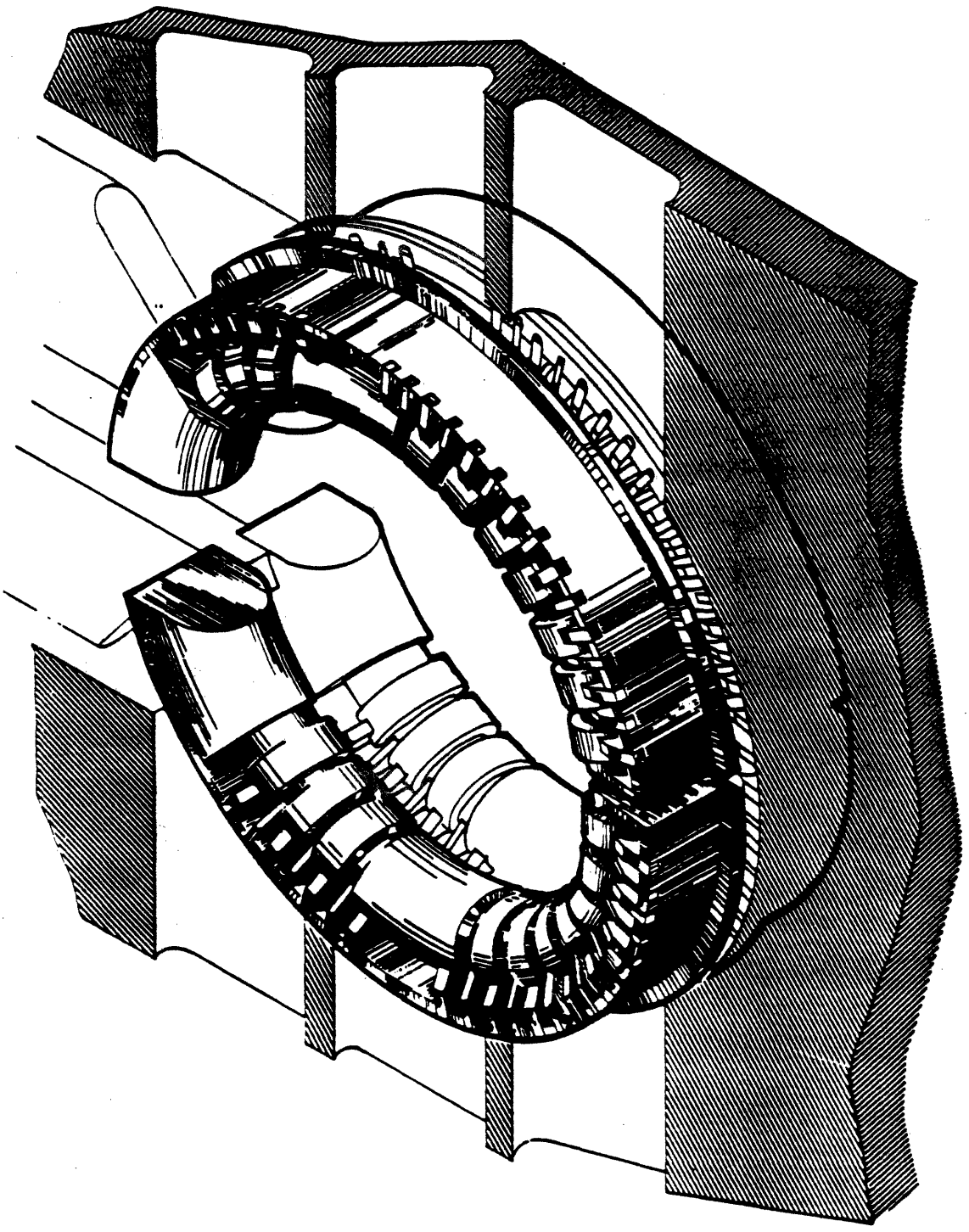

Figure 4.1 Alcator C ICRF antenna, including Faraday shield. The antenna loop is hidden from view by the shield (slotted structure). Shaded area represents Alcator C port flange; torus center is to the right.

with decay lengths λ_n and λ_T (typically a few mm on Alcator C):

$$n_{eb}(r) = n_e(r = a)e^{-(r-a)/\lambda_n}, \qquad r > a \tag{4.1}$$

$$T_{eb}(r) = T_e(r = a)e^{-(r-a)/\lambda_T}, \qquad r > a \tag{4.2}$$

The symbols n_{eb} and T_{eb} represent, respectively, the density and temperature of electrons in the *b*oundary layer. Because the coupling efficiency is improved as the distance between the antenna and the plasma is reduced [70], ICRF antennas must be immersed in the SOL plasma for optimum results.

The propagation of plasma waves is generally treated theoretically in terms of the wave equation with a spatially varying dielectric tensor:

$$\nabla \times \nabla \times \mathbf{E} = \frac{\omega^2}{c^2} \overleftrightarrow{\varepsilon}\,(\omega) \cdot \mathbf{E} \tag{4.3}$$

Assuming a wave of the form $\mathbf{E}e^{-i(\mathbf{k}\cdot\mathbf{x}-\omega t)}$ yields a wave dispersion relation,

$$D(\omega, k_\parallel, k_\perp, \mathbf{x}) = 0 \tag{4.4}$$

where the subscripts refer to the magnetic field direction. The magnetic field leads to finite off-diagonal elements of $\overleftrightarrow{\varepsilon}\,(\omega)$. The spatial variation of $\overleftrightarrow{\varepsilon}\,(\omega)$ is due to the dependence of the individual tensor elements on the magnetic field strength and the densities of the various species of particles in the plasma. This causes variations in the fundamental frequencies of the plasma, ω_{pe} and Ω_α, where α represents the different species present.

$$\omega_{pe}^2 = \frac{4\pi n_e^2}{m_e} \tag{4.5}$$

is the electron plasma frequency, and

$$\Omega_\alpha = \frac{q_\alpha B}{m_\alpha c} \tag{4.6}$$

is the gyrofrequency of the various species. The plasma electron density is normally taken to have a parabolic dependence on the minor radius,

$$n_e(r) = n_{eo}(1 - r^2/a^2)^m, \qquad m \approx 1 \tag{4.7}$$

with a similar profile for bulk ion density. Impurity ions of a particular charge state are more complicated, typically residing in a narrow cylindrical shell in which the electron temperature is about one third of its ionization potential. The main (toroidal) magnetic field strength in a tokamak varies inversely with the major radius,

$$B_T = B_o \frac{R_o}{R} = B_o \frac{1}{1 + r\cos\theta} \tag{4.8}$$

where B_o is the field strength on the magnetic axis $R = R_o$. When warm plasma kinetic effects are included, the wave dispersion is also dependent on temperature profiles. The electron temperature is usually well-represented by a Gaussian profile,

$$T_e(r) = T_{eo} e^{-(r/\alpha)^2} \tag{4.9}$$

where α is typically $0.6a$. Ion temperatures generally have similar profiles, but with lower central values. Figure 4.2 illustrates the spatial dependences of B_t, n_e, and T_e.

In a hot, multi-species plasma with spatial gradients, the problem of wave propagation would be intractable without the use of several simplifying assumptions. Without getting into too much detail, it turns out that the fast wave can be treated fairly well by a cold ($T_e = T_i = 0$) plasma dielectric tensor in regions away from cutoffs and resonances. The geometry of the problem in tokamaks dictates that the waves of interest propagate at almost constant $k_\parallel$, with $k_\perp$ varying as the wave penetrates into the plasma [7,65]. The spatial power spectrum of the antenna, related to its toroidal width, determines the $k_\parallel$ spectrum of the launched waves in most tokamak applications [7].

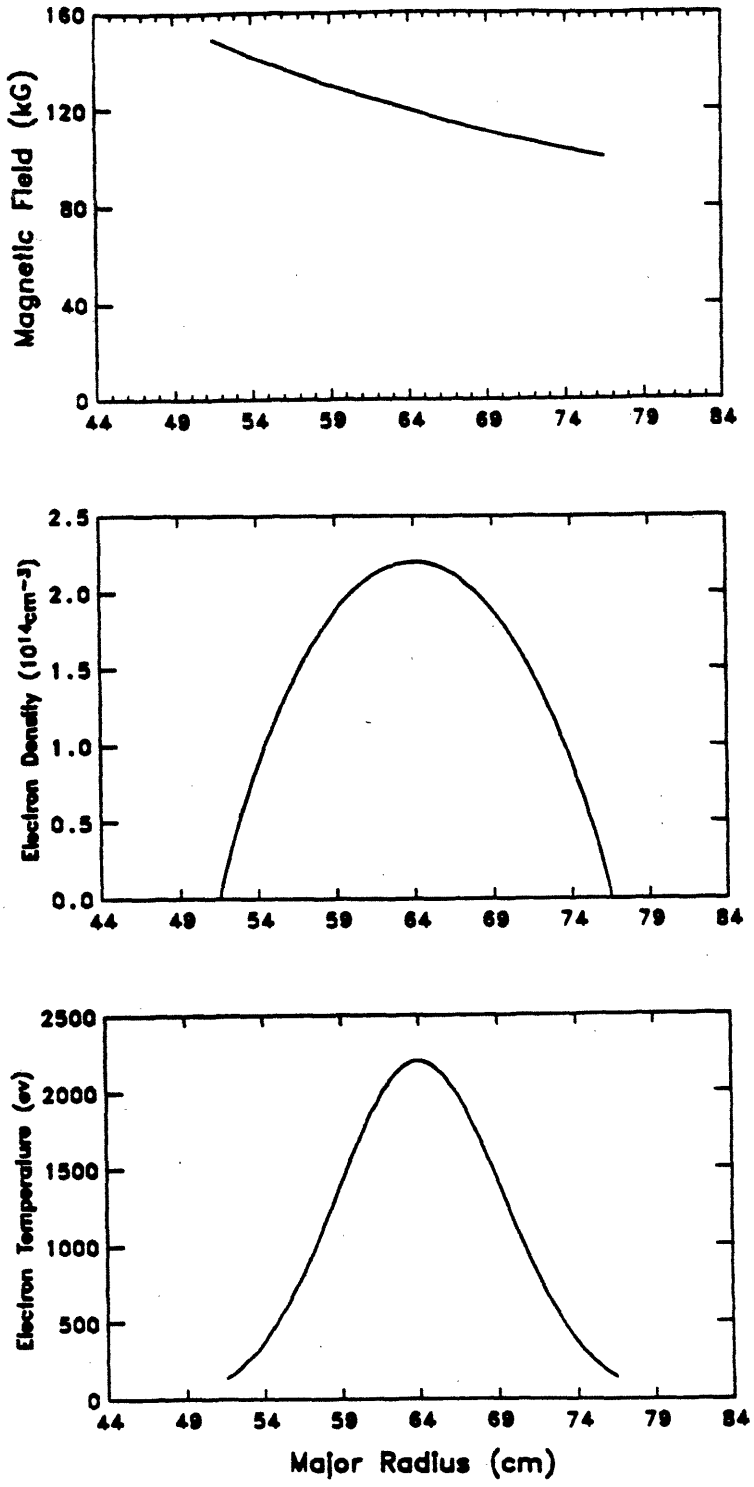

Figure 4.2 Typical spatial profiles of B_T ($1/R$ falloff), n_e (parabola to the ~ 1.0 power), and T_e (Gaussian).

In the simple picture, wave absorption occurs at resonances defined as locations at which $k_\perp \to \infty$, and wave reflection occurs at cutoffs where $k_\perp \to 0$. In a more complete description, cold-plasma resonances are resolved by the re-inclusion of neglected terms in the dispersion relation in the vicinity of the resonance. This generally converts the dispersion relation into a higher order system of differential equations, which physically corresponds to the inclusion of some other, short wavelength mode in the analysis. This process, known as mode conversion, represents a transfer of wave energy from the fast wave to a new, shorter wavelength mode whose description generally involves warm plasma ($T_e \neq 0$) kinetic theory, such as the electrostatic ion Bernstein wave. The short wavelength wave is usually rapidly damped by collisionless absorption processes, leading to plasma heating. The energy can be absorbed by either electrons or one of the ion species, depending on the particular wave [7,65].

There are two special cases of fast wave ICRF heating useful in tokamak applications. In one, the "second harmonic" regime, the impressed frequency equals twice the gyrofrequency of the major ion species near the plasma center ($\omega_{RF} = 2\Omega_i$). While intuition might suggest that absorption would be better at the fundamental gyrofrequency of the ion, it turns out that in cold plasma theory there is no wave-particle interaction in this case, due to polarization considerations. At the fundamental cyclotron resonance, the fast wave electric field has a right-hand circular polarization about the background magnetic field, while the natural gyromotion of the ions is left-handed. This ion motion "shorts out," or suppresses, the left-handed electric field at the resonance layer, leaving only the right-handed component [6]. (High electron conductivity along the field lines similarly shorts out any $E_\parallel$ fields in this approximation.) Although warm plasma effects alter the picture somewhat, the damping of fundamental cyclotron resonant waves for the majority species of

ion is so weak, in fact, that toroidal eigenmodes can be established in the tokamak [8,67,72].

However, at $\omega_{RF} = 2\Omega_i$, spatial gradients in the RF electric field cause a damping interaction between the ions and the wave near the resonant surface, which can yield large absorption. The ions acquire an oscillatory velocity at a frequency $(\omega_{RF} - \Omega_i)$, which leads to damping at a layer near the $2\Omega_i$ gyroresonance where ions exist for which $\omega_{RF} - \Omega_i - k_\parallel v_\parallel \approx \Omega_i$, where $v_\parallel$ is the ion velocity parallel to B. This phenomenon is better expressed in terms of corrections to the dielectric tensor and mode conversion, as discussed above [7].

The second special case involves the presence of a minority ion species in a multi-species plasma and is the primary heating method in most current ICRF heating experiments [65]. The damping depends on the minority/majority concentration ratio and, in this "minority ion heating" regime, is generally even stronger than that of second harmonic absorption. For example, the best ICRF heating results on Alcator C during the runs analyzed here occurred in plasmas consisting of a small concentration of hydrogen (0.5– 3.0%) in a deuterium majority plasma. In minority heating, the impressed RF frequency is set equal to the fundamental cyclotron frequency of the minority ions near the center of the plasma. If the minority species is sufficiently dilute, the polarization of the RF wave is governed by the majority species (which is generally not at the fundamental resonance), and there will be a significant left-handed circular polarization component of the electric field present. This component is then resonant with the natural gyromotion of the minority species. Thus, wave absorption can occur, and the minority ion species can then become very hot. As long as this energetic minority ion population is confined for average times long enough to transfer energy via binary Coulomb collisions to the bulk ion species, this method is very effective for heating the main plasma.

However, confinement of the energetic minority species can be a problem for small, low current tokamaks [7].

At higher concentrations of the minority species, a more complicated interaction involving mode conversion becomes important. There exists a two-ion hybrid resonance layer (also called ion-ion) between the fundamental cyclotron resonance layers of the two ion species; for dilute minority concentrations in tokamaks this ion-ion resonance (ω_{ii}) is physically very close to the fundamental minority resonance layer [6]. The ion-ion frequency is given by:

$$(\omega_{ii})^2 = \Omega_1\Omega_2 \frac{n_1\Omega_2 + n_2\Omega_1}{n_1\Omega_1 + n_2\Omega_2}, \qquad n_j = \frac{N_j}{N_e}. \tag{4.10}$$

As $k_\perp \rightarrow \infty$ at the ω_{ii} surface, the perpendicular wavelength of the fast wave approaches that of the electrostatic ion Bernstein wave, and this close coupling leads to mode conversion. The energy of the fast wave is efficiently converted to plasma thermal energy, with electron Landau damping of the Bernstein wave, fundamental cyclotron damping by the minority species, and second harmonic damping by the majority species (if applicable, as in the H-D case) all competing in the absorption process [68].

The physical locations of these various resonances are indicated in Figure 4.3 for the case where the minority component has the higher charge/mass ratio (e.g., H minority in D). For this case, the ω_{ii} resonance and mode conversion layer are on the high magnetic field side of the minority Ω_i resonance layer, i.e. closer to the center of the torus. Associated with this resonance is a nearby cutoff layer. The circular cutoff layer at the plasma edge arises from the fact that the fast wave cannot propagate below a critical plasma density, which depends on $k_\parallel$ [6]. The fast wave must therefore tunnel through a thin evanescent region at the plasma edge, which partially explains why the coupler must be fairly close to the plasma. The longer wavelength (low $k_\parallel$)components penetrate more easily than do the higher

$k_{||}$ components. The wave energy which doesn't penetrate is reflected, and it may excite the various edge modes in the SOL region and cause edge heating, as discussed earlier. In particular, the high $k_{||}$ components can couple to the slow magnetosonic wave, also called the torsional Alfvén wave, which can propagate in the low density edge region as long as the wave frequency is below the ion cyclotron frequency [8]. Thus, the antenna coupling (loading), the wave reflection coefficient, and edge heating effects can all be sensitive to the $k_{||}$ spectrum of the RF radiation fields launched by the antenna. This is especially true for antennas on the outside of the torus, or low field side (LFS) [65]. Ion Bernstein waves can also be excited directly by a fast wave antenna due to coupling between the antenna current components parallel to the magnetic field and edge density gradients [8,65]. Surface waves [6,73] and coaxial modes [73] may be excited in the plasma edge, although measurements indicate that surface waves are suppressed provided that the wall-plasma spacing is not too large [6]. Damping of these various waves, or absorption when they reach cyclotron resonance or mode conversion locations [65] or even the lower hybrid resonance layer [74] can lead to heating of the SOL plasma. As already stated, this is an undesirable effect from the standpoint of impurity generation. The lower hybrid resonance is a separate mode, which at these frequencies occurs in a low density region near the wall [6] for which $\omega_{\mathrm{RF}} \approx \omega_{pi}$, the plasma ion frequency.

A further asymmetry between low field side (LFS) and high field side (HFS) launching occurs in the minority heating and mode conversion regimes. As the minority concentration is raised, the cutoff layer near the mode conversion layer becomes more important, leading to increased reflection for LFS launching and increased absorption for HFS launching [6,68,72]. Because the antenna loops used on Alcator C launch from both sides simultaneously, and because no experiments were conducted in the mode conversion regime, the details of this asymmetry are

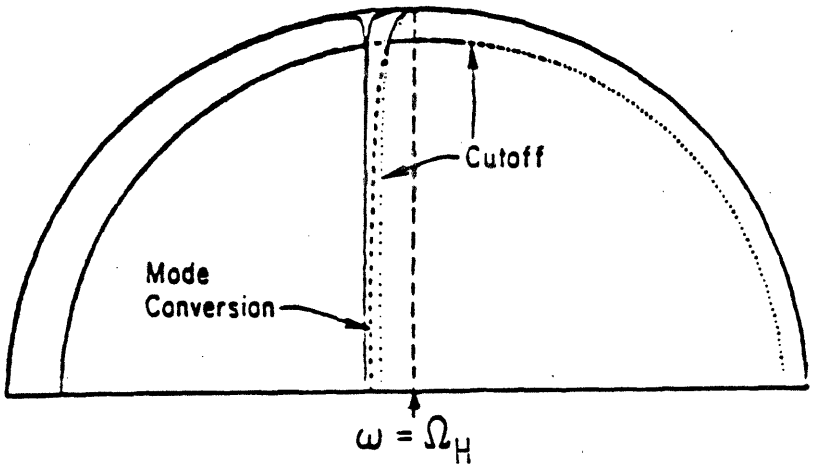

Figure 4.3 The physical locations of various ICRF resonances and cut-offs for the minority heating regime (H minority in D). Torus center is to the left.

unimportant for the work presented herein.

Experimental studies have verified the efficacy of ICRF heating, with most of the best results occurring in the minority heating regime [6,68]. Improved efficiencies can be expected for reactor regimes, as the absorption processes improve for hotter and denser plasmas [72]. In fact, thermonuclear plasmas are predicted to be opaque to the fast wave (100% single pass absorption) [6]. However, all the problems of ICRF heating have not been resolved, either theoretically [6-8,72] or experimentally. One problem is the confinement of the fast ions for a period long enough to allow them to slow down, transferring energy to the bulk plasma. This is especially of concern for the minority ion heating regime, but it seems less serious for the newer, larger tokamaks whose plasma current is high enough to confine the fast ions [6]. This is also less of a problem for high density tokamaks such as Alcator C, which have a relatively high rate of collisional energy transfer between ions. Another problem is the observation that overall plasma energy confinement times are generally adversely affected by auxiliary heating in tokamaks, relative to purely ohmic heating of the same power. ICRF heating shares this difficulty with the other methods [6]. However, the foremost experimental difficulty of ICRF heating in tokamaks is the problem of enhanced impurity influx during ICRF heating [65], which may be the source of the energy confinement degradation.

As discussed below, early ICRF experiments on tokamaks were often plagued by large metallic impurity influxes which severely limited the amount of RF power that could be successfully delivered to the plasma, and the temperature increases thereby obtained. Although several recent experiments have studied and, to some extent, overcome this problem [70,75,76], there remains no clear consensus as to the principal source of metal impurities or the dominant mechanism for their release. Impurity generation during ICRF heating involves the complex interactions between

the scrape-off layer (SOL) plasma, the RF fields, and the materials exposed to the SOL [77]: the limiter, the walls, and the ICRF antenna structure. In order to extend ICRF heating to reactor level powers, further understanding of these interactions is needed to minimize the enhanced radiated power losses and impurity concentrations which persist in most of the current high power ICRF experiments.

4.3 Impurity Effects During ICRF Experiments at Other Tokamaks

Princeton Large Torus (PLT)— Early ICRF experiments at PLT, using stainless steel limiters, found the central iron concentration saturating at elevated but acceptable levels for 500 kW RF, so long as the plasma current exceeded 300 kA [78,79]. Since the installation of carbon limiters in 1980, metal impurity levels have dropped for ohmic (OH), RF, and NBI heated discharges, with radiated power now dominated by low Z (C,O) radiation from the peripheral plasma [70,80,81]. Metal impurity generation was further reduced through the use of carbon shields on the lateral faces of the metal antenna Faraday shields. ICRF heating has been employed successfully at powers up to 3.0 MW without major radiated power losses from the center, using a low field side antenna (LFSA) in both the minority hydrogen regime ($\omega = \Omega_H$, minority hydrogen in deuterium plasma) and hydrogen 2nd harmonic regime ($\omega = 2\Omega_H$). The constraint that $I_p \geq 300$ kA was still necessary to prevent impurity accumulation. However, both total radiated power ($\approx 30\%$ P_{RF}) and metal impurity concentrations scaled linearly with RF power [80]. PLT researchers concluded that the metal surfaces closest to the plasma contribute the most metal impurities, especially the Faraday shield ($\approx$ 3 cm outside the limiter radius), although the wall (10 cm outside the limiter radius) also contributes. In fact, sputtering calculations showed that an elevated low energy ($E \leq 1000$ eV) neutral efflux, measured during ICRF, was sufficient to account for the observed

influx of iron from the stainless steel walls [81]. A large ($\times 5$) increase in low energy charge exchanged (CX) neutrals was seen at $P_{RF} = 2.0$ MW, as well as a ten-fold increase in electron density in the SOL behind the Faraday shield [81], which was attributed to either enhanced SOL radial transport or partial ICRF wave absorption in the SOL, leading to increased ionization. Higher energy CX efflux increased to an even greater extent. CX neutral sputtering could also release Faraday shield material previously deposited on the walls. Suprathermal ions were observed in PLT during H minority heating, but their loss rate was judged insufficient to cause significant impurity generation via sputtering. However, results suggested a "synergistic interaction" between these fast ions and thermal particles, which may cause enhanced evaporative sputtering of carbon limiters. For similar RF powers, the impurity influx appeared to be independent of ICRF heating mode or antenna poloidal extent.

Tokamak Fontenay-aux-Roses, France (TFR)— Early ICRF experiments on TFR, in which both the limiters and the antenna Faraday shields were made of Inconel, showed a more severe influx of metals during the RF pulse, leading to central cooling and even major disruptions [82,83]. Nickel concentrations increased linearly with RF power up to 1.5 MW from the HFS antenna; only 100 kW could be launched from the LFS antenna without causing disruptions [84]. By changing to a graphite limiter and using graphite "lateral protections" on the antenna sides normal to the toroidal field, this dominance of central radiated power losses was overcome, yielding good heating results at $P_{RF} \leq 1.2$ MW. Nickel concentrations diminished by an order of magnitude [85,86]. However, total radiated power actually increased due to large peripheral losses from carbon and oxygen, sometimes exceeding 70% of total input power, and Z_{eff} rose from about 1.0 to 2.0 and higher [87]. Metal impurity radiation, although minor in the power balance,

continued to scale linearly with P_{RF}, was higher than for comparable OH and NBI powers, and was apparently three times higher for the LFSA than for the HFSA. Results from antennas made of different materials indicated that impurities generated from the antenna Faraday shield originated chiefly on the lateral surfaces (rather than the front surface facing the plasma) [76,88]. The total shield, however, was judged not to be the dominant source of metal impurities, even without graphite lateral protections. Rather, every metal surface in the SOL, including the wall liner, contributed. Metal impurity production in TFR was a process not local to the antenna, attributed to changes in the SOL, independent of ICRF heating mode or heating of the plasma core. This conclusion was supported by Langmuir probe measurements, which revealed a prompt two- to three-fold increase throughout the entire SOL of the electron temperature in the boundary plasma, $T_{eb}(r)$, with T_{eb} proportional to P_{RF} up to 300 kW. In addition, a large rise in the boundary electron density, $n_{eb}(r)$, was observed. Larger percentage changes in n_{eb} occurred near the wall (as much as a ten-fold rise); and the e-folding length, λ_n, nearly doubled, corresponding to a large increase in wall desorption of hydrogen and increased recycling. The elevated edge temperature was believed to be responsible for enhanced hydrogenic sputtering of metal components in the SOL, especially at the wall, where the rise pushes T_{eb} above the $\sim$ 10 eV threshold for metallic sputtering through the electrostatic sheath potential ($\Phi_{sh} \approx 3$–$4T_e$). These edge effects in TFR were attributed to the direct coupling of a non-trivial fraction of the RF power into the SOL plasma by some undetermined mechanism, which was not related to central plasma conditions, predicted central wave damping, or the presence of cyclotron resonances in the edge plasma.

JFT-2 and JFT-2M, Tokai, Japan— Increases of as much as 20-fold in radiated power due to the influx of metallic impurities also forced researchers at

tokamak JFT-2 to abandon stainless steel limiters and bare molybdenum Faraday shields in favor of graphite limiters and TiC-coated Mo shields [89,90]. In the earlier experiments, during a series of HFSA ion-ion mode conversion ICRF runs, a strong correlation was noted between the impurity influx and the presence of fast ($E \geq 1$ keV) ions localized in the SOL. Enhanced impurity influx persisted, however, even in the absence of the fast ions. No fast tail was detected at the plasma core during these runs. Sputtering due to these fast ions, generated from some coupling of the ICRF power into the evanescent slow wave at the plasma edge, was offered as a possible impurity generation mechanism by Kimura *et al.* [73], who also invoked resonant cyclotron absorption by impurity ions themselves to partially explain central ion heating results.

Later, researchers at the larger JFT-2M tokamak were unable to inject more than 200 kW of ICRF power without causing a rapid, severe disruption (loss of plasma confinement) due to large radiated power losses from impurities [91,92]. Utilizing graphite limiters and Ti Faraday shields on both HFS and LFS antennas, and operating in the second harmonic regime, they found that up to 800 kW ICRF could be successfully applied only if the plasma was pre-heated by NBI. The increase in radiated power was still much higher than for similar NBI power, accounting for as much as 70% of the applied ICRF power. The increment in the deduced influx of low Z impurities (C,O) was twice as large during ICRF heating as it was for the application of similar amounts of NBI power. For metals (Fe,Ti) the ratio was higher: 5 for the HFSA and 7 for the LFSA. Langmuir probes revealed a rise in T_{eb} which was linear with respect to P_{RF}, and about twice as large as for similar NBI powers. Meanwhile, n_{eb} decreased during ICRF by a factor of 4, although the central density increased slightly. Because the brightnesses of low Z impurity lines were proportional to T_{eb} during all phases of the discharges (OH, NBI, and ICRF), it

was concluded that sputtering of the limiter by ions accelerated through the sheath potential was the dominant channel for the release of carbon and oxygen. The brightnesses of lines from edge states of Fe and Ti, however, increased faster with respect to T_{eb} during ICRF heating than they did during the OH and NBI phases. This led to the conclusion that some "additional mechanism" caused the Ti and Fe influx. Because the only possible source of Ti was the antenna Faraday shield, and the Fe lines from the stainless steel vessel walls followed the behavior of the Ti lines, it was inferred that this mechanism was localized, only releasing iron from the walls near the antenna. It must be noted, however, that a) one might expect very different profiles of $T_{eb}(r)$ during ICRF (the probe was apparently kept at one position), and b) the sputtering yields for metals are fairly non-linear with respect to the proton impact energy ($\propto T_{eb}$) in the range $T_{eb} \approx 10 - 20$ eV. It was also suggested that sputtering via acceleration of both protons and multiply- charged low Z impurity ions by the strong reactive $\mathbf{E_{RF}}$ fields generated near the antenna was the dominant source of metal impurities during these experiments. These calculations indicated that the hydrogenic sputtering contribution was important only for the highest RF powers. However, two points tend to contradict this conclusion: First, this model can match the data only if 5 times more oxygen were present at the LFSA than at the HFSA, in contradiction to observed values of n_{Ox}. Second, neon was added to TFR plasmas during ICRF heating to check this model, but no effect was seen there with regard to metal impurities [93]. On JFT-2M, no clear difference was found between the LFS and HFS antennas as regards impurity generation.

Recently, an array of 3 HFS antennas operating in the ion-ion mode conversion regime ($n_H/n_D \approx 40\%$) has been utilized in JFT-2M [94]. This system demonstrated the influence of the $k_{||}$ spectrum of the launched RF waves on edge plasma parameters and impurity production. Operation with the center antenna 180° out

of phase with the first and third shifted the $k_{||}$ peak value from 0 to 0.08 cm^{-1}, as compared to in-phase operation. Because more of the RF power reaches the plasma center, and less is absorbed in the edge, this out-of-phase mode yielded a reduction by 1.6 in the increment of total radiated power during ICRF heating, with a corresponding decrease in impurity line brightness increments. Sustained rises in T_{eo} and β_p were achieved, whereas in-phase heating experiments saw eventual decreases due to radiative cooling. Successful injection of 1.6 MW ICRF power in the out-of-phase mode enabled JFT-2M to reach $\beta_T = 1.2\%$ with only ICRF heating. (Note: β_T and β_p are the ratios of the local plasma thermal energy density to the toroidal and poloidal magnetic field energy density, respectively.)

JIPP T-II and JIPP T-IIU, Nagoya, Japan— ICRF heating experiments on the tokamak JIPP T-II [95], also encountered limitations due to metal impurity influx from the molybdenum limiter, metal Faraday shields, and Ti-gettered vessel walls. No further heating occurred beyond a threshold level of 260 kW for 10% H in D (150 kW for 4%H), in part due to radiative cooling. No threshold was seen, however, for 10% He in D, up to 350 kW. Later results from the expanded JIPP T-IIU [96] support the PLT conclusion that whatever metal surface is nearest the plasma will be the dominant source of metallic impurities during ICRF heating. When the original stainless steel limiters and Faraday shields, coated with Ti from gettering, were replaced with a graphite limiter and Ti Faraday shields, the brightness of Ti lines were much diminished, despite a 5-fold increase during the RF pulse. Plasma purity and heating efficiency both improved with the graphite limiter. In either configuration, the brightness of line radiation from the limiter material increased strongly as a function of P_{RF}. Probe measurements made at a radius between the Faraday shield and wall showed a linear increase with P_{RF}, from 0 to 220 kW, of both T_{eb} (from 9.2 to 19. eV) and n_{eb} (from 5.4×10^9 to 7.8×10^{10} cm^{-3}). The

increase in n_{eb} was attributed in part to oxygen desorption from the wall. With the steel limiter, the brightness of O-II was largest near the antenna and decreased with Ti gettering, leading to the conclusion that some RF power is absorbed near the antenna and releases O via CX neutral flux to the wall and the loss of trapped energetic ions near the antenna. When the carbon limiter was used, the O-II lines were also enhanced near the limiter, perhaps due to a chemical release process. This increase in oxygen was sufficiently large to limit the ICRF power which could be launched without causing a disruption. Hydrogen recycling at the limiter, as monitored by H_α+ D_α radiation, was reduced, perhaps by the rise in T_{eb}. More recently [97], successful ICRF heating with up to 800 kW has been achieved on JIPP T-IIU through the use of strong gas puffing and a rising current. The gas puff apparently curtails the sharp rise in T_{eb}, hence reducing impurity generation. The current rise suppresses the growth of an unstable $m = 2$ magnetohydrodynamic (MHD) mode, yielding better heating efficiencies and further reducing impurity levels. (Note: m is the poloidal, or θ, mode number, i.e., an $m = 2$ mode has a perturbation which varies as $e^{i2\theta}$.)

T-10, Moscow— Enhanced radiation losses due chiefly to metal impurities in the plasma center were also observed during ICRF experiments in the T-10 tokamak in Moscow [98]. With graphite limiters and steel antennas and walls, the concentration of carbon doubled while iron increased 10-fold. The impurity influx was attributed to enhanced ion sputtering through an elevated sheath potential, since both T_{eb} and impurity concentrations were seen to increase as the minority H component is reduced from 20% to 8%.

Macrotor, UCLA— A "distributed" ICRF antenna has been tested on Macrotor [99]. The antenna, which surrounds most of the plasma column, was designed in hopes of avoiding problems encountered there with a previous, tradi-

tional, localized ICRF antenna: prompt production of fast ions in the edge, increased electron flux to the Faraday shield, and increased plasma potential, which severely reduced particle confinement times via pumpout. The distributed antenna avoids creating the large fringing $\mathbf{E_{RF}}$ fields generated by small loop antennas (in spite of Faraday shields). These localized fields were believed responsible for the problems seen earlier, and for related impurity control difficulties. The new antenna yielded a well-defined $k_{||}$ spectrum with efficient wave production, coupling most of the RF power into waves propagating towards the plasma center. This would presumably reduce impurity production, although no explicit mention of impurity behavior was given. Tests on other localized antennas showed more non-resonant coupling to the plasma edge, generating a higher fast ion flux concentrated there.

The common thread in all of the experiments is a significant change in the SOL, but the extent to which this perturbation is judged to be localized to the antenna region (fringing $\mathbf{E_{RF}}$ field effects, loss of fast banana-trapped particles) or global (rise in $T_{eb}(r)$, changes in $n_{eb}(r)$, changes in recycling) seems to vary. Also, there is no clear agreement as to the relative importance of direct coupling to electrostatic waves in the plasma edge, causing elevated T_{eb} and/or fast ions, or of orbit or ripple losses of fast ions from the plasma core. The key to reducing impurity generation during ICRF or any auxiliary heating program requires an understanding of all possible channels, with appropriate measures taken to lessen the effects of those mechanisms which seem especially detrimental for a particular experimental configuration. It is likely that the various antenna designs, plasma edge characteristics, and choices of materials used in the above experiments have resulted in a variety of dominant impurity generation processes.

Theoretical treatment of the interactions between ICRF waves, the SOL plasma, and impurities is sparse [77], perhaps due to the lack of experimental

consensus as to the dominant impurity generating mechanism. Published work includes suggestions for compensating antennas [100] to null out edge resonance fields, waveguide launchers [101] to remove the problems of exposed antennas, a model for ionic sputtering through the reactive $\mathbf{E}_{RF}$ field near the antenna [102], and calculations of an enhanced inward diffusion rate for impurities during ICRF heating in low density, low current discharges [103].

This study does not answer all of the questions raised above, but does provide more pieces to the puzzle. While successful heating of the plasma was the primary focus of these experiments on Alcator C, rather than impurity control, the knowledge gained from the observations reported here does identify a problem area and suggests methods to minimize it or to study it further.

4.4 Alcator C Experimental Details

This thesis chiefly contains results from the first phase of the Alcator C ICRF heating program, conducted in 1984 [104]. Up to 400 kW of RF power at 180 MHz was delivered to the ICRF antenna, a full turn poloidal loop consisting of two pairs of half-turns which could be driven singly or together. The antenna Faraday shield was made of stainless steel and had an inner radius at r = 13.2 cm (see Figure 4.1). A molybdenum shield was briefly used, but it suffered weld fractures and was replaced prior to the high power RF tests. The target plasmas (a = 12.5 cm, R = 64 cm, $\overline{n_e}$ = 0.4–2.6$\times 10^{14}$ cm^{-3}, I_P = 130–460 kA, B_T = 6–12 T, T_{eo} = 900–3000 eV) had two graphite limiters separated toroidally by 180°. The antenna port was located 60° from the nearest limiter. ICRF power was launched in regimes of hydrogen second harmonic heating at $B_T \approx 6$ T, of hydrogen minority (0.5–3.0%) heating in a deuterium plasma at $B_T \approx 12$ T, and under non-resonant conditions ($B_T \approx$ 7–8 T in H, $B_T \approx$ 8–10 T in D). RF pulse lengths were typically 20–50 ms, ranging as high

as 70 ms. Significant heating was obtained for the hydrogen minority regime, with a rise in T_i of up to 500 eV at 400 kW RF (Figure 4.4). These high power shots often underwent an electron density increase (typically from 1.2 to 1.9×10^{14} cm^{-3}) as well as a rise in $Z_{\rm eff}$ (typically from 1.5 to 2.5–3.0). Results from the hydrogen second harmonic heating were ambiguous, with occasional rises in T_i of up to 100 eV for $P_{\rm RF}$ up to 200 kW.

During the ICRF experiments, T_e was measured from X-ray spectra and Thomson scattering, $n_e(r)$ was monitored by a 4-chord FIR laser interferometer, and $Z_{\rm eff}$ was deduced from visible bremsstrahlung emission. A neutral CX analyzer measured T_i and monitored fast ion tail formation. A single Langmuir probe with variable radial position was employed during some discharges to record the edge temperature and density profiles, $T_{eb}(r)$ and $n_{eb}(r)$. Soft X-ray emission (1–8 keV) was monitored by a PIN diode array with Be filters, while the X-ray PHA spectra (10–50 keV) were obtained with a HgI_2 detector. The absolutely calibrated 2.2 meter grazing incidence time-resolving vacuum ultra-violet (VUV) spectrograph monitored impurity line radiation. The instrument was described in detail in Chapter 2. The locations of the antenna and diagnostics are shown schematically in Figure 4.5. Neither the VUV spectrograph nor any of the other diagnostics was located at the toroidal position of the ICRF antenna.

4.5 Impurity Influx During ICRF Heating at Alcator C

The overall plasma cleanliness, as measured by $Z_{\rm eff}$, deteriorated as $P_{\rm RF}$ was raised. The change in impurity content, $\Delta Z_{\rm eff}$, is plotted versus $P_{\rm RF}$ in Figure 4.6, representing a wide variety of plasma conditions. Although there is a fair amount of scatter in the data, partially due to the variety of shots, $Z_{\rm eff}$ clearly increases with increasing $P_{\rm RF}$. The trend is shown more clearly by the increase with $P_{\rm RF}$ of the

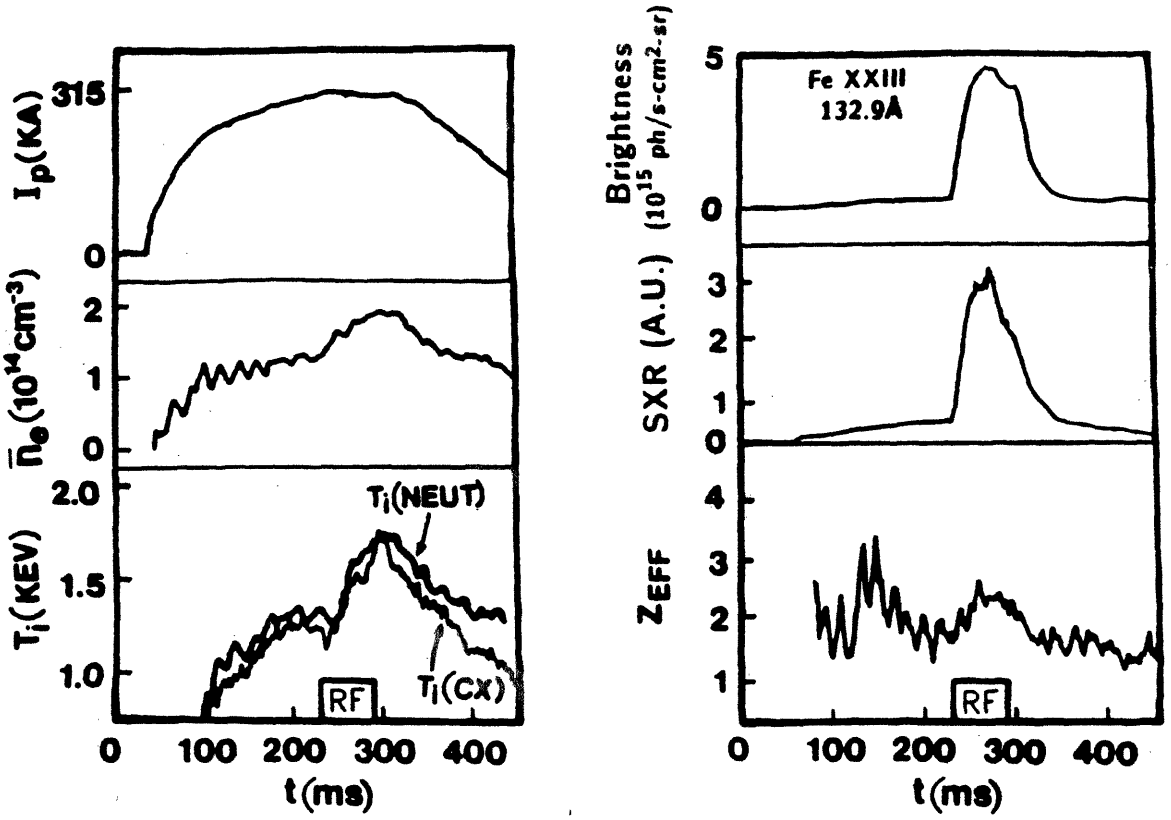

Figure 4.4 ICRF heating of H minority ions ($\sim$ 1.5–3.0%) in a D plasma. $P_{RF} \approx 380$ kW. Shown are plasma current I_P, average density $\overline{n_e}$, ion temperature of deuterium component T_i, brightness of Fe XXIII 132.87 Å resonance line (a central ionization state), soft X-ray emission (SXR, 1–8 KeV), and Z_{eff}.

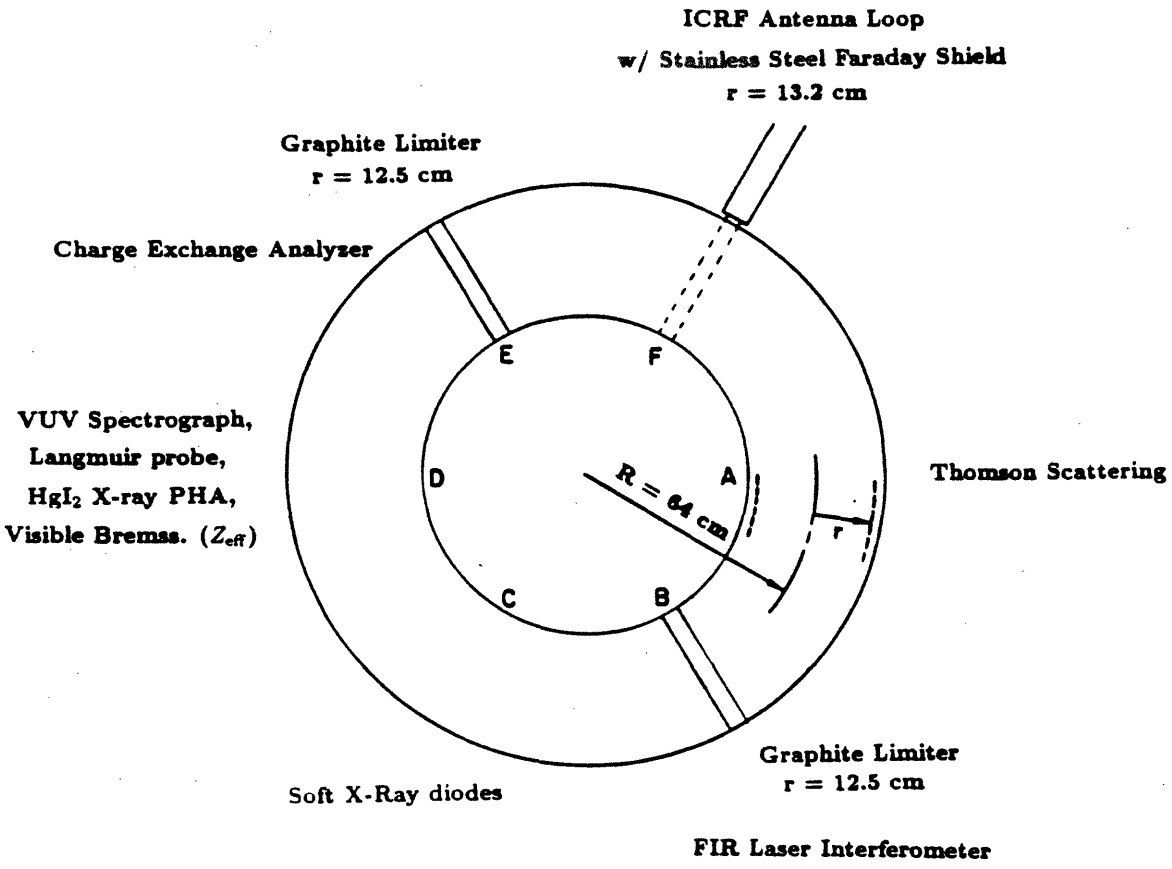

Figure 4.5 Experimental layout, as viewed from above Alcator C, showing the locations of the ICRF antenna and various diagnostics.

iron source rate as derived from spectroscopic measurements (see below). There is no clear dependence of $\Delta Z_{\rm eff}$ on resonance conditions or working gas, although all of the points with $P_{\rm RF} > 250$ kW are from D plasmas with H minority. Pre-RF values of $Z_{\rm eff}$ ranged from 1.1 to 2.2.

Figure 4.7 shows a typical VUV spectrum before and just after a 380 kW ICRF heating pulse. This spectral evolution is also presented in the surface representation format, for the same shot, in Figure 3.18. All VUV spectra utilized in the ICRF analysis were obtained by viewing horizontally along a central chord of the plasma. The large rise in metal impurity concentrations is exhibited by the brightness of the Fe-XXIII resonance line, 132.87 Å, plotted versus time for the same discharge in Figure 4.3. The behavior of the C-VI line, on the other hand, reveals the relatively small increase in low-Z impurity levels during the ICRF pulse.

The typical impurity content of the Alcator C plasmas before and during a series of high power (350–400 kW) ICRF experiments in the hydrogen minority regime at $B_T \approx 12$ T was analyzed by comparing several measured line brightnesses from each major impurity element to those simulated by an impurity transport code. Line brightnesses are obtained by fitting an instrumental response function to each viewed line, such that the summation of individual lines matches the observed spectrum. The impurity transport code used is a modified version of a one-dimensional numerical code developed by Marmar [59,60]. A good general description of such codes is given by Hulse [105]. Because particle motion is rapid along the magnetic field lines, toroidal and poloidal symmetry are assumed. Radial motion across field lines is much slower, so the code only calculates in this dimension. Cylindrical geometry is used, which for this case is a fairly good approximation to the true toroidal geometry. The code takes a given impurity source rate S_z at the plasma edge and traces the evolution due to radial diffusion and atomic processes (ioniza-

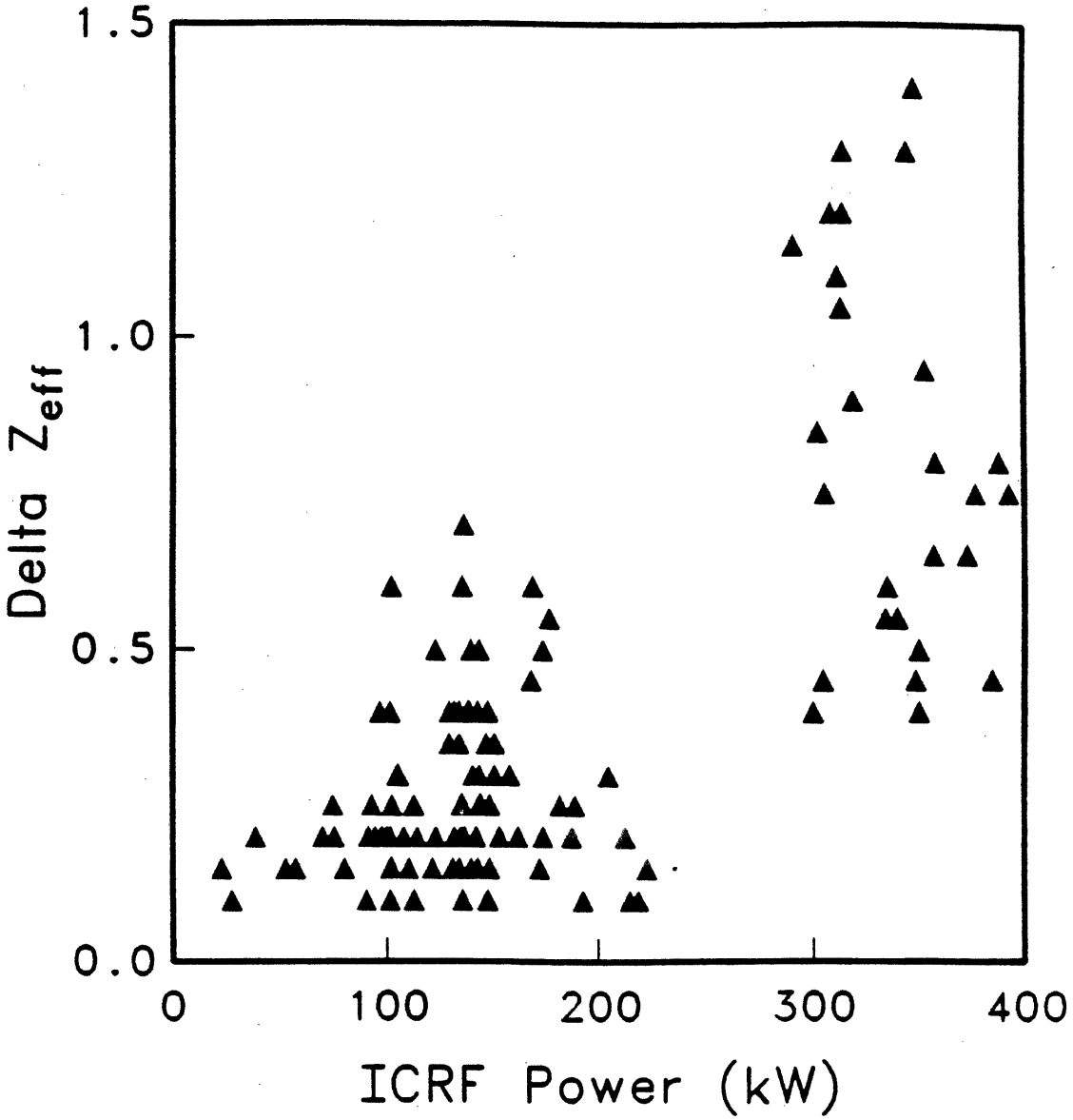

Figure 4.6 Change in Z_{eff} during ICRF pulse vs. injected RF power. Data are included for a wide variety of plasma conditions.

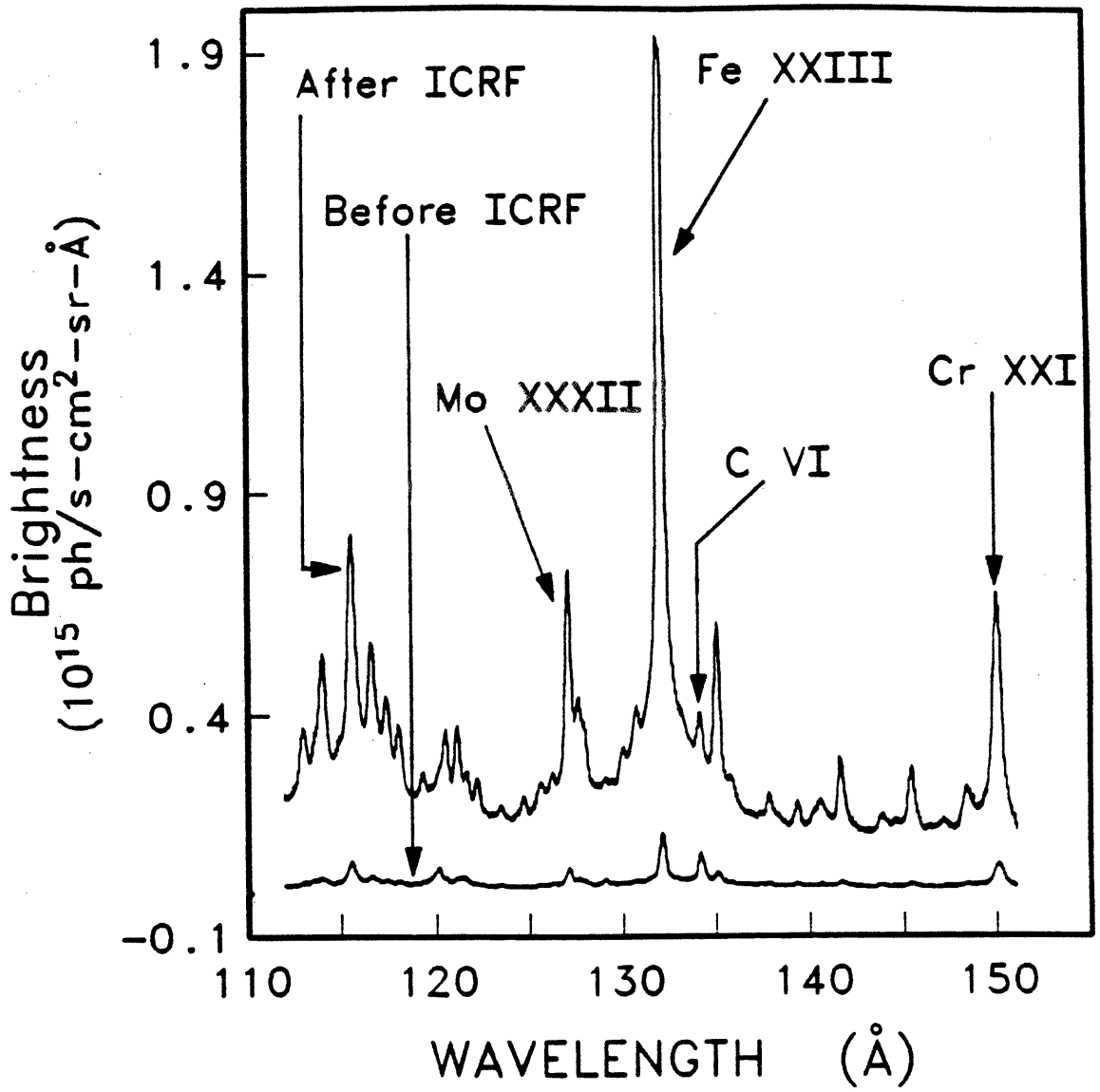

Figure 4.7 Evolution of VUV emission, 110–150 Å, during the discharge presented in Fig. 4.3, showing spectra taken before and just after the ICRF pulse. Impurity lines shown are Mo XXXII (127.81 Å), Fe XXIII (132.87 Å), C VI (134.94 Å and 33.74 Å in 4th order), and Cr XXI (149.90 Å). The Cr XXI line is blended with O VI (150.1 Å), which is dominant before the ICRF pulse.

tion, radiative and dielectronic recombination, and excitation). The evolution of the various ionization state densities is described by a system of coupled partial differential equations,

$$\frac{\partial n_j}{\partial t} = -\frac{1}{r}\frac{\partial}{\partial r}(r\Gamma_j) + n_e[S_{j-1}n_{j-1} - S_j n_j + \alpha_j n_{j+1} - \alpha_{j-1}n_j]$$

$$j = 1, \ldots, Z \qquad 4.11$$

where n_j is the density of the j^{th} ionization state, Γ_j is the flux, S_j is the ionization rate coefficient, and α_j is the recombination rate coefficient (radiative and dielectronic). The flux is usually taken to be of the form

$$\Gamma_j = -D\frac{\partial n_j}{\partial r} + v(r)n_j \qquad 4.12$$

where D is the diffusion coefficient and $v(r) = v_o r/a$ is a convection velocity which is usually found to be inward. This diffusion model is appropriate for simple random-walk, spreading diffusion with superimposed convection. The code solves the system of equations explicitly, starting from an initial condition. This is usually taken to be a narrow profile of singly ionized ions at the outer edge of the plasma, corresponding to a single injection of impurities (delta function in time). This situation describes the single injection of trace impurities by the laser blow-off technique [59], and the response obtained may be considered a Green's function solution, since the equations are linear in the n_j's. This solution is integrated over time in order to obtain the steady state response for a continuous impurity source at the edge of the plasma.

The formulas used for all atomic processes (ionization, radiative and dielectronic recombination, and excitation) are generally the same as those used by Breton *et al.* [106], incorporating earlier work such as the ionization rate formulas of Lotz [107,108]. Atomic data such as oscillator strengths were obtained from such tables

as the one by Fuhr *et al.* [109]. The transport equations yield the density profiles of each ionization state $n_j(r,t)$. The emissivity of selected transition lines is calculated in the coronal approximation, i.e., collisional electron excitation rates from the ground state of density n_j are assumed to populate the excited states, which then undergo radiative decay. Oscillator strengths have been adjusted for some ions of iron to agree with the calculations of Mann [110]. Emissivity profiles and chordal brightnesses are calculated as a function of time for these lines. Given the impurity transport coefficients, the plasma temperature and density profiles, and the measured impurity emission, the total impurity concentration $n_z(r)$ and source rate S_z can be deduced.

The transport model used is based on impurity confinement times measured by laser blow-off injection of trace amounts of non-intrinsic impurities into purely ohmic discharges [60]. It was found that the impurity confinement times were much shorter than those predicted by neo-classical transport theory [111], implying an anomalously large impurity diffusion coefficient. The observations were well matched by including only anomalous spreading diffusion, with the flux given by

$$\Gamma_j = -D\frac{\partial n_j}{\partial r} \tag{4.13}$$

where n_j is the density of the j-th ionization state. D is an empirically determined, spatially constant, impurity diffusion coefficient [60],

$$D(\mathrm{cm}^2/\mathrm{sec}) = 102\ \frac{a_l q_l (Z_{\mathrm{bg}}/Z_{\mathrm{eff}})}{m_{\mathrm{bg}}} \tag{4.14}$$

where a_l is the minor radius (cm), q_l is the safety factor at the limiter (defined in Eqn. 5.5), and m_{bg} and Z_{bg} are the mass and charge of the background gas in atomic units. Inward convection was not included because the impurity concentrations derived from brightness measurements are not very sensitive to that parameter, and because it was assumed to be small anyway. This can lead to uncertainties in the source rate, however, as discussed in Chapter 5.

To check if this model adequately described impurity transport during ICRF heated discharges, laser blow-off injections were conducted during the RF pulse. The transport was found to be similar to that of OH heated discharges. This lack of significant differences in impurity transport between ICRF heated and purely ohmic discharges was also reported on TFR, along with the conclusion that the capture of injected impurities from the scrape off layer to the region inside the limiter was unaffected by ICRF heating, despite measured perturbations to the SOL plasma during the ICRF pulse [112].

Table 4.1 presents typical concentrations of the major impurities both before and just after high power (350–400 kW) ICRF pulses in the minority heating regime. The concentrations are estimated to be accurate to within ±50%, based on uncertainties in the measured brightnesses (instrument sensitivity), the transport code, and the shot-to-shot variations in plasma and impurity parameters. Calculated contributions to the central value of $Z_{\rm eff}$ are also given; the total agrees well with the measured values deduced from visible bremsstrahlung. The modest fractional increases in carbon and oxygen levels are dwarfed by the fractional increases in metallic impurities, especially iron and chromium (the main constituents of the stainless steel Faraday shield and walls). Iron supplants carbon as the dominant non-hydrogen component of $Z_{\rm eff}$. The electron density rose typically 40% during these highest power RF pulses; but this increase is not fully due to the electrons from the increased impurity content. As no reproducible change in the edge density was observed (see Chapter 5), this increase in n_e may be due to some change in bulk plasma transport.

Total radiated power, estimated using densities determined here and the calculations of Post *et al.* [113], increased by an amount comparable to the injected RF power, with the largest increase due to iron. The fact that significant ion heat-

Table 4.1

Impurity Concentrations* Before and After ICRF

350–400 kW, 50 msec pulse into D plasma with H minority

	Pre-RF	End of RF
Central Impurity Densities (cm^{-3})		
Carbon	3.1×10^{12}	3.6×10^{12}
Oxygen	1.6×10^{11}	3.0×10^{11}
Chromium	1.1×10^{10}	1.2×10^{11}
Iron	3.5×10^{10}	4.0×10^{11}
Molybdenum	1.7×10^{9}	1.2×10^{10}
Central ($Z_{eff} - 1$) contributions		
Carbon	0.42	0.36
Oxygen	0.04	0.06
Chromium	0.02	0.24
Iron	0.09	0.70
Molybdenum	0.01	0.05
Total	0.58	1.41
Total Z_{eff}	1.58	2.41
Measured Z_{eff} (vis. brems.)	1.6 $\pm$0.2	2.4 $\pm$0.3
Central Electron Density ($10^{14}cm^{-3}$)	2.2 ± 0.4	3.0 ± 0.5
Total Radiated Power (kW)	$\sim$ 25–35	$\sim$300–400
Input Power (kW):		
Ohmic	$\sim$460	$\sim$640
ICRF	0	$\sim$350
Total	$\sim$460	$\sim$990

* Uncertainties in impurity concentrations are approximately $\pm$50%

ing was observed during these shots ($\Delta T_i \approx 500$ eV, Figure 4.3), coupled with the observation that T_e remained approximately constant at ~ 2.1 keV, indicates that this estimate of radiated power is somewhat high.

The transport code predicts that, as long as the background plasma in not changing, the brightness of Fe-IX (171 Å), an edge state, should closely track the Fe influx rate, S_{Fe}. Therefore, a sudden increase in the brightness of this line implies that S_{Fe} has increased to a new steady state value. Such behavior is indeed seen during a number of ICRF pulses (Figure 4.8), consistent with a rapid (2–5 ms) increase in S_{Fe} coincident with the RF pulse. The temporal behavior of highly ionized Fe lines (e.g. Fe-XXIII, Figure 4.3) is generally also in agreement with this model. It must be noted, however, that a more gradual rise in the Fe-IX line is sometimes seen, perhaps indicative of an impurity self-sputtering contribution with its inherent positive feedback. This behavior is seen in Figure 4.9, in which the ICRF power was on for 30 ms, off for 10 ms, and then back on for 10 ms (due to an automatic restart after a protective shutdown). Note that the Fe-IX line rises continuously during the initial 30 ms period, but falls rapidly (within the 4 ms time resolution) during the shutdown. Once power is restored, the brightness immediately returns to its prior value. This is consistent with an increasing self-sputtering (Fe $\rightarrow$ Fe) contribution which grows as the amount of iron in the edge plasma increases. The quick recovery would be due to the large iron concentration already present in the edge at the time of the restart.

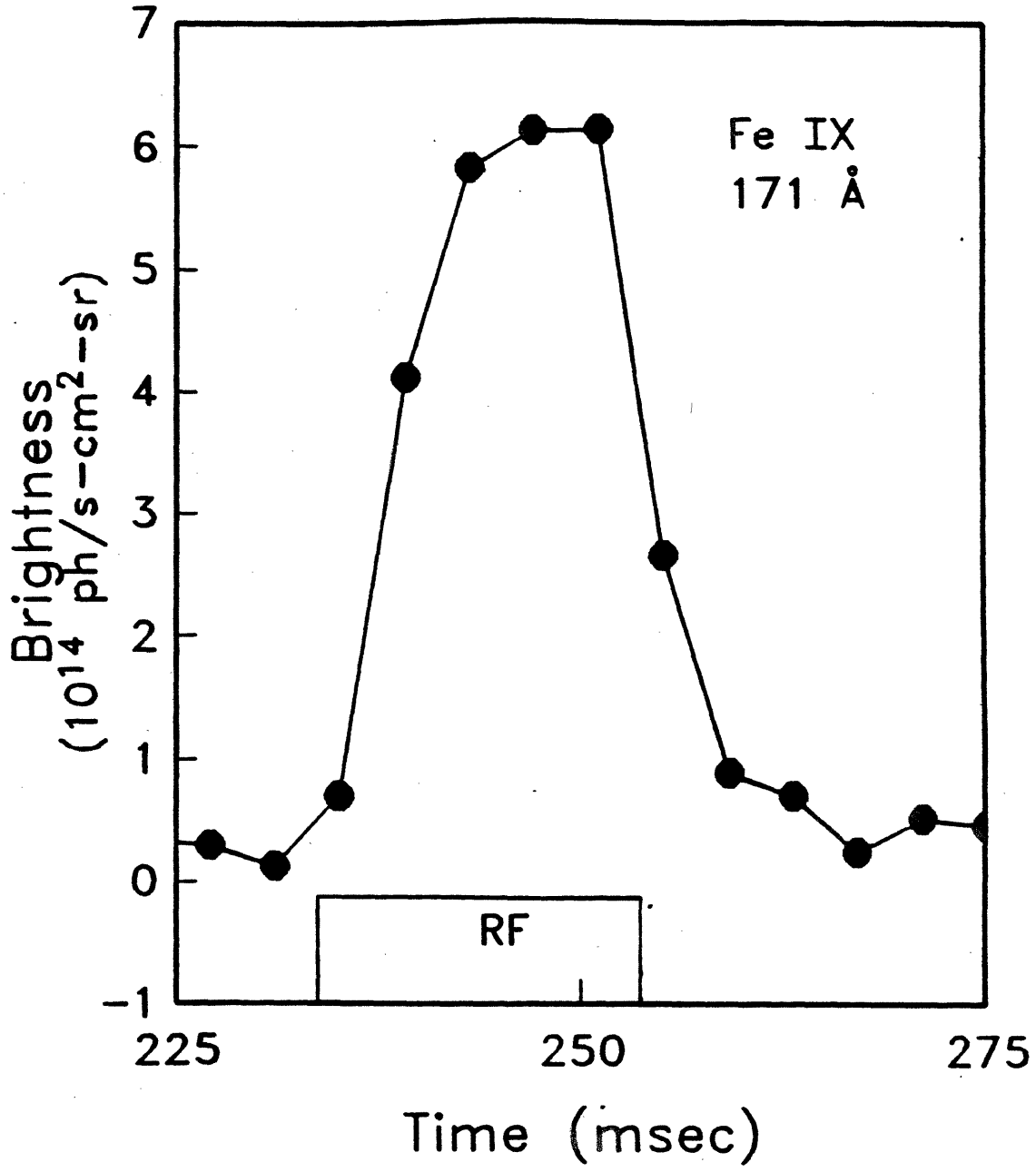

Figure 4.8 Evolution of the brightness of the Fe IX resonance line (171.09 Å) during ICRF, showing rapid rise ($P_{RF} \approx 350$ kW, minority hydrogen regime).

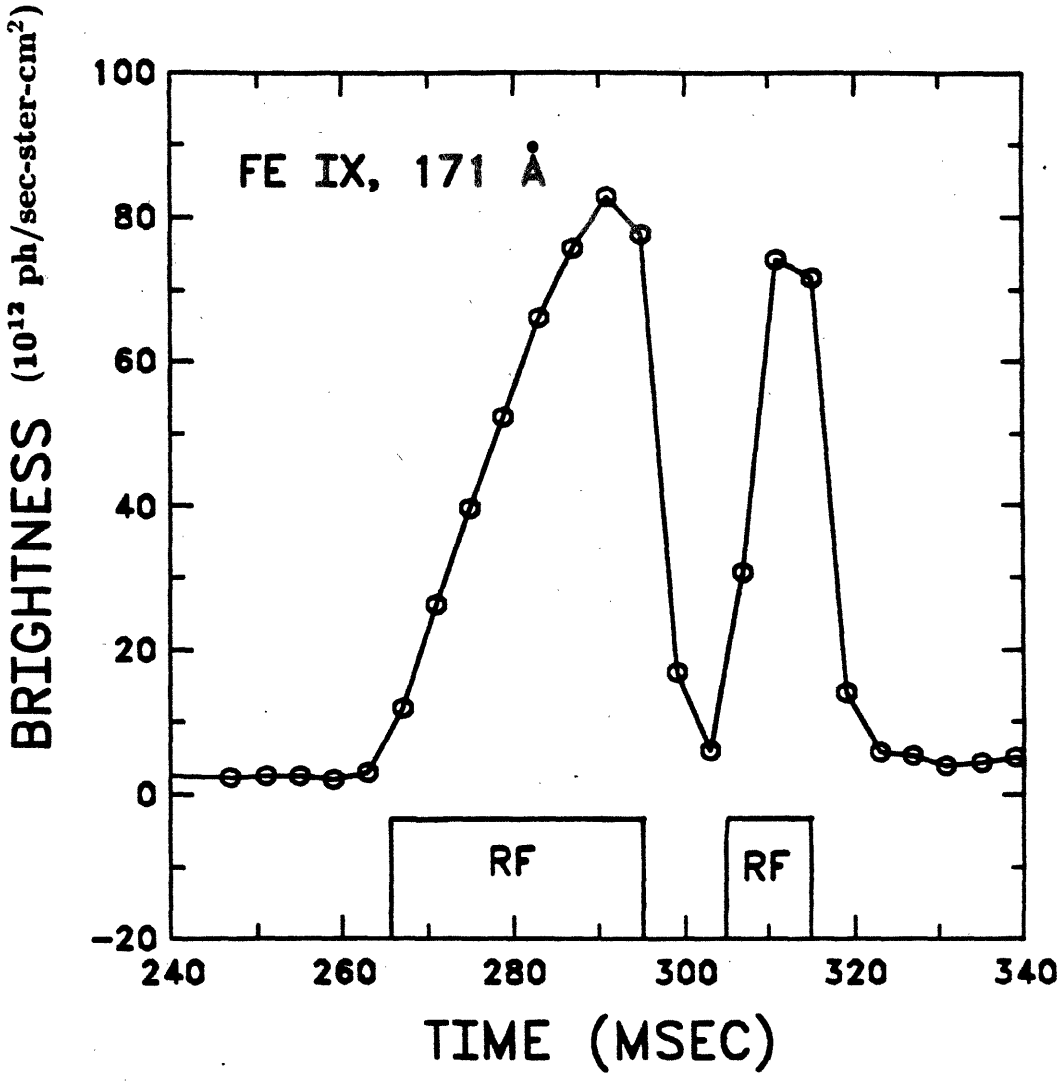

Figure 4.9 Evolution of the brightness of the Fe IX resonance line (171.09 Å) during ICRF, showing gradual rise ($P_{RF} \approx 350$ kW, minority hydrogen regime). The ICRF power was interrupted for 10 ms due to a protective shutdown of the power supply.

Chapter 5

Sources of ICRF Generated Impurities

In this chapter, the principal processes which could be responsible for the enhanced impurity influx during ICRF heating on Alcator C are examined, and sputtering by the thermal edge ions is identified as the most likely cause. Section 5.1 is concerned with the possible release mechanisms involved, while section 5.2 deals with the exposed surfaces from which impurities may be generated. Results from surface analysis of the graphite limiter are presented, showing significant metal contamination. In order to compare the impurity influx with various plasma and RF parameters, data from many shots were compiled and analyzed. The edge source rate of iron (the dominant metal impurity), was selected as the variable best representing impurity generation. This parameter, S_{Fe}, was deduced from measured iron line brightnesses through use of the transport code. Results of this survey (section 5.3), along with correlations with edge probe measurements and other observations (section 5.4) strongly suggest that physical sputtering of both the limiters and Faraday shields through enhanced sheath potentials (due to elevated edge temperatures) is the primary cause of impurity release. Section 5.5 discusses the edge erosion code, the results of which are consistent with the above conclusion. A discussion of the Alcator C results and conclusions follows in section 5.6, with an attempt to place them in the context of the other tokamak ICRF experiments.

5.1 Physical Processes

Metal impurity ions can be liberated from edge structures by the following mechanisms [114]: arcing, evaporation, flaking or blistering, and sputtering due to neutrals, working gas ions, or impurity ions. Arcing within the antenna structure or between the antenna and wall is judged to be unimportant in these experiments because: 1) the iron influx appeared to be steady and reproducible during the RF pulse, unlike the erratic or intermittent behavior characteristic of such arcing; 2) no threshold value of P_{RF} (and hence $V_{antenna}$) was seen; 3) no dependence on resonance conditions (which also affect the loading and thus $V_{antenna}$) was seen; 4) no clear difference in impurity production was seen between the top half-loop and the bottom half-loop antennas, presumably eliminating arcing due to positioning errors; 5) the circuits driving the RF antennas shut down rapidly in the event of an arc detection, as manifested by a sudden increase in the reflected power. However, arcing may explain the few shots in which the iron level rose anomalously rapidly, leading to a disruption. A small melted spot found later at the base of one of the antenna sections is in fact attributed to arcing, but it is extremely unlikely that these large arcs are the typical mechanism for impurity generation. The possibility of many small unipolar arcs between the antenna structure and the plasma sheath cannot be completely excluded. A steady production of such short-lived arcs, yielding neutral impurity atoms with energy in the 10 eV range [115], might produce the observed impurity influxes during ICRF heating. This phenomenon would be undetected by the arc detector or other diagnostics. However, visual inspection with a 10x-power eyepiece revealed no tiny pits or tracks, characteristic of such arcs, on the antenna or Faraday shield. Thus, small unipolar arcs are probably not the major contributor.

Flaking and blistering are also deemed unlikely due to their erratic nature. Evaporation is also considered an improbable explanation for the enhanced impurity

influx during the ICRF pulse. The erosion code discussed below predicts a negligibly small contribution from this process, since the calculated heat load to the edge structures is too small and brief to cause major evaporation, unless it was for some reason very localized. As there is no cause to suspect localized heating in these plasmas, this mechanism is not believed to play a major role. Furthermore, evaporative processes generally result from an extended flux of extra heat to a localized area, and would exhibit a steadily increasing yield as the temperature of the structures involved rises towards the melting point. The temporal dependence of the impurity rise on Alcator C, however, more closely resembled a sudden and large incremental rise in impurity production, as discussed above. Evaporation could be more of a concern in future ICRF heated reactors, with higher power levels and long pulses or continuous operation.

This leaves physical sputtering of some kind as the most likely mechanism generating the enhanced impurity influx. Sputtering results from an ion or neutral striking a surface and releasing an atom from the surface material. It is essentially a momentum transfer process, which effectively eliminates electrons from consideration for the release of impurity atoms. Neutrals impact with their ordinary kinetic energy, but bulk or impurity ions are accelerated through the sheath potential which forms at any plasma-surface boundary. This sheath potential, Φ_{sh}, is usually given by $\Phi_{sh} \approx 3.5T_e$. In the absence of a good Faraday shield, however, plasma rectification of the antenna RF electric fields can cause a dc value of Φ_{sh} approaching the antenna voltage. Thus thermal ions of charge Z_i arrive at the surface with an energy $E_i = T_i + Z_i\Phi_{sh}$. Suprathermal hydrogenic ion tails can be created by ICRF; these particles can cause significant sputtering if they reach a surface before slowing down by collisions with the bulk plasma. In order for sputtering to take place, enough energy must be transferred from the incident ion or neutral to the lattice atoms to

allow a surface atom to receive sufficient energy to exceed the binding energy. This results in threshold energies; the theoretical threshold value for hydrogen incident on iron is 68 eV for normal incidence collisions [114]. The sputtering coefficient for this case is plotted versus proton impact energy in Figure 5.1. Sputtering yields (atoms released per incident particle) therefore have a very steep dependence on the impact energy of the arriving ion or neutral in the regime corresponding to typical SOL temperatures. Sputtering yields for impurity ions can be orders of magnitude higher due to the higher mass. This can lead to runaway impurity production if the self-sputtering yield exceeds unity. It remains to ascertain which structures (limiters, antennas, or walls) are the main impurity sources, and which particles (thermal or fast ions, impurity ions, or neutrals) are doing most of the sputtering, and under what conditions this process is most pronounced (scalings). These questions are addressed below.

5.2 Exposed Surfaces

The limiter, being in close contact with the plasma, is always suspect when impurity levels rise. Graphite limiters are known to become contaminated with surface deposits of metals after a period of exposure to tokamak plasmas with metal impurities [116-118]. Subsequent to the ICRF experiments, a graphite block from one of the Alcator C limiters was analyzed for surface composition via proton induced X-ray emission (PIXE), using 4.5 MeV protons. The results, shown in Figure 5.2, revealed metal deposits with iron surface concentrations as high as 2.4×10^{17} atoms/cm^2, corresponding to an average thickness of roughly 100 monolayers. Also detected were smaller concentrations of molybdenum, chromium, nickel, and vanadium. The vanadium is believed to be an intrinsic impurity in the graphite, since during these experiments it was not otherwise knowingly introduced into the vessel.

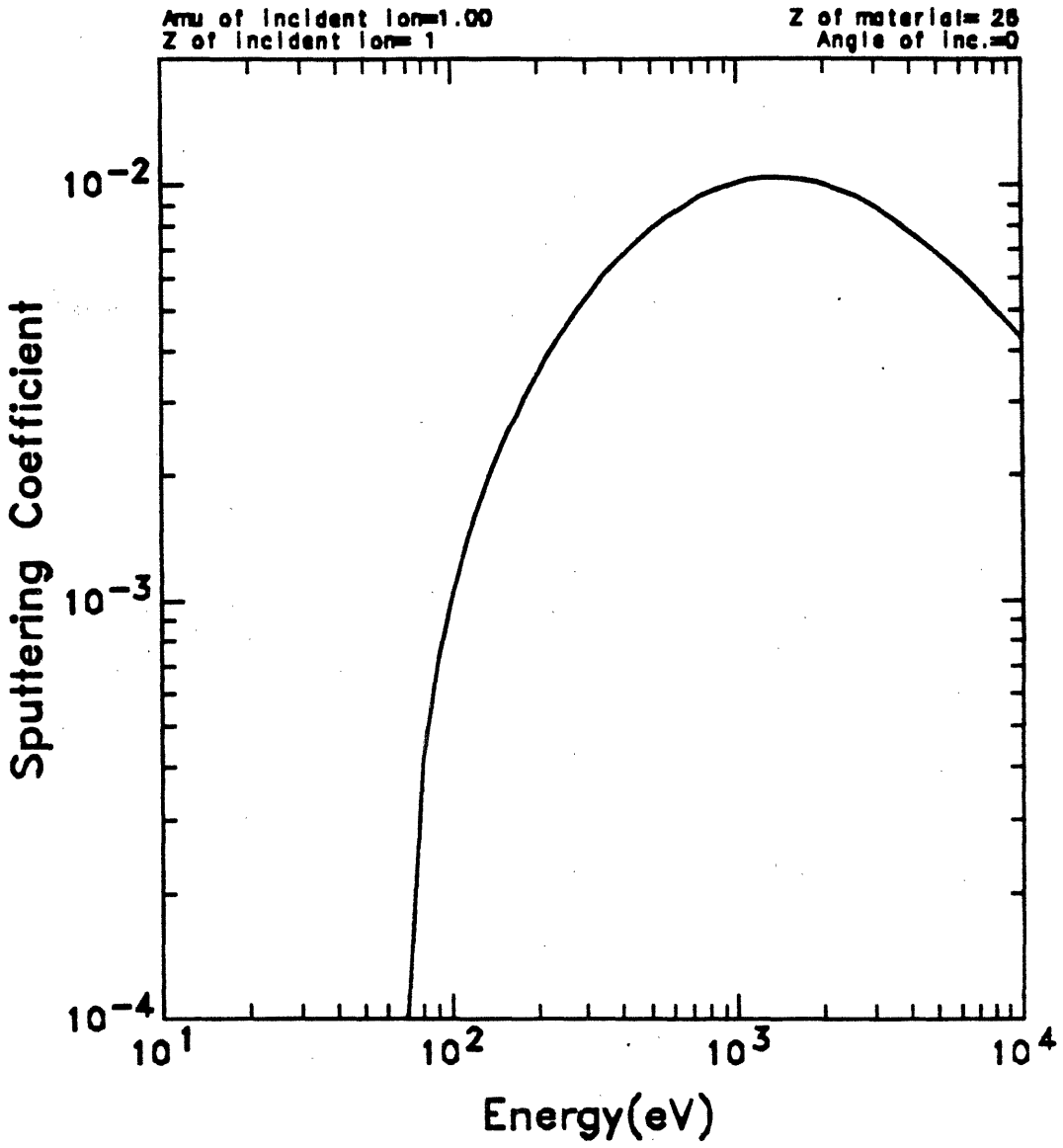

Figure 5.1 Sputtering coefficient for hydrogen ions striking iron at normal incidence (courtesy of B. Lipschultz).

The impurity deposition profiles are peaked at the sides of the limiter, with minima at the center, where the plasma flux is tangent to the surface. This effect has been seen in previous studies of other tokamak limiters [119,120]. Electron microscopy of contaminated graphite limiters from other tokamaks [117,120] indicates that the metal deposits are generally in the form of droplets, with dimensions of up to 2 μm, residing on a very rough graphite surface with topographical features of the order of several microns. It is assumed that the surface of the Alcator C graphite limiter tile is similarly covered with metal droplets, as opposed to a uniform metal film, many monolayers thick and covering the carbon.

The contaminated limiters are believed to be the dominant source of metal impurities during the ohmic phase of the discharge. Results from the initial operations of JET indicated that contaminated graphite limiters were in fact the dominant source of metal impurities during ohmic discharges, even though Auger spectroscopy revealed the limiter surface still to be $\sim$ 90% carbon [121,122]. Although the metal concentrations observed on the Alcator C limiters are sufficient to allow for the amount of metallic impurity influx seen during ICRF heating pulses, it is very difficult to reconcile the dramatic increase in iron with the small change in carbon influx if the limiters are the source for both. No reasonable combination of changes in $T_e(r = a)$ and $n_e(r = a)$ could produce this effect in the erosion code simulations described below. This indicates that the main iron source during the RF pulse was *not* the contaminated limiters, but some other structure (the antenna Faraday shield, as seen below).

Another argument concerns the presence of vanadium revealed by the PIXE analysis of the limiter block surface (Figure 5.2). Believed to be an intrinsic impurity in the graphite, it has a surface concentration only slightly less than that of nickel (present at a level of $\sim$ 9% in the 304 stainless steel used in the Faraday shield).

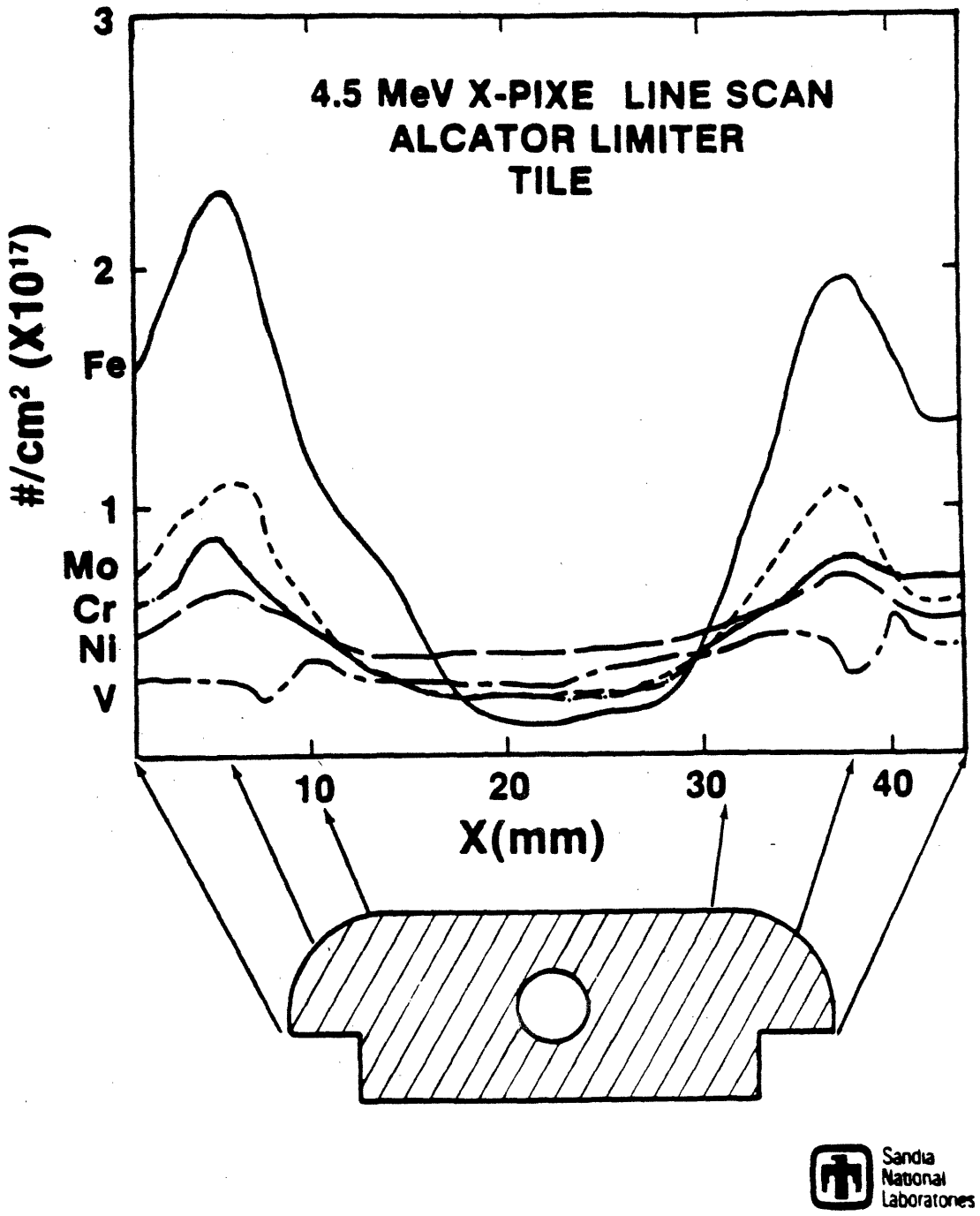

Figure 5.2 PIXE scan of Alcator C graphite limiter tile, showing metal surface contamination.

While the resonance lines of highly ionized nickel become clearly visible during the RF pulse, similar lines from isoelectronic states of vanadium could not be detected. This might imply that the limiters are not the main source of nickel (or iron, etc.) during the RF pulse. It must be noted, however, that an alternative explanation exists for this vanadium result. Given that the PIXE analysis sampled a layer a few microns thick, a relatively low concentration of vanadium, distributed uniformly throughout the sampled volume, could give the same signal as a high concentration of nickel, localizeded at the surface. In this case, the nickel would be much more susceptible to surface erosion processes during the RF pulse.

Other structures exposed to the edge plasma during these experiments include the stainless steel antenna Faraday shield at $r = 13.2$ cm, stainless supports for the graphite limiter blocks (exposed for $r \geq 14.5$ cm), secondary molybdenum limiters at 16.5 cm, stainless virtual limiters at 18.0 cm, and the stainless bellows wall at 19.2 cm. The Faraday shield, situated closer to the main plasma than any other structure than the limiter, must now be considered the prime candidate for the source of the metal influx during ICRF. The rapid falloff of plasma density with radial distance ($\lambda_n \approx 3$ mm, where λ_n is defined in Eqn. 4.1), along with a somewhat slower decrease in temperature, tends to diminish the probability that plasma sputtering of the more recessed and protected structures is the dominant source. However, sputtering by CX neutrals could be involved for the recessed structures, especially the wall with its large surface area, since the CX flux out of the main plasma is only diminished by a $1/r$ geometric factor.

5.3 Database Survey

In order to gain insight into the impurity production mechanism, the scaling of the iron influx with various plasma and RF parameters was studied. For a limited

group of similar discharges with similar RF pulse lengths, the change in iron influx, ΔS_{Fe}, may be taken to be proportional to the change in brightness, ΔB, of a given iron line. However, the variety of plasma parameters employed in these experiments led to such a broad range of temperature profiles, density profiles, and transport conditions, that in general such a simple comparison of line brightnesses can be misleading. The total impurity concentration in the plasma for a given source rate at the edge is dependent on the transport coefficients, and both the ionization balance and the excitation rates for the observed lines are strongly dependent on the electron temperature and, to a lesser extent, the electron density.

A summary of the variety of plasma and RF parameters encountered in this database is given below:

Magnetic Field:	6—12 Tesla
Plasma Current	145—460 kA
T_{eo}	750—2300 eV
$\overline{n_e}$	0.8—2.5×10^{14} cm^{-3}
Density profile factor, m	0.66-1.25
Safety factor q	2.4—4.8
Initial Z_{eff}	1.1—1.8
Impurity diffusion coefficient D	1000—5550 cm^2/sec
Working gas	Hydrogen, Deuterium

In addition, the spectrometer monitored several different regions of the VUV spectrum during the course of these ICRF heating experiments, with a large number of shots including the following bright lines: a) the Fe-XVI resonance line ($3s - 3p$) at 335.407 Å, b) the Fe-XXIII resonance line ($2s^2 - 2s2p$) at 132.87 Å and the nearby Fe-XXII line ($2s^22p - 2s2p^2$) at 135.78 Å, c) the same Fe-XXIII line in second order at 265.74 Å, and d) a smaller number of shots viewing the Fe-XXIV

resonance line ($2s-2p$) at 192.02 Å. The second order Fe-XXIII line was normalized to the first order brightness for a series of similar plasma discharges. Many other lines were viewed, of course, but these were chosen for the database study due to the amount of data on each and the quality of the atomic data (oscillator strengths and branching ratios) for the resonance lines. These lines were among the brightest iron lines observed. To compare the iron influx based on lines of different transitions and different ionization states, one must rely on the brightnesses calculated in the impurity code.

The impurity transport code was originally used to study impurity particle confinement times, based on the time response of emission lines during the injection of non-intrinsic impurities. This code also served quite well to deduce impurity concentrations based on measured brightnesses. Neither of these functions is very sensitive to the manner in which the initial impurity distribution is handled at the edge. However, the connection of measured line brightnesses to the absolute impurity source rate at the edge is sensitive to the initial conditions, and to the care with which the calculations are handled in the edge region. For this reason, a modified version of the transport code was developed to reflect this change in emphasis. Both a finer spatial grid at the edge and a finer time step (determined numerically by the characteristic time scales of the ionization balance and diffusion processes) were employed during the early phase of the calculation. Also, the program calculates the initial ionization profile of neutral impurity ions entering the edge plasma with a characteristic energy for sputtered particles. This initial profile of singly charged impurity ions was generally narrow, decaying to zero about a centimeter inside the limiter radius. A hard boundary condition at the limiter radius was retained from the original code, specifying that the impurity density be always zero for $r \geq a$.

The modified impurity transport code was run for each set of plasma param-

eters used in order to arrive at a pre-RF value and an RF value for the iron influx in each discharge. The change in influx,

$$\Delta\, S_{\rm Fe} = S_{\rm Fe}^{RF} - S_{\rm Fe}^{Pre\ RF} \qquad 5.1$$

was then used to compare the impurity production due to ICRF power launched into different discharges. Within each set, individual shots were adjusted via first order corrections for minor variations in B_T, I_P, $Z_{\rm eff}$, n_e , and RF pulse length. The effect of finite integration times (typically 4–8 ms/frame) on dynamic spectra was taken into account by calculating a maximum and minimum value of the deduced iron influx during RF, rather than a single number.

For example, for a particular shot, brightnesses $B_m^{\rm Pre}$ and $B_m^{\rm RF}$ of the 133 Å Fe-XXIII line before and just after a 40 ms ICRF pulse were measured, taken with a spectral frame integration period of 4 ms. The transport code predicts a brightness $B_c(t)$ for the 133 Å line, given a source term S_o (atoms/sec) and plasma parameters similar to those of this discharge. The source is assumed constant during the 50 ms nominal RF pulse and zero afterwards. This is effected in the code by integrating the Green's function response for the first 50 ms, giving the response to a constant source turned on at $t = 0$. At 50 ms the time-integrated profiles (i.e., profiles for the step-function source) are used as the initial conditions to follow the behavior after the source is turned off (dropped instantaneously to zero). This yields a predicted brightness versus time curve $B_c(t)$ which rises for 50 ms, then decays away. Figure 5.3 shows the code simulated curves for Fe-IX (edge ionization state, fast response), Fe-XVI, Fe-XX, and Fe-XXIV (central ionization state, slowest time response) for a simulation with diffusion coefficient D = 1400 cm^2/sec and T_{eo} = 2200 eV. By sliding a 4 ms average across a plot of $B_c(t)$, one obtains the maximum and minimum brightness values for the particular emission line that could be expected for a 40 ms RF pulse. The brightness is assumed to decay away for $t > 40$ ms in

the same manner as the code shows for $t > 50$ ms. By running the simulation for a longer time ($t > 80$ ms, i.e several particle confinement times) and without a source cut-off, one can obtain the steady state solutions $B_c(\infty)$. First order corrections for this individual shot are made, assuming that the brightness B_c is proportional to $n_e(S/D)$ for small ($< 10\%$) variations of electron density n_e and impurity diffusion coefficient D (Eqn. 4.14) about the values used in the code for the set of discharges to which the particular shot belongs. This procedure yields a correction factor f, given by:

$$f = \frac{n_e}{n_{eo}} \frac{B_\phi}{B_{\phi o}} \frac{I_o}{I} \frac{Z_{\text{eff}o}}{Z_{\text{eff}}}, \tag{5.2}$$

where the subscript o indicates the values used in the code for the set of similar shots and the unsubscripted values correspond to the particular shot. Finally, one arrives at the desired values for S_{Fe}:

$$S_{\text{Fe}}^{\text{Pre RF}} = f S_o \frac{B_m^{\text{Pre RF}}}{B_c(\infty)} \tag{5.3}$$

$$S_{\text{Fe}}^{\text{RF}} = f S_o \frac{B_m^{RF}}{B_c(40 \pm 4)} \tag{5.4}$$

By bringing in transport parameters, this approach introduces additional quantitative uncertainties which may mask subtle dependences.

The main conclusion of this survey is that the change in source rate during RF, ΔS_{Fe}, increases with P_{RF} in a fashion that is approximately linear, *regardless of other parameters.* This is especially evident, at least up to $P_{\text{RF}} = 200$ kW, in Figure 5.4, in which only data points from a restricted group of shots with similar plasma parameters and RF pulse lengths are plotted. In this case, as discussed above, the trend would be clear from simply plotting ΔB for a given iron line. For the entire data set, however, line brightnesses must be converted to inferred impurity source rates for comparison. These data are shown in Figure 5.5, which shows the maximum and minimum calculated values of ΔS_{Fe} as error bars about

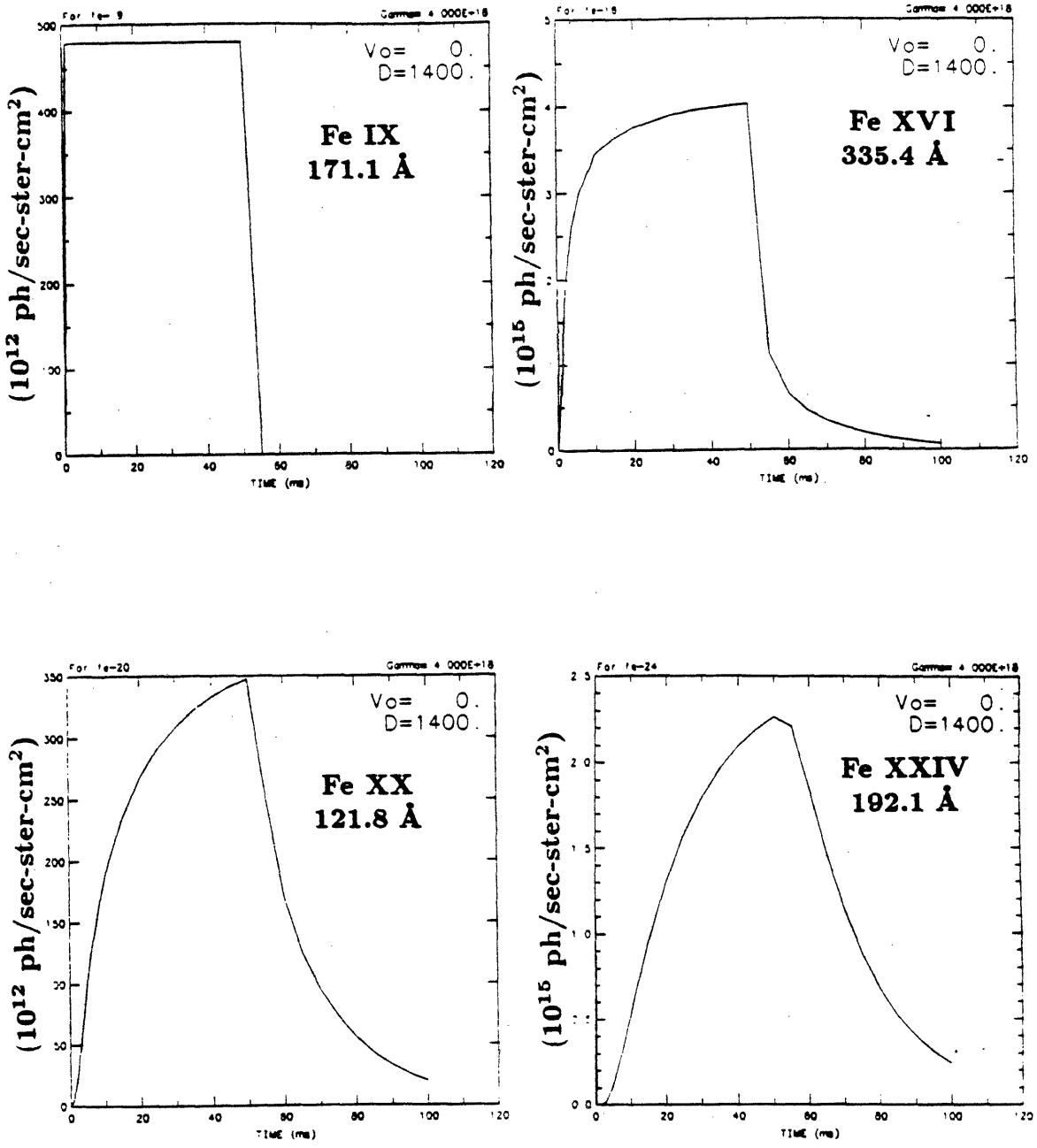

Figure 5.3 Temporal behavior of selected iron emission lines predicted by impurity transport code for constant source term turned on for 50 ms .

an average. Although the scatter in the data shown in Figure 5.5 is fairly large, the linear trend is revealed when many points are grouped and averaged (Figure 5.6). For this unrestricted data set the values for a given P_{RF} have been averaged, and the error bars indicate statistical variations of the individual points. Within the scatter, no clear dependence is seen on working gas, resonance conditions, or bulk plasma properties (with the exception of $\overline{n_e}$, at low densities, described below).

While the data shown are all based on the Fe-XXIII line, the same result is obtained with the other lines used in the database. Unfortunately, the absolute source rates inferred from the lines from different ionization states can disagree by a up to factor of two. This disagreement could be due to errors in the plasma profiles, the atomic physics coefficients, or the transport model. The finest details of scaling can only be seen by looking at the same emission line from similar plasma discharges. More uncertainty is added by using either the same line from different types of discharges (different simulations), or different lines from similar discharges (same simulation). Comparison of iron source terms deduced from different wavelengths and different code runs can only be used to observe the grossest scaling features. Nonetheless, the modelling is absolutely necessary in order to study source rates based on measured impurity line emissions.

Errors in the plasma density and temperature profiles, as well as uncertainties in the atomic physics and spectrometer sensitivity calibration all contribute to the uncertainty in source rates. However, the largest uncertainty is due to a lack of detailed knowledge related to impurity transport in the peripheral plasma ($r > 0.75a$), i.e., the fraction of impurity ions generated in the scrape-off layer (SOL) which actually diffuses into the main plasma. For example, the diffusion coefficient is assumed to be spatially constant in the calculations, but could easily be enhanced in the edge region due to turbulence and fluctuations. Increasing

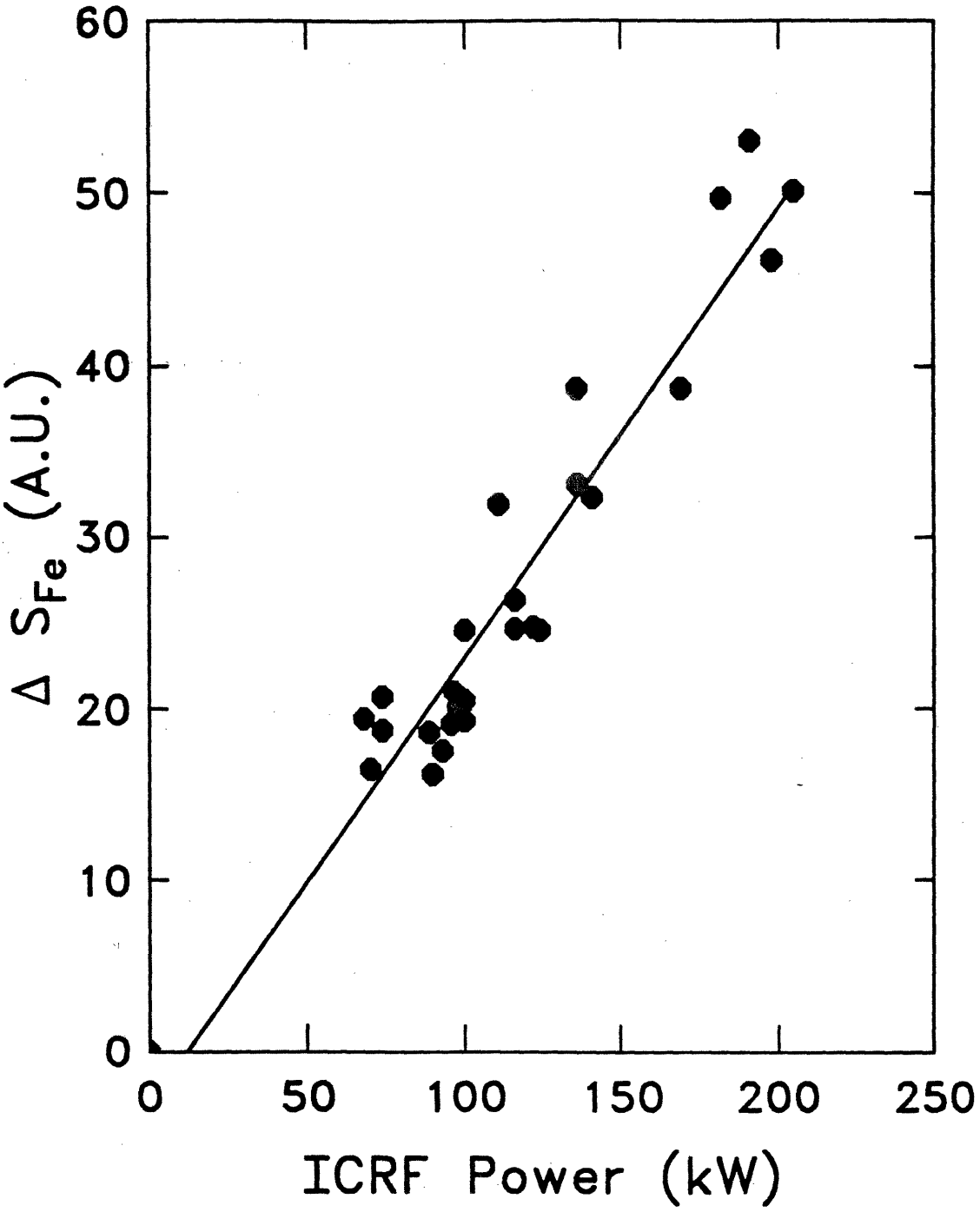

Figure 5.4 ΔS_{Fe} vs. P_{RF} for a restricted group of shots with similar plasma parameters and RF pulse lengths. All source rates inferred from the Fe-XXIII resonance line (133 Å) in first or second order.

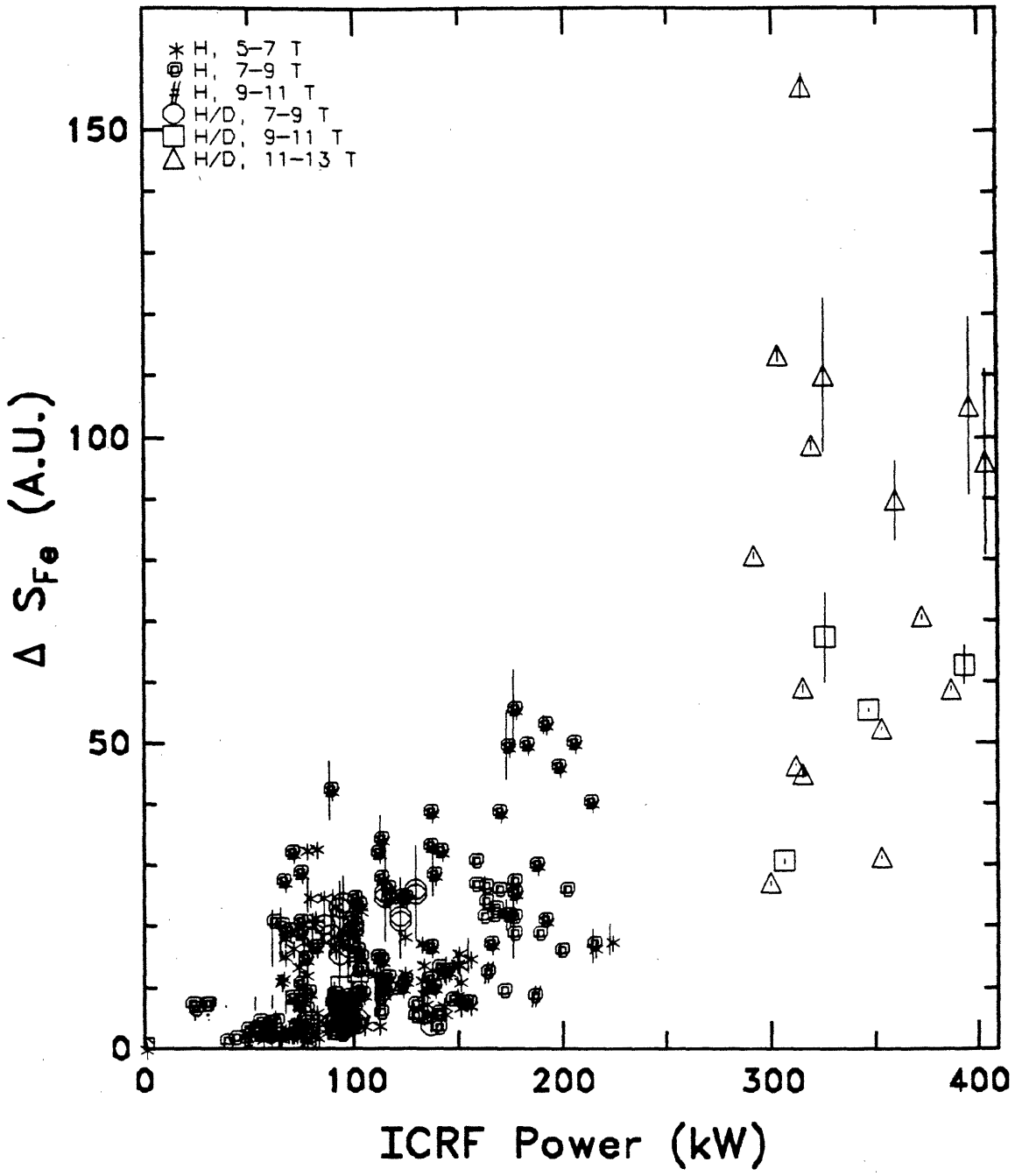

Figure 5.5 ΔS_{Fe} vs. P_{RF} for unrestricted shots. The maximum and minimum calculated values of ΔS_{Fe} are shown as error bars about an average. All source rates inferred from the Fe-XXIII resonance line (133 Å) in first or second order.

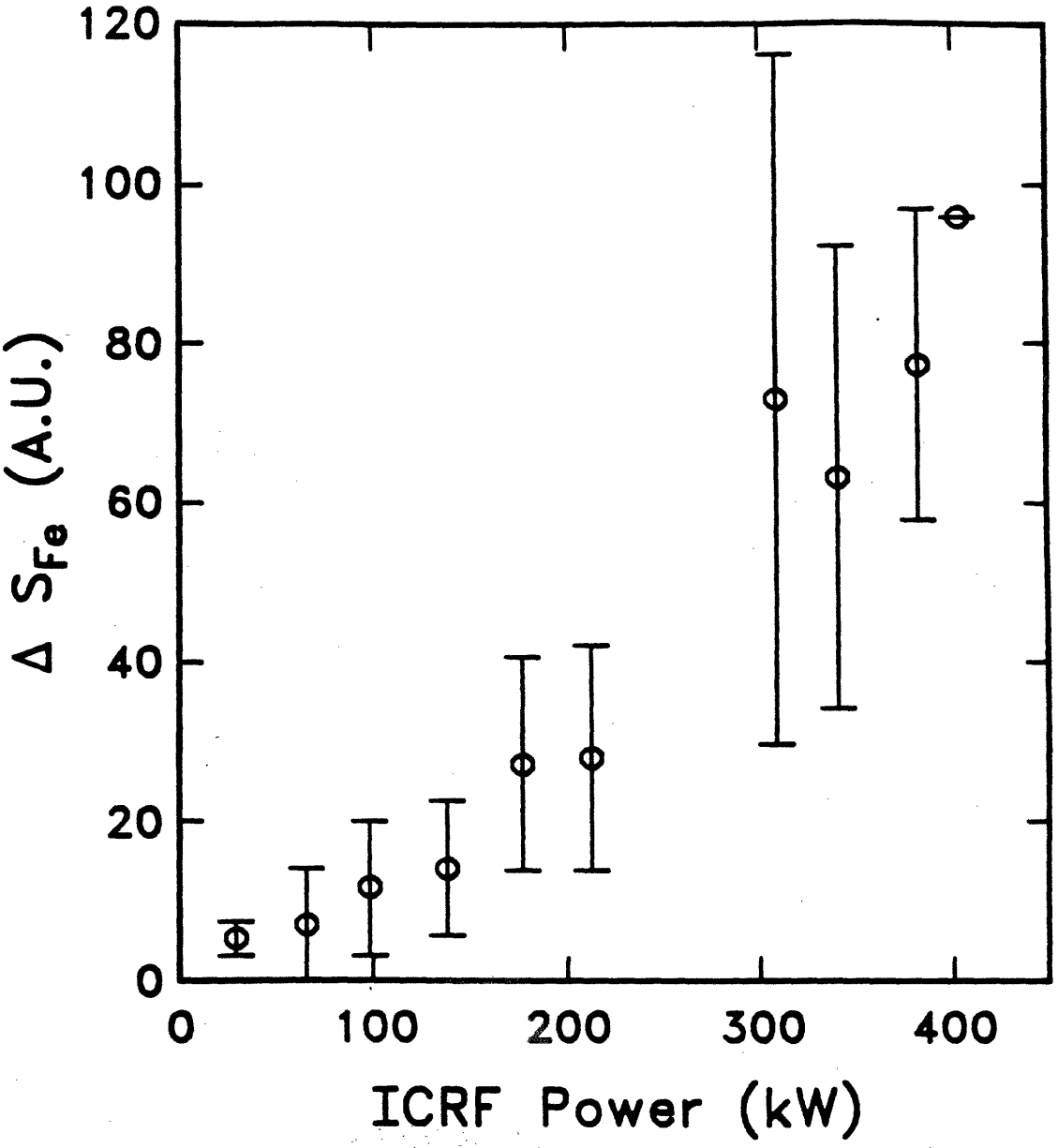

Figure 5.6 Averaged ΔS_{Fe} vs. P_{RF} for unrestricted shots. All points in 40 kW bin are averaged together, and error bars show statistical deviations. All source rates inferred from the Fe-XXIII resonance line (133 Å) in first or second order.

the diffusion coefficient in this region by a factor of three leads to source rates ~four times higher. On the other hand, relaxation of the hard boundary condition ($n_j(a) = 0$) would lower the deduced source rate somewhat by allowing some particles which diffuse outside the limiter radius to diffuse back into the main plasma before striking the limiter or other structure, thereby raising the particle confinement time. Zero inward convection velocity was also assumed to adequately model the impurity transport, based on the reasonably good agreement found between the predicted and measured brightnesses from both central and peripheral ionization states. However, adding the *maximum* inward impurity convection consistent with Alcator C impurity transport experiments leads to source rates ~five times lower.

A further question arises regarding the penetration into the main plasma ($r \leq a$) of impurity ions generated at the antenna or other recessed structure. The impurity transport simulation uses a simplified picture with no particles outside the limiter radius. Neutral impurity atoms, emitted at various angles from various surfaces with an energy of typically a few eV, either strike another surface or drift from the SOL into the main plasma and are ionized, giving an initial distribution of singly ionized particles just inside the limiter radius. In fact, the plasma density and temperature in the SOL are sufficient to ionize most impurity atoms generated at the antenna or further back before they ever reach the main plasma. In the hard boundary picture, these particles are redeposited on the limiter and never penetrate to the main plasma. In reality, the limiter structure only fills a small fraction of the volume outside $r = a$, and impurity ions created in the SOL have some probability of diffusing into the main plasma before striking a limiter or other redeposition surface. It is assumed that these impurities stick to whatever surface they hit (deposition), without recoiling off or being quickly re-emitted (recycling). A test calculation assuming iron ions originating at the antenna ra-

dius but drifting toroidally away with a velocity corresponding to 5 eV indicated that, given high but reasonable SOL transport parameters ($D = 20,000$ cm^2/sec, $V = 1000$ cm/sec), fully 35% of the particles could make it inside the imaginary boundary surface $r = a$ before reaching a limiter location. Impurities originating from the limiter would have a higher probability of entering the main plasma, with those emitted from the side facing the plasma being already inside by definition. Those emitted from the lateral sides of the limiter very near the plasma woule have a $\sim 50\%$ ($V \approx 0$) or greater ($V > 0$) chance of making it in, assuming a randomly directed initial velocity. Clearly, the detailed particle transport is not very well known in this region. Despite these uncertainties in the absolute source rates, however, the relative changes are believed to be much more reliable and should allow determination of the major trends.

A spectral scan was conducted on two successive days with similar plasma parameters but different RF power levels injected. The power on one day was in the range $130 - 150$ kW; the power on the next was in the range $300 - 400$ kW. The subtracted spectrum for the high power case, showing the difference between the VUV spectrum just after ICRF heating and the spectrum taken prior to ICRF, is presented in Appendix 1. Because the plasma and transport parameters were otherwise similar, direct comparisons of several iron emission lines not used in the database could be performed. This study supported the conclusion that the scaling of iron influx with P_{RF} was approximately linear. By forcing the scaling for each line to be of the form $B = c(P_{RF})^{\alpha}$, the analysis indicated that $1 \leq \alpha \ll 2$.

There is no correlation of ΔS_{Fe} with the fast ion distribution as inferred from CX spectra; the impurity production seems unrelated to the presence of fast ion tail formation or to the change, if any, in T_i due to ICRF heating. Whether or not the ion temperature rose, dropped, or remained the same during the ICRF

pulse made no significant difference regarding the amount of iron that entered the plasma. Whether or not fast ion tails were observed in any of the heating regimes also mattered little. However, it must be emphasized that the CX neutral analyzer was not at the same toroidal location as the ICRF antenna, and would therefore probably not detect any local production of fast, promptly lost ions. Superheated ions with sufficiently large perpendicular energy may be unconfined, drifting to the vacuum wall before traveling around the torus to the location of the CX analyzer. Also, the lack of a low energy neutral analyzer prevented any study of thermal CX flux having $E \leq 900$ eV. However, the absolute flux of all CX channels, including the 900 eV channel, dropped during the ICRF pulse by factors as high as two or three [123], making it difficult to believe that the lower energy neutral flux could have significantly increased. The drop in neutral CX flux is consistent with a heating of the SOL plasma, decreasing via ionization the number of thermal ($E \leq 10$ eV) edge neutrals. It is these slow neutrals which diffuse into the main plasma and lose their electrons via charge exchange to the fast ions, which come back out as fast neutrals. The CX flux recovered quickly to pre-RF levels or higher after the RF pulse ended.

The lower half-loop antenna was installed first and operated alone for the first three weeks. Upon the installation of the upper half-loop, the antennas were usually operated together, with the RF power being split roughly equally between them. At times, however, each half-loop was also operated individually. For all cases, the iron influx was approximately the same for a given total P_{RF} , indicating no strong dependence on either antenna poloidal extent or on the total exposed antenna area (activated or not). Of course, this would be consistent with a localized impurity generation process at the antenna surface which scaled as (Power/area activated) times (area activated and thereby locally exposed). However, the scatter in the data could mask the factor of 2 changes in iron influx that one might have expected

from other scaling laws (e.g. Power/Total antenna area in the machine).

Two conditions associated with elevated edge temperatures are correlated with enhanced impurity production: low density and low q, which corresponds to high plasma current for a given magnetic field. Below a threshold value of $\overline{n_e}$ $\approx 1.8\times10^{14}$ cm^{-3}, $\Delta S_{Fe}/P_{RF}$ is seen to increase as $\overline{n_e}$ decreases (Figure 5.7). The probable explanation for this result involves the deterioration of energy confinement times on Alcator C at lower values of $\overline{n_e}$ (Alcator scaling) [124]. The edge temperature T_{eb} generally increases as $\overline{n_e}$ decreases past a certain value, [125], which would lead to increased sputtering losses. This mechanism has been suggested previously to explain high metal concentrations during low density ohmic discharges on Alcator C [126]. Furthermore, $\Delta S_{Fe}/P_{RF}$ is often higher for low q discharges with $q_a \leq 3.4$, another condition associated with elevated edge temperatures (Figure 5.8). Thus a change in edge plasma parameters is implicated in the enhanced impurity production. Note: q is the so-called safety factor (inverse rotational transform of the helical field lines), important in MHD calculations and stability considerations. Its value at the limiter for the circular Alcator C discharges is approximately given by

$$q_a = \frac{B_T a}{B_\theta R} = \frac{5a^2 B_T}{I_p R} \qquad 5.5$$

where a and R are the minor and major radii in cm, B_T is the toroidal magnetic field strength in kG, and I_p is the plasma current in kA.

5.4 Evidence for Sputtering

Further corroboration of this effect of edge conditions on impurity influx is seen from the Langmuir probe data, which yielded strong evidence for a prompt and large change in T_{eb} at the antenna radius during the RF pulse (Figure 5.9). Only minor changes in n_{eb} were seen, with some increases and some decreases. The

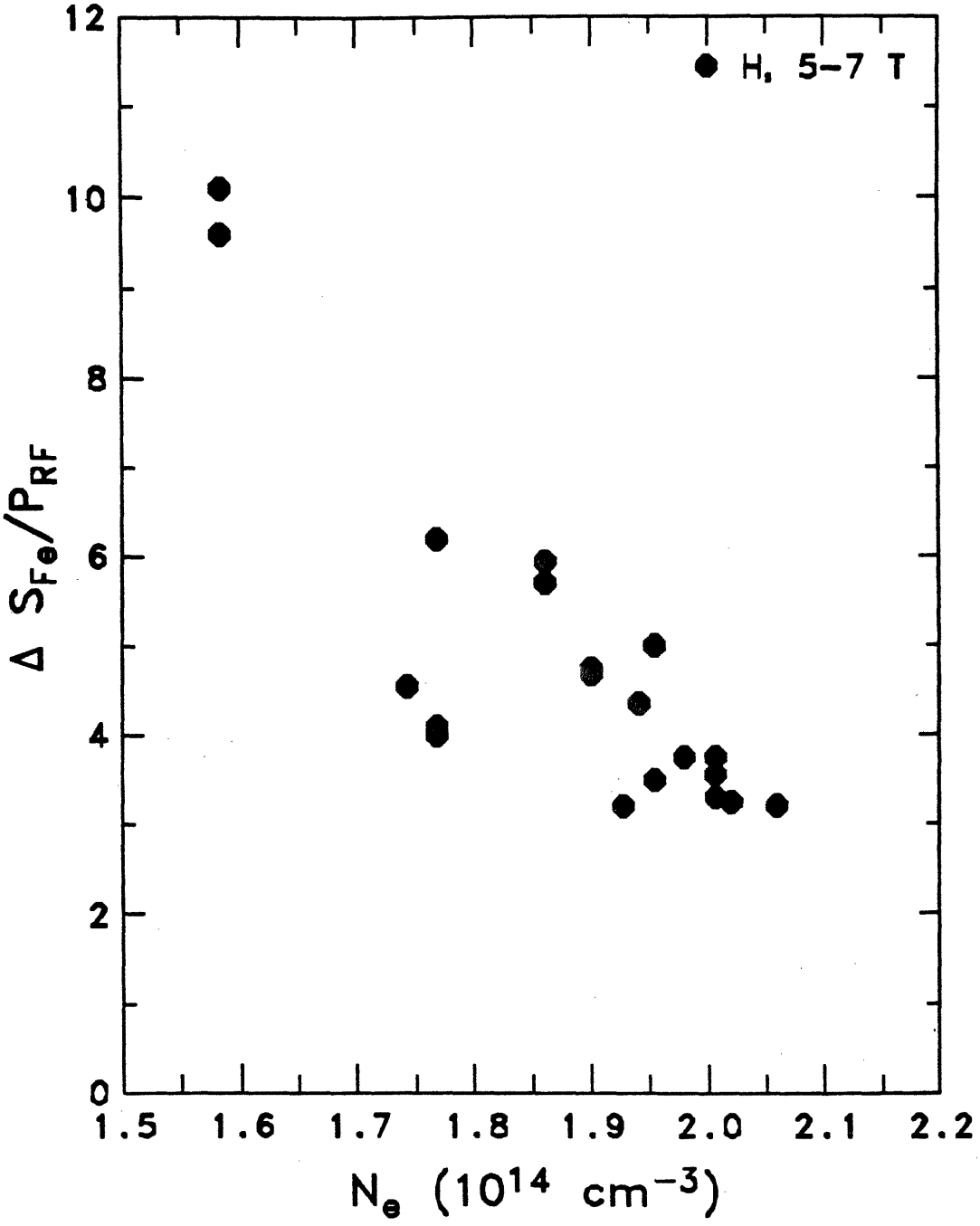

Figure 5.7 Change in iron source rate per kW of injected ICRF power, $\Delta S_{Fe}/P_{RF}$, plotted vs. line averaged density, $\overline{n_e}$, for a selected group of similar discharges.

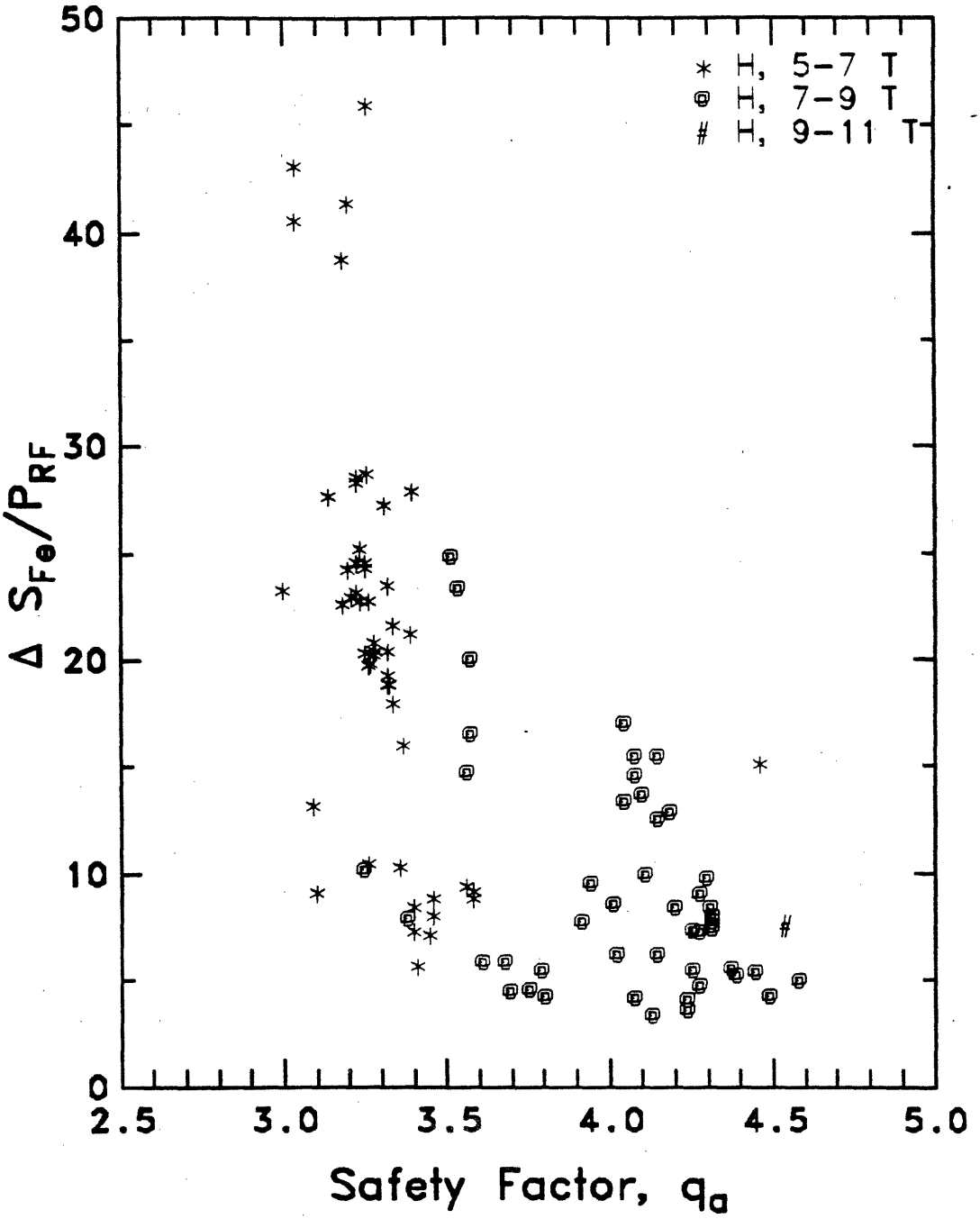

Figure 5.8 Change in iron source rate per kW of injected ICRF power, $\Delta S_{Fe}/P_{RF}$, plotted vs. safety factor, q_a, for a selected group of similar discharges.

probe floating potential (that potential at which no current is collected from the plasma) usually decreased by a few eV when T_{eb} rose. Plotted in Figure 5.10 are the iron source terms before and during the RF pulse ($S_{\rm Fe}^{Pre\ RF}$ and $S_{\rm Fe}^{RF}$) versus T_{eb} at the antenna radius, for a series of shots with $P_{\rm RF}$ in the 50 kW range, showing a clear correlation. The increase, if any, in T_{eb} at the limiter radius was less dramatic, leading to an effective increase in the edge temperature scrape off length, λ_T, by a factor of three or more during the 350 kW RF pulses (Figure 5.11). Since the Langmuir probe was located toroidally away from the antenna, this change in the edge plasma was not a local effect. Of course, the perturbation may have been larger at the antenna port.

The above evidence strongly suggests that thermal sputtering of the Faraday shield through a significantly increased sheath potential ($\Phi_{\rm sh} \approx 3.5T_{eb}$) was the dominant source of iron, chromium, and nickel during the ICRF pulse. An increase in T_{eb} from 6 eV to 20 eV at the antenna, as shown in Figure 5.9, would cause the sputtering of iron by protons to increase by an order of magnitude due to the sharp increase in sputtering coefficient with increasing impact energy [114]. The more modest changes in the carbon and oxygen influx are ascribed to the more modest increases in T_{eb} at the limiter, again via thermal sputtering. The increased levels of molybdenum probably originate from the recessed molybdenum limiters, still somewhat exposed to the edge plasma. Sputtering contributions from the limiter supports and wall are estimated to be minor because they are ~ 7 and 22 density scrape-off lengths behind the limiter, respectively ($\lambda_n \approx 2-4$ mm). Coupled with the observed lack of dependence on CX neutral flux, this tends to eliminate these structures from consideration.

An observation from the current (1985-86) ICRF heating experiments on Alcator C supports the identification of the Faraday shield as the primary metal source

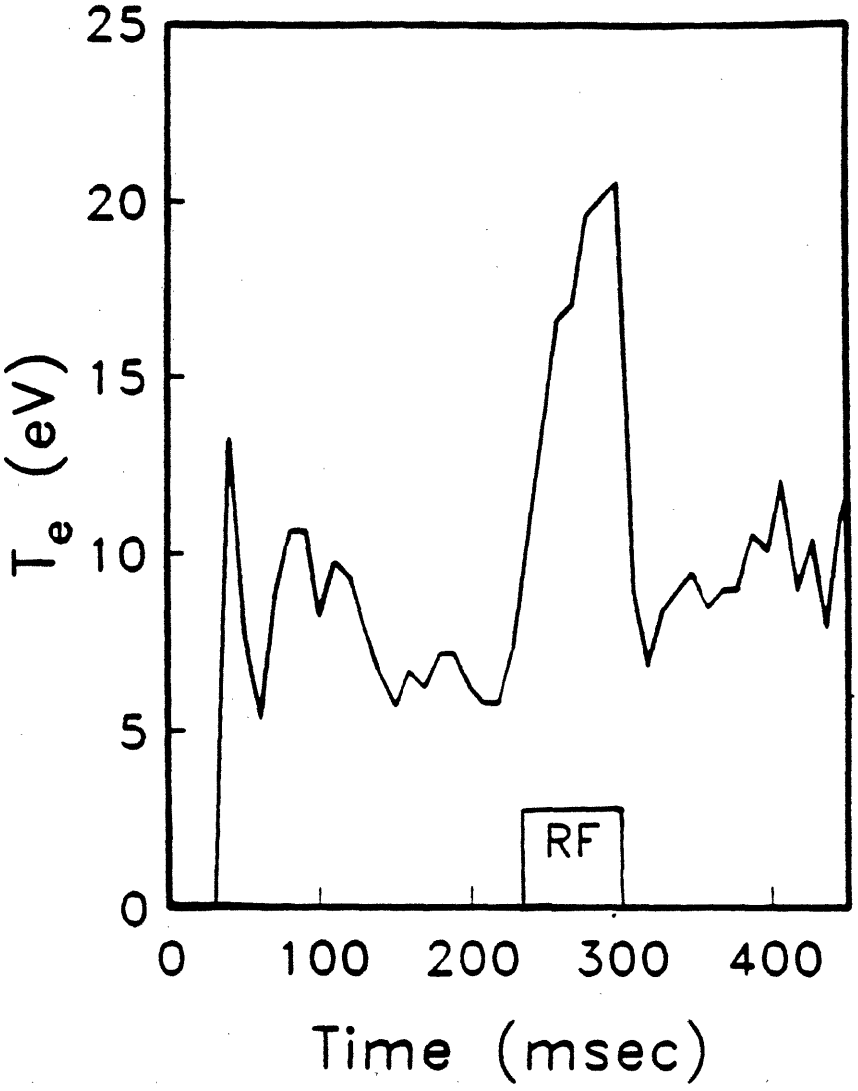

Figure 5.9 Increase in electron temperature at the antenna radius for a 350 kW ICRF pulse, as measured by a Langmuir probe.

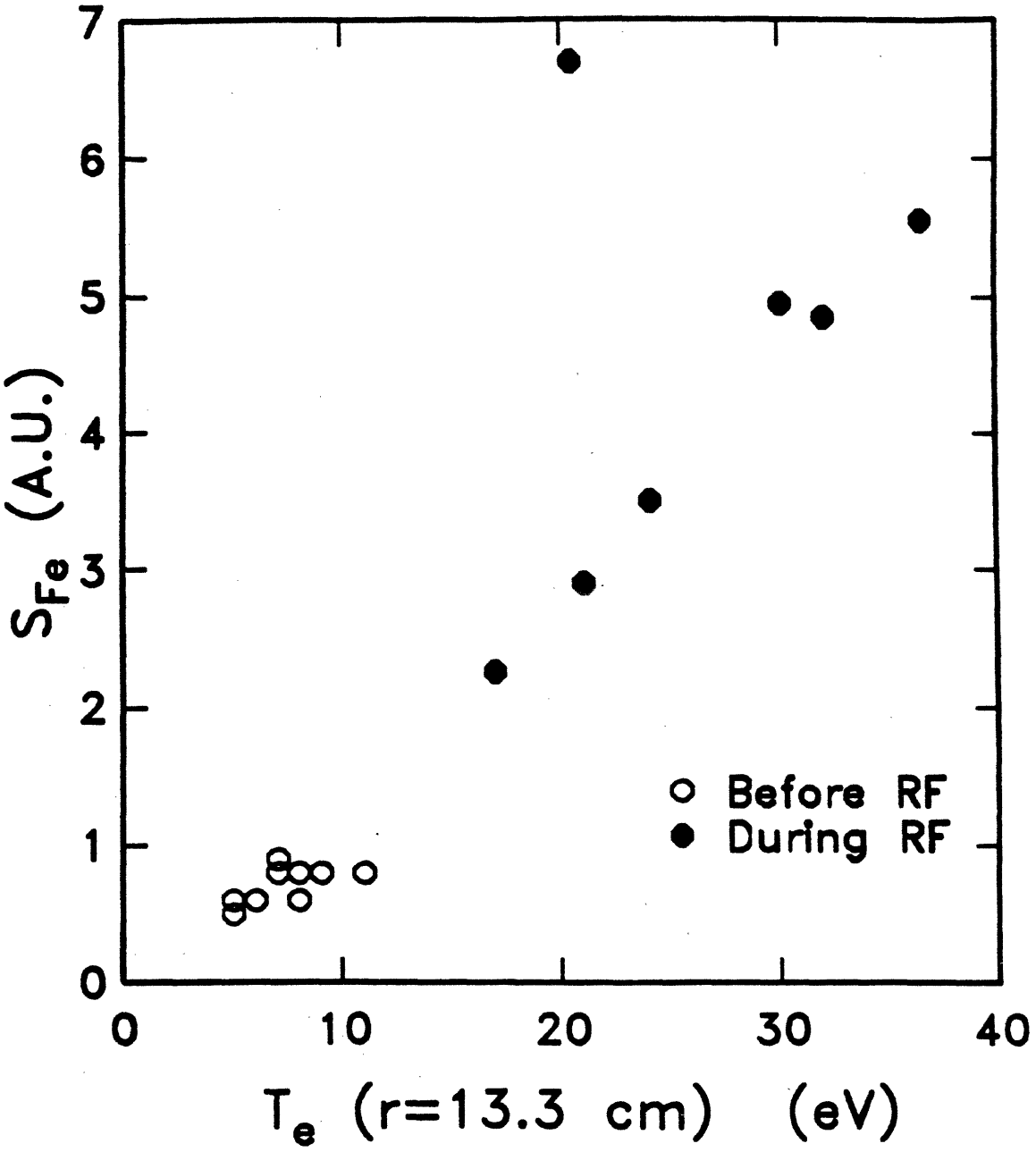

Figure 5.10 Iron source rate, S_{Fe}, plotted vs. electron temperature at the antenna radius for a selected group of similar discharges. Open circles represent pre-RF values, while closed circles are values taken during the ICRF pulse.

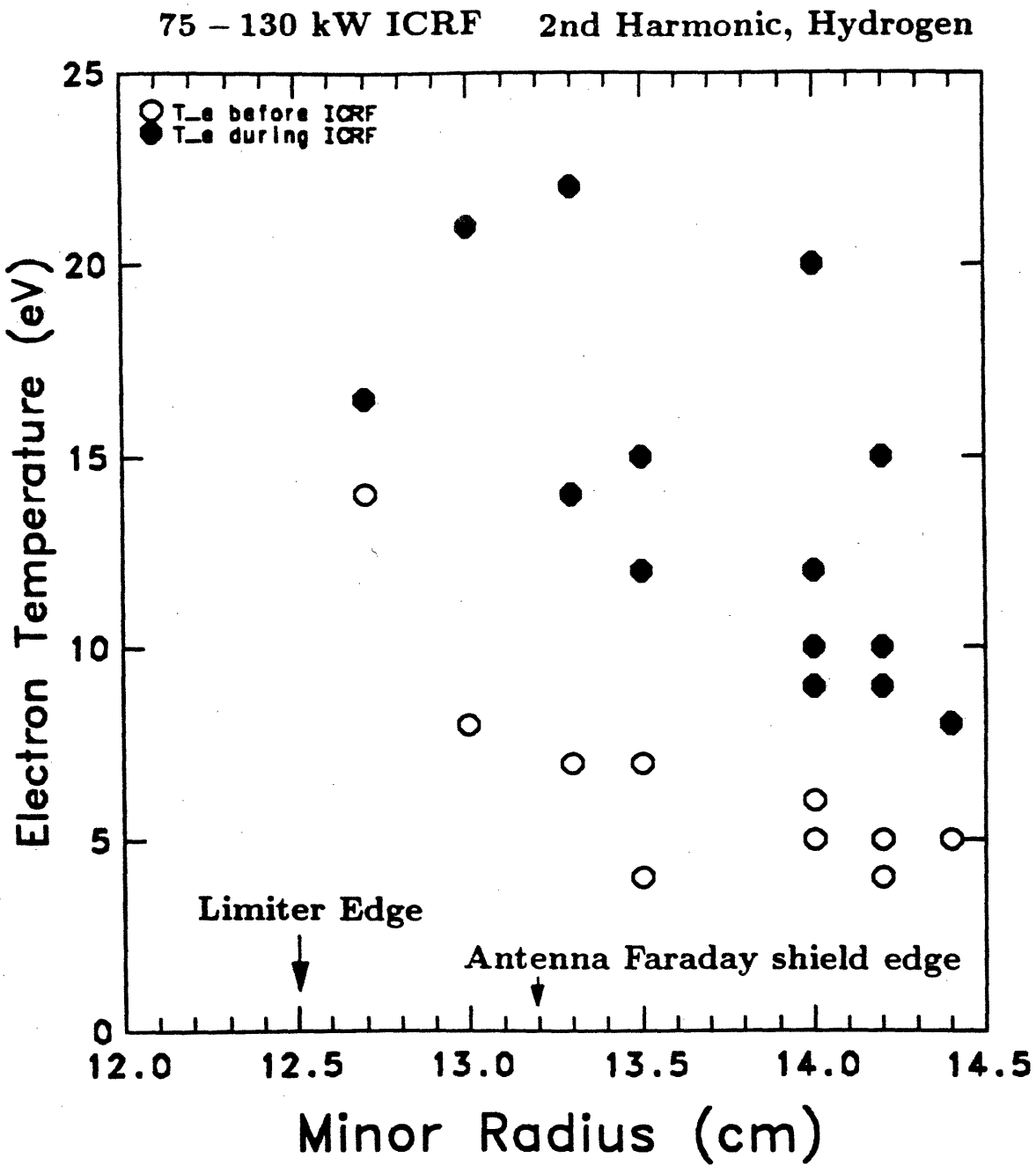

Figure 5.11 Edge electron temperature profiles, $T_{eb}(r)$, before and during ICRF heating for a selected group of similar discharges. Open circles represent pre-RF values, while closed circles are values taken during the ICRF pulse.

during ICRF heating. Visible light emission from the antenna region was seen to increase during the RF pulse, and in fact it closely tracked the time dependence of P_{RF} . An H_α filter cuts off this light, implying that it is not due to hydrogen or deuterium. Rather, the emission is believed to be radiated from neutral or lightly ionized metal atoms entering the plasma.

Total sputtering yields are predicted to be roughly a factor of $\sqrt{2}$ higher for deuterium than for hydrogen, since for a given impact energy the yield per deuteron is roughly twice that for protons, but the flux is reduced for deuterons by $\sqrt{2}$ due to their slower velocity at fixed energy. This effect is either not seen or obscured by the scatter in the data. This scatter is attributed largely to small changes in the edge plasma parameters, which can vary in subtle ways during nominally similar plasma discharges. The Langmuir probe was available for only a few days during these experiments, so only limited comparisons of impurity influx with edge parameters (such as in Figure 5.10) are possible. A further limitation is the fact that the probe was often subject to noise and/or large fluctuations in the collected current during the RF pulse, and was unable to accurately measure values of T_{eb} greater than 40 eV due to the biasing voltage employed. These limitations were especially severe during high power shots with $P_{RF} > 200$ kW. A more extensive study of edge parameters during ICRF heating is currently underway at Alcator C [127].

5.5 Erosion Code Comparison

To check the validity of the above conclusions quantitatively , an edge erosion code was used to simulate heating, evaporation/sublimation rates, and thermal sputtering rates. Using edge plasma parameters ($n_{eb}(r)$, $T_{eb}(r)$, initial background impurity fractional concentration, etc.) and the physical properties of the exposed

structural materials (heat capacity, thermal conductivity, vapor pressures, sputtering data curves, etc.) as input, this simulation yields calculated impurity source rates from both the limiter (carbon source) and Faraday shield (iron source) [128]. The overall sputtering yield includes thermal sputtering by bulk ions (H or D) and self-consistent contributions from impurity ions (background plus ions which are sputtered and then return to the edge). Edge profiles $T_{eb}(r)$ and $n_{eb}(r)$ consistent with values measured by the Langmuir probe during a series of 350 kW ICRF discharges were used in order to compare calculated iron and carbon source rates with those inferred from the data in Table 4.1. The edge temperature profile $T_{eb}(r)$ was assumed to change rapidly from pre-RF to RF conditions. Edge ion temperatures, $T_{ib}(r)$, were taken to be three times $T_{eb}(r)$, consistent with recent edge measurements on Alcator C [127] .

By adjusting the edge plasma parameters within the experimental uncertainties, excellent qualitative and reasonable quantitative agreement could be obtained (Figure 5.12). In this calculation, thermal sputtering by deuterons accounts for almost half the iron and carbon influx, with the remainder due to impurity ion sputtering. A pre-RF background density of carbon with $n_C(r) = 0.05 n_e(r)$ was assumed in this calculation; this density is reasonable based on the brightness of emission lines from low ionization states of carbon. The fraction of impurity ions reaching the main plasma ($r \leq a$) was taken to be 50% for both iron and carbon. The contributions from evaporation and sublimation are much too small to explain the observed influxes. As stated earlier, no conditions could be found to produce the observed influxes of both carbon and iron solely from the contaminated graphite limiter.

While the agreement between the erosion code and the observed impurity behavior strongly supports the hypothesis that thermal sputtering is the dominant

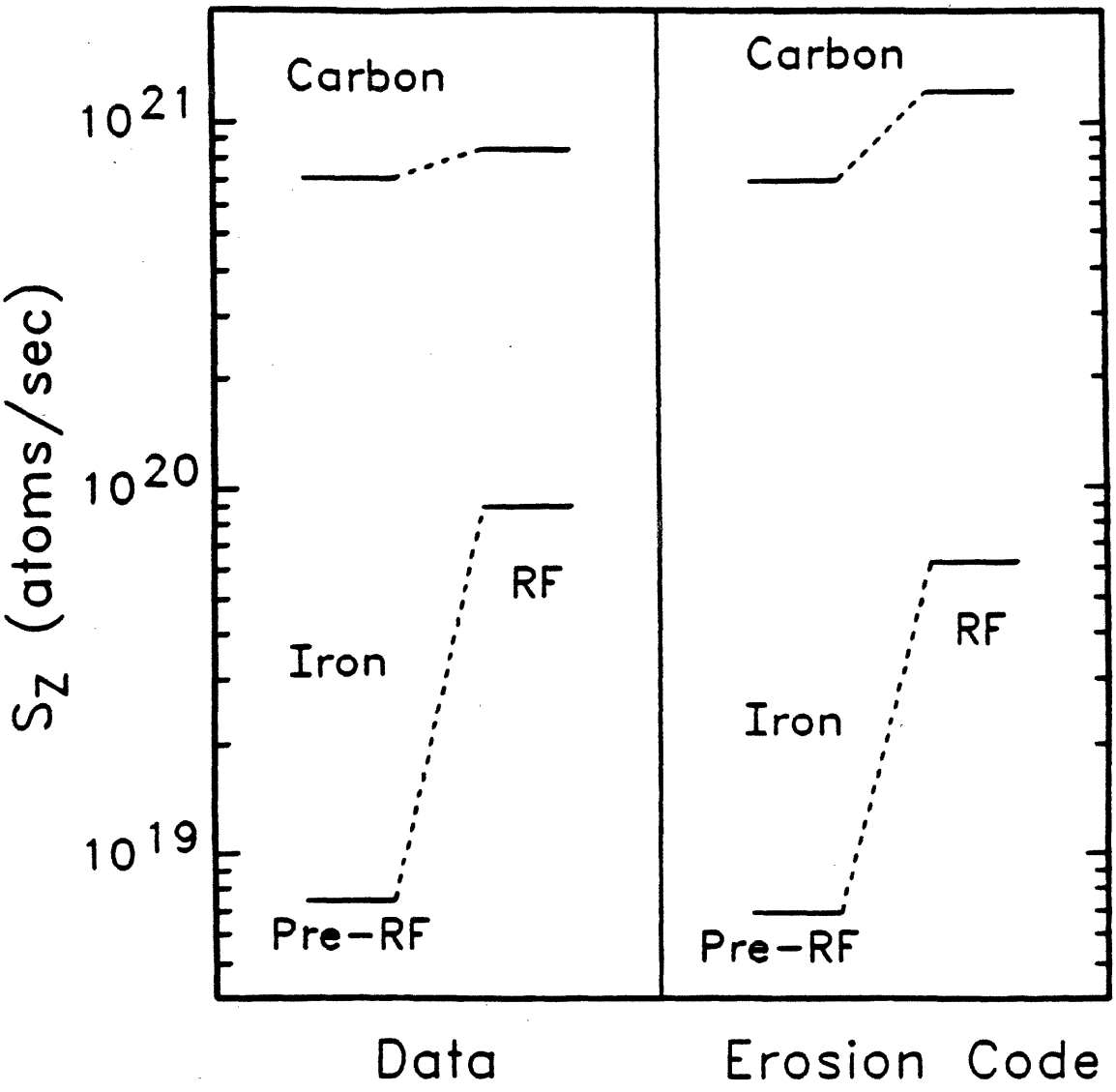

Figure 5.12 Comparison of carbon and iron impurity influxes deduced from measurements with values calculated by the erosion code. In this calculation, only the edge temperature scrape-off length λ_T changed during the ICRF pulse, increasing from 7 mm to 45 mm (nearly flat profile on the scale of interest).

mechanism generating the impurities, it can not be construed as a proof which eliminates other possible mechanisms. There are significant uncertainties in the detailed plasma profiles in the scrape off layer, as well as uncertainties in the impurity transport in the plasma periphery (from $r = .75a$ out to the wall). It should be noted that the total power flux to the limiters can be calculated from the edge profiles used in the erosion code. For the edge values giving the reasonable match shown in Figure 5.12, the calculated power to the limiters is $\sim 50\%$ higher than the total input power minus the radiated power. Edge values giving better agreement in the scraped off power reduce the predicted source rates by factors of ~2–3, but these are still within the uncertainties of the source rates implied by the spectroscopic measurements and transport analysis. The possibility of a hotter temperature at the antenna than at the limiter would remedy the problem, giving high iron source rates without over-extending the scraped-off power at the limiter. Such a locally peaked $T_{eb}(r)$ profile could result from toroidally localized strong heating of the SOL plasma near the antenna radius. In addition, the effects of possible toroidal or poloidal asymmetries in the edge are not included in the calculations. In particular, the temperature and density near the antenna during the RF pulse might differ considerably from the values recorded by the Langmuir probe and modeled in the erosion code. Any of the above considerations might resolve the difficulty in obtaining a perfect match between the erosion code and the source terms inferred from measurements. Nonetheless, the reasonably good agreement shown in Figure 5.12 does give significant credibility to the impurity production model. However, it can not be used to rule out those processes which are difficult to model, such as unipolar arcing or sputtering due to reactive $\mathbf{E_{RF}}$ fields.

5.6 Discussion

The picture which emerges from the above analysis is one of elevated edge temperatures in the SOL during ICRF, which in turn leads to an enhanced impurity influx due to physical sputtering through an elevated sheath potential. Because the relative increase in edge temperature is larger at the radius of the antenna than at the radius of the limiter, the largest percent increase in impurity influx is that for the materials in the antenna shield (chiefly iron, chromium, and nickel). This explanation of enhanced impurity production in Alcator C during ICRF heating is consistent with both experimental evidence and results from other tokamaks. Thermal sputtering due to elevated T_{eb} during ICRF was also blamed for enhanced metallic impurity levels at T-10 [98] and at TFR, where the results and conclusions are generally similar to those reported here for Alcator C. This process is also blamed for enhanced sputtering of C and O from the graphite limiter of JFT-2M. The rise in T_{eb} is also seen in JIPP T-IIU. Although T_{eb} was not reported to rise on PLT, it is stated that noise on the probe signals could have prevented the detection of such an effect.

However, this picture does not explain how the ICRF power changes the edge plasma. The fact that both the impurity influx and T_{eb} change quickly upon turning on the RF power implies that the change is due to some direct heating of the edge plasma from the antenna, rather than to increased energy flux out of the central plasma, (which often showed little change in T_e or T_i anyway). This edge heating appears to be relatively insensitive to how well the launched ICRF power propagated and was absorbed by the bulk plasma, as evidenced by the lack of correlation with resonance conditions. Possible edge heating processes include the damping of coaxial modes or surface waves [71], excitation and damping of the slow wave in the SOL, or absorption at the lower hybrid resonance layer, which occurs in the SOL at n_i

$\approx 10^{12}$ cm^{-3} for these experiments. The scaling with P_{RF} may indicate that some constant fraction of the launched ICRF power goes directly into the edge plasma. To raise the temperature of the low density plasma in the SOL by 20 ev or so would require less than 2% of the 400 kW delivered to the antenna for the high power shots, assuming an energy confinement time of 0.5 ms in the SOL. The possibility of a local maximum in $T_{eb}(r)$ at the radius of the antenna would require that the power was absorbed in a fairly narrow radial zone. Indeed, some indication of such a profile has been seen in the more recent Alcator C ICRF experiments [127].

Increased sputtering from CX neutrals was invoked by PLT researchers to explain the Fe influx, and by JIPP T-IIU workers to explain increased O levels. Metal influx on JFT-2 during ICRF was correlated with fast ions in the edge. No such correlation with fast ions or neutrals ($E > 900$ eV), was observed on Alcator C, although local effects near the antenna cannot be completely dismissed. However, such an effect, if due to a resonance, should yield a significant correlation between impurity influx and resonance conditions, yet no such dependence was observed on Alcator C. Non-linear local damping processes which could create fast ions near the antenna regardless of resonant conditions cannot be excluded from consideration, although there is no evidence for this occurring. The lack of a low energy neutral analyzer prevented any such study of ions having $E \leq 900$ eV. Consequently, this process cannot be entirely eliminated as a possible source of iron on Alcator C, but is considered as a possible supplementary process to the thermal sputtering.

Sputtering of the antenna Faraday shield and walls due to the acceleration of ions by the reactive $\mathbf{E}_{RF}$ fields near the antenna was blamed for metallic impurity generation at JFT-2M and Macrotor [99] during ICRF. To examine this possibility on Alcator C, calculations based on the formulas of Itoh *et al.* [102] were performed to estimate the impact energy with which ions accelerated by the $\mathbf{E}_{RF}$ fields would

strike the Faraday shield. The electric field was estimated to be ≤ 1000 V/cm near the Faraday shield, resulting in predicted impact energies generally too small ($E \leq$ 10eV) to cause much sputtering. An exception is the case of minority hydrogen ions in a magnetic field of $\mathbf{B} = 12$ Tesla, for which the fundamental cyclotron resonance layer of hydrogen occurs on axis. In this case the predicted impact energy is very large due to a resonant pole in the equations. The lack of observed dependence of impurity influx on magnetic field or working gas, coupled with the low impact energy predicted under most conditions, indicates that this process is not a dominant source of iron on Alcator C.

The occurrence of a large number of small unipolar arcs between the Faraday shield and the plasma sheath, yielding an iron source which increases with P_{RF} , also cannot be ruled out. However, the arc tracks would have had to be so small that they were not identifiable upon visual inspection of the antenna. The Alcator C results are consistent with the conclusion, also reached at PLT and JIPP T-IIU, that the closest metal surface to the plasma, if unprotected, will yield the largest metal impurity influx. Thus the unprotected antenna Faraday shield on Alcator C is the dominant source of iron, chromium, and nickel during ICRF despite metallic contamination of the graphite limiter. The use of graphite protective shields on the antenna surfaces which intercept magnetic flux lines, as employed at TFR and PLT, apparently minimizes the antenna contribution to the metallic impurity influx. Good ICRF heating results at $P_{RF} \leq$2.8 MW have also been recently reported in preliminary results at JET [75,129] which uses graphite protective tiles around the antenna in conjunction with carbonization of the walls to reduce metal impurity production. Despite a modest rise in the edge temperature during ICRF heating and some increase in density near the wall, the level of nickel (dominant metal impurity) in the plasma rises no faster than the total input power, and does not

play a dominant role in the central power balance. The price for such success, however, is substantial amounts of carbon in the plasma, with $Z_{\rm eff}$ as high as 4.5 for lower density shots [121]. The most recent report is that metal impurities are again problematical at higher ICRF powers on JET, is spite of the carbonization program [130].

The effects of ICRF heating on n_{eb} have varied from one experiment to the next. Large rises in n_{eb} are seen on PLT and TFR, while researchers at JFT-2M report a four-fold decrease. Desorption of oxygen from the walls is believed responsible for a linear increase in n_{eb} with $P_{\rm RF}$ on JIPP T-IIU. These effects are generally attributed to changes in desorption and recycling at the wall; the variety of n_{eb} responses to ICRF may be due to differences in the details of the limiter-antenna-wall spacings in the various experiments. Neither large nor reproducible effects were seen on Alcator C, where the distance from the wall to the front of the ICRF antenna is ~ 6.0 cm, or ~ 20 times the density scrape-off length, λ_n.

Chapter 6

Summary and Suggested Future Work

This thesis deals with two main topics: 1)— the development, characterization, and use of the VUV time-resolving spectrograph, and 2)— impurity generation during ICRF experiments on Alcator C. While the latter study depended on the former, the two topics are summarized separately, along with suggestions for future work in each area.

6.1 VUV Spectrograph

Summary: A grazing incidence VUV monochromator has been converted into a time-resolving VUV spectrograph by the addition of a new detector array system, consisting of a MCP image intensifier linked through a fiber optic image conduit to a 1024-element 1-D photodiode array with a digital readout. The performance of the detector system and spectrograph was studied and was found to meet or nearly meet all of the design objectives. The most significant of the minor failings were in the instrumental response function: spectral resolution was slightly poorer than desired, and too much of the signal was contained in the broad wings. Reliability has surpassed expectations. The system was absolutely calibrated below 150 Å by a soft X-ray source referenced to a proportional counter. Cross-calibration with an absolutely calibrated EUV monochromator was performed in the region 400 Å $< \lambda <$ 1100 Å, by simultaneously monitoring several bright impurity emission lines from the tokamak plasma.

The spectrograph was installed on the Alcator C tokamak, where it has become the principal impurity monitor. It has performed reliably and routinely for over 30 months on the tokamak at this writing, and has proven its usefulness as a tokamak diagnostic of plasma impurity behavior. The absolute sensitivity calibration of the instrument has enabled users to calculate absolute impurity concentrations in the plasma as a function of time. In addition to its primary role as a powerful survey spectrometer, it has been used for studies of impurity transport. The temporal resolution combined with the ability to fully cover the available spectral range in 15 plasma shots has also made it possible to assemble emission spectra from several artificially injected impurities, using the differential spectra technique. The ability to simultaneously monitor emission lines from several different impurities has yielded rapid identification of natural (unexpected) impurity injections, a very useful feature for troubleshooting. This feature has made the instrument very useful for the study of impurity generation during auxiliary heating experiments, in particular during the ICRF heating experiments described below.

Suggested Future Work: While the spectrograph has been a success as a tokamak diagnostic instrument, it nevertheless could be improved upon in a variety of ways, most of which are related to improved spectral resolution. To that end, perhaps the most rewarding change in any future design would be an insistence on opaque cladding between the optical fibers in the image conduit. This feature was unavailable in the taper assembly at the time of purchase, but should have been incorporated into the straight piece. The lack of cladding was made clear by the effectiveness of the black paint for removing ambient light pickup from the sides of the fiber bundle. Two technological improvements developed subsequent to the order of this system would also improve resolution. The first involves a redesign of the MCP mounting assembly, allowing a smaller gap to the phosphor screen

without arcing. This is accomplished by taking care to avoid any sharp edges in the mounting rings which hold the components in place. The second feature is an MCP manufacturing step which reduces the transverse momentum spread of the electron bunch exiting the output side of the MCP. Both of these improvements reduce the single microchannel spot size on the phosphor, yielding better resolution.

The distortion (variable reduction factor) in the fiber optic reducing taper could have been carefully measured, if not completely avoided, by a thorough inspection of the optical components prior to the assembly of the detector system. This distortion is the largest contributor to the uncertainty in absolute wavelength measurements for unknown lines. Although local distortion specifications were supplied to the vendor, the non-uniformity of the reduction factor was not anticipated.

The repeller plate was shown to be of limited use, due to the non-uniform gain across the detector. The gain problem is no doubt due to the presence of a conducting metal cylindrical shield surrounding the space between the plate and the MCP, and could easily be minimized by using a non-conductive material for the shield. This would allow operation at a reduced voltage difference, which might also go a long way toward removing the ion feedback problem.

The Reticon photodiode chip was rigidly bonded with optical epoxy to the fiber optic bundle. In retrospect, the use of micrometer-adjusted motion stages to accurately position an unbonded chip would have allowed more flexibility. Optical index matching fluid would be used at the interface in this case. The Reticon appeared to be one or two millimeters high relative to the centerline of the fiber optic bundle, but there was no way to correct this, short of disassembly. While a concave grazing incidence grating does not focus in the vertical direction, there is a slight curvature to the image. This could result in some loss of resolution (presumably in the Lorentzian part of the response function only). With a rigidly

attached Reticon, there is no simple way to check this or correct it, if misaligned.

A thermo-electric cooling system on the Reticon would substantially reduce the dark current in the photodiode array, which increases the noise level on the data due to temporal variations. In order to usefully employ the last bit or two of the digitizers, a cooling system would be necessary in most cases, as the current noise level is in the few counts per pixel range for 4 ms scans.

Finally, the focusing elements (the linear and rotary motion stages) inside the detector chamber proved stiff and awkward to use when the chamber was under vacuum, due to the atmospheric pressure forces on the flexible bellows. External focusing screws arranged so as to position the entire chamber might prove more easy to adjust, and would simplify the internal layout of the mounting chamber.

In terms of future general VUV work on Alcator C, the possibilities are boundless, as there are always questions as to how various plasma conditions affect the impurity levels and behavior, plus questions as to how the impurities affect the plasma itself. The spectrograph is particularly well suited for studies which simultaneously make use of its spectral coverage and temporal resolution, as film spectrometers have only the former and ordinary monochromators have only the latter. Searching for weak predicted lines whose wavelengths are not precisely known is a good example. The ability to view an extended region of the VUV spectrum makes it possible to view even relatively weak lines above the background, whereas the difference in brightness from peak to background might be hard to resolve with a scannable monochromator due to shot to shot variations. The temporal resolution allows the user to see if the behavior of the line in question follows the predicted course (e.g. appears at the impurity injection and peaks the expected number of milliseconds later).

Another application is the measurement of $T_e(r,t)$ or $n_e(r,t)$ from brightness

ratios of selected impurity lines. As long as both lines can be viewed by the detector, their brightness ratio can be monitored during a shot. Radial scans could give the spatial variation on a shot to shot basis. While this is simple enough to do, there has been little impetus due to the availability of other, more precise diagnostics at Alcator C for the same purpose.

While several composite impurity emission spectra have been constructed for convenience, there are many elements whose spectra at temperatures found in Alcator C plasmas are relatively poorly documented. This is especially true for elements which do not appear strongly in the solar corona, the best-studied plasma of this sort. One could spend a lot of time constructing and identifying such emission spectra for the wavelength range covered. Not only are there many elements to choose from, but the emission spectrum from a single element is quite dependent on plasma temperatures due to changes in the population balance of the different ionization states.

6.2 ICRF Generated Impurities

Summary: Although ICRF heating of tokamak plasmas holds considerable promise as a means of economically raising the ion temperature to the level necessary for a fusion reactor, it must first overcome several technological problems. One of the main problems with ICRF heating is the enhanced rate of impurity production, which has been observed during ICRF pulses at numerous tokamaks around the world. No general consensus exists as to the sources and mechanisms responsible for this increase in impurities in the plasma, although several models have been suggested. A study of impurity generation during a series of ICRF heating experiments at MIT's Alcator C tokamak has been completed. Many shots, involving a range of plasma and ICRF conditions, were analyzed to determine the influx

rate of iron, the dominant impurity during ICRF heating. A detailed analysis was performed to study the dependence of this impurity source term on other plasma or RF parameters. Impurity concentrations and source rates were inferred from data taken with the VUV spectrograph discussed above. The following conclusions have been drawn from the analysis of spectroscopic and other data taken during ICRF heating experiments on Alcator C:

(a) Large increases in metallic impurity concentrations were observed (factor of ~ 12 for 400 kW RF). Smaller increases were seen in the light impurities (factor of ~ 1.2 for carbon and ~ 1.9 for oxygen). Graphite limiters and stainless steel Faraday shields were used during these experiments.

(b) The change in deduced iron influx, ΔS_{Fe}, increases approximately linearly with P_{RF} for a variety of plasma and RF conditions.

(c) A prompt increase in T_{eb} at the antenna radius is seen during the ICRF pulse. The magnitude of this increase correlates well with ΔS_{Fe}.

(d) No correlation of ΔS_{Fe} is detected with working gas, plasma conditions, heating mode, antenna area exposed or activated, bulk ion heating, ion tail formation, or fast neutral particle flux.

(e) It is concluded that physical sputtering of the stainless steel antenna Faraday shield due to an elevated sheath potential ($\Phi_{\mathrm{sh}} \approx 3T_{eb}$) is the primary source of metallic impurities during ICRF heating on Alcator C. The same process, occurring at the graphite limiter, is believed to be the dominant source of carbon and oxygen. Modeling suggests that the sputtering is due to thermal particles, both from the working gas and from impurity ions.

(f) These conclusions are consistent with calculated sputtering yields obtained from an edge erosion code which utilized the measured changes in edge temperature profiles. The code predicts negligible contributions from evaporation

and sublimation, and strongly discredits the possibility of the contaminated limiter being the dominant source of metal impurities during ICRF.

Suggested Future Work: To unravel further the effects of ICRF heating on impurity production, it is desirable to monitor closely the edge plasma conditions, both globally and near the antenna structure. Probe measurements of temperature and density changes at the location of the antenna, rather than some distance away as in this study, would be useful for estimating the sputtering rate, etc., at the antenna. The estimates used in this study were based on probe measurements taken 120° toroidally away from the antenna, and it is not clear to what extent a localized absorption process near the antenna might create toroidal asymmetries in these parameters. Similarly, the lack of correlation of impurity production during ICRF with the charge exchange neutral flux carries the caveat that the CX flux was measured 60° away from the antenna. Visible spectroscopy of the edge plasma regions could be used to identify sources of specific impurities through the emission lines of neutral impurities and of low ionization states. These lines tend to be peaked near the point of origin of the impurity.

Several specific measures could be implemented in the antenna design at Alcator C. For example, use of a non-intrinsic impurity material, such as copper, for the Faraday shield would clearly allow a distinction between the impurity source contributions from the Faraday shield and those from the stainless steel vessel walls. Also, a biased Faraday shield, held at a fixed potential relative to the limiters, could be tested for its influence on impurity production. A large positive potential might reduce sputtering from ions.

Quantitative studies of erosion from the limiters, Faraday shield, probes, and other edge structures is possible. For example, these surfaces could be coated with controlled layers of slightly different materials. By using surface analysis methods,

the thickness of these layers could be measured as a function of position before and after a series of carefully controlled ICRF heated plasma discharges. By using a series of such probes positioned at different radii in the SOL plasma, one could also study the transport of impurities from regions behind the limiter into the central plasma. Knowledge of the amount of material lost per shot, for a series of reproducible shots, plus spectroscopic determination of the impurity concentrations in the plasma interior, would reveal the fraction of impurities generated at a given location which make it into the main plasma without first being deposited on some surface in the edge region. This question represents one of the largest uncertainties in the iron source rate analysis performed herein.

An investigation into the possible mechanisms for direct deposition of RF energy into the SOL plasma would also help antenna designers minimize this process, which appears closely tied to impurity generation. More theoretical analysis of this question would also be useful. An array of RF probes, particle flux analyzers, Langmuir probes, etc., located throughout the scrape-off layer could be used to confirm or eliminate various proposed processes. Non-intrusive measurements, such as CO_2 laser scattering off of plasma waves, could be used to study the amplitude and $\mathbf{k}$ spectrum of scattered or coupled RF waves in the edge plasma, especially near the antenna structure. Such techniques are used already to study plasma waves in the central plasma.

Broadly speaking, a shift in experimental emphasis may be required to fully resolve the issues surrounding the interactions between the ICRF waves, the edge plasma, and impurity generation. The primary focus of the Alcator C ICRF experiments discussed here was the successful heating of the plasma, not the study of impurity generation processes. While the large influx of impurities was a matter of concern, it was not serious enough to impair the primary research efforts.

In that situation, the program emphasis concerned such issues as antenna tuning, impedance matching, coupling studies, and maximum deliverable power. While this is to be expected in such a program, it is not necessarily conducive to careful studies of impurity generation during ICRF. That would require a more systematic scan of various plasma parameters, using many reproducible plasma shots where only one or two variables were changed at a time, rather than the mixed bag of shots seen in the original series of experiments. While the gross features of the impurity behavior were clearly identified in this study, subtle dependences on resonance conditions, working gas, etc., may have been overlooked due to scatter in the data and uncertainties built into the comparative analysis of dissimilar shots.

References

1. Rose, D.J., Feirtag, M., *Technology Review* (MIT), Dec. 1976, 21.
2. Furth, Harold P., *Sci. Amer.* **241**, 51 (Aug. 1979).
3. Furth, H.P., *Nucl. Fus.* **15**, 487 (1975).
4. Coppi, B., Rem, J. *Sci. Amer.* **227**, 65 (July 1972).
5. Lawson, J.D., *Proc. Phys. Soc.*, London, Sect. B **70**, 6 (1957).
6. Colestock, P.L., in *Applications of RF Waves to Tokamak Plasmas*, ed. Bernabei, S., Gasparino, U., Sindoni, E., Intl. School of Plasma Physics, Varenna, Italy, Vol. 1, 60 (1985).
7. Perkins, F.W., *IEEE Trans. on Plasma Sci.* **PS-12**, 53 (1984).
8. Colestock, P.L., "An Overview of ICRH Experiments," in *Wave Heating and Current Drive in Plasmas*, ed. by V.L. Granatstein and P.L. Colestock, Gordon and Breach Science Publishers, New York, 1985, p. 55.
9. Freidberg, J.P., *Rev. Mod. Phys.* **54**, 801 (1982).
10. Wesson, J.A., *Nucl. Fus.* **18**, 87 (1978).
11. Grieger, G., Renner, H., Wobig, H., *Nucl. Fus.* **25**, 1231 (1985).
12. Uo, K., *Nucl. Fus.* **25**, 1243 (1985).
13. Porkolab, M., "Lower Hybrid Wave Propagation, Heating,and Current Drive," in *Wave Heating and Current Drive in Plasmas*, ed. by V.L. Granatstein and P.L. Colestock, Gordon and Breach Science Publishers, New York, 1985, p. 219.
14. Porkolab, M., *et al., Phys. Rev. Lett.* **53**, 450 (1984).
15. Bernabei, s., *et al., Phys. Rev. Lett.* **49**, 1255 (1982).
16. Dylla, H.F., *J. Nucl. Mater.* **93 & 94**, 61 (1980).
17. Greenwald, M., *et al., Phys. Rev. Lett.* **53**, 352 (1984).
18. Isler, R.C., *Nucl. Fus.* **24**, 1599 (1984).

19. McCracken, G.M., Stott, P.E., *Nucl. Fus.* **19** (1979), 889.

20. Post, D.E., "The Role of Atomic Collisions in Fusion," Princeton Plasma Physics Lab. report PPPL-1877 (1982).

21. Hulse, Russell A., *Nuclear Tech./Fusion* **3**, 259 (1983).

22. Kirillov, V.D., *Sov. Phys.-JETP* **10**, 812 (1960).

23. Dolgov-Savel'ev, G.G., *et al., Sov. Phys. -JETP* **11**, 287 (1960).

24. Hinnov, E. *et al, Nucl. Fus.* **18**, 1305 (1978).

25. Meade, D.M., *Nuc. Fus.* **14**, 289 (1974).

26. Jensen, R.V. *et al., Nucl. Fus.* **17**, 1187 (1977).

27. DeMichelis,C. and M. Mattioli., *Nucl. Fusion* **21**, 677 (1981).

28. Griem,H. *Plasma Spectroscopy.* McGraw-Hill, New York, 1964.

29. Foord,M.E., E.S.Marmar, J.L.Terry. *Rev. Sci. Inst.* **53**, 1407 (1982).

30. Coppi,B., *et al, Phys. Fluids* **19**, 1144 (1976).

31. Lipschultz, B., *et al., Nucl.Fus.* **24**, 977 (1984).

32. Takase, Y. MIT Plasma Fusion Center, Private communication, (1985).

33. Gabriel, A.H. and Carole Jordan, in *Case Studies in Atomic Collision Physics*, Vol.2, Chap.4, North Holland, Amsterdam, 1971.

34. McWhirter, R.W.P., "Spectral Intensities," in *Plasma Diagnostic Techniques*, ed. by R.H. Huddleston and S.L. Leonard, Academic Press, New York, 1965, chap. 5.

35. Mason, H.E. *et al., Astron. Astrophys.* **73**, 74 (1979).

36. Lawson, K.D. and N.J.Peacock, "Electron Densities of Solar Flares from Intensity Ratios of $n = 2 - 2$ Transitions," Culham Lab. (Euratom/UKAEA Fusion Assn.) Report CLM-P711 (1982).

37. Kallne, E., *et al., Phys. Scripta* **31**, 551 (1985).

38. Bitter, M., *et al., Phys. Rev.* **32**, 3011 (1985).

39. Marmar,E.S., *et al., Nucl. Fus.* **22**, 1567 (1982).

40. Molvig, K., "Recent Progress toward a Self-Consistent Theory of Anomalous Transport in Tokamaks," in *Proc. Intl. Conf. on Plasma Physics*, Nagoya, Japan (1980).

41. Lipschultz, B., LaBombard, B., Manning, H.L., Terry, J.L., Knowlton, S., *et al.*, "Impurity Sources During Lower-Hybrid Heating on Alcator C," M.I.T. Plasma Fusion Center Report PFC/JA-85-45 (1985).

42. Sampson, J., *Techniques of Vacuum Ultraviolet Spectroscopy*, Wiley and Sons, New York, 1967.

43. Zaidel', A.N., and E.Ya. Shreider, *Vacuum Ultraviolet Spectroscopy*, trans. by Z. Lerman, Ann Arbor–Humphrey Science Publishers, Ann Arbor, 1970.

44. Bell R.E., Finkenthal, M., Moos, H.W., *Rev. Sci. Instrum.* **52** (1981) 1806.

45. Sandel, Bill R., Broadfoot, A. Lyle, *Appl. Optics* **15**, 3111 (1976).

46. Fonck, R.J., Ramsey, A.T., Yelle, R.V., *Appl. Optics* **21** (1982) 2115.

47. Hodge, W.L., Stratton, B.C., Moos, H.W., *Rev. Sci. Instrum.* **55** (1984) 16.

48. Wiza, Joseph L. *Nucl. Instr. and Methods* **162**, 587 (1979).

49. Lukirskii, A.P., Savinov, E.P., Brytov, I.A., Shepelev, Y.F., *Bull. Acad. Sci. USSR Phys. Ser.* **28** (1964) 774.

50. Saloman, E.B., Pearlman, J.S., Henke, B.L., *Applied Optics* **19** (1980) 749.

51. Timothy, J. Gethyn, *Rev. Sci. Instrum.* **52**, 730 (1981).

52. Sandel, B.R., Broadfoot, A.Lyle, Shemansky, D.E., *Appl. Optics* **16**, 1435 (1977).

53. Malina, Roger, Ph.D. Thesis, U.C.-Berkeley, (1980) (unpublished).

54. Talmi, Yair, and Simpson, R.W., *Appl. Optics* **19**, 1401 (1980).

55. Simpson, Raymond W., *Rev. Sci. Instrum.* **50**, 730 (1979).

56. Manning, H.L., Terry, J.L., Marmar, E.S. *Bull. Am. Phys. Soc.* **28** (1983),

1250.

57. J.E. Manson Co., P.O. Box 1288, Concord, Mass. 01742. Details and literature regarding Soft X-ray Calibration systems may be obtained from Mr. Manson at the above address.

58. Martin, C., Bowyer, S., *Applied Optics* **21** (1982) 4206.

59. Marmar, E.S., Cecchi, J.L., Cohen, S.A., *Rev. Sci. Instr.* **46**, 1149 (1975). See also: Marmar, E.S., Ph.D. Thesis, Princeton University, (1976) (unpublished).

60. Marmar, E.S., Rice, J.E., Terry, J.L., Seguin, F.H., *Nucl. Fus.* **22** (1982), 1567.

61. Terry, J.T., Greenwald, M., *et al.*, "Particle Transport Following Pellet Injection into the Alcator C Tokamak," MIT Plasma Fusion Center Report PFC/JA-86-23 (1986).

62. Kelly, R.L., "Atomic and Ionic Spectrum Lines Below 2000 Angstroms: Hydrogen through Argon," Oak Ridge Natl. Lab. report ORNL-5922 (also DOE report DE83 002582), (1982). See also R.L. Kelly with L.J. Palumbo, "Atomic and Ionic Spectrum Lines Below 2000 Angstroms: Hydrogen through Krypton," Naval Research Lab. report NRL-7599, (1973).

63. Bauche, J., Bauche-Arnoult, C., Luc-Koenig, E., Wyart, J.-F., Klapisch, M., *Phys. Rev. A* **28**, 829 (1983).

64. Hinnov, E., Mattioli, M., *Phys. Letters* **66A**, 109 (1978).

65. Swanson, D.G. *Phys. Fluids* **28** (1985) 2645.

66. *PPL Digest*, Information Services, Princeton Plasma Physics Lab., March 1982.

67. Takahashi, H., *J. de Physique* **38**, C6-171 (1977).

68. Hwang, D., Colestock, P.L., Phillips, C.K. "The Theory of Minority Species Fast Magnetosonic Wave Heating in a Tokamak," in *Wave Heating and Current*

Drive in Plasmas, ed. by V.L. Granatstein and P.L. Colestock, Gordon and Breach Science Publishers, New York, 1985, p. 1.

69. Krapchev, V.B., *Nucl. Fus.* **25**, 455 (1985).

70. Cohen, S.A., Bernabei, S., Budny, R., Chu, T.K., Colestock, P., *et al.*, *J. Nucl. Materials* **128-9** (1984) 280.

71. Messiaen, A.M., Koch, R., Bhatnagar, V.P., Vandenplas, P.E., Weynants, R.R., in *Heating in Toroidal Plasmas*, (Proc. 4th Intl. Sympos., Rome, 1984), Vol.I, Intl. School of Plasma Physics, Varenna (1984) 315.

72. Colestock, P.L., Davis, S.L., Hosea, J.C., Hwang, D.Q., Thompson, H.R., in *Heating in Toroidal Plasmas*, (Proc. 2nd Joint Grenoble-Varenna Intl. Sympos., Como, 1980), Vol.I, Commission of the European Communities, Brussels (1981) 471.

73. Kimura, H., Matsumoto, H., Odajima, K., Konoshima, S., Yamamoto, T., *et al.*, in *Plasma Physics and Controlled Nuclear Fusion Research*, Proc. 9th Int. Conf. Baltimore 1982), Vol.2, IAEA, Vienna (1983) 113.

74. Adam, J., Lapierre, J., TFR Group, in *Heating in Toroidal Plasmas*, (Proc. 3rd Joint Varenna-Granoble Intl. Sympos., Grenoble, 1982), Vol. III, Commission of the European Communities, Brussels (1982) 1175.

75. Jacquinot, J., Anderson, R., Arbez, J., Bartlett, D., Beaumont, B., *et al.*, "Preliminary ICRF Results from JET," JET Joint Undertaking, Abingdon, Report JET-P(85)09 (1985).

76. TFR Group, Sand, F., *Nucl. Fus.* **25** (1985) 1719.

77. Weynants, R.R., in *Heating in Toroidal Plasmas*, (Proc. 4th Intl. Sympos., Rome, 1984), Vol.I, Intl. School of Plasma Physics, Varenna (1984) 211.

78. Hosea, J., Bell, R., Budny, R., Cavallo, Cohen, S., *et al.*, in *Heating in Toroidal Plasmas*, (Proc. 4th Intl. Sympos., Rome, 1984), Vol.I, Intl. School of Plasma

Physics, Varenna (1984) 261.

79. Suckewer,S., Hinnov, E., Hwang, D., Schivell, J., Schmidt, G.L., *et al.*, *Nuclear Fusion* **21**, (1981) 981.

80. Stratton, B.C., Moos, H.W., Hodge, W.L., Suckewer, S., Hosea, J.C., *et al.*, *Nucl. Fus.* **24** (1984), 767. *et al.*, *J. Nucl. Materials* **128-9** (1984) 280.

81. Cohen, S.A., Ruzic, D., Voss, D.E., Budny, R., Colestock, P., *et al.*, *Nucl. Fus.* **24** (1984), 1490.

82. Equipe TFR, in *Heating in Toroidal Plasmas*, (Proc. 3rd Joint Varenna-Granoble Intl. Sympos., Grenoble, 1982), Vol. III, Commission of the European Communities, Brussels (1982) 1177.

83. TFR Group, ICRF Heating in T.F.R., Association EURATOM-CEA sur la Fusion, Fontenay-aux-Roses, Report EUR-CEA-FC-1186 (1983).

84. Equipe TFR, *Plasma Physics and Controlled Fusion* **26** (1984) 165.

85. Equipe TFR, in *Heating in Toroidal Plasmas*, (Proc. 4th Intl. Sympos., Rome, 1984), Vol.I, Intl. School of Plasma Physics, Varenna (1984) 277.

86. TFR Group, in *Proc. 11th European Conf. on Cont. Fusion and Plasma Physics, Aachen (1983)*, Europhysics Conf. Abstracts, Vol. 7D, European Phys. Soc., Geneva (1983) 493.

87. TFR Group, *J. Nucl. Materials* **128-9** (1984) 292.

88. Breton, C., De Michelis, C., Hecq, W., Mattioli, M. Ramette, J., Saoutic, B.,*Plasma Physics and Cont. Fusion* **27** (1985), 355.

89. JFT-2 Group, in *Heating in Toroidal Plasmas*, (Proc. 3rd Joint Varenna-Granoble Intl. Sympos., Grenoble, 1982), Vol. I, Commission of the European Communities, Brussels (1982) 259.

90. JFT-2 Group, in *Heating in Toroidal Plasmas*, (Proc. 3rd Joint Varenna-Granoble Intl. Sympos., Grenoble, 1982), Vol. III, Commission of the Euro-

pean Communities, Brussels (1982) 1191.

91. Odajima, K., Matsumoto, H., Kimura, H., Hoshino, K., Kasai, S., *et al.*, in ***Heating in Toroidal Plasmas***, (Proc. 4th Intl. Sympos., Rome, 1984), Vol.I, Intl. School of Plasma Physics, Varenna (1984) 243.

92. Ogawa, H., Odajima, K., Ohtsuka, H., Matsumoto, H., Kimura, H., *et al.*, *J. Nucl. Materials* **128-9** (1984) 298.

93. TFR Group, F. Sand. "Test of the JET TFR Antenna," Association Euratom-CEA sur la Fusion, Fontenay-aux-Roses, Report EUR-CEA-FC-1219 (1984).

94. Mori, M., Hasegawa, K., Honda, A., Hoshino, K., Ishibori, I., *et al.*, in *Plasma Physics and Controlled Nuclear Fusion Research*, Proc. 10th Int. Conf. London, 1984), Vol.1, IAEA, Vienna (1985) 445.

95. Ichimura, M., Fujita, J., Hirokura, S., Kako, E., Kawahata, K., *et al.*, "ICRF Heating Experiments on JIPP T-II," Nagoya Univ., Inst. of Plasma Physics, Rep. IPPJ-650 (1983).

96. Noda, N., Watari, T., Toi, K., Kako, E., Sato, K., *et al.*, *J. Nucl. Mat.* **128-9** (1984) 304.

97. Toi, K., Watari, T. Ohkubo, K., Kawahata, K., Noda, N., *et al.*, in *Plasma Physics and Controlled Nuclear Fusion Research*, Proc. 10th Int. Conf. London, 1984), Vol.1, IAEA, Vienna (1985) 523.

98. Vertiporokh, A., Kurchatov Inst., Moscow,private communication (1985).

99. Taylor, R.J., Evans, J., Keller, L., Lai, K.F., Rossing, V., *et al.*, in *Plasma Physics and Controlled Nuclear Fusion Research*, Proc. 10th Int. Conf. London, 1984), Vol.1, IAEA, Vienna (1985) 581.

100. Ohkawa, T., Hino, T., Andrews, P.L., Chan, V.S., Chiu, S.C., "ICRF Launcher for Reduction of Impurity Production," GA Technologies Inc. Report GA-A17777 (1984) (submitted to IEEE Trans. on Plasma Sci.).

101. Itoh, K., Itoh, S., Fukuyama, A., "Excitation of ICRF Waves in Tokamaks by Waveguide Launcher," Hiroshima Univ., Inst. for Fusion Theory Report HIFT-94 (1984).

102. Itoh, K., Fukuyama, A., Itoh, S., "A Possible Origin of Metal Impurities in ICRF Heating Experiments," Hiroshima Univ., Inst. for Fusion Theory Report HIFT-93 (1984).

103. Chan, V.S., Chiu, S.C., Wong, S.K., *Nucl. Fus.* **25** (1985), 697.

104. Porkolab, M., Blackwell, B., Bonoli, P., Griffin, D., Knowlton, S., *et al.*, in *Plasma Physics and Controlled Nuclear Fusion Research*, Proc. 10th Int. Conf. London, 1984), Vol.1, IAEA, Vienna (1985) 463.

105. Hulse, Russell A., *Nuclear Tech./Fusion* **3**, 259 (1983).

106. Breton, C., de Michelis, C., Mattioli, M, J. Quant. Spectrosc. Radiat. Transfer **19**, 367 (1978).

107. Lotz, Wolfgang, *Astrophys. J., Suppl.* **14**, 207 (1967).

108. Lotz, Wolfgang, *Zeitschrift f. Phys.* **216**, 341 (1968).

109. Fuhr, J.R., Martin, G.A., Wiese, W.L., Younger, S.M., *J. Phys. and Chem. Ref. Data* **10**, 305 (1981).

110. Mann, Joseph B., *Atomic Data and Nuclear Data Tables* **29**, 407 (1983).

111. Hirshman, S.P., Sigmar, D.J., *Nucl. Fus.* **21**, 1079 (1981).

112. TFR Group, "Laser-Injected Impurity Transport in Ohmic and ICRF-Heated TFR Plasmas," Association Euratom-CEA sur la Fusion, Fontenay-aux-Roses, Report EUR-CEA-FC-1274 (1985) (subm. to Nucl. Fusion).

113. Post, D.E., Jensen, R.V., Tartar, C.B., Grasberger, W.H., Lokke, W.A., *Atomic Data and Nucl. Data Tables* **20** (1977), 397.

114. McCracken, G.M., Stott, P.E., *Nucl. Fus.* **19** (1979), 889.

115. Demidenko, I.I., Leonov, V.M., Lomino, N.S., Ovcharenko, V.D., Padalka,

V.G., Polyakova, G.N., *Sov. J. Plasma Phys.* **10** (1984) 292.

116. Ehrenberg, J., Behrisch, R., "Surface Analysis of a Central Part of the JET Graphite Limiter," Max-Planck-Inst. für Plasmaphysik, Garching, Report IPP 9/47, (1984).

117. Behrisch, R., Børgesen, P., Ehrenberg, J., Scherzer, B.M.U., Sawicka, B.D. *et al.. J. Nucl. Materials* **128-9** (1984), 470.

118. Staudenmaier, G., *J. Vac. Sci. Technol. A* **3** (1985), 1091.

119. Doyle, B., Sandia National Lab., Albuquerque, private communication (1985).

120. Ehrenberg, J., Behrisch, R., " Surface Analysis of a Central Part of the JET Graphite Limiter," Max-Planck-Institute für Plasmaphysik, Munich, Report IPP 9/47 (1984).

121. Behringer, K.H., Carolan, P.G., Denne, B., Decker, G., Engelhardt, W., *et al.*, "Impurity and Radiation Studies During the JET Ohmic Heating Phase," JET Joint Undertaking, Abingdon, Report JET-P(85)08 (1985) (subm. to Nucl. Fusion).

122. Ehrenberg, J., Behrisch, R., Coad, J.P., Erents, K., De Kock, L., *et al.*, *Bull. Am. Phys. Soc.* **30** (1985), 1525.

123. Fiore, C.L., Zhao, F., *Bull. Am. Phys. Soc.* **29**, p. 1224 (1984).

124. Parker, R.R., Greenwald, M., Luckhardt, S.C., Marmar, E.S., Porkolab, M., Wolfe, S.M, *Nucl. Fus.* **25**, 1127 (1985).

125. LaBombard, B., Plasma Fusion Center, Mass. Inst. of Tech.,private communication (1985).

126. Rice, J.E., Marmar, E.S., Lipschultz, B., Terry, J.L., *Nucl. Fusion* **24**, (1984) 329.

127. Wan, A., Plasma Fusion Center, Mass. Inst. of Tech., private communication (1985).

128. Lipschultz, B., LaBombard, B., Manning, H.L., Terry, J.L., Knowlton, S., *et al.*, "Impurity Sources During Lower-Hybrid Heating on Alcator C," M.I.T. Plasma Fusion Center Report PFC/JA-85-45 (1985).

129. Erents, S.K., Stangeby, P.C., Tagle, J.A., McCracken, G.M., De Kock, L., Stott, P.E., *Bull. Am. Phys. Soc.* **30** (1985), 1525.

130. Behringer, K.H., private communication, 1986.

Appendix 1

"Stainless Steel" Spectra

The following spectra were taken by using the differential spectra technique, described in Chapter 3, to observe the change in the VUV spectrum due to the effects of ICRF heating. A large influx of metal impurities was seen, chiefly due to erosion of the stainless steel Faraday shield covering the ICRF antenna. Note, for example, the spectrum from about 120 Å to 147 Å was obtained by subtracting the *Before ICRF* spectrum from the *After ICRF* spectrum in Figure 4.7. This composite spectrum is mostly taken from shots with over 350 kW of ICRF power. Central electron temperatures were about 2100 eV. Vertical scale is somewhat relative; individual spectra were normalized so as to smoothly join the preceding portion of the spectrum.

A keyed listing of all the prominent lines on a given page is placed under the figure. The lines are listed by impurity ionization state, e.g. Fe-XXIII, followed by the wavelength of the line in Å. The notation "(x2)" means that the line is viewed in second order. The notation "Fe-XVIII, 93.92 (Fe-XX, 93.79) " means that the line is a blend of two closely spaced lines, with the stronger component being listed first and the weaker given in parentheses. Several lines are listed only as "Mo-?". This indicates that the line is known to be due to molybdenum, but the ionization state is uncertain.

There are a few gaps and "negative" lines in the spectrum, denoted by an asterisk (*). These are due to argon lines which were decreasing in brightness while the iron lines, etc. were increasing due to ICRF heating. The decrease in argon is due to the timing of the argon gas injection, used for another diagnostic, and is not related to the ICRF experiments.

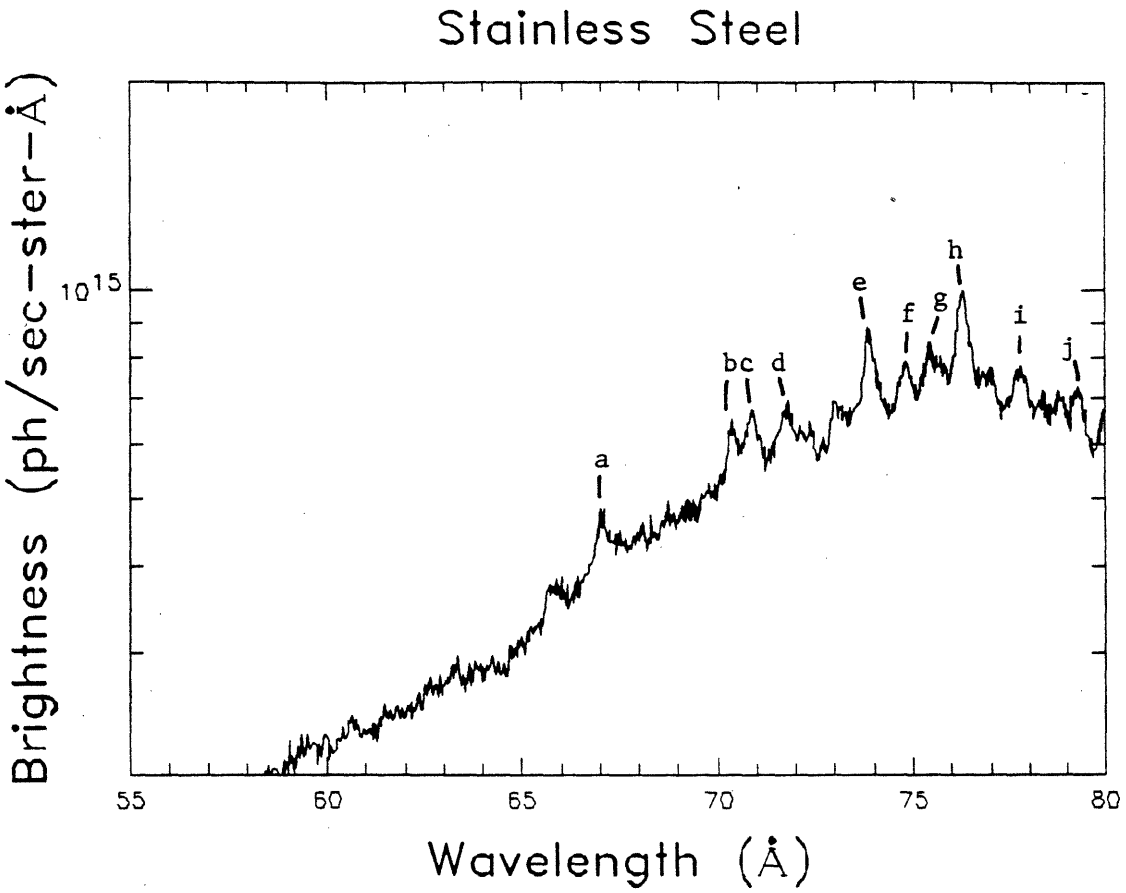

a) C-VI, 33.74 (x2) b) through i) Moly band, ~Mo-XXV

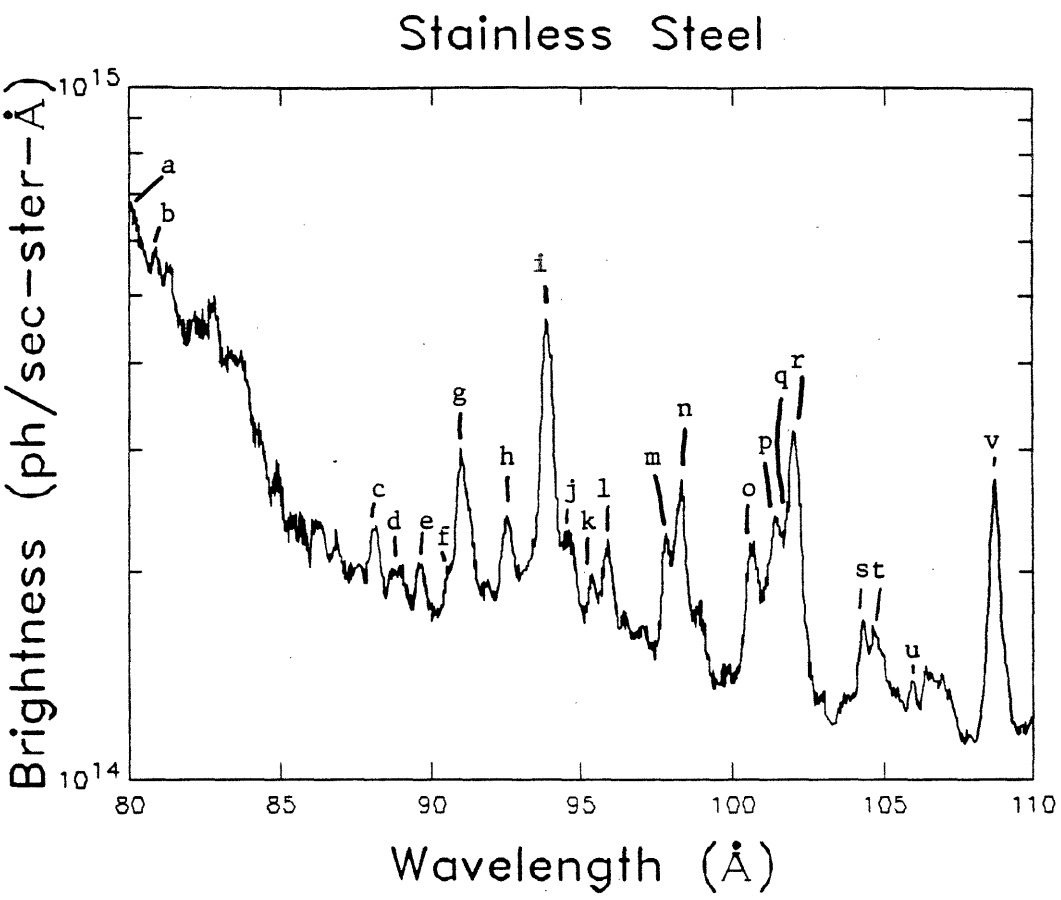

a) C-V, 40.27 (x2) b) C-V, 40.73 (x2) c) Mo-?

d) Ni-XXI, 88.82 (Mo-?) e) Mo-? f) Fe-XX, 90.60

g) Fe-XIX, 91.02 h) Mo-? i) Fe-XVIII, 93.92 (Fe-XX, 93.79)

j) Fe-XX, 94.65 k) Mo-? l) Ni-XXI, 95.86 (Mo-?)

m) Fe-XXI, 97.88 n) Fe-XXI, 98.36 (Fe-XX, 98.37)

o) Fe-XXII, 100.78 p) Fe-XIX, 101.55

q) Cr-XVIII, 101.93 r) Fe-XXI, 102.22 s) Fe-XVIII, 103.94

t) Mo-XXXII, 104.26 u) Mo-XXX, 105.58 v) Fe-XIX, 108.35

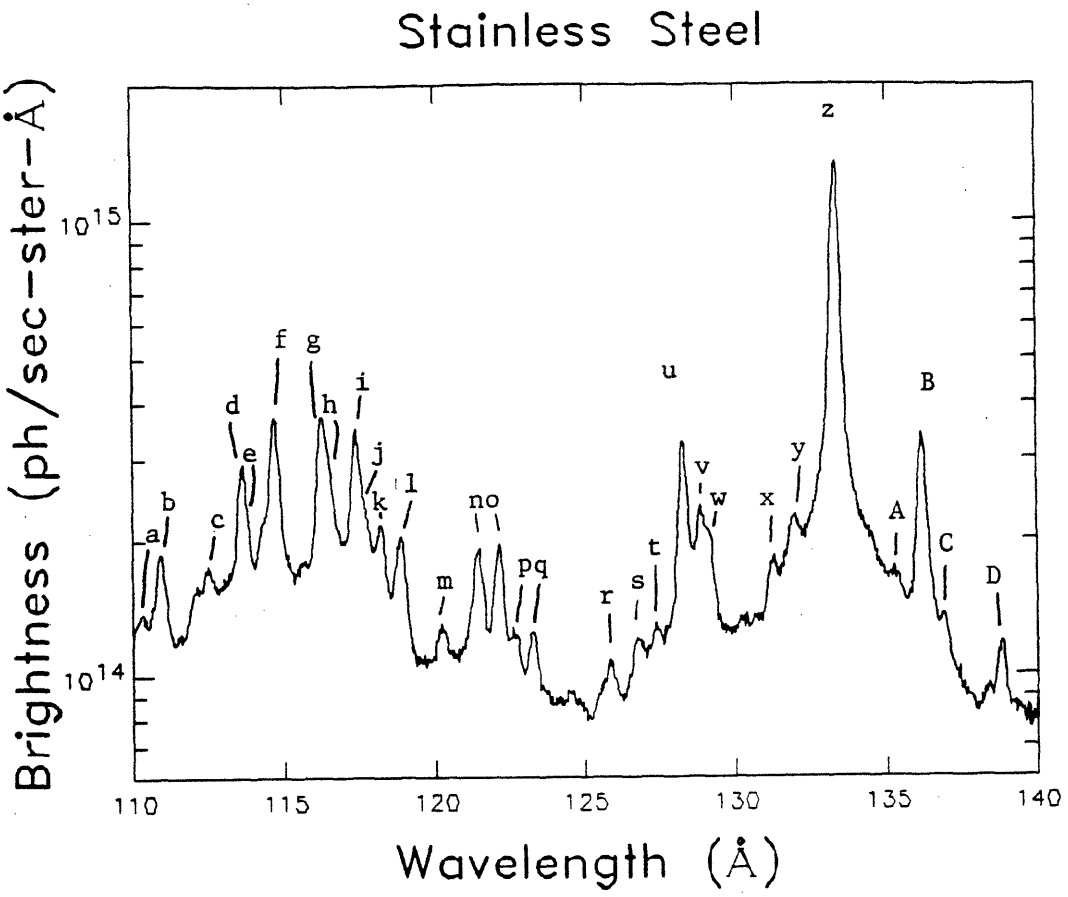

a) Fe-XIX, 109.95 b) Fe-XX, 110.64 c) Mo-?

d) Fe-XX, 113.35 (Fe-XXI, 113.30) e) Cr-XIX, 113.97

f) Fe-XXII, 114.41 g) Mo-XXXI, 115.97 h) Fe-XXII, 116.28

i) Fe-XXII, 117.17 j) Fe-XXI, 117.51 k) Ni-XXV, 117.95

l) Fe-XX, 118.66 (Fe-XXI, 118.69) m) Fe-XIX, 119.98

n) Fe-XXI, 121.21 o) Fe-XX, 121.83 p) Mo-?

q) Cr-XVII, 122.96 r) Cr-XVIII, 125.51 s) Cr-XIX, 126.33

t) Mo-XXXII, 126.94 u) Mo-XXXII, 127.81 v) Cr-XX, 128.42

w) Fe-XXI, 128.73 x) Cr-XX, 130.76 y) Cr-XX, 131.50

z) Fe-XXIII, 132.87 (Fe-XX, 132.85) A) C-VI, 33.74 (x4)

B) Fe-XXII, 135.78 C) Cr-XVIII, 136.52 D) Cr-XIX, 138.45

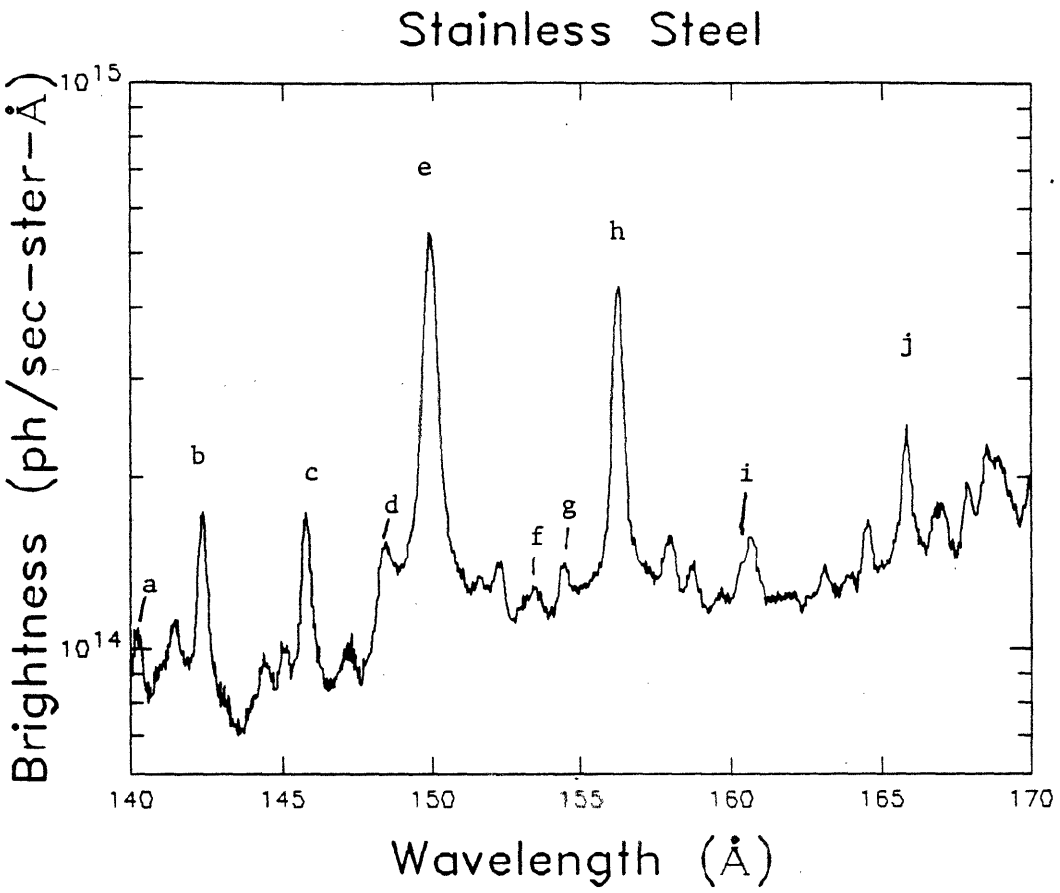

a) Cr-XVIII, 139.87 b) Fe-XXI, 142.16 c) Fe-XXI, 145.65

d) Mo-? (x2) e) Cr-XXI, 149.90 f) Mo-? (x2)

g) Fe-XXIII, 154.33 h) Fe-XXII, 155.92 i) Cr-XIX, 160.30

j) Cr-XIX, 165.46

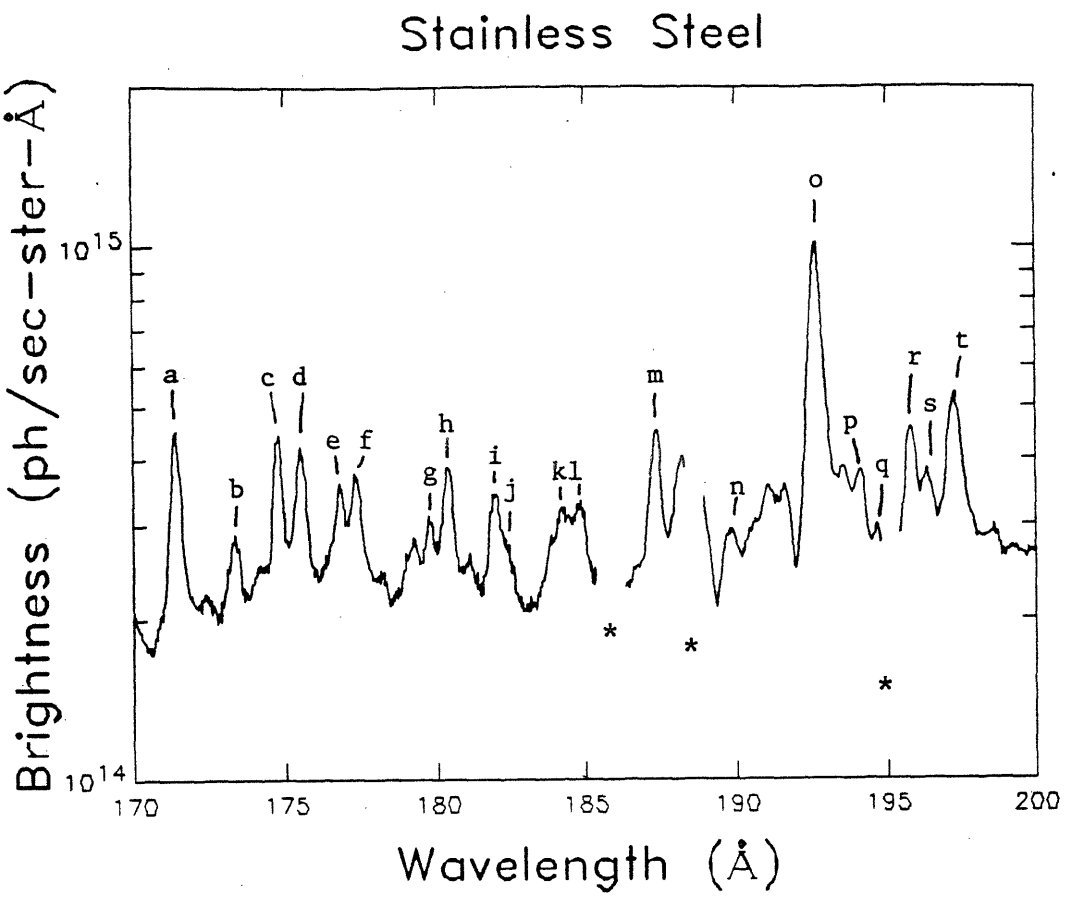

a) Fe-IX, 171.07 b) O-VI, 172.94 & 173.08 c) Fe-X, 174.58

d) Fe-X, 175.26 (Cr-XX, 175.42) e) Mo-XXXII, 176.67

f) Fe-X, 177.24 g) Fe-XI, 179.76

h) Fe-X, 180.45 (Fe-XI, 180.41) i) Fe-XIX, 91.02 (x2)

j) Fe-XI, 182.17 (Fe-X, 182.31) k) Fe-X, 184.53

l) Fe-XI, 184.80 m) Fe-XII, 186.88 n) Fe-XX, 94.65 (x2)

o) Fe-XXIV, 192.02 p) Fe-XII, 193.52 q) Ni-XVI, 194.04

r) Fe-XII, 195.13 s) Fe-XXI, 97.88 (x2)

t) Fe-XXI, 98.36 (x2) (Fe-XX, 98.37 (x2))

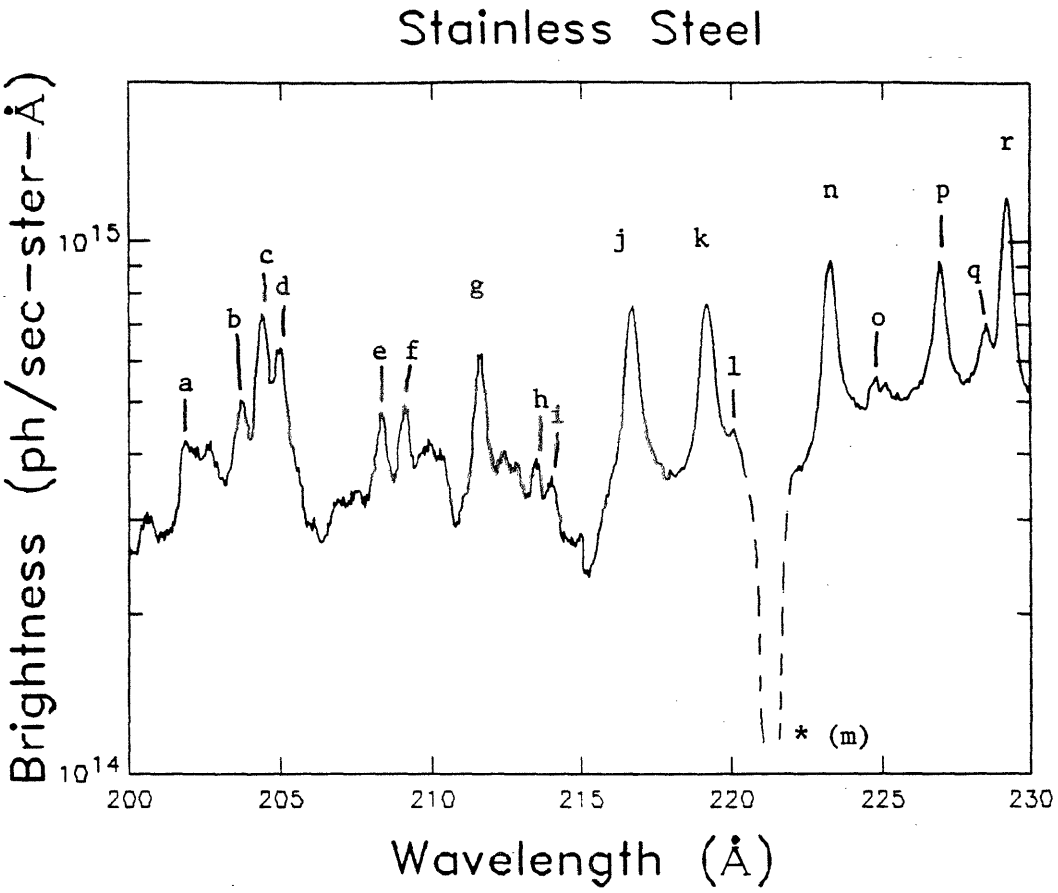

a) Fe-XXII, 100.78 (x2) b) Fe-XIX, 101.55 (x2) c) Cr-XVII, 101.93 (x2)

d) FeXXI, 102.22 (x2) e) Fe-XVIII, 103.94 (2) f) Mo-XXXII, 104.26 (x2)

g) Fe-XIV, 211.32 h) Cr-XVI, 106.63 (x2) i) Cr-XVIII, 106.83 (x2)

j) Fe-XIX, 108.37 (x2) k) Fe-XIV, 219.13 l) Fe-XIX, 109.95 (x2)

m) Ar-XV, 221.10 n) Cr-XXII, 223.02 o) Mo-? (x2)

p) Fe-XX, 113.35 (x2), (Fe-XXI, 113.30 (x2)) q) Cr-XIX, 113.97 (x2)

r) Fe-XXII, 114.41 (x2)

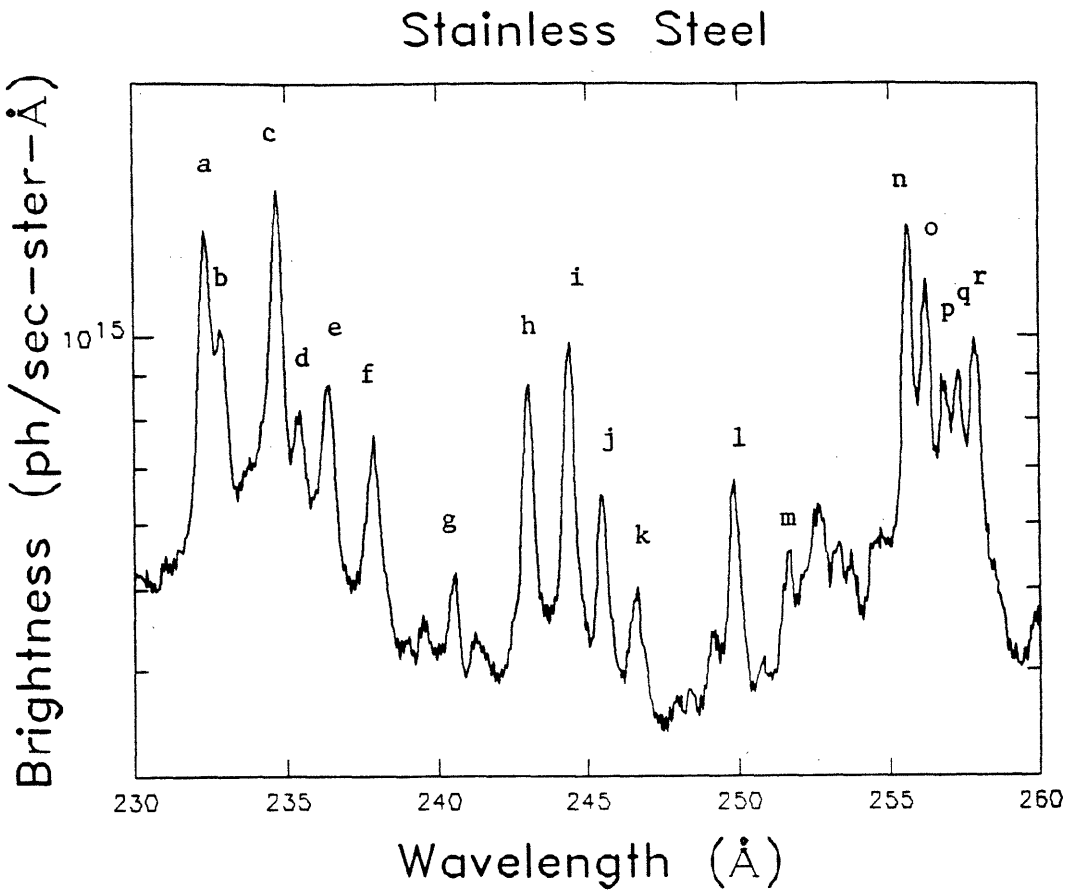

a) Mo-XXXI, 115.97 (x2) b) Fe-XXII, 116.28 (x2) c) Fe-XXII, 117.17 (x2)

d) Fe-XXI, 117.51 (x2) e) Ni-XXV, 117.95 (x2) f) Fe-XX, 118.69 (x2)

g) Fe-XIX, 119.98 (x2) h) Fe-XXI, 121.21 (x2) i) Fe-XX, 121.83 (x2)

j) Mo-? (x2) k) Cr-XVII, 122.96 (x2) l) Ni-XVII, 249.18

m) Fe-XVI, 251.06 n) Fe-XXIV, 255.10 o) Mo-XXXII, 127.81 (x2)

p) Cr-XVIII, 128.10 (x2) q) Cr-XX, 128.42 (x2) r) Fe-XXI, 128.73 (x2)

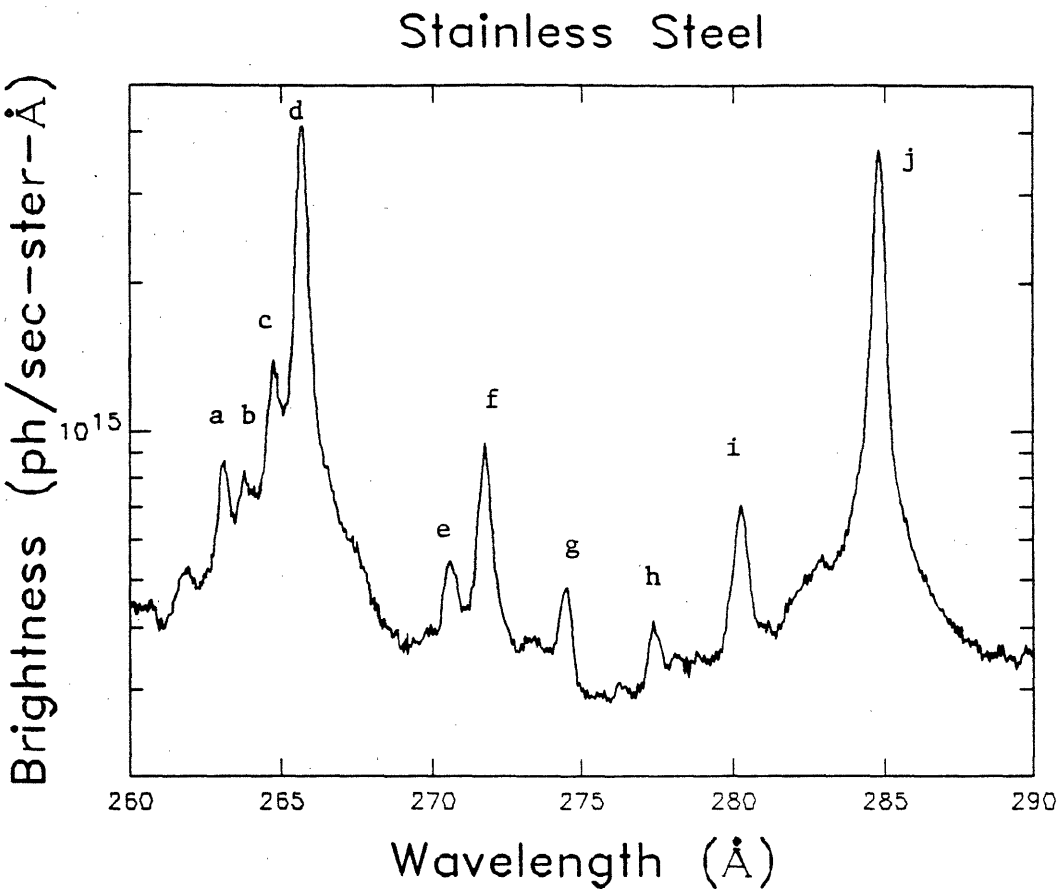

a) Fe-XVI, 262.97 b) Fe-XXIII, 263.74

c) Fe-XVI, 265.01 (Fe-XIV, 264.80) d) Fe-XXIII, 132.87 (x2)

e) Fe-XIV, 270.51 f) Fe-XXII, 135.78 (x2) g) Fe-XIV, 274.22

h) Cr-XIX, 138.45 (x2) i) Cr-XXII, 279.71 j) Fe-XV, 284.15

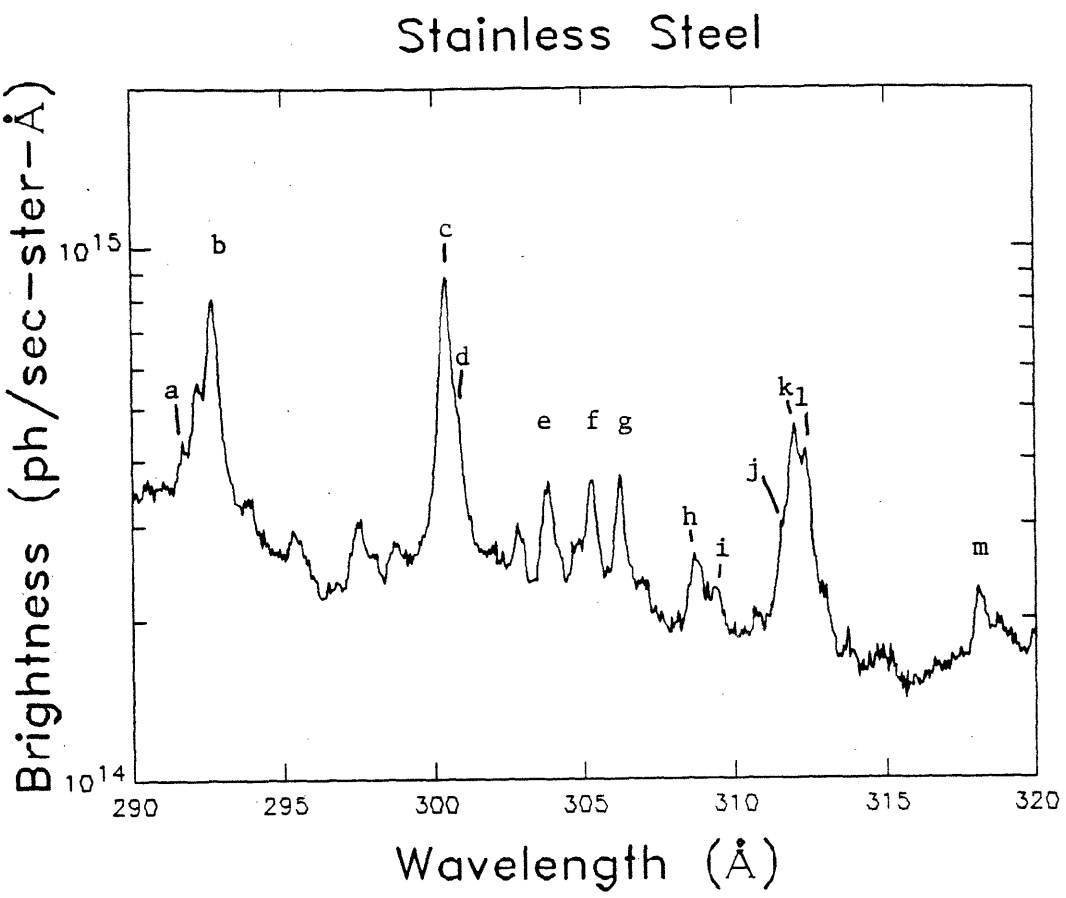

a) Fe-XXI, 145.65 (x2)
b) Ni-XVIII, 292.00
c) Cr-XXI, 149.90 (x2)
d) O-VI, 150.10 (x2)
e) Si-XI, 303.31
f) Mn-XIV, 304.85
g) Cr-XII, 305.81
h) Fe-XXII 154.33 (x2)
i) Fe-XX, 309.25
j) Cr-XII, 311.55
k) Fe-XXII, 156.01 (x2)
l) C-IV, 312.43
m) Fe-XIII, 318.21

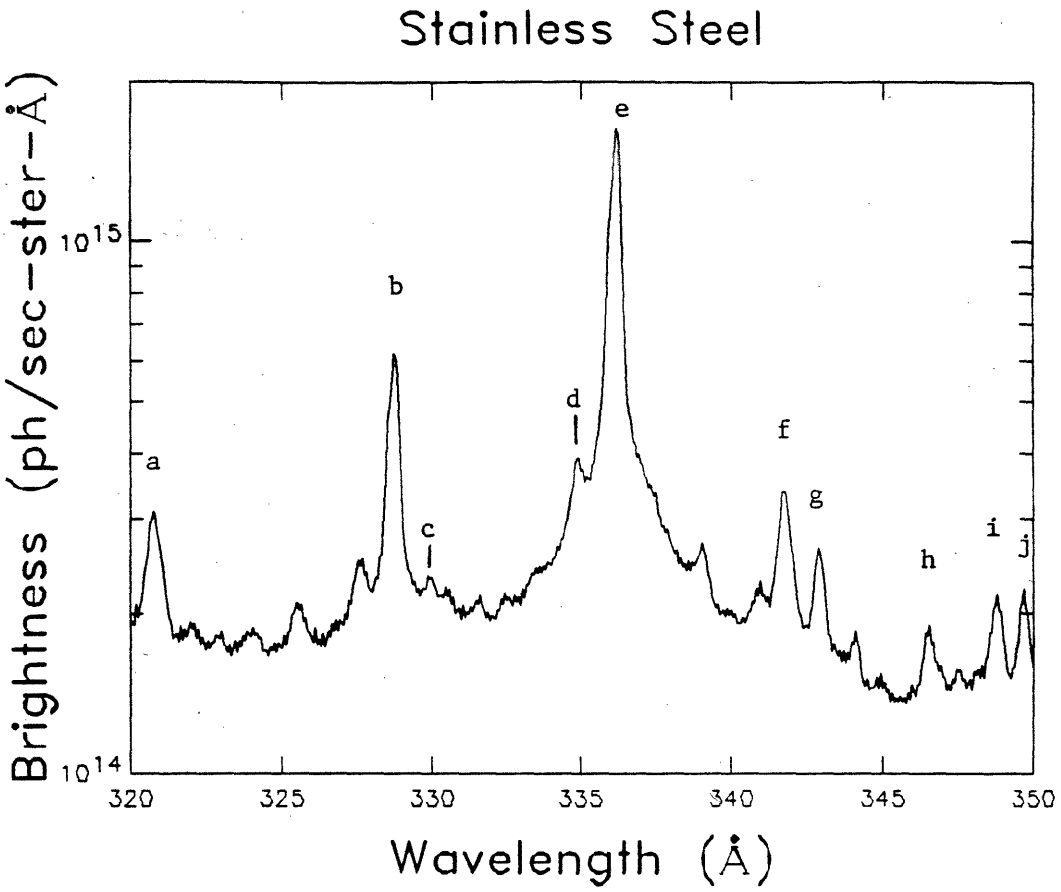

a) Ni-XVIII, 320.56 b) Cr-XIII, 328.29 c) Mo-XII, 329.41

d) Fe-XIV, 334.15 e) Fe-XVI, 335.41 f) Mo-XIII, 340.9

g) Fe-IX, 171.07 (x2) h) Fe-X, 345.75 i) Fe-XIII, 348.20

j) Fe-X, 174.58

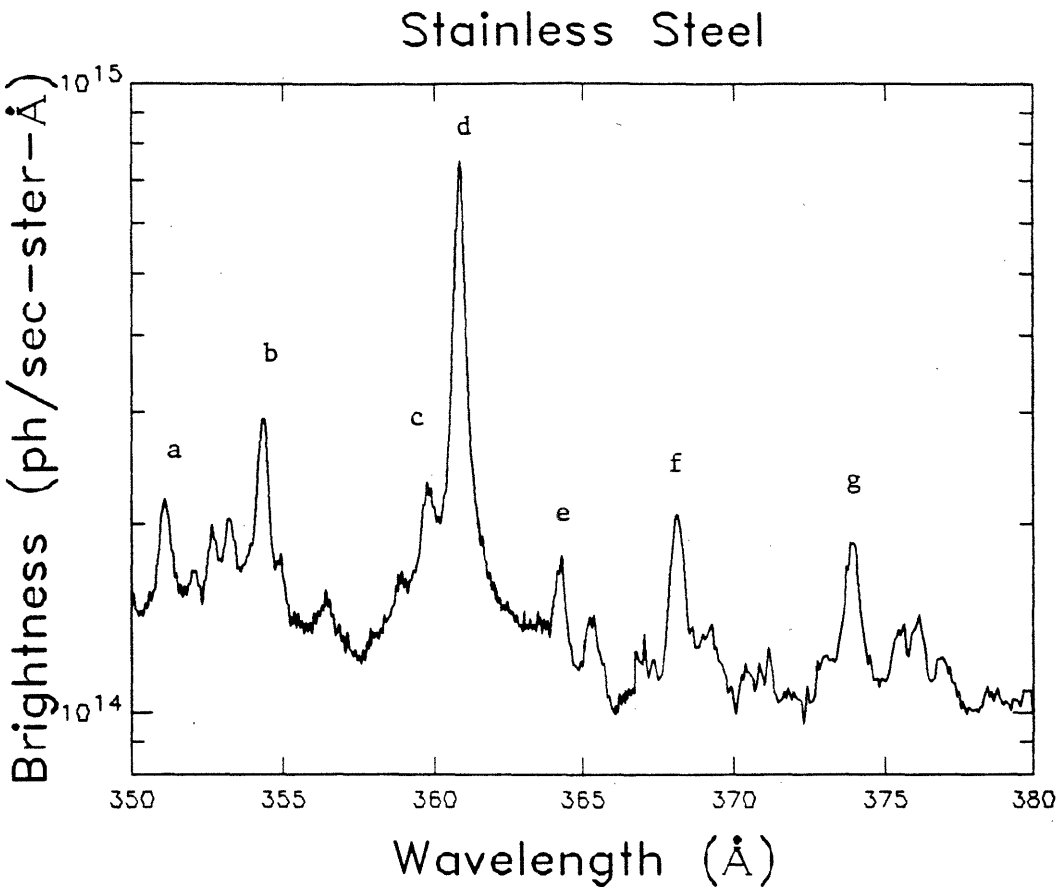

a) Cr-XX, 175.42 (x2)
b) Fe-XIV, 353.84
c) Fe-XIII, 359.63
d) Fe-XVI, 360.80
e) Fe-XII, 364.48
f) Fe-XIII, 368.12
g) Mo-XIV, 373.65

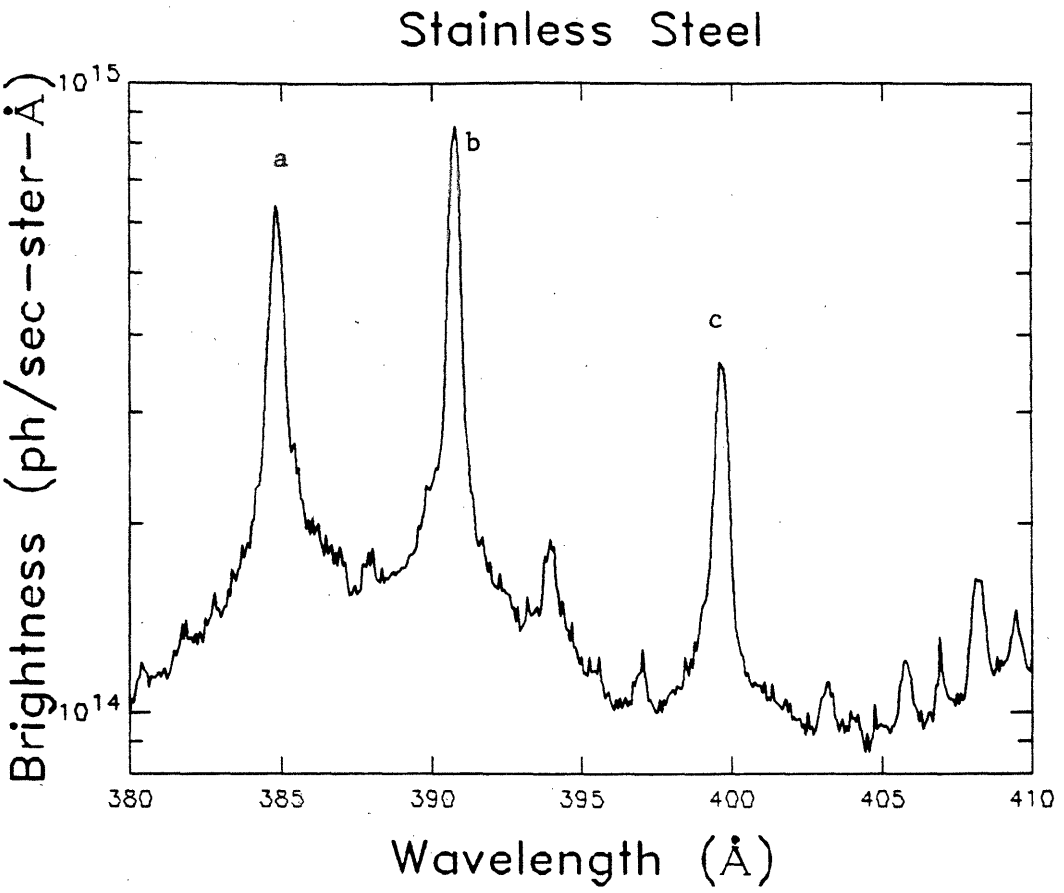

a) C-IV, 384.1 b) Cr-XIV, 389.81 c) Fe-XXIII, 132.87 (x3)

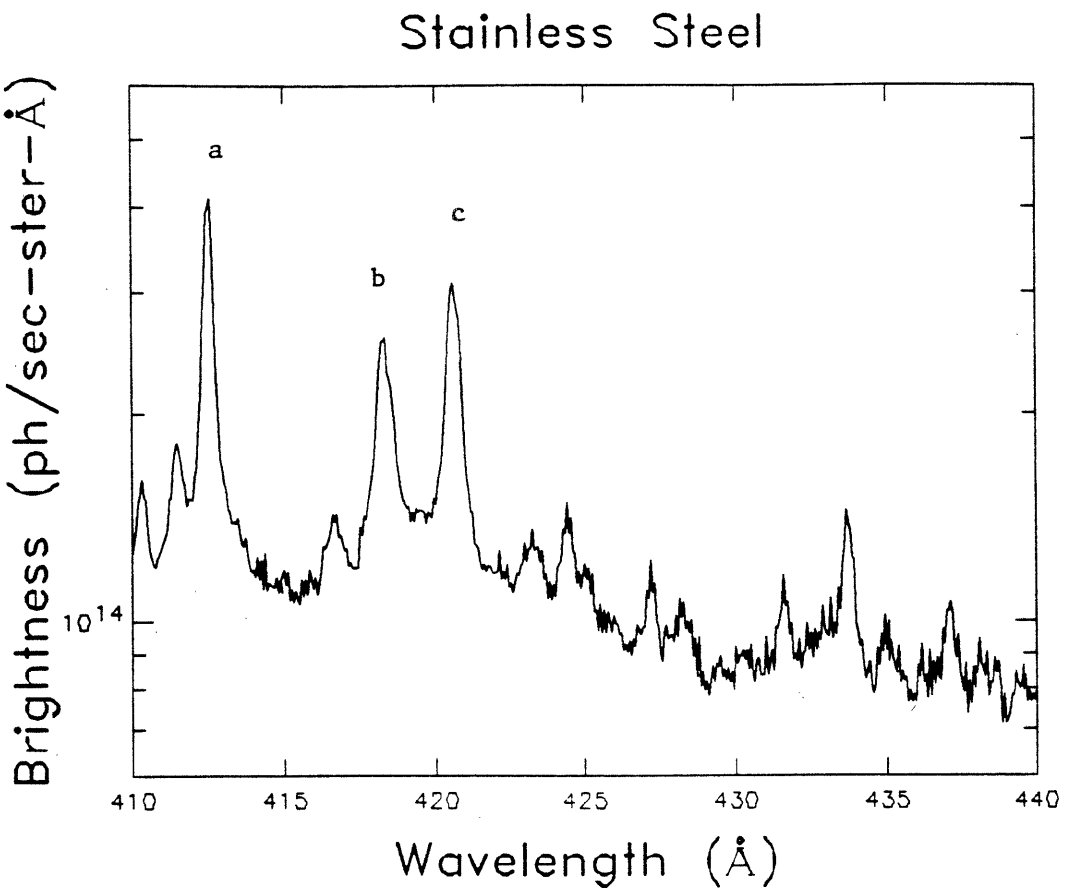

a) Cr-XIV, 411.99 b) S-XIV, 417.6 c) C-IV, 419.6